

**Quantitative measurements of many-body exciton dynamics
in GaAs quantum-well structures**

by

Ryan P. Smith

B.S. Physics, Georgia Institute of Technology, 2004

A thesis submitted to the
Faculty of the Graduate School of the
University of Colorado in partial fulfillment
of the requirements for the degree of
Doctor of Philosophy
Department of Physics

2010

This thesis entitled:
Quantitative measurements of many-body exciton dynamics in GaAs quantum-well
structures
written by Ryan P. Smith
has been approved for the Department of Physics

Dr. Steven T. Cundiff

Dr. Chris H. Greene

Date _____

The final copy of this thesis has been examined by the signatories, and we find that both the content and the form meet acceptable presentation standards of scholarly work in the above mentioned discipline.

Smith, Ryan P. (Ph.D., Physics)

Quantitative measurements of many-body exciton dynamics in GaAs quantum-well structures

Thesis directed by Professor Dr. Steven T. Cundiff

Heterostructures in semiconductors, such as quantum wells, give rise to new optoelectronic properties compared to bulk materials by confining the motion of carriers. We study quasiparticles in gallium arsenide (GaAs) quantum wells known as excitons. The absorption spectrum of these excitons exhibits changes at elevated carrier-excitation levels because of many-body interactions between particles. While the spectral absorption changes from these interactions have been studied, a connection between measurements and a microscopic theory has been lacking.

The quantitative spectrally resolved transient absorption measurements described in this thesis are combined with a microscopic theory. This combination relates observed spectral changes in the probe after ultrashort optical excitation to a unique mixture of electron-hole plasma, exciton, and polarization effects. Through theory-experiment comparison, we deduce the actual carrier-density levels, exciton populations, and other correlations in the system. We find that Coulomb scattering of polarization with free-carrier densities dominates the excitation-induced shifting and broadening of the exciton resonance and that exciton populations do not significantly contribute to the excitation-induced effects. We observe a strong transient gain and attribute this feature to a coherent transfer of energy between the pump and probe.

Since the excitation-induced effects are strong, theory predicts that the system should display light-statistic-dependent excitation-induced effects. To demonstrate that light statistics of optical fields have a meaningful effect on the many-body dynamics, we develop a measurement technique involving optical pulse shaping. Our measurements are consistent with

theoretical predictions that light with incoherent statistics gives rise to weaker excitation-induced effects than does a coherent source that creates the same density of electron-hole pairs. Preliminary results suggest that the observed effects are related to the increased temporal duration of the exciting light source. We explore the effects of different pulse shapes to elucidate the primary underlying effects that give rise to the observed weaker excitation-induced effects.

Dedication

To my parents, who have nurtured me and encouraged me on my path.

Acknowledgements

I would like to thank my advisor, Steve Cundiff, for his thoughtful and patient guidance as I explored uncharted territory. He has inspired me by his enthusiasm for exploring new ideas and for developing helpful intuitive models.

Working with Mack Kira has been an incredible pleasure. He has been generous in taking the time to discuss his theories to me, and he continues to challenge me and inspires me to be curious about nature.

I am grateful to all the group members of the Cundiff lab. They have helped me enormously to find empowerment and confidence in my work, and have been an incredible team. Pete Roos introduced me to the lab and helped me to develop my own system for successful research. Jared Wahlstrand guided me through the early stages of this project and encouraged me to push forward even when I experienced uncertainties in the research. Andy Funk has inspired me to be inquisitive and to produce quality work through practice. I would like to thank Alan Bristow, Xingcan Dai, and Tianhao Zhang for helpful discussions, and Qing Chao, Hebin Li, Galan Moody, Andy Funk, Haipeng Zhang, Andy Hunter, Mark Siemans, Soobong Choi, and Martina Carsjens for their proof-reading help and encouragement with this thesis.

My ‘chunch’ ($|chess\rangle \otimes |lunch\rangle$) buddy, John Willits, frequently brought me fresh perspective and kept my brain charged.

A number of people have been generous and helpful to me while here at JILA. Jim Fallner mentored me and helped me to cultivate an enthusiasm about science even when I was

buried in technical challenges. Carl Sauer and Terry Brown assisted me and educated me in many electronics issues. Dave Erickson, Jeff Sauter, and Brian Lynch smoothed the road with their unrelenting dedication; it was always a pleasure talking with them – thank you for so many days in paradise. Loree Kaleth helped our group organization, and always brought light into the lab whenever she stepped foot inside. Mike Paige and J. R. Raith patiently helped me with many computing difficulties. Ariel Paul inspires me to continue striving to be a quality scientist, regardless of the path I take in life. Julie Phillips helped me to become a better writer. Dave Alchenberger assisted with many technical issues. I thank Rich Mirin of NIST for high quality quantum-well samples. Wayne Knox brings a smile to my face.

I thank Rich Muller (of UC Berkeley) and Mike Dubson for creating the opportunity for me to teach “Physics for future presidents.” John Wood from Georgia Tech introduced me to the joys of physics.

I thank my friends, who have been supportive and curious about my work and have offered insight and perspective on this long path; especially David Biagioni, Angela Janzen, Adam Israel Cohen, Elizabeth Merchant, Charles Philbrick, Tara Lanich-LaBrie, Charles Bloch, Stephanie Chasteen, Dana Müller-Hoeppe, Michael Barber, Janice Brahney, Ryan Wilson, James McCutchan, Sherry Gillespie, Justin Kuzcynski, Aaron Donner, Joseph Britton, Ethan Townsend, Mark DeRespinis, Candace Gilet, Meghan Barritt, Michael Teves, Caroline Mitchell, Pam and John Bowlan, Rachel Weitz, Tom Phillip.

I would lastly like to thank my incredible parents, and my three beautiful sisters: Mom, Dad, Meaghan, Caitlin, and Cara, for being a joyful blessing my life.

Contents

Chapter	
1	Introduction 1
1.1	Thesis organization 3
2	Background on excitons in semiconductors 5
2.1	Interest in semiconductors and GaAs 5
2.2	Semiconductors and direct band-gap picture 6
2.3	Excitons in bulk GaAs 8
2.4	Excitons in GaAs quantum wells 12
2.5	Polarization selection rules QW electronic transitions 16
2.6	Optical Bloch Equations 20
2.7	Decoherence and relaxation dynamics of QW excitons 24
2.8	Homogeneous vs. inhomogeneous broadening 27
2.9	Spectroscopy of semiconductors 28
2.9.1	Driven oscillator model 28
2.9.2	Linear spectroscopy 29
2.9.3	Nonlinear spectroscopy 33
2.10	Many-body effects in GaAs QWs 37
2.10.1	Excitation-induced dephasing and shifting 38
2.10.2	Bleaching the exciton resonance 40

2.10.3	Band-gap renormalization	41
2.10.4	Excitonic gain	42
2.10.5	Biexcitons	43
3	Experimental techniques	45
3.1	Sample characterization	45
3.2	Linear absorption spectrum	49
3.3	Transient absorption in the nonlinear regime	49
3.3.1	Experimental setup	50
3.3.2	Choosing appropriate pump and probe spot sizes	53
3.3.3	Estimation of excitation densities	55
3.3.4	Quantitative measurement of the probe and pump absorption	58
3.4	Extraction of line shape parameters	60
3.5	Cross-correlation measurement of the pump	62
3.6	Conclusion	63
4	Coulomb-induced nonlinearities in semiconductor quantum wells	64
4.1	Introduction	64
4.2	Theory development	64
4.3	Results and discussion	67
4.4	Conclusion	73
4.5	Transition to the study of QW system response to light statistics	74
5	Background on light statistics and predicted interaction with matter	75
5.1	Coherence of a classical field	75
5.1.1	First-order coherence	76
5.1.2	Second-order coherence	79
5.2	Statistics of the quantized electromagnetic field	82

5.2.1	Quantum-mechanical representation of the field	82
5.2.2	Density matrix	83
5.2.3	Coherence properties of light sources	83
5.2.4	Photon number distributions	86
5.2.5	Singlet quantities	88
5.2.6	Coherent state is the classical field	88
5.3	Phase-space representations of light fields	89
5.4	Theoretical predictions concerning many-body interactions excited by light having incoherent statistics	91
5.4.1	Why excitons in GaAs quantum wells?	91
5.4.2	Semiconductor Bloch equations	93
5.4.3	Coherent on-resonance excitation	94
5.4.4	Radiative recombination of carriers and excitons	95
5.4.5	Impact of quantum light statistics on matter	96
5.4.6	Quantum-optical spectroscopy	97
5.4.7	Jaynes-Cummings model	99
5.5	Summary: thermal vs. coherent light statistics	105
6	Toward a thermal source	106
6.1	Early efforts for a thermal light source	107
6.1.1	Incandescent bulbs	107
6.1.2	Light-emitting diodes	109
6.1.3	Below-threshold diode laser	110
6.1.4	Cavity dumping	111
6.2	Phase modulation of ultrashort pulses for incoherent light generation	115
6.2.1	Density-matrix ensemble averaging	115
6.2.2	Ensemble averaging for phase-randomized fields	117

6.3	Philosophical issues	121
7	Pulse-shaping techniques	123
7.1	Concept of a pulse shaper	123
7.2	Experimental setup	123
7.3	Shaper design considerations in the frequency domain	125
7.3.1	Spectral resolution constraints	125
7.3.2	Phase mask device	126
7.4	Physical limitations in pulse shaping	129
7.5	Relationship between time- and frequency-domains	132
7.5.1	Time duration and bandwidth	132
7.5.2	Effects of the spectral phase in the time domain	134
7.6	Alignment of the pulse shaper apparatus	138
7.6.1	Spatial mode filtering	139
7.7	Calibration and testing of phase masks	141
7.7.1	Calibration procedure	141
7.7.2	Comparison of simulation with experiment	142
7.8	Comparison of chirp parameter range with material dispersion	144
7.9	Arbitrary pulse shape generation	146
7.10	Prepared for density-matrix ensemble averaging	146
8	Phase-randomized pulse experiments	148
8.1	Characterization of average statistics	148
8.2	Qualitative predictions using the optical Bloch equations	156
8.3	Experimental methods	160
8.4	Results of phase-randomized experiments	161

	xii
9 Quantum-well response to other pulse shapes	164
9.1 Three-pulse (zero- Φ) excitation	165
9.2 Chirped pulses	173
10 Conclusion	178
10.1 Outlook	179
 Bibliography	 181
 Appendix	
 A Double chop method for probe measurements	 189
 B Calibration of the pump and probe powers	 193
B.1 Correction for reflection losses	193
B.2 Calibration of probe powers in the presence of the pump	197

Figures

Figure

- 2.1 Absorption of a photon by a direct-gap semiconductor. When an electron is promoted to the conduction band, it can move freely about the material and thus conduct electricity. 7
- 2.2 (a) A Wannier-Mott exciton with a large spatial extent compared with the size of a unit cell, typically found in semiconductors with large dielectric constant. (b) A tightly bound (Frenkel) exciton with smaller radius, more common to insulator crystals. Figure from [1]. 9
- 2.3 (a) Schematic diagram of exciton states and the continuum in the center of mass picture. Excitons can form at discrete energies below E_{gap} . Photons with energy exceeding E_{gap} can create unbound electron-hole pairs. (b) Calculated absorbance spectrum of GaAs at 1.2 K including Sommerfeld enhancement, based on Ref. [2]. As the photon energy increases, discrete peaks in the absorption correspond to the $n = 1, 2$, and higher bound states of the exciton. 12
- 2.4 Lowest-lying energy states, $n = 1$, for QW excitons. Growing a thin layer of GaAs between two layers $\text{Al}_{0.3}\text{Ga}_{0.7}\text{As}$ creates a quantum well (QW). The confinement pushes the electron (e) and hole energies away from each other and lifts the degeneracy between light-hole (LH) and heavy-hole (HH) states. 14

2.5	(a) Schematic of the hole sub-bands in GaAs, with the lifting in degeneracy at $k = 0$ due to confinement in one dimension between the light-hole (LH) ($J = \frac{3}{2}, J_z = \pm\frac{1}{2}$) and heavy-hole (HH) ($J = \frac{3}{2}, J_z = \pm\frac{3}{2}$) sub-bands. The split-off band ($J = \frac{1}{2}$) is shifted in energy because of spin-orbit coupling. (b) A diagram of selection rules for optical interband excitation with σ^+ and σ^- polarized light.	18
2.6	Visualization of the Lorentz oscillator model [Eqn. 2.38]. (a) The real and imaginary parts of the induced polarization. (b) The magnitude of the polarization and the phase. . . .	30
2.7	Linear absorption. An input field E_{in} induces a polarization in a sample which in turn radiates E_{sig} in the same direction, producing a cancelation with the input field.	30
2.8	Schematic for a two-pulse nonlinear experiment. The sample is tilted for clarity. Two pulses are separated by a delay τ , and focused with a lens onto a sample with directions \vec{k}_1 and \vec{k}_2 , respectively. For transient absorption (TA), the pump \vec{k}_1 and probe \vec{k}_2 generate a signal (green dashed lines) in the reflected and transmitted probe beam directions. For second-harmonic generation (SHG), the signal (blue dashed line) is detected in the $\vec{k}_1 + \vec{k}_2$ direction. A four-wave mixing (FWM) signal (black dashed line) may be detected in the $2\vec{k}_2 - \vec{k}_1$ direction.	35
2.9	Excitation-induced dephasing (EID) observed in the differential transmission of a probe spectrum. The inset shows the probe absorbance in the absence of strong optical excitation. Figure from [3].	39
2.10	Blue shift in exciton absorption in a multiple QW structure. At positive delays (+2 and +15 ps), a blue-shift of the exciton resonance is observed compared to the unexcited (-5 ps) delay. Figure from [4].	39
2.11	Optical gain observed in a transient-absorption experiment according to [5]. The unexcited transmittance spectrum (solid line) is shown in comparison to the excited probe spectra at two time delays. Cross-hatched regions correspond to optical gain.	43
2.12	Exciton and biexciton features in a time-integrated luminescence spectrum. Figure from [6].	44

3.1	Schematic of the multiple quantum-well (QW) sample studied in this thesis. The 300 nm GaAs layer is referred to as the bulk layer in the discussion. The direction of the incoming laser beam is shown.	46
3.2	Detailed geometry of cryostat optics. The light source enters from the left side. There are losses due to reflection from the two surfaces of the sapphire disc (surf1 and surf2) in addition to the cryostat windows.	47
3.3	Measured (red) and theoretical (black) sample reflection probabilities. The reflection and transmission (not shown) spectra, recorded in absolute units, allow the fixing of a model using transfer-matrix theory. The bulk and QW exciton resonances are marked. The spacing ΔE between fringes allows inference of the sample thickness.	47
3.4	Linear absorption (blue line) from the QWs in absolute units in the region of the 1s heavy-hole (HH) exciton resonance. In arbitrary units, the probe spectrum before the sample is shown (green line) along with the narrowed pump spectrum used in transient-absorption experiments (shaded area).	50
3.5	Schematic setup for spectrally resolved transient absorption experiments. BS, beam splitter; ND filter, neutral-density filter; τ delay, controls relative time delay between pump and probe; POL, polarizer; QWP, quarter-wave plate; BB, computer-controlled beam blockers; PD, photodetector.	51
3.6	Result of beam-sampling calculation. The error due to the probe sampling an inhomogeneous portion of the pump spatial intensity is shown.	55
3.7	Setup for simultaneous measurement of the pump powers on photodetectors (PDs); BS, 1% beam sampler.	59

- 3.8 Model-independent fit procedure. The black triangle is the first guess of the resonance peak. The parabola fit (cyan line) results in a maximum (black diamond) that yields the peak height and center resonance position. The two baselines (blue lines) at high and low energy are used to estimate the half-widths (blue and red diamonds) on either side of the resonance. Note that the low-energy baseline is used to estimate the bulk absorption ($\alpha_{\text{Bulk}} = 0.28$). 61
- 4.1 Probe QW absorption at large $\tau = 13$ ps delay. (a) The measured CC-configuration α_{QW} (shaded areas) are shown for pump-pulse photon densities $n_p = 3.9, 16,$ and $27 \times 10^{11} \text{ cm}^{-2}$ and compared to microscopically computed spectra (solid lines) for e-h densities $n_{eh} = 0.14, 2.2,$ and $3.4 \times 10^{10} \text{ cm}^{-2}$, from top to bottom. The spectra are vertically offset by 15%. The horizontal lines indicate the HWHM of the respective exciton resonances. (b) The corresponding CL comparison with 3.9, 27, and $48 \times 10^{11} \text{ cm}^{-2}$ pump-photon densities (shaded areas) and calculations for the densities $0.21, 4.4,$ and $5.0 \times 10^{10} \text{ cm}^{-2}$ (solid lines). (c) and (d): The deduced ML e-h densities (circles, left scale) and exciton fraction (squares, right scale) as a function of photon density for CC and CL experiments, respectively. The arrows indicate the spectra presented in the left-side panel; the dashed vertical lines mark saturation. 68
- 4.2 Internal decay rates γ_{int} (circles) and radiative-decay rates Γ_{rad} (squares) extracted from the experimental measurements (squares and circles) along with theoretical predictions (lines). The excitation saturates the probe response at intensity I_{sat} 70

4.3 Probe QW absorption for the short $\tau = 3$ ps delay. (a) CC conditions with pump photon density $n_p = 16 \times 10^{11} \text{ cm}^{-2}$: the measured α_{QW} (dark shaded), the computed α_{th} (solid line), and the long-time delay α_{QW} (light shaded). Inset: the measured (open circles) and computed (shaded area) absorption dip (gain maximum) as a function of pump-photon density. The dashed vertical line marks saturation. (b) Same as (a), but for the CL configuration with the photon density $27 \times 10^{11} \text{ cm}^{-2}$. Inset: the absorption peak shift for CL (squares) and CC (circles) measurements compared with theory (lines). 72

4.4 Influence of exciton populations on nonlinear α_{QW} . The long-delay measured α_{QW} (shaded area) for $n_p = 16 \times 10^{11} \text{ cm}^{-2}$ pump is compared with the ML result (solid line) as well as computations having 0% (dashed line) and 100% (dotted line) excitons. Inset: The ML configuration (square) and the 5% confidence interval (shaded area) plotted in (n_{eh}, x) space. The 0% (open circle) and 100% (filled circle) represent exciton configurations used for the dashed and dotted lines, respectively. 73

5.1 A Michelson interferometer with adjustable relative delay τ between the optical path lengths of the two beams, split by a beam splitter (BS). As the delay is scanned, the beams constructively and destructively interfere on a photodetector (PD), producing ‘fringes.’ This measurement yields information about the coherence properties of the light source. . . . 77

5.2 (a) The signal $I_{\text{PD}}(\tau)$ read on a photodetector in a Michelson interferometer for varying delay τ . The coherence time was chosen to be five times longer than the optical period. (b) The power spectrum of the light source is the Fourier transform of $I_{\text{PD}}(\tau)$. The inverse relationship between the widths of in the time and frequency domains are depicted with arrows. 78

5.3 A temporal coherence measurement based on the Hanbury-Brown and Twiss experiment. The intensity of the light source is recorded on two separate photodetectors, and a variable delay (typically digital) allows a computer to correlate the intensities at two times in the same light source, yielding the second-order coherence function. 80

5.4	Second-order coherence for classical chaotic and coherent light sources.	81
5.5	Comparison of photon number probability distributions for coherent and thermal light sources, both with $\bar{n} = 10$	87
5.6	Phase-space portraits in \hat{q} - \hat{p} space. (a) The schematic for how amplitude n and phase θ of a single measurement are plotted, resulting in a ‘fuzz-ball’ of uncertainty with widths Δq and Δp . The distribution of measurements is shown for (b) a coherent state and (c) a thermal state.	90
5.7	Quantum wire (1D) calculation of on-resonance excitation dynamics. (a) A short pulse generates a carrier density and polarization $ P ^2$. (b) The polarization decays, generating an exciton population. Most of the excitons are created in the ground $1s$ state. Figure from [7].	94
5.8	(a) Computed $1s$ exciton and (b) free carrier distributions in center-of-mass k -space for three times after coherent resonant excitation. The absence of excitons in the low-momentum states is due to radiative recombination. Figure from [7].	95
5.9	Comparison of excitation dynamics resulting from a pulse with coherent vs. incoherent statistics. (a) Coherent excitation; the optical excitation pulse (dashed line, scaled) is shown with the generated polarization (shaded area, scaled) and the bright $1s$ exciton population (solid line). (b) Incoherent excitation; the incoherent optical pulse (dashed line, scaled) is shown with the generated density of bright $1s$ exciton populations (solid line). Note the dramatically different scale for the density compared with the coherent excitation, and that no polarization is generated. (c) The generated exciton population in momentum space for coherent excitation (solid line, multiplied by 5) and incoherent excitation (shaded area) 11 ps after optical pulse maximum. Figure from [7].	98

5.10	Theoretical prediction of the excitation-induced dephasing (EID) half-width at half maximum (HWHM) in addition to the linear $1s$ resonance width (≈ 0.75 meV) for coherent vs. thermal excitation. Thermal excitation is predicted to suppress scattering compared with coherent excitation for similar carrier excitation levels. Suppressed scattering leads to lower dephasing rates.	99
6.1	Photon densities per second within a 1 meV bandwidth for blackbody radiation at a few temperatures. The intensity at 1.55 eV increases with blackbody temperature.	108
6.2	Diode laser output spectra for a range of carrier-injection currents. The peaks in the spectra are evidence of lasing above a current threshold of 55 mA.	110
6.3	Schematic of setup used for cavity-dump experiment. OC, output coupler; AOM, acousto-optic modulators; Xtal, the Ti:sapphire gain crystal. A 5 watt Verdi laser pumps the gain crystal. The dumped light is collected with a fiber.	112
6.4	“Pump and dump” technique. The pump AOM switches on at t_1 to allow cavity build up. The intracavity AOM switches on at t_2 before the onset of lasing (at t_3) to dump the incoherent photons out of the laser cavity.	113
6.5	The dumped spectra at $t = t_2$ (blue), and for $t > t_3$ (red), corresponding to ASE and lasing, respectively.	114
6.6	A spectrum from a mode-locked ti:sapphire laser with a random spectral phase function with spectral bin sizes of $\Delta\omega_{\text{bin}} = 200 \mu\text{eV}$. There are $N_{\text{bins}} = 30$ spectral bins across this spectrum.	118
7.1	Layout for a $4f$ pulse-shaper apparatus. The spatial spread D corresponds to a spread in optical wavelengths $\Delta\lambda$	124
7.2	Layout for a $4f$ pulse-shaper apparatus in reflective geometry. Reflected beam is vertically offset from the input beam, but shown at a slightly different horizontal angle here only for illustration purposes.	127

7.3	Schematic of the Spatial Light Modulator (SLM) [8]. (a) A front-view drawing of the device. (b) Detail of the pixel geometry. (c) Principle of operation using liquid crystals.	128
7.4	(a) Illustration of the intensity distribution of overlapping single-color modes (A–E, blue lines) at the plane of the phase mask in a pulse shaper. The spectral phase function across the mask (thick black line) is shown with arbitrary units. (b) The consequence of finite spot size in a pulse shaper is amplitude modulation at phase discontinuities with width corresponding to Eqn.7.8.	131
7.5	Pictorial relationship between the power spectrum (frequency domain) and temporal intensity (time domain) features. Figure from [9].	133
7.6	Spectrograms for ultrashort pulses with varying chirp: (a) no chirp ($b = 0$, or transform-limited), (b) moderate chirp ($b = 0.5 \text{ ps}^{-2}$), and (c) strong chirp ($b = 5 \text{ ps}^{-2}$). Chirp ‘rotates’ the spectrogram in this phase space.	137
7.7	Relationship between the temporal chirp parameter \tilde{b} and the spectral chirp parameter b . Increasing the spectral chirp beyond $ b > 0.18 \tau_p^2$ weakens the instantaneous frequency dependence on time as the pulse spreads in time.	138
7.8	Spatial mode filtering using two lenses with a pinhole. The input distorted spatial mode is ‘cleaned up’ into a $\text{TEM}_{0,0}$ spatial mode by focusing the light through the pinhole.	140
7.9	Transmission of the Hermite-Gaussian modes $\text{TEM}_{m,0}$ through a spatial mode filter. A series of diameters D and $\text{TEM}_{0,0}$ spot sizes w_0 (both in μm) allow choice of appropriate mode-filtering geometry.	141
7.10	(a) A variety of power spectra, each with a single phase discontinuity that results in a dip in the spectrum. (b) The center positions of the dips along with the recorded pixel number on the SLM allow calibration of the SLM via a linear fitting procedure.	142
7.11	Simulated and measured time shifts generated by a linear phase mask.	144
7.12	Simulated and experimentally measured cross-correlation widths $\Delta\tau_S$ for a range of chirp parameters. Cross-correlation width of $\Delta\tau_S = 520 \text{ fs}$ for a transform-limited pulse is shown as a baseline.	145

7.13	Comparison of simulation and experiment for a randomized phase mask function applied to a pulse spectrum.	147
8.1	Cross-correlation traces for six different scrambled realizations. All traces are normalized so that the area is unity. For comparison, the normalized transform-limited pulse (flat spectral phase mask) is shown as a dashed red line.	149
8.2	(a) Cross-correlation values at time delay $\tau' = 0$. (b) Probability distribution function for the normalized cross-correlation values. (c) Cross-correlation values for several τ values. (d) m^{th} -order coherence values calculated by Eqn. 8.2.	151
8.3	Convergence of the measured second-order coherence function values $g^{(2)}$ as the number of realizations is increased. The measured $g^{(2)}$ function (blue squares) is fit with an asymptotic function \tilde{g} (green line) to determine the error in $g^{(2)}$ measuring a finite number of realizations. Asymptote of \tilde{g} is shown for $\lim_{N \rightarrow \infty} \tilde{g}$. This example uses the data from $\Delta\omega_{\text{bin}} = 0.3$ meV, or the 20-bins case.	153
8.4	Measured second-order coherence function values for several different bin spacings. Measured values correspond to the trend predicted in Eqn. 6.17.	155
8.5	The average scrambled pump spectrum (shown for $N_{\text{ens}} = 1, 14, 50$) converges to the flat mask spectrum as the number of realizations N_{ens} is increased.	156
8.6	Simulation using the optical Bloch equations (Eqn. 2.30) of the optical excitation of a two-level system including phenomenological decay terms. The population term is offset such that 0 means population is completely in the ground state.	158
8.7	Population-to-polarization ratios for three cases where the temporal duration is systematically varied.	159
8.8	Nonlinear observables as a function of power. Peak heights of α_{QW} are shown for varying (a) $P_{\text{QW}}^{\text{pump}}$ and (b) $P_{\text{QW}}^{\text{pump}}$. Center resonance positions are shown for varying (c) $P_{\text{QW}}^{\text{pump}}$ and (d) $P_{\text{QW}}^{\text{pump}}$. Fits (solid lines) through each set of points clarify the trends for the observables.	162

8.9	The average spectrum from the scrambled realizations saturates the HH 1s-resonance less than from coherent excitation with the same $P_{\text{IN}}^{\text{pump}}$. The spectra are shown with the linear absorption (pump off) for comparison.	163
9.1	(a) Frequency and (b) time domain representations of a zero- Φ (or three-pulse) realization. The simulation is shown to roughly match the experimental cross-correlation data. In (a), the parameters θ and Φ are labeled as described in the text.	165
9.2	Nonlinear observables as a function of power. Peak heights are shown for varying (a) $P_{\text{QW}}^{\text{pump}}$ and (b) $P_{\text{QW}}^{\text{pump}}$. Center resonance positions are shown for varying (c) $P_{\text{QW}}^{\text{pump}}$ and (d) $P_{\text{QW}}^{\text{pump}}$	167
9.3	Fractional absorption by the QW system as a function of input power, shown for (a) scrambled realizations and (b) zero- Φ realizations.	168
9.4	Temporal dynamics for observables of the probe absorption line shape: (a) center resonance position and (b) peak height of the HH 1s-resonance. The observables in the absence of any pump excitation are also shown (cyan lines).	169
9.5	Dynamics of the nonlinearity for single-pulse excitation, shown with fits (black dashed lines) for the same powers as shown in Fig. 9.4. The nonlinearity in the absence of pump excitation is also shown (cyan line) near zero.	170
9.6	Decay parameters extracted from the single-pulse temporal data using Eqn. 9.1.	172
9.7	Nonlinearity dynamics for the three-pulse realization with a simulation that uses parameters from the single-pulse data and accounts for saturation behavior based on the three-pulse data. The poor fit suggests that the temporal dynamics are nontrivial.	173

9.8	Measurements of the QW system response to chirped pulses. From the probe absorption, we extract (a) the peak resonance position and (b) the peak height. The observables in the absence of the pump light are shown for comparison (cyan lines). (c) The power absorbed by the QW exhibits nontrivial dependence on chirp parameter. (d) The nonlinear observables do not follow a simple trend with the absorbed powers. The extreme chirp parameter values at $\pm 5.8 \text{ meV}^{-2}$ are marked. All four frames show the measurement from the transform-limited case for comparison and the black lines guide the eye through the chirp values near $\phi''(\omega_0)/2 = 0 \text{ meV}^{-2}$	174
9.9	Spectra for a variety of spectral chirp parameters $\phi''(\omega_0)/2$ with units meV^{-2} in the legend. Negative chirp parameters produce similar spectra. A quadratic spectral phase $\phi''(\omega_0)/2 = 1.9 \text{ meV}^{-2}$ is also shown (dashed line).	175
A.1	Schematic shown for pump and probe beams traveling perpendicular to the plane of the optical chopper wheel. As the wheel spins, the pump and probe beams are modulated at slightly different frequencies, a critical aspect to resolving the probe spectra in the presence and absence of the pump.	190
B.1	Schematic for light path going into and out of the cryostat. We account for reflection losses at interfaces (dotted lines) to construct the true transmission and reflection probabilities.	194

Chapter 1

Introduction

Semiconductors and their nanostructures respond to light fields in a wide variety of ways, including changes in conductivity and the formation of short-lived quasiparticles in the lattice [1]. For intense optical excitation, the interactions between particles inside the materials can dramatically affect the optical response. Research has explored the optical and electronic dynamics in semiconductors; however, the complicated many-body interactions between particles that give rise to optical responses need further investigation.

To elucidate the nature of many-body interactions, ultrashort laser pulses are used to study the dynamics of quasiparticles, known as excitons, in GaAs quantum wells (QWs). These excitons are of particular interest because they result in a strong spectral resonance feature and tend to dominate the nonlinear optical response [10, 11]. Thus, the spectral features of excitons can be used to monitor effects that occur at high excitation densities.

The effects at high densities are complicated. When carrier-excitation levels are elevated in a QW, the lowest-lying $1s$ -exciton resonance can undergo spectral changes such as broadening and shifting due to excitation-induced effects [12, 3, 13, 14, 15]. Physically, these effects result from Coulomb-induced scattering of polarization from carrier densities, polarization itself, and exciton populations. These nonlinear interactions build up on picosecond time scales, and it is typical that dephasing, phase-space filling, energy-renormalization, and screening effects become mixed in a nontrivial manner. These effects are many-body interactions between a large number of particles, as compared with one- or two-body interactions as

are typically observed in atomic experiments [16]. Since the many-body effects are strongly coupled, it is very challenging to determine the many-body effects that give rise to nonlinear observables. Even though much research has been performed on the nonlinear properties of GaAs QWs in the past few decades [17, 18, 19], to the best of our knowledge no work until now has quantitatively determined how many-body configurations affect the exciton line shape.

The experimental work described in this thesis combined with a microscopic theory clarifies the many-body effects that give rise to nonlinear exciton spectra in GaAs QWs. The microscopic theory was constructed by our theorist collaborators: Mackillo Kira, Martin Schäfer, Johannes Steiner, and Stephan Koch at the Department of Physics and Material Sciences Center, Philipps-University, Marburg, Germany.

In addition to characterizing the many-body configurations, we find the nonlinearities observed in GaAs QWs to be strong enough that the light statistics of the optical excitation may have an effect on the observed nonlinearities. The study of a system's response to the light statistics of an excitation source is termed "quantum-optical spectroscopy." Although experiments in atomic vapor systems have explored nonlinear interactions between exciting light statistics and atoms in a cavity [20, 21, 22], no experiments of this type have been performed in semiconductors. The extremely high photon densities required to observe nonlinearities in semiconductors are typically outside of the regime of quantum-optical experiments, which deal with a small number of photons.

To demonstrate quantum-optical spectroscopy in GaAs QWs, we perform several experiments involving optical pulse shaping to realize theory predictions concerning the response of excitons to an excitation source with incoherent light statistics. Specifically, theory predicts that an excitation source with incoherent light statistics gives rise to lower scattering rates than for coherent excitation that creates the same carrier density. The lower scattering rates are predicted to be observable in the line shape of the exciton.

1.1 Thesis organization

This thesis reports the results of studies of the many-body exciton dynamics in a GaAs QW system. Specifically, we perform spectrally resolved transient absorption measurements. The thesis is divided into two parts: (i) the characterization of many-body configurations through quantitative measurement techniques, and (ii) a study of the system response to light statistics using pulse-shaping techniques.

In the first part, we describe pump-induced many-body configurations using a quantitative measurement technique combined with a microscopic theory. Chapter 2 introduces direct-gap semiconductors, then explores the background and theory involved in optical studies of the nonlinearities in GaAs QWs. Previous optical studies of excitons in GaAs QWs are also reviewed. Chapter 3 introduces a novel quantitative measurement technique. Spectrally resolved transient absorption recorded in absolute units characterizes the nonlinear optical response of excitons in a GaAs multiple QW system. The techniques presented here are common to both the transform-limited excitation studies and the pulse-shaping studies. In Chapter 4, the results of the transform-limited excitation are combined with microscopic theory, and the results are presented.

The second part of the thesis begins in Chapter 5 with some background on light statistics. We explain the predictions of our theorist collaborators concerning the nonlinear exciton response to light with thermal statistics. A simple model validates the prediction that a light source with thermal statistics should induce a pure exciton population without creating a polarization. Chapter 6 describes the possibilities we explored for creating an intense thermal light source and discusses the paradigm of density-matrix ensemble averaging for exploring the exciton response to thermal light. The protocol for an ensemble of phase-randomized realizations is discussed. To realize these protocol, Chapter 7 explains the details of pulse shaping. In Chapter 8 we characterize the phase-randomized light source generated by pulse shaping and discuss the results from the QW response. The nontrivial results inspire

exploration of the QW response to other pulse shapes. This work is described in Chapter 9.

We summarize our studies of many-body exciton dynamics in Chapter 10. In Appendix A, a method for accurate detection of the probe absorption is explained. Appendix B contains the details of the procedure for calibrating the pump and probe pulse energies.

Chapter 2

Background on excitons in semiconductors

2.1 Interest in semiconductors and GaAs

Semiconductors have become an integral part of our modern world. Personal computers, cell phones, satellite communications systems, solar cells, traffic lights, and compact disc players are all based on semiconductor devices [23]. The proliferation of these devices in society has inspired much research into the understanding of the electronic and optical properties of a variety of materials.

Although semiconductors were being studied in laboratories as early as the 1830s, semiconductor research expanded with the 1947 development of the transistor in Bell Labs. The transistor revolutionized the fields of electronics and semiconductors. The fundamental interest and industrial applications have driven research into the properties of semiconductor structures [24].

Semiconductors are often studied with spectroscopic techniques using lasers [11]. The advent of ultrashort pulsed mode-locked lasers has allowed investigation into extremely fast time dynamics (10^{-15} seconds, or a femtosecond) inside materials [25]. These lasers can also produce intense pulses of energy that can create novel regimes not previously available experimentally, such as high electron densities. The latter and other unexplored regimes may hold keys to developing new technologies and a better understanding of semiconductor physics.

The semiconductor gallium arsenide (GaAs) has a rich optoelectronic structure that

has many industrial applications [26]. GaAs offers certain advantages over the indirect-gap semiconductor, silicon (Si), the primary semiconductor used in industrial applications. The advantages over Si include a higher saturated electron velocity and electron mobility, insensitivity to heat, and the possibility to emit light. Si has the advantages of higher hole mobility, allowing fast switching in field-effect transistors, and is less brittle than GaAs, abundant, and cheap to process. Despite the disadvantages of GaAs compared to Si, its application to high-speed electronic devices, laser diodes, light-emitting diodes, and photovoltaics has fueled an enormous amount of research in the last 40 years [17, 18, 19, 27].

2.2 Semiconductors and direct band-gap picture

A semiconductor can be technically defined as a solid with a conductivity somewhere between a metal and an insulator. A more useful explanation involves a map of the electronic energy bands, a large number of discrete quantum states resulting from the extended wave nature of the electrons in a periodic structure. In the unexcited semiconductor, electrons fill the valence band, corresponding to no net motion of charge, or an insulating state. An energy exceeding the band gap energy can promote a valence band electron to the conduction band, which corresponds to electrons being free to move about the material and thus conduct electricity. A population of electrons in the conduction band and the absence of electrons in the valence band mark the transition from insulator behavior to conducting behavior. Although electrons may be excited via thermal energy or optical excitation, this discussion focuses on the latter.

We can visualize the optical interaction with a semiconductor by representing the energy bands in momentum (k) space. Figure 2.1 depicts the absorption of a photon in the first Brillouin zone, the central cell in reciprocal lattice space (around $k=0$). A photon with energy $\hbar\omega$ that exceeds the gap energy, $E_{\text{gap}} = E_c - E_v$, can be absorbed by this material. Here E_c and E_v are the conduction band and valence band energies, respectively. Photon absorption results in an interband transition that promotes an electron from the valence

band to the conduction band, leaving the absence of an electron, or a “hole,” in the valence band. Since the momentum of the photon is negligible compared to the electron momentum, the electron and hole must have the same wave vector \mathbf{k} .

A photon may also stimulate emission, inducing a transition of the electron back to the valence band, resulting in the emission of a photon. Stimulated emission in semiconductors has allowed the development of semiconductor lasers [28, 29].

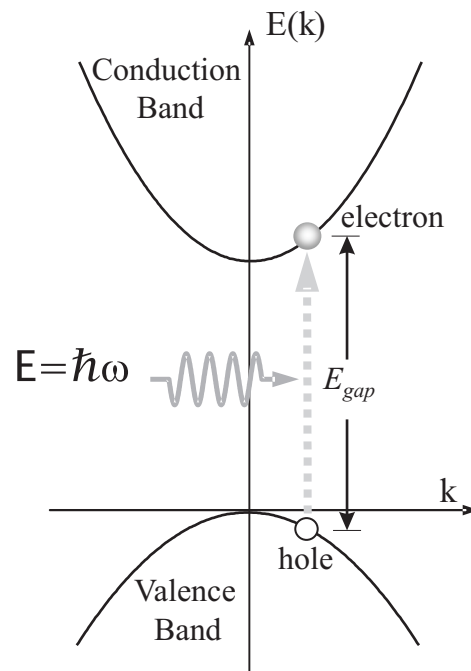


Figure 2.1: Absorption of a photon by a direct-gap semiconductor. When an electron is promoted to the conduction band, it can move freely about the material and thus conduct electricity.

In a direct-gap semiconductor, an electron can undergo a transition from the highest-energy state in the valence band to the lowest-energy state in the conduction band without any change in crystal momentum. The transition shown in Fig. 2.1 is an interband transition for a direct-gap semiconductor. The low-momentum transition in direct-gap semiconductors allows use in light-emitting diodes and laser diodes [29]. This low-momentum transition will be relevant to our discussion of bound exciton states.

2.3 Excitons in bulk GaAs

We study the optical properties of the direct-gap semiconductor, gallium arsenide (GaAs), a III-V compound with a zincblende lattice structure. The dominant optical features at low temperature below the band-gap energy are resonances due to the exciton, a bound quasiparticle state between the electron and hole [10, 30]. The wave function and energy levels of an exciton are analogous to those of a hydrogen atom.

When an electron is excited into the conduction band by the absorption of a photon, a hole is created in the valence band, which has opposite charge of the electron and can also conduct electricity in the lattice. In GaAs (and other semiconductors), the electron and hole can form a bound state through Coulomb attraction. The resulting quasiparticle, an exciton, has slightly less energy than the unbound electron and hole. The exciton that is formed in bulk GaAs can move throughout the lattice and can transport energy. However, it cannot transport charge because it is electrically neutral.

Excitons can form when the electron and hole have the same group velocity. This condition is necessary for the electron and hole to move together as a bound pair. The group velocity of an electron or hole is given by:

$$v_g = \frac{1}{\hbar} \frac{\partial E}{\partial k}, \quad (2.1)$$

where E is the band dispersion shown in Fig. 2.1. To satisfy this condition, the gradients of the conduction and valence bands must be the same. The bands in a direct-gap semiconductor have zero gradient at $k = 0$. Hence, excitons can form efficiently during direct transitions in these materials [1].

The bound state is stable for a short period of time. When the electron ‘falls’ into the hole, the recombination results in an effective annihilation of the exciton particle and is accompanied by the emission of a photon. The lifetime of the bulk exciton, influenced by many factors including temperature and scattering with other excitons, is on the order of 100 picoseconds in GaAs.

There are two basic types of excitons, as shown in Fig. 2.2: (a) Wannier-Mott, that have a large radius encompassing many atoms; and (b) Frenkel, or tightly bound excitons that have a correlation radius to within one lattice spacing. For GaAs, excitons are the Wannier-Mott type. In both cases the exciton wavefunction is delocalized in the lattice.

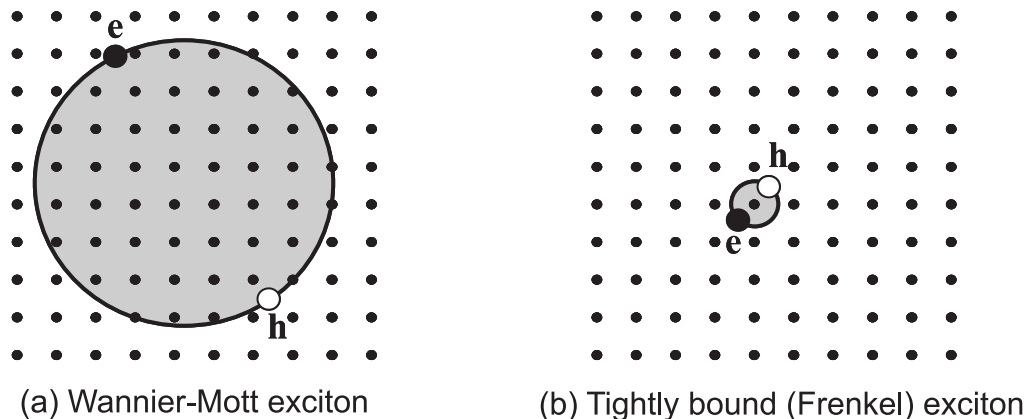


Figure 2.2: (a) A Wannier-Mott exciton with a large spatial extent compared with the size of a unit cell, typically found in semiconductors with large dielectric constant. (b) A tightly bound (Frenkel) exciton with smaller radius, more common to insulator crystals. Figure from [1].

The wave function $\psi(\mathbf{R}_e, \mathbf{R}_h)$ of an exciton is a solution to a Schrödinger equation that is similar to hydrogen (or positronium), but with different masses and dielectric constant [31]:

$$\left[\left(E_c - \frac{\hbar^2}{2m_e^*} \nabla_e^2 \right) - \left(E_v + \frac{\hbar^2}{2m_h^*} \nabla_h^2 \right) - \frac{e^2}{4\pi\epsilon_b |\mathbf{R}_e - \mathbf{R}_h|} \right] \psi(\mathbf{R}_e, \mathbf{R}_h) = E\psi(\mathbf{R}_e, \mathbf{R}_h). \quad (2.2)$$

The background dielectric constant $\epsilon_b = \epsilon/\epsilon_0 = 12.8$ is a scaling of the vacuum dielectric constant, ϵ_0 ; typical numbers for the effective electron and hole masses are $m_e^* = 0.067m_0$ and $m_h^* = 0.51m_0$, where m_0 is the free electron mass and e is the charge of the electron. The electron energy (E_c) and hole energy (E_v) in the conduction and valence bands, respectively, are modified by the kinetic energy operators ($\nabla_{e(h)}^2$) and their Coulomb attractive potential $\propto 1/|\mathbf{R}_e - \mathbf{R}_h|$. In solving the Schrödinger equation to find the binding energies of the exciton states, it is helpful to separate the motion into that of the center of mass \mathbf{R}_{CM} and the relative coordinate $\mathbf{R} = \mathbf{R}_e - \mathbf{R}_h$ of the electron and hole. The center of mass is

$$\mathbf{R}_{CM} = \frac{m_e^* \mathbf{R}_e + m_h^* \mathbf{R}_h}{m_e^* + m_h^*}. \quad (2.3)$$

The reduced mass is

$$\frac{1}{\mu} = \frac{1}{m_e^*} + \frac{1}{m_h^*}. \quad (2.4)$$

The Schrödinger equation in the transformed coordinate system $(\mathbf{R}_{CM}, \mathbf{R})$ is

$$\left[\left(-\frac{\hbar^2}{2(m_e^* + m_h^*)} \nabla_{CM}^2 \right) + \left(E_{\text{gap}} - \frac{\hbar^2}{2\mu} \nabla^2 \right) - \frac{e^2}{4\pi\epsilon_b |R|} \right] \psi(\mathbf{R}_{CM}, \mathbf{R}) = E \psi(\mathbf{R}_{CM}, \mathbf{R}). \quad (2.5)$$

The transformed coordinate system allows the wave function to be factored into a product of the functions of \mathbf{R}_{CM} and \mathbf{R} since the operators with \mathbf{R}_{CM} and \mathbf{R} appear additively. The equation for the center of mass part is simply a plane wave with energy $\hbar^2 K_{CM}^2 / 2(m_e^* + m_h^*)$.

The equation for the relative coordinate is

$$\left[-\left(\frac{\hbar^2}{2\mu} \nabla^2 \right) - \frac{e^2}{4\pi\epsilon_b R} \right] \phi(\mathbf{R}) = (E - E_{\text{gap}}) \phi(\mathbf{R}), \quad (2.6)$$

resulting in a binding energy for the n th level of the exciton in bulk GaAs relative to the ionization limit of

$$E_{\text{binding}}(n) = -\frac{\mu}{m_0} \frac{1}{\epsilon_b^2} \frac{R_H}{n^2} = -\frac{R_X}{n^2}, \quad (2.7)$$

where R_H is the Rydberg constant for hydrogen, or 13.6 eV. The new quantity $R_X = (\mu/m_0\epsilon_b^2)R_H$ introduced here is the Rydberg constant for the exciton [1]. Additionally, the oscillator strength f of the exciton drops off with decreasing n as $f(n) \propto 1/n^3$, leading to a decrease in the height of absorption peaks for higher n exciton states. Experimentally, however, only a few exciton states can be seen because of line-broadening mechanisms such as the scattering of electron-hole pairs with phonons.

The optical transition energy for center of mass momentum K_{CM} is the sum of the band-gap energy, the binding energy (intrinsically negative), and the kinetic energy:

$$\Delta E(n, K_{CM}) = E_{\text{gap}} + E_{\text{binding}} + E_{\text{kinetic}} = E_{\text{gap}} - \frac{R_X}{n^2} + \frac{\hbar^2 K_{CM}^2}{2M}. \quad (2.8)$$

The modified Bohr radius for the exciton is

$$a_X = \frac{\epsilon_b m_0}{\mu} a_H, \quad (2.9)$$

where a_H is the hydrogen Bohr radius of 0.053 nm. Similar to hydrogen, the maximum probability separation distance between the electron and hole changes with n as $r_n = n^2 a_X$. Using the above numbers for GaAs, the $n = 1$ exciton binding energy is $R_X = 4.2$ meV and the Bohr radius is $a_X = 13.5$ nm. This radius compared with the $a = 0.56$ nm lattice constant for GaAs confirms that the excitons are the Wannier-Mott since the electron and hole are separated by many lattice sites. Furthermore, the binding energy is small compared to the room temperature energy $k_B T \approx 25$ meV. Room temperature thermal energy prevents the formation of excitons in bulk GaAs since it provides the exciton ionization energy. Thus cryogenic cooling is necessary before observation of the bound exciton state is possible.

Since an exciton is a two-particle state, its energy levels cannot be represented as the promotion of an electron to the conduction band, as shown in Fig. 2.1. This picture is unable to capture the energy of both the electron and hole that make up the total energy of the bound state. Rather, the center of mass picture, as shown in Fig. 2.3a, correctly describes the excitation of bound exciton states. The absorption of a photon creates a state that lies along the photon dispersion line $E(k) = \hbar ck/n$, where c is the speed of light and $n = \sqrt{\epsilon_b} \approx 3.7$ is the nonresonant index of refraction for light at energies near the band gap. The optical excitation to one of the bound exciton states follows Eqn. 2.8.

Excitons are the dominant spectral feature below the band gap edge. The absorbance spectrum of GaAs, shown in Fig. 2.3b, illustrates the sharp peaks in absorption that correspond to the bound exciton states below the gap energy, E_{gap} . Photons absorbed by the semiconductor sample that exceed the gap energy create unbound electron-hole pairs. The continuum absorption approaches a finite value as the photon energy decreases to E_{gap} , instead of going to zero as predicted by free-carrier theory. This difference is known as the Coulomb (or Sommerfeld) enhancement of continuum absorption [32].

For bulk GaAs at low temperature (< 10 K), the direct band-gap energy is 1519.1 meV [33]. This energy less the binding energy of $R_X = 4.2$ meV of the $n = 1$ exciton at $K_{CM}=0$ is 1514.9 meV, which is the photon energy at which a peak occurs in the absorption spectrum. This photon energy corresponds to E_1 in Fig. 2.3b.

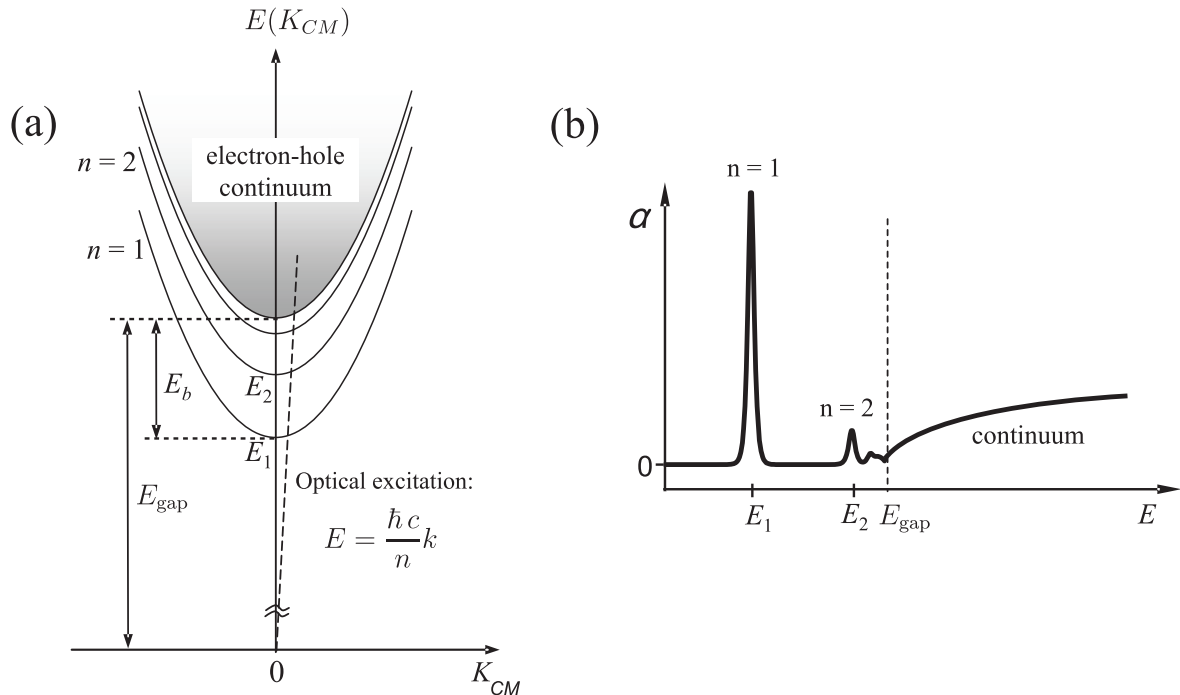


Figure 2.3: (a) Schematic diagram of exciton states and the continuum in the center of mass picture. Excitons can form at discrete energies below E_{gap} . Photons with energy exceeding E_{gap} can create unbound electron-hole pairs. (b) Calculated absorbance spectrum of GaAs at 1.2 K including Sommerfeld enhancement, based on Ref. [2]. As the photon energy increases, discrete peaks in the absorption correspond to the $n = 1, 2$, and higher bound states of the exciton.

The above description of exciton formation is modified when carrier motion is confined to two dimensions in a QW structure.

2.4 Excitons in GaAs quantum wells

It is possible to confine the motion of carriers to two dimensions by growth of heterostructures [34]. The basic technique typically involves molecular-beam epitaxial crystal growth of different layers of semiconductor material. In our studies, a thin (10 nm) layer of

GaAs is grown between two layers of $\text{Al}_{0.3}\text{Ga}_{0.7}\text{As}$, as illustrated in Fig. 2.4. The two materials have similar lattice constants, which allows for convenient growth of layers. However, $\text{Al}_{0.3}\text{Ga}_{0.7}\text{As}$ has a band-gap energy of 1.95 eV, whereas GaAs has a band-gap energy of 1.52 eV. This means that carriers that are promoted to the conduction band in GaAs are not free to move through the adjacent layers. The confinement of carriers in one dimension is known as a quantum well (QW).

QWs are of interest to industry because of their potential for applications. Their efficiency, speed, and optical response are superior to bulk semiconductors [35, 36]. QWs are also of interest from a fundamental point of view, since they are simple structures that clearly show quantum confinement effects [30, 37]. Confinement elevates the energy levels of the electron in the conduction band and moves the hole energy levels down in energy, leading to a stronger binding energy and a blue-shift in the exciton resonance as compared with bulk GaAs. In fact, because of the stronger binding energy between electrons and holes in QWs, strong optical exciton signatures in QWs may be observed at room temperature [38]. In addition to modification of the binding energy, confinement modifies the Bohr radius and oscillator strength of the exciton.

The effect of confinement on the exciton in one dimension becomes meaningful when the size of confinement is comparable to the spatial extent of the exciton. Since the Bohr radius is $a_X = 13.5$ nm in three dimensions, a GaAs layer thickness of 10 nm leads to modifications in the properties of the exciton. The wave function is modified such that the degrees of freedom parallel to the growth plane (\hat{x} - \hat{y}) remain the same, but the \hat{z} -direction component is the solution to the quantum mechanical problem of a particle in a box. Essentially, the n in the solutions to 2.2 must be replaced by $n - 1/2$ when going from 3D to 2D. When we include this modification, the binding energy becomes [39]

$$E_{\text{binding}}^{(2D)}(n) = -\frac{R_X}{(n - 1/2)^2} \quad (2.10)$$

which means that the 2D exciton is more strongly bound than in bulk material. For example,

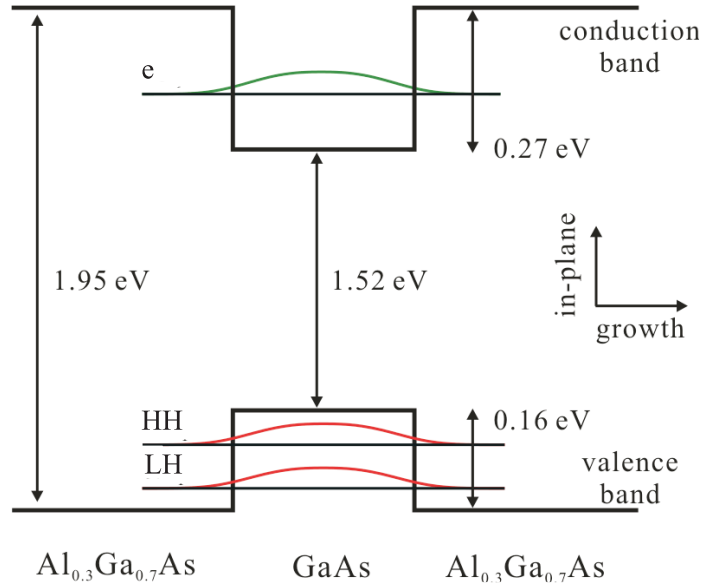


Figure 2.4: Lowest-lying energy states, $n = 1$, for QW excitons. Growing a thin layer of GaAs between two layers $\text{Al}_{0.3}\text{Ga}_{0.7}\text{As}$ creates a quantum well (QW). The confinement pushes the electron (e) and hole energies away from each other and lifts the degeneracy between light-hole (LH) and heavy-hole (HH) states.

the $n = 1$ exciton in the ideal 2D case has a binding energy 4 times that in the bulk, or $E_{\text{binding}}^{(2D)}(n = 1) = -16.8 \text{ meV}$. In practice, the binding energy is about half this value because of the finite size of the barriers [40]. The oscillator strength increases with n as $f(n) \propto 1/(n - \frac{1}{2})^3$ in two dimensions compared with $f(n) \propto 1/n^3$ for the bulk. The Bohr radius decreases compared with the bulk exciton radius to $a_X = (n - \frac{1}{2})^2 a_B$. Continuing the example for the ideal $n = 1$ exciton in 2D, the oscillator strength thus increases by a factor of 8 compared with the exciton in bulk GaAs. The dramatic increase in oscillator strength is because the confinement increases the overlap between the electron and hole wave functions as well as decreasing the Bohr radius. The increased overlap leads to stronger interaction between electrons and holes, increasing the probability of exciton formation. A more detailed analysis of confinement on excitons can be found in [41].

Excitons in QWs couple with the light field only for the low-momentum states. This can be visualized in Fig. 2.3 by picturing K_{CM} in two dimensions, with the energy level parabolas rotated about $K_{CM} = 0$ into paraboloids. The light line with slope $\frac{\hbar c}{n}$ sweeps out

a cone upon rotation. It is within this ‘light cone’ that QW excitons couple with light.

The wave functions for electron states in the conduction band in GaAs QWs are similar to those in the bulk; however, the holes’ wave functions in the valence band are more complicated since the valence band at the center of the Brillouin zone ($k = 0$) is degenerate. In bulk GaAs, the conduction band at the Brillouin center has s -orbital character with two-fold degeneracy since the electron spin $J = \frac{1}{2}$. The valence band around $k = 0$ has p -orbital character wave functions for the upper sub-bands and the lower sub-band, with total angular momenta $J = \frac{3}{2}$ and $J = \frac{1}{2}$, respectively. The lower sub-band, known as the split-off band ($J = \frac{1}{2}$), is separated by 0.34 eV from the upper band at $k = 0$ because of spin-orbit coupling. The two upper valence bands ($J = \frac{3}{2}$) are called the heavy-hole and light-hole sub-bands, with projection of their angular momenta along the \hat{z} -axis J_z equal to $\pm\frac{1}{2}$ and $\pm\frac{3}{2}$, respectively.

The upper valence bands are named the heavy-hole (HH) and light-hole (LH) sub-bands because of their different effective masses, which lead to a lifting of band degeneracy when confined in one dimension. Differentiating the dispersion relation (Eqn. 2.8) with respect to momentum K_{CM} and solving for the mass, we find that the effective mass m^* of a carrier depends on the curvature of its band:

$$\frac{1}{m^*} = \frac{1}{\hbar^2} \frac{d^2 E(k)}{dk^2}. \quad (2.11)$$

This equation is used to calculate the effective masses in bulk, m_e^* and m_h^* , based on the band structure of GaAs. Calculations of the band structure [32] in 2D yield a stronger curvature for the LH band than for the HH band, thus yielding a lighter effective mass for the light holes. When holes are confined in one dimension, the effective hole masses in the direction of quantization yield a lifting in degeneracy, as depicted in Fig. 2.5. The lifting of degeneracy can be seen by noticing that the different masses have different energies in the solution to the particle in a box $E \propto 1/mL^2$, where L is the confinement size of the box, i.e., the quantum-well thickness.

In this thesis, we focus on the HH $1s$ exciton spectral feature, a bound state between a hole in the HH band and an electron in the conduction band. The exciton binding energy corresponds to $n = 1$ in Fig. 2.3, and has s -orbital character like the hydrogen ground state.

When a light field interacts with a QW, optical polarization plays a role in the transition rates between the various bands. These rates are determined by the spin-selection rules dictated by the angular momentum states in the valence and conduction bands.

2.5 Polarization selection rules QW electronic transitions

For the bands of interest near $k = 0$, the conduction band wave function has an “ s -like” character, and the valence band has a “ p -like” character. The wave function characteristics reflect the relative contributions to the density of states in each band from the atomic s - and p -orbitals of the atoms that form the solid.

The s -like electron in the conduction band is an eigenfunction of the momentum operator described by the extended-state Bloch function

$$\psi_{\vec{k}m} = u_m(\vec{r})e^{i\vec{k}\cdot\vec{r}} \quad (2.12)$$

where m is the spin ($m = \pm\frac{1}{2}$), \vec{k} is the crystal momentum, and u_m is the Bloch amplitude, invariant under periodic translations. The Bloch function is delocalized in the crystal, extending over many lattice sites. The Bloch amplitudes may be approximately separated into orbital and spin parts [23]:

$$u_{1/2}(\vec{r}) = R(r) \uparrow, \quad (2.13)$$

$$u_{-1/2}(\vec{r}) = R(r) \downarrow, \quad (2.14)$$

where R denotes the symmetrical coordinate part, and \uparrow (\downarrow) the spin part of the Bloch amplitude.

The valence band has “ p -like” character ($L = 1$) meaning that there exists large spin-orbit coupling. The large spin-orbit coupling suggests that the Bloch amplitudes for the

valence-band electrons can be expressed as eigenstates of the total angular momentum operator, $\hat{\mathbf{J}} = \hat{\mathbf{L}} + \hat{\mathbf{S}}$, and \hat{J}_z , the $\hat{\mathbf{z}}$ -projection of total angular momentum. Written in $|J, J_z\rangle$ notation, the eigenstates are $|\frac{3}{2}, \pm\frac{3}{2}\rangle$ for the HH valence band, $|\frac{3}{2}, \pm\frac{1}{2}\rangle$ for the LH valence band, and $|\frac{1}{2}, \pm\frac{1}{2}\rangle$ for the split-off band. We neglect the split-off band because it is energetically separated by $\Delta = 0.34$ eV from the HH and LH bands.

Electrons may undergo interband optical transitions following selection rules. The transition probability per unit time for an electron to be excited from the valence band to conduction band by interacting with an incident electromagnetic field \vec{E} is given in the electric dipole approximation by Fermi's golden rule:

$$R_{vb \rightarrow cb} = \frac{2\pi}{\hbar} \left| \langle cb | \vec{d} \cdot \vec{E} | vb \rangle \right|^2 \delta(E_{\text{gap}} - \hbar\omega) = \frac{2\pi}{\hbar} \left| \vec{E} \cdot \langle cb | \vec{d} | vb \rangle \right|^2 \delta(E_{\text{gap}} - \hbar\omega), \quad (2.15)$$

where $\langle cb | \vec{d} | vb \rangle = q_e \langle cb | \vec{r} | vb \rangle$ is the electric dipole matrix element that connects the valence and conduction bands, with $q_e = -|e|$ as the charge of the electron. From equation 2.15, we see that calculation of the dipole matrix elements (also called dipole moments) allow determination of the probability for an optical transition to occur given an optical excitation field.

In evaluating the dipole matrix elements, we consider electrons in a QW interacting with photons that have electric fields in the in-plane ($\hat{\mathbf{x}}\text{-}\hat{\mathbf{y}}$) direction. Thus, we consider the electric field is of the form $\vec{E} = E_x \hat{\mathbf{x}} + E_y \hat{\mathbf{y}}$, and we only evaluate the components $\langle cb | x | vb \rangle$ and $\langle cb | y | vb \rangle$ of the dipole moments. The dipole matrix elements can be calculated by decomposing the J states into the irreducible L and S representations using the Clebsch-Gordan coefficients $C_{L_z S_z J_z}^{L S J}$, according to [42]:

$$|J, J_z\rangle = \sum_{L+S=J} C_{L_z S_z J_z}^{L S J} |L, L_z; S, S_z\rangle. \quad (2.16)$$

This representation allows direct calculation of the dipole matrix elements with by using the radial hydrogen wave functions $R_{nl}(r)$ and the spherical harmonics $Y_l^m(\theta, \phi)$. For example, the HH state $|J = \frac{3}{2}, J_z = \frac{3}{2}\rangle = |L = 1, L_z = 1; S = \frac{1}{2}, S_z = \uparrow\rangle$. The dipole ma-

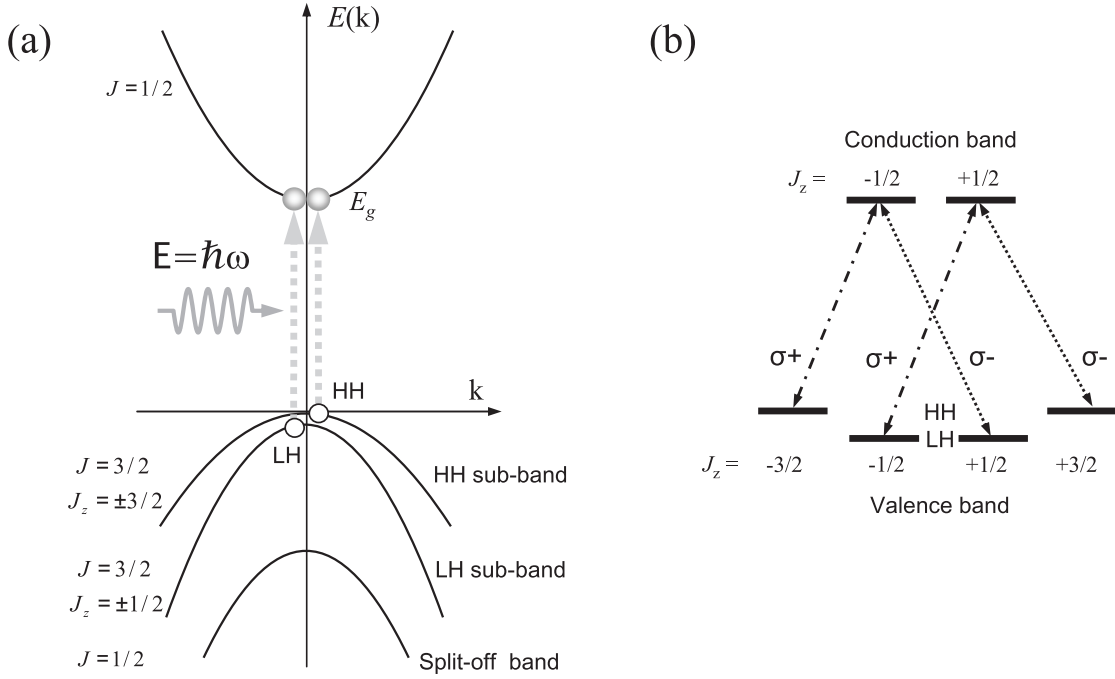


Figure 2.5: (a) Schematic of the hole sub-bands in GaAs, with the lifting in degeneracy at $k = 0$ due to confinement in one dimension between the light-hole (LH) ($J = \frac{3}{2}, J_z = \pm\frac{1}{2}$) and heavy-hole (HH) ($J = \frac{3}{2}, J_z = \pm\frac{3}{2}$) sub-bands. The split-off band ($J = \frac{1}{2}$) is shifted in energy because of spin-orbit coupling. (b) A diagram of selection rules for optical interband excitation with σ^+ and σ^- polarized light.

trix elements in the uncoupled representation between this valence-band state and the $|\uparrow\rangle$ conduction-band state ($|J = \frac{1}{2}, J_z = \frac{1}{2}\rangle = |L = 0, L_z = 0; S = \frac{1}{2}, S_z = \uparrow\rangle$) are calculated:

$$\begin{aligned} \langle cb | x | vb \rangle &= \langle 0, 0; 1/2, \uparrow | x | 1, 1; 1/2, \uparrow \rangle \\ &= \int d^3\vec{x} R_{10}^*(r) Y_0^{0*}(\theta, \phi) x R_{21}(r) Y_1^1(\theta, \phi) = \frac{1}{\sqrt{2}} \mu_0 \end{aligned} \quad (2.17)$$

$$\begin{aligned} \langle cb | y | vb \rangle &= \langle 0, 0; 1/2, \uparrow | y | 1, 1; 1/2, \uparrow \rangle \\ &= \int d^3\vec{x} R_{10}^*(r) Y_0^{0*}(\theta, \phi) y R_{21}(r) Y_1^1(\theta, \phi) = \frac{-i}{\sqrt{2}} \mu_0 \end{aligned} \quad (2.18)$$

$$\therefore \langle cb | \vec{d} | vb \rangle = \langle cb | (x\hat{x} + y\hat{y}) | vb \rangle = \mu_0 \frac{1}{\sqrt{2}} (\hat{x} - i\hat{y}), \quad (2.19)$$

where μ_0 is the transition dipole modulus of the HH exciton, and \hat{x} and \hat{y} are unit vectors. The forms of these transition calculations are identical in both 3D and 2D.

Continuing this calculation for all eight relevant transitions, the four nonvanishing

dipole matrix elements between initial and final J_z states in the form $\mu^{(\text{Initial } J_z \rightarrow \text{Final } J_z)} = \langle cb | \vec{d} | vb \rangle$ are:

$$\begin{aligned}
\mu^{(-\frac{3}{2} \rightarrow \frac{1}{2})} &= \mu_0 \frac{1}{\sqrt{2}} (\hat{\mathbf{x}} + i\hat{\mathbf{y}}) = \mu_0 \sigma^+ \\
\mu^{(-\frac{1}{2} \rightarrow \frac{1}{2})} &= \mu_0 \frac{1}{\sqrt{6}} (\hat{\mathbf{x}} + i\hat{\mathbf{y}}) = \frac{1}{\sqrt{3}} \mu_0 \sigma^+ \\
\mu^{(\frac{3}{2} \rightarrow \frac{1}{2})} &= \mu_0 \frac{1}{\sqrt{2}} (\hat{\mathbf{x}} - i\hat{\mathbf{y}}) = \mu_0 \sigma^- \\
\mu^{(\frac{1}{2} \rightarrow -\frac{1}{2})} &= \mu_0 \frac{1}{\sqrt{6}} (\hat{\mathbf{x}} - i\hat{\mathbf{y}}) = \frac{1}{\sqrt{3}} \mu_0 \sigma^-,
\end{aligned} \tag{2.20}$$

where σ^+ and σ^- are the Pauli operators, and μ_0 is the transition dipole modulus of the HH exciton. The transition dipole modulus of LH excitons is $\frac{1}{\sqrt{3}}$ times that of HH excitons, implying that the transition probability $|\mu|^2$ is three times smaller. Calculation of the transition dipole moments for the HH and LH excitons yields a selection rule that $\Delta J_z = \pm 1$ in an interband optical transition [43]. The selection rule is consistent with the fact that a photon carries an angular momentum of 1 in the dipole approximation.

The matrix elements are conveniently written to clarify the result of interaction with different polarization states of light. For right-circularly (left-circularly) polarized light, the field may be written as $E = \frac{1}{\sqrt{2}} E_0 (\hat{\mathbf{x}} + i\hat{\mathbf{y}}) = E_0 \sigma^+$ (as $E = \frac{1}{\sqrt{2}} E_0 [\hat{\mathbf{x}} - i\hat{\mathbf{y}}] = E_0 \sigma^-$). This field vector dotted into the first two (last two) dipole moments in Eqn. 2.20 yields unity (zero), while the dot product with the last two (first two) dipole moments is zero (unity). These facts, summarized in Fig. 2.5b, dictate the selection rules for the polarization of light in interband transitions. Circularly polarized light excites a valence-band electron exclusively into one of the two conduction-band states.

It is also worth noting that linearly polarized light $E = E_0^x \hat{\mathbf{x}} + E_0^y \hat{\mathbf{y}}$ may be written in the basis of circularly polarized light, e.g., $E = A\sigma^+ + B\sigma^-$, where A and B are constants determined by the linear transformation. In the simple case of horizontal and vertical polarizations, $E_x = \frac{1}{\sqrt{2}} E_0 (\sigma^+ + \sigma^-)$ and $E_y = E_0 \frac{1}{\sqrt{2}} (\sigma^+ - \sigma^-)$, respectively. If the linearly polarized light source is tuned to the heavy-hole resonance, it would cause interband excitations with equal probability into both conduction-band spin states, in contrast to the case for circular polarization.

While we have derived the optical transition rates for the electronic states, we wish next to understand carrier dynamics in the presence of an exciting electric field. We uncover the basic dynamics by modeling a two-level system using the optical Bloch equations.

2.6 Optical Bloch Equations

Most of the semiconductor community's understanding of optical excitation of semiconductors comes from the semiconductor Bloch equations [44], discussed in §5.4.2. These equations describe the coupled dynamics of electrons, holes, and optical polarization. The model includes Coulomb interactions between particles and the extended-state nature of particles expressed by Eqn. 2.12 by summing over a wide range of \vec{k} -vectors.

We can gain insight about the response of a semiconductor system through a simpler set of equations, known as the Optical Bloch Equations (OBEs). The OBEs describe the dynamics of a two-level system in the presence of an electric field. The two levels in our system are the valence and conduction bands of the semiconductor. We neglect Coulomb interactions and \vec{k} -dependence.

We seek the dynamics of a system

$$|\psi(t)\rangle = c_g(t) |g\rangle + c_e(t) |e\rangle, \quad (2.21)$$

where $|g\rangle$ and $|e\rangle$ represent the electron in the valence band (ground state) and the electron in the conduction band (excited state), respectively. The coefficients $c_i(t)$ determine the time dynamics. Since we have an ensemble of carriers in our system, we use the density matrix in the $\{|g\rangle, |e\rangle\}$ basis to solve for the temporal evolution:

$$\begin{aligned} \hat{\rho} = |\psi\rangle \langle\psi| &= \begin{pmatrix} \rho_{gg} & \rho_{ge} \\ \rho_{eg} & \rho_{ee} \end{pmatrix} \\ &= \begin{pmatrix} c_g c_g^* & c_g c_e^* \\ c_e c_g^* & c_e c_e^* \end{pmatrix}. \end{aligned} \quad (2.22)$$

From this definition, we see that $\rho_{ge}^* = \rho_{eg}$. The density matrix also has the property $\text{Tr}[\hat{\rho}] = 1$, from which it follows that $\rho_{gg} + \rho_{ee} = 1$. The density matrix $\hat{\rho}$ can be used to calculate the expectation value of an observable \hat{A} by taking a trace [45]:

$$\langle \hat{A} \rangle = \text{Tr} [\hat{\rho} \hat{A}]. \quad (2.23)$$

The time evolution of the density matrix follows from Schrödinger's equation [45]:

$$\frac{\partial \hat{\rho}}{\partial t} = \dot{\hat{\rho}} = -\frac{i}{\hbar} [\hat{H}, \hat{\rho}] - \text{decays}, \quad (2.24)$$

where “decays” must be added phenomenologically to this simplistic theory, although they can be determined rigorously in by quantizing the electromagnetic field [46]. The Hamiltonian $H = H_0 + V$ of the two level system can be written in our two-state basis as

$$\begin{aligned} H &= \sum_{j,k=e,g} |j\rangle \langle j| (H_0 + V) |k\rangle \langle k| \\ &= \begin{pmatrix} E_g & 0 \\ 0 & E_e \end{pmatrix} + \begin{pmatrix} 0 & V_{eg} \\ V_{ge} & 0 \end{pmatrix}, \end{aligned} \quad (2.25)$$

where E_g and E_e are the eigenenergies of H_0 for the ground and excited states, respectively. The elements V_{eg} and V_{ge} represent the interaction between an electric field E and the two-level system. The interaction is

$$V = -\hat{\mu} \cdot \vec{E} = -q_e \vec{r} \cdot \vec{E}, \quad (2.26)$$

where \vec{E} is the envelope of the electric field. While the electric field and \vec{r} generally have three space components, we reduce the problem to a single dimension for simplification, using $\vec{r} = \hat{x}$ and $\vec{\varepsilon} = \varepsilon(t)\hat{x}$. The interaction term has the representation:

$$\begin{aligned} V &= \begin{pmatrix} 0 & \langle g| E(t) q_e x |e\rangle \\ \langle e| E(t) q_e x |g\rangle & 0 \end{pmatrix} \\ &= E(t) \begin{pmatrix} 0 & \mu_{eg} \\ \mu_{ge} & 0 \end{pmatrix}, \end{aligned} \quad (2.27)$$

where $\mu_{ge} = \mu_{eg}$ is the dipole matrix element that couples two levels that have an allowed dipole transition, e.g., a $1s$ state with a $2p$ state. Dipole matrix elements were computed for our system in §2.5.

The electric field magnitude has the form:

$$E(t) = \frac{1}{2} [\varepsilon(t)e^{i\omega t} + \varepsilon^*(t)e^{-i\omega t}], \quad (2.28)$$

where $\varepsilon(t)$ is the slowly varying time envelope of the electric field and ω is the driving frequency of the electric field.

We assume that the driving frequency is very close to the natural frequency of the system. Knowing that the matrix elements ρ_{eg} and ρ_{ge} couple directly to the applied electric field through the dipole moment μ_{ge} , it is convenient to write these in the rotating frame as :

$$\begin{aligned} \rho_{eg} &\rightarrow \rho_{eg}e^{i\omega t}, \\ \rho_{ge} &\rightarrow \rho_{ge}e^{-i\omega t}. \end{aligned} \quad (2.29)$$

By evolving $\hat{\rho}$ in time through Eqn. 2.24, we find the time evolution of the matrix elements of $\hat{\rho}$ in the rotating frame. In the rotating wave approximation, we neglect terms that oscillate at frequencies 2ω , -2ω , or $-\omega$ since they oscillate very fast in the rotating frame. The OBEs in the rotating wave approximation are [47]:

$$\begin{aligned} \dot{\rho}_{gg} &= -\frac{i}{\hbar}\mu_{ge} \left(\frac{\varepsilon^*}{2}\rho_{ge} - \frac{\varepsilon}{2}\rho_{eg} \right) + \gamma_{ee}\rho_{ee} \\ \dot{\rho}_{ee} &= \frac{i}{\hbar}\mu_{ge} \left(\frac{\varepsilon^*}{2}\rho_{ge} - \frac{\varepsilon}{2}\rho_{eg} \right) - \gamma_{ee}\rho_{ee} \\ \dot{\rho}_{eg} &= i\omega_{eg}\rho_{eg} + \frac{i}{2\hbar}\varepsilon\mu_{ge} (\rho_{ee} - \rho_{gg}) - \gamma_{eg}\rho_{eg} \\ \dot{\rho}_{ge} &= -i\omega_{eg}\rho_{ge} - \frac{i}{2\hbar}\varepsilon^*\mu_{ge} (\rho_{ee} - \rho_{gg}) - \gamma_{eg}\rho_{ge}, \end{aligned} \quad (2.30)$$

where $\omega_{eg} = [E_e - E_g]/\hbar$, and γ_{ee} and γ_{eg} are phenomenological terms describing the decay the excited state into the ground state and decay of the off-diagonal density-matrix element,

respectively. The relations $\dot{\rho}_{ge}^* = \dot{\rho}_{eg}^*$ and $\dot{\rho}_{gg} = -\dot{\rho}_{ee}$ both follow from the definition of the density matrix in Eqn. 2.22. We have assumed our two-level system to be closed, i.e., the population is conserved.

The OBEs describe the temporal evolution of the system. The electric field drives the population ρ_{ee} via the off-diagonal density-matrix elements ρ_{ge} and ρ_{eg} . The polarization is in turn driven by the electric field and the difference in population between the ground and excited states $\rho_{ee} - \rho_{gg}$ and the energy difference between the ground and excited states.

The population in the ground or excited states can be found by calculating the expectation value of the projection operator $|g\rangle\langle g|$ or $|e\rangle\langle e|$ using Eqn. 2.23:

$$\begin{aligned}\langle |g\rangle\langle g| \rangle &= \text{Tr}[\hat{\rho}|g\rangle\langle g|] = \rho_{gg} = c_g^*c_g = |c_g|^2 \\ \langle |e\rangle\langle e| \rangle &= \text{Tr}[\hat{\rho}|e\rangle\langle e|] = \rho_{ee} = c_e^*c_e = |c_e|^2,\end{aligned}\tag{2.31}$$

where $|c_g|^2$ and $|c_e|^2$ are the probabilities of finding the electron in the ground and excited state, respectively.

The optical polarization response of the system can be found by calculating the expectation value of the dipole operator $\hat{\mu}$ also using Eqn. 2.23:

$$\begin{aligned}\langle \hat{\mu} \rangle &= \text{Tr}[\hat{\rho}\hat{\mu}] \\ &= \text{Tr} \left[\begin{pmatrix} \mu_{ge}\rho_{ge} & 0 \\ 0 & \mu_{eg}\rho_{eg} \end{pmatrix} \right] \\ &= \mu_{ge}\rho_{ge} + c.c.\end{aligned}\tag{2.32}$$

The induced macroscopic polarization for a group of N oscillators is

$$P = N \langle \hat{\mu} \rangle = n [\mu_{ge}\rho_{ge} + c.c.].\tag{2.33}$$

Since the term ρ_{ge} is driven by the electric field, the induced polarization is proportional to the electric field as $P = \chi E$, where χ is the complex susceptibility. The polarization radiates a field in the direction of the exciting electric field according to Maxwell's equations [48].

The OBEs predict observed phenomena such as Rabi flopping, self-induced transparency, and photon echoes in atomic and solid systems [49]. We will refer to these equations in this chapter, and we will use them for simulations of our system in Chapter 8.

2.7 Decoherence and relaxation dynamics of QW excitons

A light field absorbed by a semiconductor generates a carrier population and polarization according to Eqns. 2.30. Following optical excitation, a series of decay processes occur until thermal equilibrium is reached. The processes can be considered in two regimes: coherent and incoherent.

The coherent regime begins directly after an excitation and occurs for GaAs QWs on a time scale of several picoseconds. As shown in the last section, optical excitation of a transition can create a superposition state between the ground and excited states, Eqn. 2.21, leading to a nonzero off-diagonal density-matrix element, ρ_{eg} . After optical excitation, we can transform the operator ρ_{eg} out of the rotating frame and see that it evolves in time as [44]:

$$\rho_{eg}(t) = \rho_{eg}^{\text{ind}} e^{i\omega t} e^{-\gamma_{eg} t}, \quad (2.34)$$

where ρ_{eg}^{ind} is the element induced by the optical field. The element ρ_{eg} determines the macroscopic polarization P . We see from Eqn. 2.34 that the polarization oscillates, radiating light at a frequency ω_{eg} , while decaying in magnitude. For this reason, the response of a two-level system to an optical field is often referred to as an oscillator, in analogy to a classical spring excited by an impulse [44]. As the polarization decays, it emits radiation according to $I_{\text{rad}} \propto |\ddot{P}|^2$. This radiation is known as the ‘free polarization decay’ in analogy to the ‘free induction decay’ radiation observed in magnetic systems [50].

For the case of excitons in GaAs QWs, the energy separation $E_e - E_g = E_1 = E_{\text{gap}} - E_{\text{binding}}$, as in Fig. 2.3. Directly after pulsed on-resonance optical excitation, the induced excitonic polarization oscillates with a period of ≈ 3 fs.

A polarization decays as a result of the oscillators becoming out of phase with one another because of fluctuations in their energy spacings. The phenomenological term γ_{eg} in Eqn. 2.34 accounts for the decay of the polarization, or dephasing of oscillators. We explore the physical origins of dephasing.

A fluctuation in the energy spacing between ground and excited states corresponds to a fluctuation in the frequency of a oscillation. In an ensemble of oscillators, the fluctuations in frequencies cause phase distortions of the oscillators with respect to each other, giving rise to dephasing. Phase-destroying processes can be considered scattering processes. These scattering processes include scattering with impurities or lattice defects, phonons, and other electronic excitations (e.g., exciton-exciton or exciton-carrier scattering) [50]. Elastic scattering events leave the energy level unchanged while perturbing the phase of an oscillator, whereas inelastic scattering causes energy relaxation. Either situation brings the oscillators out of phase with each other, or causes decoherence [11]. The characteristic time of phase relaxation, T_2 , is called the decoherence time (or dephasing time). In the absence of any scattering processes, the phase will ultimately be lost in the incoherent regime via an incoherent recombination process, discussed below.

The second, incoherent regime of the exciton dynamics is characterized by the polarization having decayed. In this regime, the electron and hole populations undergo intraband relaxation and interband recombination processes. Both mechanisms are considered incoherent relaxation processes [51].

Intraband relaxation occurs when carriers within the conduction band lose their kinetic energy and move in momentum space toward the band minima [50]. The relaxation occurs via energy-losing processes such as inelastic scattering and phonon emission. In the process of intraband relaxation, the temperature of the carriers (bound and unbound electron-hole pairs) approaches thermal equilibrium with the temperature of the lattice.

Interband recombination is the radiative process of an electron and hole recombining, or an electron relaxing in energy back into the valence band. This process is the opposite of the

previously described interband absorption process and is accompanied by the emission of a photon. Like interband absorption, the electron and hole must have similar momentum wave vectors because the momentum of a photon is small compared to the carrier momentum. Recombination of carriers via interband recombination occurs with higher probability at band minima since the time scale of intraband relaxation is faster than that of interband recombination in GaAs QWs [52]. The population lifetime, T_1 , is the time scale for incoherent relaxation.

For light to couple with excitons through the induced polarization, both the created electron and hole in a QW must have a low momentum. In other words, QW excitons must be within the light cone (described in §2.4) in order to couple with the light field and emit light out of the plane of the QW. Consequently, excitons in QWs radiatively recombine only at the lowest momentum states. Higher-momentum excitons may relax through scattering processes into low-momentum states where they may radiatively recombine. In GaAs QWs, populations of excitons decay at time scales on the order of tens of picoseconds, and free carriers decay at much longer time scales (nanoseconds).

As mentioned above, the recombination process limits the dephasing time in the absence of scattering processes. Since for optical excitation the number of excited oscillators N is proportional to the excitation field amplitude squared, according to Eqn. 2.15, and from the polarization $P = \chi E$,

$$N = N_0 e^{-t/T_1} \propto P^2 \propto [P_0 e^{-t/T_2}]^2, \quad (2.35)$$

it follows that $2T_2 \leq T_1$ [50]. The equality holds in the absence of any phase destroying processes. In GaAs (and in most semiconductors), $T_2 \ll T_1$ because of the various scattering processes that cause dephasing [53].

2.8 Homogeneous vs. inhomogeneous broadening

Effects that lead to dephasing and relaxation can be classified as homogeneous or inhomogeneous. While both lead to a broader resonance line shape, their origins are fundamentally different. We specifically discuss $1s$ excitons in QWs in this section.

In a homogeneously broadened situation, all oscillators have the same frequency ω_0 , and the linewidth is determined exclusively from the dephasing time T_2 . This type of broadening may be due to either radiative decay or scattering events. Scattering events in general are considered homogeneous dephasing because all groups of excitons have the same probabilities of undergoing a given scattering event. Excitons may scatter with other excitons, polarization, free carriers, and phonons.

Inhomogeneous broadening refers a distribution of oscillator frequencies. The primary example in our system is the effect of disorder. Disorder describes fluctuations in the lattice spacing due to impurities in the lattice. In QWs, differences in well width size L lead to different oscillator energies since the particle-in-a-box energy depends on the size of confinement as $1/\sim L^2$ [42]. Disorder is an inhomogeneous source of dephasing since different groups of excitons have different energy levels, or oscillation frequencies, depending on their position in the QW.

In GaAs QW systems at low temperatures, inhomogeneous broadening dominates the width of the resonance because of disorder. There exists disorder in thin QW systems because fluctuations in well-thickness of a single-atom layer (0.56 nm) is sizeable compared to the well thickness (10 nm). In high-quality bulk samples or in QW systems at elevated temperatures, homogeneous broadening can dominate as a result of inelastic scattering of excitonic resonances with optic and acoustic phonons [50].

At high excitation densities, interactions between excited amplitudes (polarization, free carriers, excitons, phonons) can be so strong that the linewidth is homogeneously broadened. This effect, known as excitation-induced dephasing (EID), together with inhomogeneous

broadening and other effects that depend on excitation density, can be explored with the use of nonlinear optical spectroscopy techniques. We review the common spectroscopy techniques used to characterize exciton resonances, and then consider the potential of nonlinear techniques for accessing information about the system beyond the capabilities of linear techniques.

2.9 Spectroscopy of semiconductors

The linear and nonlinear properties of semiconductors can be explored by using optical spectroscopy. Spectroscopic techniques have provided information about semiconductors including electronic band structure, phonons, excitation spectra such as excitons, and properties of defects for a variety of materials [24]. The utility of optical spectroscopy is introduced with a simple model which elucidates the relationship between the optical field and polarization. The remainder of this chapter explores linear and nonlinear spectroscopic techniques.

2.9.1 Driven oscillator model

To understand the spectroscopy of semiconductors, is helpful to have the analogy of a driven oscillator in mind [44, 47]. The displacement x for a mass m with charge e on a spring is governed by:

$$m \frac{d^2x}{dt^2} + m\gamma \frac{dx}{dt} + m\omega_0^2 x = q_e E, \quad (2.36)$$

where γ is the damping rate, ω_0 the resonant frequency of oscillation, $q_e = -|e|$ is the charge of the electron, and E the driving electric field. We find that the position of the oscillator in response to a sinusoidal field $E(t) = E_0 e^{-i\omega t}$ to be:

$$x(t) = \frac{e/m}{\omega_0^2 - \omega^2 - i\gamma\omega} E(t). \quad (2.37)$$

The polarization of an oscillating charge is given by $p(t) = ex(t)$. For a group of N oscillators, the macroscopic polarization may be computed as

$$\begin{aligned}
P(t) &= Np(t) = Nex(t) \\
&= \frac{Ne^2/m}{\omega_0^2 - \omega^2 - i\gamma\omega} E(t) \\
&= Ne^2/m \left(\frac{\omega_0^2 - \omega^2}{(\omega_0^2 - \omega^2)^2 - (\gamma\omega)^2} + i \frac{\gamma\omega}{(\omega_0^2 - \omega^2)^2 - (\gamma\omega)^2} \right) E(t) \\
&= [\chi' + i\chi''] E(t)
\end{aligned} \tag{2.38}$$

where χ' and χ'' represent the real and imaginary parts of the susceptibility, respectively.

We learn from the plot of the polarization response in Fig. 2.6a that the amplitude of the induced polarization frequency response is at its maximum when the driving electric field is on resonance with the oscillator, or $\omega = \omega_0$. The phase of the polarization is in phase with the electric field well below resonance, and 180° out of phase far above resonance. On-resonance corresponds to a 90° phase shift of the polarization with respect to the electric field. The real and imaginary parts of the polarization response are shown in Fig. 2.6b. These are the χ' and χ'' , respectively, which relate the polarization response of a material to the incident electric field.

A group of oscillators responds to an electric field by reradiating light. We explore the material response to optical excitation in the linear and nonlinear regimes in the next section.

2.9.2 Linear spectroscopy

A simple way to observe the linewidths of an excitonic resonance is to perform an absorbance experiment, as illustrated in Fig. 2.7. In this experiment, a low-intensity tunable monochromatic light source is incident on a sample. The light intensities $I_{\text{in}}(\omega)$ and $I_T(\omega)$ before and after the sample, respectively, are measured for a series of optical frequencies.

This experiment is called ‘linear’ because in the regime of a low-intensity light source, the induced polarization P is linear to the electric field E , which is just the frequency-domain

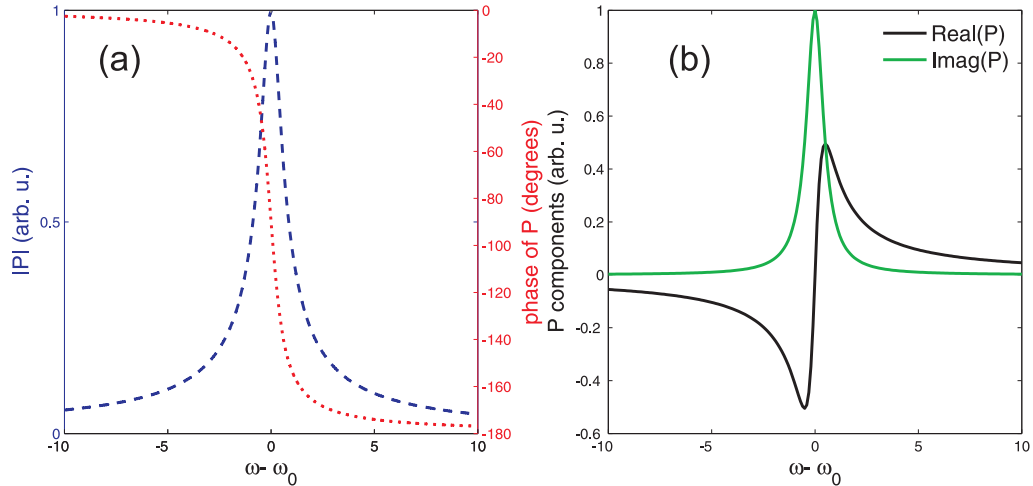


Figure 2.6: Visualization of the Lorentz oscillator model [Eqn. 2.38]. (a) The real and imaginary parts of the induced polarization. (b) The magnitude of the polarization and the phase.

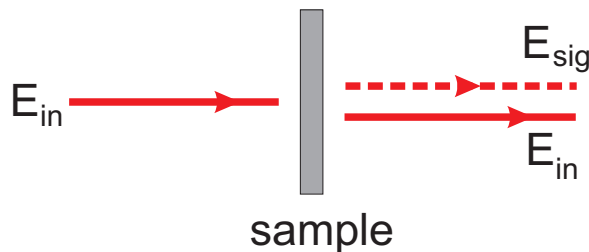


Figure 2.7: Linear absorption. An input field E_{in} induces a polarization in a sample which in turn radiates E_{sig} in the same direction, producing a cancellation with the input field.

expression of Eqn. 2.38:

$$P(\omega) = \chi(\omega)E(\omega) = [\chi'(\omega) + i\chi''(\omega)]E(\omega), \quad (2.39)$$

where χ' and χ'' represent the real and imaginary parts of the susceptibility, respectively. We note here that the real and imaginary parts of the polarization directly correspond to the real and imaginary parts of the susceptibility in the linear regime, as shown in the Lorentz oscillator model in Fig. 2.6. The induced polarization radiates light with two phases, in phase (real part of Eqn. 2.39) and with a 90° phase shift (imaginary part), both in the direction of the input beam. Maxwell's equations show that the electric field from a polarization is another 90° out of phase, meaning that the light radiated from the dipole at ω_0 is 180° out of

phase with the incident field, causing destructive interference in the direction of the driving electric field. The intensity measured in the direction of the input beam is the interference between the input field E_{in} and the reradiated field from the induced polarization E_{sig} [54]:

$$\begin{aligned} I_{out} &= |E_{in} + E_{sig}|^2 \\ &= |E_{in} + i\chi E_{in}|^2 \\ &\approx I_{in}(1 - 2\chi''), \end{aligned} \tag{2.40}$$

where $I_{in} = |E_{in}|^2$ is the intensity of the input field. The linear approximation assumes $\chi \ll 1$ so that the χ^2 terms vanish. This approximation is acceptable in the situation where the medium is sufficiently dilute. In the case where the medium becomes very dense, local-field corrections need to be applied [47]. We can see here a partial cancellation of the incoming field in the measured intensity. The imaginary part of the susceptibility contains information regarding the absorption as a function of frequency. Experimentalists typically perceive the linear absorption as a measurement of the absorption coefficient, which is related to χ'' .

According to the Lambert-Beer law [55], the transmitted light through a material has a logarithmic dependence on the absorption coefficient: $I_T(\omega) = I_{in}(\omega)e^{-\alpha(\omega)L}$, where L is the optical path length through the sample and α is the ‘absorption coefficient.’ Solving for αL yields the absorbance spectrum:

$$\alpha(\omega)L = -\ln\left(\frac{I_T(\omega)}{I_{in}(\omega)}\right). \tag{2.41}$$

The absorption coefficient α is related to the index of refraction, $n(\omega) = n'(\omega) + in''(\omega)$, as proportional to the imaginary part [47]:

$$\alpha(\omega) = 2n''(\omega)\omega/c. \tag{2.42}$$

The index of refraction is related to the linear susceptibility χ :

$$n(\omega) = \sqrt{\epsilon(\omega)} = \sqrt{1 + \chi(\omega)} \approx 1 + \frac{1}{2}\chi(\omega), \tag{2.43}$$

where we have again invoked $\chi \ll 1$. From Eqns. 2.43 and 2.42, we may conclude the relationship $\alpha(\omega) \approx \chi''(\omega)\omega/c$. This relationship shows that the linear susceptibility is directly related to optical absorption.

Linear absorption experiments have been performed in semiconductors to observe exciton spectral features, determine dielectric structure, and study the temperature dependence of exciton linewidths [56]. Linear absorption measurements can also be extended to the case where the effects of an electric field applied across the sample on the absorbance spectrum can be recorded. This technique is known as electroabsorption [57].

Another technique, known as photoluminescence (PL), is a measurement of the spontaneous emission from a material. The experiment involves illuminating a sample with an energy greater than the band-gap energy. Electrons are promoted into the conduction band, relax into low-momentum states, and then recombine, radiating light in 4π steradians. A portion of this light is collected with a lens and focused into a spectrometer, where it can be spectrally resolved. PL experiments can reveal information about the intraband and interband relaxation processes through observation of the different intensities emitted as each of the resonances. For example, the intensity of the $1s$ emission relative to other resonances can help to quantify the recombination rates [58, 59].

In another linear technique, photoluminescence excitation spectroscopy (PLE), a sample is excited with a tunable laser, and the peak luminescence intensity is measured as the laser wavelength is tuned. The shape of the emission is independent of the way that the carriers are excited, and so the signal strength is proportional to the carrier density, which is determined by the absorption coefficient [1]. While this technique provides the same information as the linear absorption experiment, it can be useful in situations where direct transmission is impossible, e.g., for thick substrates.

While these techniques are very helpful in characterizing the linear properties of a sample, experiments in the nonlinear regime provide a greater range of information regarding processes and kinetics in a sample.

2.9.3 Nonlinear spectroscopy

In nonlinear spectroscopy, the intensity of light is sufficiently intense that the induced polarization in the sample is no longer proportional to the electric field strength of the incident light [11]. Rather, higher powers of the electric field must be considered, i.e.,

$$P = \chi^{(1)}E + \chi^{(2)}E^2 + \chi^{(3)}E^3 + \dots, \quad (2.44)$$

where the nonlinear susceptibility $\chi^{(n)}$ is an $n + 1$ order tensor that may be sensitive to the directions in which the electric fields are applied with respect to the crystalline axes of solid materials.

For example, if two optical fields are applied to a sample in different directions, a second-order nonlinear polarization $P^{(2)} = \chi^{(2)}E_1E_2$ may be generated in along a third direction. This may be computed [47] through the second-order susceptibility $\chi^{(2)}$:

$$P_i^{(2)} = \sum_{j,k=x,y,z} \chi_{ijk}^{(2)} E_j E_k. \quad (2.45)$$

For materials lacking inversion symmetry, the induced polarization reradiates a field in a direction that is a linear combination of the electric field wave vectors. For the example of two-field mixing, if two beams with wave vectors \vec{k}_1 and \vec{k}_2 and frequencies ω_1 and ω_2 were incident on a sample, the second-harmonic generation signal (with frequency $\omega_1 + \omega_2$) would be found in the $\vec{k}_1 + \vec{k}_2$ direction, as indicated in Fig. 2.8. Additionally, a difference-frequency signal ($\omega_1 - \omega_2$) may be found in the $\vec{k}_1 - \vec{k}_2$ direction.

Many materials have inversion symmetries that result in vanishing $\chi^{(2)}$. For the GaAs QW sample used in this work, the QWs were grown along the (100) plane. For this orientation, the zinc-blende structure of GaAs is inversion symmetric. In an inversion symmetric plane, the sign of the induced polarization must change if the sign of the electric field in Eqn. 2.45 is changed. However, for $\chi^{(2)}$ (and $\chi^{(2n)} \forall n \in \mathbb{N}$) processes, the polarization does not change sign since it depends on E^2 . Since $-P = P$, the only possibility is that the generated polarization is zero. Thus it is impossible to observe any signals related to $\chi^{(2)}$ unless

symmetry is broken because of, e.g., application of strain or a strong static electric field. However, two fields may still generate a nonlinear polarization through $\chi^{(3)}$ regardless of crystal symmetry. This is the susceptibility involved in a variety of nonlinear spectroscopies.

Nonlinear spectroscopy techniques typically involve multiple light fields incident on the sample. Because of the fast (\sim ps) dephasing and band-relaxation processes, ultrafast (femtosecond) laser pulses are often used to study the coherence and quantum kinetics in semiconductors. A thorough review of ultrafast spectroscopy is given by Shah [24].

2.9.3.1 Transient absorption

A common spectroscopy technique using two pulses is the transient-absorption experiment. The majority of the experiments reported in this thesis involve this technique. The concept is illustrated in Fig. 2.8. In transient absorption, a high-intensity pump pulse (E_{pump}) incident on the sample generates a nonequilibrium state in the quantum wells. Some time τ later, a weak-intensity probe pulse (E_{probe}) monitors the sample, and the light in the direction of the probe is recorded by a photodetector. Information about the state created by the pump may be then read by scanning the time delay and/or spectrally resolving light in the direction of the probe beam.

In the experiments in this thesis, we perform spectrally resolved transient absorption. Measurement of the probe spectrum for a series of τ delay times yields information about the incoherent population dynamics. The line shape of the probe absorption allows investigation of the many-body configuration created by the pump pulse.

Although the pump pulse itself could be spectrally resolved to gain information about the many-body effects, it is more complicated to analyze since the dynamics that determine its line shape happen during the pump pulse duration. Additionally, a single-pulse nonlinear absorption measurement does not allow resolution of time dynamics. It is for these reasons that we perform spectrally resolved transient absorption.

For a transient-absorption experiment, the nonlinear signal is radiated in the direction

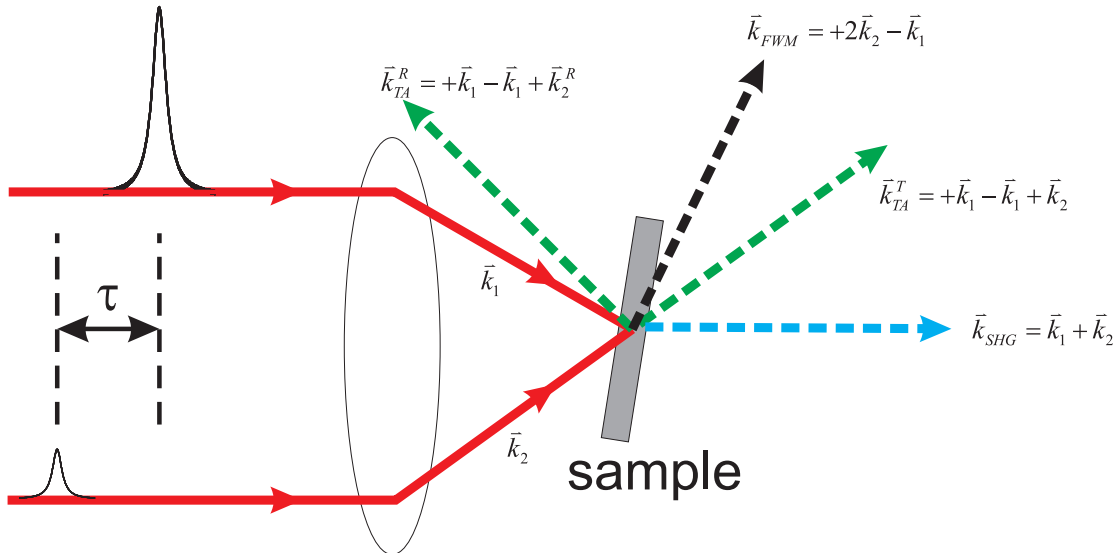


Figure 2.8: Schematic for a two-pulse nonlinear experiment. The sample is tilted for clarity. Two pulses are separated by a delay τ , and focused with a lens onto a sample with directions \vec{k}_1 and \vec{k}_2 , respectively. For transient absorption (TA), the pump \vec{k}_1 and probe \vec{k}_2 generate a signal (green dashed lines) in the reflected and transmitted probe beam directions. For second-harmonic generation (SHG), the signal (blue dashed line) is detected in the $\vec{k}_1 + \vec{k}_2$ direction. A four-wave mixing (FWM) signal (black dashed line) may be detected in the $2\vec{k}_2 - \vec{k}_1$ direction.

of the transmitted and reflected probe. This follows from calculating the induced $\chi^{(3)}$ polarization, similarly to Eqn. 2.45, as proportional to three electric fields, with the pump field (\vec{k}_1) acting twice, and the probe field (\vec{k}_2) acting once [54]:

$$\begin{aligned}
 P^{(3)} &\propto E_1 E_1^* E_2 \\
 &\propto (e^{-i\omega_1 t + i\vec{k}_1 \cdot \vec{r}})(e^{+i\omega_1 t - i\vec{k}_1 \cdot \vec{r}})(e^{-i\omega_2 t + i\vec{k}_2 \cdot \vec{r}}) \\
 &= e^{-i\omega_{sig} t + i\vec{k}_{sig} \cdot \vec{r}}, \tag{2.46}
 \end{aligned}$$

$$\therefore \omega_{sig} = +\omega_1 - \omega_1 + \omega_2 \tag{2.47}$$

$$\vec{k}_{sig} = +\vec{k}_1 - \vec{k}_1 + \vec{k}_2, \tag{2.48}$$

The emitted signal field $E_{sig} \propto P^{(3)}$, assuming that only pump-induced absorption changes matter. The total signal measured in transient absorption (valid for both the probe transmission and reflection directions) is typically the differential intensity with and without the

pump field present:

$$\Delta I(\tau) = [|E_{probe} + E_{sig}(\tau)|^2 - |E_{probe}|^2]. \quad (2.49)$$

We see that E_{sig} depends on the relative delay τ between pump and probe. Furthermore, for $|E_{probe}| \gg |E_{sig}|$, the detected differential intensity is dominated by the cross term:

$$\Delta I(\tau) \approx 2E_{probe}E_{sig}(\tau) \propto P^{(3)}. \quad (2.50)$$

The differential transmission represents then a direct measurement of the induced third-order polarization. This signal yields information about the incoherent dynamics, since $\Delta I(\tau) \propto |\mu_{eg}|^8 e^{-\gamma_{ee}\tau}$, where γ_{ee} is the decay rate of the excited state and $|\mu_{eg}|$ is the transition dipole modulus between the ground and excited state, both in Eqn. 2.30. The differential intensity can be interpreted as the change in population of the states observed by the probe field. Measurement of the effects due to population changes and relaxation is the strength of the transient-absorption technique. Spectrally resolved transient absorption is discussed in more detail in Chapter 3.

2.9.3.2 Four-wave mixing

Another common technique involving third-order polarization is called four-wave mixing (FWM). A generalization of the transient-absorption technique, FWM allows resolution of the coherent dynamics, i.e., dephasing. While there are many versions of FWM experiments, the geometry of Fig. 2.8 can be used to detect a FWM signal. The only required change is setting up a detector in a direction $2\vec{k}_2 - \vec{k}_1$. The interpretation of this experiment is that the \vec{k}_1 and \vec{k}_2 pulses form a population grating inside the sample from which the \vec{k}_2 pulse then diffracts. This experiment can reveal information about the nature of broadening (homogeneous or inhomogeneous), dephasing times, and non-Markovian relaxation dynamics. Many forms of FWM are used to probe QW response, including time-resolved, time-integrated, and spectrally resolved FWM. Additionally, the new technique

of two-dimensional Fourier spectroscopy can be used to resolve coupling between excitonic resonances and distinguish sources of dephasing [60, 61, 43, 62, 63].

Transient-absorption spectroscopy and FWM spectroscopy are both forms of nonlinear spectroscopy commonly used to investigate semiconductor systems. Other nonlinear experiments include time-resolved and time-integrated photoluminescence [64, 6, 2] as well as interferometric measurements of pulses transmitted through the sample [65]. Nonlinear experiments are particularly helpful in revealing the effects of intense fields that produce effects that can only be attributed to the interactions between particles and polarizations, i.e., many-body effects. The next section discusses some of the many-body effects discovered using nonlinear spectroscopy that motivated the experiments performed in my thesis work.

2.10 Many-body effects in GaAs QWs

Much research has been performed in the nonlinear regime for bulk GaAs over the past 40 years [17, 18, 19]; with the development of molecular-beam epitaxy techniques in the 1960s, the study of QW structures became possible. Many-body interactions in QW structures have application in optical switching [66, 67], integrated circuits [68], terahertz applications [69], communications [70], photovoltaics [71], and potentially in quantum computation [72] devices.

A wide variety of observable many-body effects manifest in a GaAs QW system upon excitation by intense laser light. The effects are strongly coupled, which makes it challenging to determine in practice which nonlinear observables can be attributed to which many-body effects.

When a light source excites a QW system at low densities, interactions between bound excitons and free carriers can be neglected in the theory and still match the experimental result with accuracy [73]. This is known as the linear regime. At high densities, however, many-body effects become important. These effects include scattering events (e.g., exciton-exciton, exciton-phonon, exciton-polarization), phase-space filling, screening, energy

renormalization, radiative decay, effects of exciton populations, blue shifting of the exciton resonance, transient gain, and the formation of biexcitons. These effects are in general coupled to each other. These effects can be probed with nonlinear spectroscopy, and their influence may be observed in the spectral line shape or in the time dynamics of emitted light.

Many-body effects may be observed when the intensity of the excitation source is high, generating a $P^{(3)}$ material response that is measurable. When coherent light with resonant frequencies is incident upon a QW, a portion of the light is absorbed, generating polarization and free carriers. The interactions between polarization and carriers can influence the dynamics and can even change the band structure. These changes influence the spectral line shape or the time dynamics of emitted light and can be observed using nonlinear spectroscopy.

2.10.1 Excitation-induced dephasing and shifting

One manifestation of these excitation-induced interactions can be observed via a broadened excitonic linewidth due to dephasing [74, 3]. For example, in [3] the researchers observe the broadening of the exciton linewidth as the excitation density is increased in a transient-absorption experiment in bulk GaAs. The broadening is inferred through the differential transmission signal, as shown in Fig. 2.9, which represents the difference in the exciton absorption profile with and without the pump excitation. The effect of excitation-induced dephasing (EID) may be interpreted as the effect of scattering between excited amplitudes (polarization, free carriers, excitons, phonons) leading to decoherence in the phase of the induced polarization, as discussed in §2.7.

The many-body interactions may also lead to a shifting of the exciton resonance energy. For example, in [4] a blue shift of a QW exciton resonance is observed for positive pump-probe delay, when the pump pulse precedes the probe, as shown in Fig. 2.10. The -5 ps delay is considered unexcited since the probe comes before the pump. The researchers in this paper attribute the blue-shift to repulsive interactions between excitons and screening

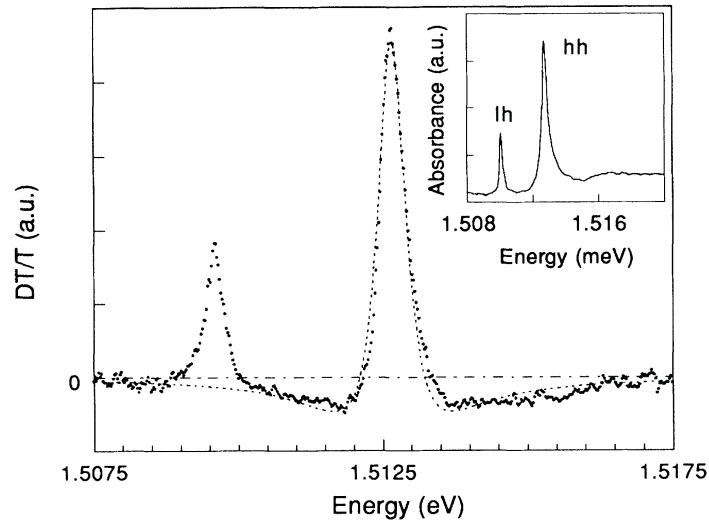


Figure 2.9: Excitation-induced dephasing (EID) observed in the differential transmission of a probe spectrum. The inset shows the probe absorbance in the absence of strong optical excitation. Figure from [3].

of the Coulomb potential. We discuss these effects in more detail below.

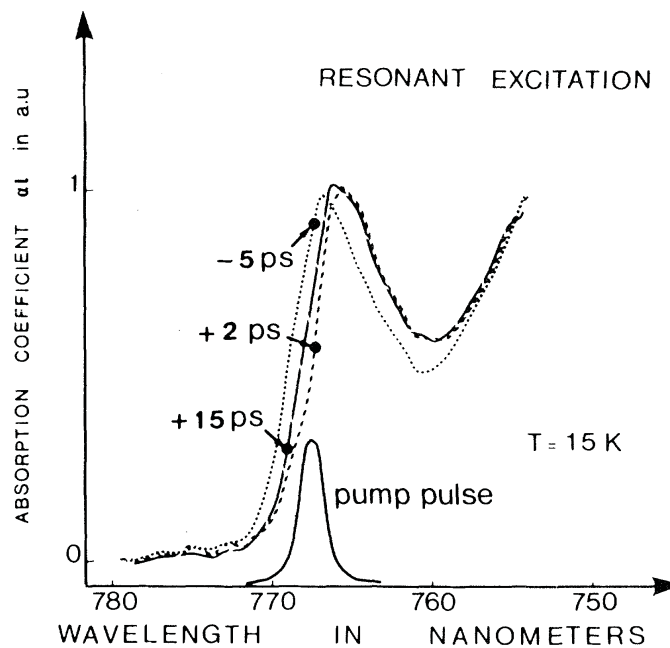


Figure 2.10: Blue shift in exciton absorption in a multiple QW structure. At positive delays (+2 and +15 ps), a blue-shift of the exciton resonance is observed compared to the unexcited (-5 ps) delay. Figure from [4].

2.10.2 Bleaching the exciton resonance

At very high excitation densities, a ‘bleaching’ or saturation of the exciton population is achieved where a smaller fraction of the light is absorbed by the quantum well as the intensity of the light source is increased [75, 76, 77, 78]. The observation of bleaching in transient-absorption measurements happens when increasing the pump intensity causes no further change in the probe response.

Bleaching can be attributed two effects: (i) phase-space filling, and (ii) Coulomb screening of the electric potential.

The phase-space filling effect is a consequence of the Pauli exclusion principle. Although excitons themselves are bosons, their constituent particles (electrons and holes) are fermions. Fermions have the property that no two identical particles may occupy the same state in phase space. Electrons in the conduction band and holes in the valence band must both be available in order to create bound exciton states. As more electrons are excited from the valence band to create excitons, the excitation probability decreases because of the limited availability of unique states in the bands. Phase-space filling contributes to a reduction in the absorption of light via reduction of the exciton oscillator strength [75]. The effect is also referred to as Pauli blocking since carriers in the conduction band block the promotion of valence band electrons into the same states.

Electrical screening, the other dominant effect that results in excitonic saturation, comes about from an alteration in the mean field in the QW structure [77]. In the limit where many carriers (free and bound) are created in the QW, the presence of charge changes the mean field. To understand this, we consider the example of a positive charge in a plasma of free carriers and excitons. The electric potential from the positive charge will fall off with increasing distance r faster than $1/r$ because the negative carriers in the plasma will tend to gather around the positive charge, weakening its Coulomb potential [79]. Although the bound exciton states have neutral charge, they have the possibility of screening the Coulomb

potential through the dipole interaction. The many-body effect of exciton populations on the nonlinear line shape has not been quantified before the research presented in this thesis. Our findings concerning the effects of the presence of exciton populations on the nonlinear line shape is discussed in Chapter 4.

The effect of the screening of the electric potential on the excitons is a weakening of the long-range Coulomb correlation between excitons, causing each exciton to be less tightly bound. The broadening of the exciton lines has been attributed to screening of the electric potential [75]. Although screening effects partly explain the line shape of the exciton, other effects are involved, which we will explore.

When the screening is so large that the Coulomb attraction between the electron and hole is weakened, a bound exciton state cannot form, and increasing the excitation intensity does not change the spectral features. A rough estimate of the densities at which excitons dissociate is given by the Mott density. For a pure exciton system, bleaching of excitons occurs when the density of carriers approaches the inverse volume of the exciton [80, 81]:

$$N_{Mott}^{3D} \approx \frac{1}{\frac{4}{3}\pi r_n^3} \quad (2.51)$$

$$N_{Mott}^{2D} \approx \frac{1}{4\pi r_n^2}, \quad (2.52)$$

where r_n is the exciton radius. Although this measure is inaccurate because of myriad effects, it is a reasonable guideline for understanding the saturation density. For example, using the value of the $n = 1$ exciton radius in §2.3, the 3D Mott density is $1 \times 10^{17} \text{cm}^{-3}$, and the 2D Mott density is $2 \times 10^{11} \text{cm}^{-2}$. These estimates agree with the literature for reported saturation densities of $2 \times 10^{17} \text{cm}^{-3}$ for the bulk and $1 \times 10^{11} \text{cm}^{-2}$ for 10 nm QWs [82, 83].

2.10.3 Band-gap renormalization

Another nonlinear effect of a large number of electrons into the conduction band is the modification of the band structure, known as band-gap renormalization [30]. The band structure has influence over dipole matrix elements, broadness of energy levels, and the

exciton binding energy [24, 84, 85]. In GaAs QW structures, the valence- and conduction-band energies are pushed closer to each other in energy, decreasing the band-gap energy E_{gap} . The exciton energy levels stay at the same energies relative to the band gap, and so the excitation energy necessary to create excitons actually decreases. The result is a red-shift of the exciton energy [30]. This is a competing effect with the blue-shift described earlier. The combined effects of screening and band-gap renormalization make possible overlap between the continuum and exciton energies. If the conduction band energy matches the exciton energy, the excitons are then said to have zero binding energy, thus ionizing the excitons and promoting electrons into the conduction band. The effect of more free carriers causes an intensifying of the screening.

While attempts have been made to distinguish such effects as being modifications of the band structure (e.g., band-gap renormalization) and occupation effects (e.g., phase-space filling affecting transition rates), we recognize that these effects are coupled and do not attempt to make a distinction. Many-body effects depend on the total density of photoexcited carriers (and excitons) and on their distribution functions in phase space.

2.10.4 Excitonic gain

Another interesting many-body effect is the transfer of energy between pump and probe in a transient-absorption experiment. This effect was observed in Ref. [5]. The researchers observed an anomalous transmittance compared to the unexcited case near the exciton resonance in a GaAs QW system, as seen in Fig. 2.11. The maximum gain was observed for short time delays. The researchers explain their observations by using ‘dressed’ states of excitons. The anomalous transmittance in the presence of the pump excitation implies that the QW may be used as a gain medium or as an optical switch for communications devices. The theory of gain for application of a QW laser was explored in [86]. Although the gain has been observed before in GaAs QWs, the results presented in this thesis provide the most detailed understanding of this experimental phenomenon since the results are matched using

the semiconductor Bloch equations.

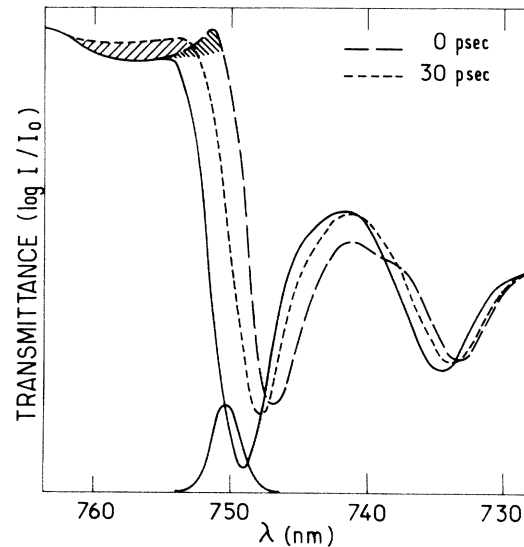


Figure 2.11: Optical gain observed in a transient-absorption experiment according to [5]. The unexcited transmittance spectrum (solid line) is shown in comparison to the excited probe spectra at two time delays. Cross-hatched regions correspond to optical gain.

2.10.5 Biexcitons

Another effect that can be observed at high exciton densities is the formation of exciton molecules called biexcitons, which are similar to an H_2 molecule [87, 88]. Formation of biexcitons requires high densities because two excitons need to be near each other to form a bound molecular state. Biexcitons are difficult to observe in bulk GaAs because the relatively small binding energy of the exciton (4 meV) leads to a theoretical biexciton binding energy of only a few tenths of a meV [39]. Thus, the exciton density at which biexcitons could form is beyond the Mott density, at which excitons dissociate because of scattering. However, in QWs the enhanced binding energy of excitons compared with the bulk allows the formation of biexcitons below the Mott density. The binding energy in a GaAs QW is typically around 1 meV [89]. This results in a new optical resonance around 1 meV below the exciton resonance in energy, in agreement with the photoluminescence spectrum in Fig. 2.12. The spectrum

shows two nearby spectral features, the exciton and biexciton, which are fit by a double Gaussian function.

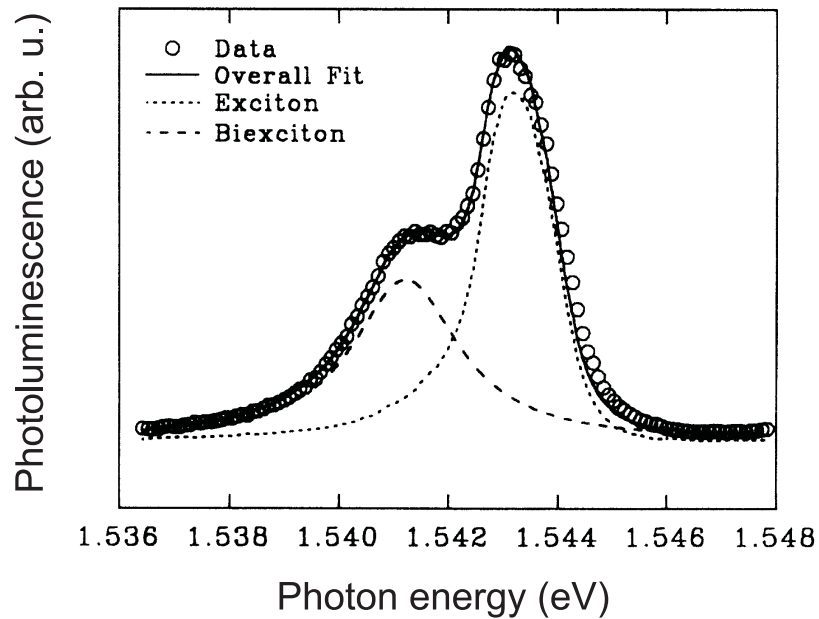


Figure 2.12: Exciton and biexciton features in a time-integrated luminescence spectrum. Figure from [6].

While many-body effects have been roughly explained by previous research, a more detailed understanding of the physics of the many-body interactions comes through analysis of quantitative data using the semiconductor Bloch equations (SBEs). The experimental research in this thesis combined with a robust theory using the SBEs makes possible a new level of quantitative analysis that allows a deeper understanding of the many-body interactions in GaAs QWs.

Chapter 3

Experimental techniques

In this chapter we present the techniques used to perform quantitative experimental characterization of the many-body configurations. We perform spectrally resolved transient absorption measurements in a pump-probe configuration, as discussed in §2.9.3.1. While many transient absorption measurements have been performed in the past, we make *quantitative measurements* of the probe absorption spectra in carefully calibrated *absolute units*. These measurements, combined with a characterization of the sample structure, allow quantitative comparison with a microscopic theory that connects the nonlinear changes in the probe absorption to many-body effects. The experiment-theory combination reveals new insight about the physics of many-body interactions, as we will discuss in Chapter 4.

These techniques are applicable to our quantitative studies of Coulomb-induced nonlinearities (Chapter 4) and of the effects of phase-modulated excitation pulses (Chapters 8,9) in a GaAs quantum-well (QW) sample.

The first step in characterizing the nonlinear effects in the sample is a full characterization of the sample structure. We then proceed to discuss the details of our transient absorption technique.

3.1 Sample characterization

We chose a well-understood system to demonstrate our new characterization technique: a molecular beam-epitaxy sample containing ten layers of 10 nm GaAs QWs, each separated

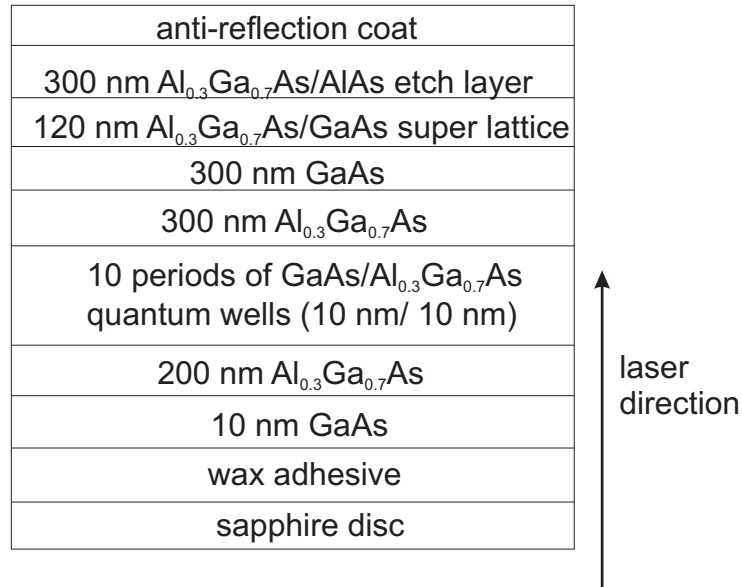


Figure 3.1: Schematic of the multiple quantum-well (QW) sample studied in this thesis. The 300 nm GaAs layer is referred to as the bulk layer in the discussion. The direction of the incoming laser beam is shown.

by 10 nm-thick $\text{Al}_{0.3}\text{Ga}_{0.7}\text{As}$ barriers [10, 30, 11]. Figure 3.1 shows a schematic of the sample. Rich Mirin of NIST fabricated the high-quality QWs by growing GaAs in a between barrier layers of $\text{Al}_{0.3}\text{Ga}_{0.7}\text{As}$ in a superlattice structure. Oxidation is avoided by terminating the sample with a GaAs cap layer on one side. A bulk layer of GaAs is grown to smooth the growth front before the QWs are grown on the sample substrate. We affixed the sample to a sapphire disk using optically clear epoxy, then thinned the sample by mechanical polishing and chemical etching. David Alchenberger, of the JILA instrument shop, then applied an antireflection coating for 800 nm light to the surface of the sample. This coating suppresses multiple reflections within the material that could lead to destructive interference at the location of the QWs.

We perform all measurements at 4 Kelvin in a helium-flow cryostat. To fix the model for sample-thickness parameters at low temperatures, we first measure a broad-spectrum absorption from our sample. To measure the absorption spectrum in absolute units, we carefully measure the transmission (T) and reflection (R) probabilities of the unexcited GaAs sample using a white-light source. In this case our source was broad-spectrum ampli-

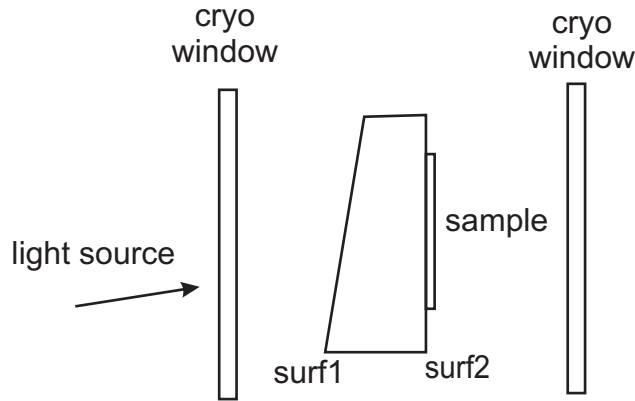


Figure 3.2: Detailed geometry of cryostat optics. The light source enters from the left side. There are losses due to reflection from the two surfaces of the sapphire disc (surf1 and surf2) in addition to the cryostat windows.

fied spontaneous emission from a Ti:sapphire laser cavity, with a bandwidth of around 400 meV and an average power of 100 nW. We calibrate the measured T and R spectra into true probabilities by careful consideration of the geometry of the elements in the cryostat (Appendix B). A schematic of the geometry of the cryostat optics is shown in Fig. 3.2. The sapphire disc is wedged to prevent interference between the reflecting surfaces.

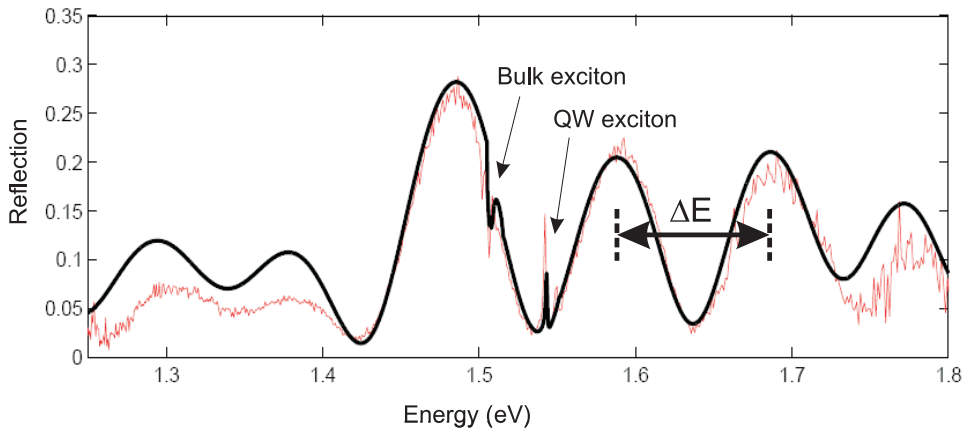


Figure 3.3: Measured (red) and theoretical (black) sample reflection probabilities. The reflection and transmission (not shown) spectra, recorded in absolute units, allow the fixing of a model using transfer-matrix theory. The bulk and QW exciton resonances are marked. The spacing ΔE between fringes allows inference of the sample thickness.

We compare the spectra (Fig. 3.3) with a transfer-matrix computation [90] that includes all dielectric layers and QWs of the sample. We fine tune the refractive indices and

thicknesses of the dielectric layers to reach a full agreement between linear theory and measurements for the energy range 1.4–1.7 eV. This procedure determines our sample parameters, which are fixed in our subsequent quantitative theory-experiment comparisons.

The data and theory both show sharp resonances at energies corresponding to the bulk and QW excitons. The fact that the QW exciton is higher in energy than the bulk exciton is a consequence of confinement, explained in §2.4. The large oscillations are due to Fabry-Perot resonances that arise from interference between multiple reflections between the extremal interfaces of the sample structure. The energetic spacing ΔE (labeled in Fig. 3.3) of the oscillations is related to the thickness of the sample L by:

$$L = \frac{hc}{2n\Delta E}, \quad (3.1)$$

where $n \approx 3.7$ for GaAs at 4 K [91], h is Planck's constant, and c is the speed of light. From this equation along with a measured spacing of 118 meV we infer a sample thickness of 1.42 μm , which is very close to the grower's specifications of 1.43 μm after the etching process. We can see from Fig. 3.3 that the exciton line shape is critically affected by the sample structure. The exciton resonance can even dip up or down, depending on where a feature occurs on the Fabry-Perot oscillatory curve, as can be seen by comparing the bulk and QW exciton features. Thus, a model that includes the sample structure is essential for understanding the detailed physics.

We also measure the T and R spectra at multiple positions across the sample, and find very small changes change in the shape of the fringes, indicating that the sample has uniform thickness within ± 50 nm. The uniform thickness means that the position on the sample at which measurements are made does not critically affect the line shape. With the different layer thicknesses in the sample structure fixed in the theoretical model, linear and nonlinear absorption spectra can be analyzed to reveal the physics that generates the observed line shapes.

3.2 Linear absorption spectrum

Although there are several spectral features in the broad-spectrum absorption, we study the optical response of the heavy-hole (HH) $1s$ excitons from the ten QWs in the sample. This resonance at $E_{1s} = 1.546$ eV is well separated from other absorption resonances in the sample. In addition, it has a strong oscillator strength. These features make the line shape of the HH $1s$ exciton resonance a good observable for revealing details of the many-body dynamics inside the QWs.

In order to study the many-body signatures of the exciton resonance, we characterize the physics in the linear regime. The linear absorption spectrum $\alpha^{\text{QW}}(\omega) = 1 - T(\omega) - R(\omega)$ of the 10 QWs in the spectral region near the $1s$ HH exciton resonance is shown in Fig. 3.4. The confinement of the exciton wave functions remove the degeneracy between the HH and light-hole (LH) sub-bands. The HH exciton resonance is slightly lower in energy than the light hole exciton resonance, consistent with the theory presented in Chapter 2 (Fig. 2.5).

For low excitation densities, the unexcited exciton absorption line shape has finite broadness primarily because of radiative dephasing, phonon scattering, and disorder. Radiative dephasing refers to the emitted fields from the QWs decaying because of radiative coupling with the QW system. Phonon scattering depends on the temperature of the sample. Both of these processes are homogeneous in nature since all excitons respond in the same way to the frequency range contained in the line shape. In contrast, the inhomogeneous-broadening mechanism of disorder results from fluctuations in QW thickness, as described in §2.8.

3.3 Transient absorption in the nonlinear regime

Elevated densities of carriers and polarizations lead to modifications of the absorption spectrum of a probe pulse. The changes to the probe include broadening of the absorption line shape (i.e., excitation-induced dephasing, or EID), shifting the resonance center fre-

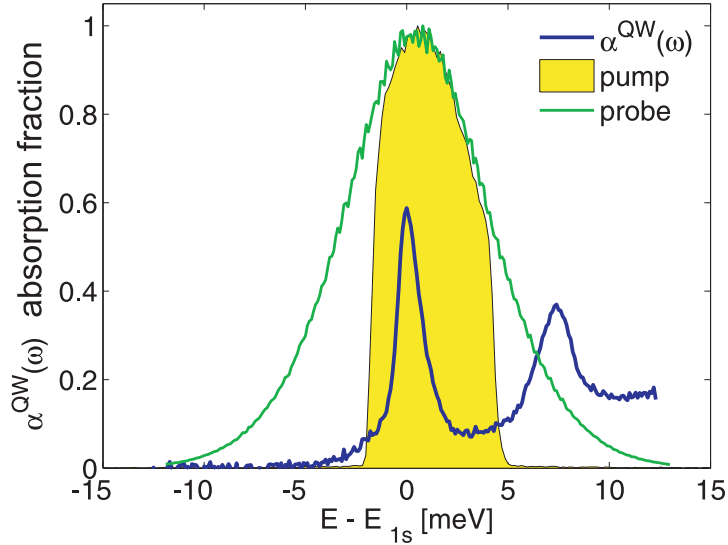


Figure 3.4: Linear absorption (blue line) from the QWs in absolute units in the region of the $1s$ heavy-hole (HH) exciton resonance. In arbitrary units, the probe spectrum before the sample is shown (green line) along with the narrowed pump spectrum used in transient-absorption experiments (shaded area).

quency (i.e., excitation-induced shift, or EIS), and saturation. We described these effects in chapter 2. We describe in this section the experimental parameters and considerations for the spectrally resolved transient absorption measurements performed in this work.

3.3.1 Experimental setup

To study the optical properties of the sample at densities where many-body dynamics dominate the absorption line shape, we perform spectrally resolved transient absorption. The concept of this measurement experiment was explained in §2.9.3.1. The experimental setup is illustrated in Fig. 3.5.

In our experiment, we use a pump and probe pulse, both provided by a tunable Kerr-lens mode-locked Ti:Sapphire laser system (Coherent Mira 900), pumped by a 5 W diode-pumped laser centered at 532 nm (Coherent Verdi V5). The laser produces optical pulses in the near-infrared ($\lambda_0 = 800$ nm), with a repetition rate of 76 MHz and a pulse duration of $\Delta\tau = 287$ fs full-width half maximum (FWHM). We estimate this pulse duration from an

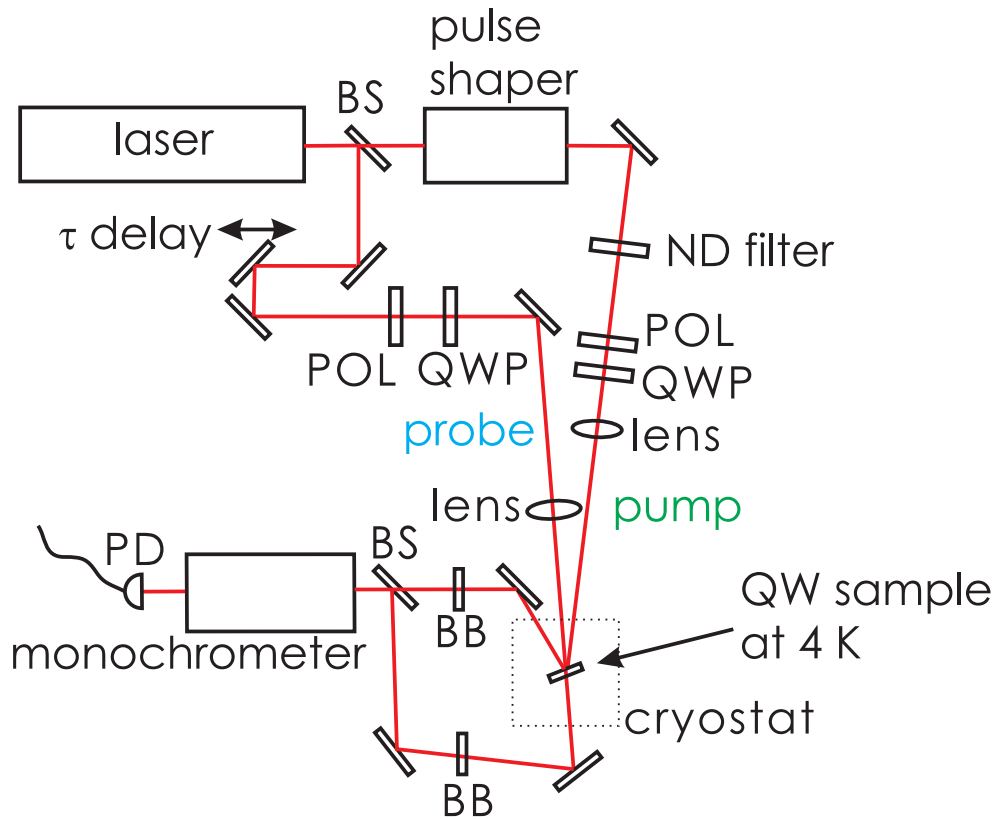


Figure 3.5: Schematic setup for spectrally resolved transient absorption experiments. BS, beam splitter; ND filter, neutral-density filter; τ delay, controls relative time delay between pump and probe; POL, polarizer; QWP, quarter-wave plate; BB, computer-controlled beam blockers; PD, photodetector.

intensity autocorrelation width of 406.5 fs FWHM and by assuming a Gaussian line shape. The details of temporal pulse measurement are discussed in §3.5. The laser spectrum for both pump and probe are tuned near the interband transition of the GaAs QW HH exciton at E_{1s} with a bandwidth of $\Delta E = 6.8$ meV ($\Delta\lambda = 3.5$ nm) FWHM. The pump pulse is spectrally narrowed to $\Delta E = 5.9$ meV FWHM ($\Delta\lambda = 3.05$ nm) by a pulse shaper apparatus in order to have a spectrum which is resonant with the HH $1s$ -resonance and avoids exciting the e-h continuum or LH resonance. The pulse shaper is able to alter the spectral phase of the pump as well; this will be discussed in Chapter 7. The probe and pump spectra are shown in Fig. 3.4.

Both the pump and probe beams are focused onto the GaAs QW sample within the cryostat. The intense pump creates a many-body configuration in the sample, and the

weak probe pulse with delay τ interrogates the configuration. We guide the transmitted and reflected probe beams with mirrors into a monochromator, where they are spectrally resolved and recorded with a photodetector. We record the probe transmission T and reflection R spectra as functions of the photon energy $\hbar\omega$ for a matrix of pump powers, time delays, and polarization configurations.

We adjust the pump power by varying the light transmitted through a neutral-density filter. The original experiments performed in this work used a neutral-density plate filter that attenuated the pump power as the position of the plate was translated. To increase the stability of the experiment, we replace this with a variable phase retarder (Meadowlark LVR-100) along with a polarizer. Amplitude modulation of a 2 kHz square-wave signal to the phase retarder allows variation in the pump power over three orders of magnitude, ranging from the linear regime past the saturation density, without modifying the polarization state. The saturation density is explained in §2.10.2.

We concentrate on short and long time delays between the pump and probe. For a short delay ($\tau = 3$ ps), the probe interrogates the QW in the coherent regime, when polarization is active in the QWs. For longer time delays ($\tau > 5$ ps), the probe arrives in the incoherent regime, when the polarization has decayed and only carrier populations remain. We choose $\tau = 13$ ps (or 27 ps for experiments in Chapter 8) for the long time delay.

We place a polarizer and quarter-wave plate in the each path for the pump and probe beams. This configuration allows us to manipulate the polarization states, which influences the interaction a subspace of spin states. Circular polarization (σ^+ or σ^-) excites one optical transition of the spin-degenerate HH states, as described §2.5. In contrast, linear-polarized light excites both states with a combination of left and right circular-polarized light with equal probability. For the experiments, the pump and probe are configured to either be the same circular polarization (i.e., co-circular, or CC), or the same linear polarization (i.e., co-linear, or CL). In either case, the pump and probe interact with the same subspace.

By varying this matrix of experimental parameters, we measure a set of probe absorp-

tion spectra that reveal details of many-body interactions in our sample. The experimental procedure involves using computer control (LabView) to loop through a matrix of pump intensities and pump-probe delays. The polarizers and quarter-wave plates are adjusted manually to create pure circular and linear polarization states to within 0.1%. The transmission and reflection of the probe beams are incident on a beam splitter, which guides both beams into a monochromator. While the measurement would be faster with two monochrometers, we use one monochromator and switch alternately between recording the transmission and reflection of the probe beam by using computer-controlled beam blockers in both arms. We next explain how we choose the pump and probe spot sizes that determine the excitation densities.

3.3.2 Choosing appropriate pump and probe spot sizes

The spot sizes of the pump and probe were carefully chosen to balance several constraints. We desire high enough pump intensities to reach saturation of the QW. However, we find experimentally that average pump powers beyond ≈ 100 mW (peak pulse power ≈ 13 kW), heating of the sample can occur which can distort the spectral features and potentially damage the sample. To avoid heating the sample with the pump, we desire a small focus of the pump beam so that the power can be relatively low and still create carrier densities that saturate the QW.

The probe beam must sample a spatially homogeneous part of the pump beam. To satisfy this constraint, we would like a probe spot size which is much smaller than the pump spot size at the sample plane. However, a smaller probe spot size means higher excitation density. The probe must create carrier densities that are in the linear regime so that the nonlinear effects we measure are completely due to the pump light. Additionally, a minimum amount of average probe power is necessary to obtain good signal-to-noise ratio in the probe measurement.

To determine the optimal pump and probe spot sizes that satisfy these constraints,

we first experimentally determine the saturation densities with the pump and probe beams. We then perform a calculation using a model which estimates the error due to the relative spot sizes of the pump and probe. Since the probe must have a finite spot size, there is an unavoidable error in the measurement of the pump-generated configuration because of the sampling of spatial inhomogeneity across the intensity profile of the pump spot. We calculate this error by assuming that both beams have a Gaussian spatial intensity profile at the focus:

$$I_j(\rho) = I_{0j} e^{-\rho^2/2w_{0j}^2}, \quad (3.2)$$

where ρ is the radial coordinate, I_0 is the peak intensity at the center of the profile, and w_0 is the beam waist size, and j stands for either pump or probe. We also assume that the nonlinear broadening γ changes proportionally with the pump intensity, or:

$$\gamma(\rho) = \gamma_0 + a I_{\text{pump}}(\rho), \quad (3.3)$$

where γ_0 is the low-intensity FWHM of the $1s$ -resonance, and a is a constant chosen to match experimental measurements. We integrate the probe intensity over the spatial distribution of gamma to find the average contribution to the measured broadening:

$$\gamma^{\text{meas}} = \int_0^\infty \int_0^{2\pi} \gamma(\rho) I_{\text{probe}}(\rho) \rho d\rho d\theta \int_0^\infty \int_0^{2\pi} I_{\text{probe}}(\rho) \rho d\rho d\theta. \quad (3.4)$$

The result of this calculation for varying probe waist size is shown in Fig. 3.6. We plot the fractional error in a measurement of the nonlinear broadening γ as the probe beam waist increases as a fraction of the pump beam waist. From this estimate, we find that the waist of the probe beam may be up to 20% of the pump waist and still sample the homogeneous part of the pump pulse to within a error of 2% in the measured nonlinearity.

In addition to these constraints, we also considered geometric constraints of the experiment including the distance a lens could realistically be before the cryostat windows and the focusing power of lenses. We wrote a ray-tracing program [92] to visualize these constraints

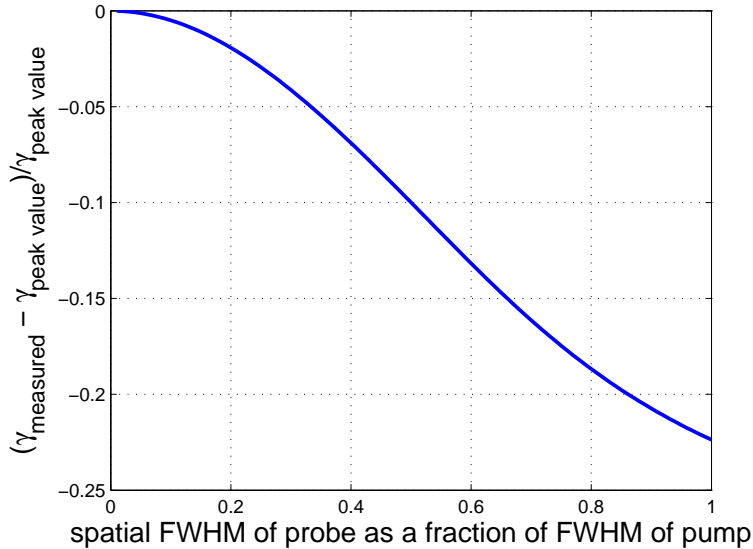


Figure 3.6: Result of beam-sampling calculation. The error due to the probe sampling an inhomogeneous portion of the pump spatial intensity is shown.

within the above framework. Considering all constraints, we chose the beam waists to be $100\mu\text{m}$ and $20\mu\text{m}$ for the pump and probe waists, respectively.

3.3.3 Estimation of excitation densities

The energy in an optical pulse along with the spatial profile determines the density of electron-hole pairs generated in the QW. We estimate the excitation densities reported above by considering the beam and sample parameters. These estimations apply to both the pump and probe pulses. First, we calculate the photon density for a single pulse at the beam focus. With a measurement of the beam power, we may use the formula

$$E = N_{\text{ph}} h\nu = N_{\text{ph}} \frac{hc}{\lambda}, \quad (3.5)$$

where E is the photon energy, N_{ph} is the number of photons, and λ is the center wavelength of the laser. A quasi-monochromatic approximation of the laser source is appropriate since $\frac{\Delta\lambda}{\lambda} \approx \frac{3.5\text{ nm}}{800\text{ nm}} < 1\%$. Considering this formula along with the repetition rate of the laser, f_{rep} ,

and an average laser power P_{avg} , we calculate the number of photons in a pulse to be

$$N_{\text{ph}} = P_{\text{avg}} f_{\text{rep}}^{-1} \frac{\lambda}{hc}. \quad (3.6)$$

The beam is focused onto a spot size w_0 . The beam out of the laser has a Gaussian spatial intensity profile that may be expressed in radial coordinates:

$$I(\rho) = I_0 e^{-\rho^2/2w_0^2}, \quad (3.7)$$

where ρ is the radial coordinate, I_0 is the average peak intensity at the center of the profile.

The average power P_{avg} is the integration of the intensity profile:

$$\begin{aligned} P_{\text{avg}} &= \int_0^\infty \int_0^{2\pi} I(\rho) \rho d\rho d\theta \\ &= 2\pi I_0 w_0^2. \end{aligned} \quad (3.8)$$

This result shows that the intensity at the center of the profile is

$$I = \frac{P_{\text{avg}}}{2\pi w_0^2}, \quad (3.9)$$

which is equivalent to considering the power over in a circle with radius $\sqrt{2}w_0$. This is a valid approximation for the pump density as sampled by the probe since the probe samples the density near the center of the pump beam and $w_{\text{probe}} \ll w_{\text{pump}}$. Using Eqns. 3.6 and 3.9, we estimate the photon density n_{ph} [W/cm²] in a single pulse as:

$$\begin{aligned} n_{\text{ph}} &= N_{\text{ph}}/2\pi w_0^2 \\ &= P_{\text{avg}} f_{\text{rep}}^{-1} \frac{\lambda}{hc} \frac{1}{2\pi w_0^2}. \end{aligned} \quad (3.10)$$

The photon density is converted into an electron-hole carrier density in the QWs through absorption. It is important to note that the energy from the pulse is (a) subject to loss at interfaces and the bulk, and (b) distributed over the 10 QWs. The reflection loss at the vacuum–sapphire and sapphire–GaAs interface is about 20%, calculated through Fresnel’s equations [93]. We measure a 28% loss due to absorption in the bulk material. We divide the

remaining photon density by 10 to account for the 10 QWs. Assuming that all remaining photons are absorbed by the QWs, the electron-hole carrier density n_{eh} in each QW is estimated as:

$$\begin{aligned} n_{\text{eh}} &= n_{\text{ph}} \times (1 - 0.20) \times (1 - 0.28) \times \frac{1}{10} \\ &= 0.058n_{\text{ph}}. \end{aligned} \tag{3.11}$$

This estimate does not take into account the spectral overlap between the pulse spectrum and the exciton absorption probability spectrum. Taking into account the spectral overlap for the pump spectrum shown in Fig 3.4 yields an additional factor of 0.21, yielding $n_{\text{eh}} = 0.012n_{\text{ph}}$.

We use the above arguments to estimate the excitation density of electron-hole pairs for the pump and probe pulses. The pump power is varied over a range of 1.6 to 40.5 mW, with a spot size of 100 μm . These parameters correspond to intensities of 5.1 kW/cm² to 128.9 kW/cm², or estimated excitation densities of $1.6 \times 10^9 - 8.3 \times 10^{10}$ electron-holes/cm²/layer. The low-intensity probe beam has a power of 30.8 μW and a spot size of 20 μm , corresponding to an intensity of 2.5 kW/cm², or a density of 7.9×10^8 electron-holes/cm²/layer. The probe thus samples the spatially homogeneous part of the pump-generated excitation. The probe is also low enough in intensity to be in the linear regime. In this regime, changes in the probe power (by up to about 50%) do not affect the absorption line shape.

A more careful estimate of the actual carrier densities would include taking into account the full dielectric structure of the sample. The theoretical microscopic calculation takes this into account, as discussed in Chapter 4. We will use the above estimate of the pump electron-hole densities to compare with the theoretically extracted excitation densities in Chapter 4. With the parameters in the experiment fixed, we now explain how the quantitative measurements in the experiment are performed.

3.3.4 Quantitative measurement of the probe and pump absorption

We spectrally resolve the probe beam using a 1/4-meter monochromator with a 0.07 nm (140 μeV) resolution. The monochromator scans through a range of wavelengths, and we record the probe intensity at each wavelength. We also spectrally resolve the pump beam using the same 1/4-meter monochromator as for the probe.

In order to calibrate the probe powers, we measure the input power ($P_{\text{IN}}^{\text{probe}}$), transmitted power (P_T^{probe}), and reflected power (P_R^{probe}) for the probe beam using a Coherent Fieldmaster GS power meter. This sensor for this meter has a Silicon photosensitive material which is responsive wavelengths in the near infrared.

For some of the transient-absorption experiments performed in this work, the pump input power, and the transmitted and reflected powers from the sample are simultaneously recorded in calibrated units to estimate the excited carrier densities. The schematic for measuring these quantities is shown in Fig. 3.7, which is a zoomed-in version of Fig. 3.5, where the probe is omitted for clarity.

The input pump power $P_{\text{IN}}^{\text{pump}}$ is measured by a sampling window that reflects 1% of the light into a photodetector. The transmitted P_T^{pump} and reflected P_R^{pump} powers are measured on photodetectors after attenuation by neutral density filters that ensure that the response of the detectors is in the linear regime. A measurement of the powers in absolute units with a Coherent Fieldmaster GS power meter allows continuous measurement of the pump powers.

To accurately estimate the absorbed powers from the measurements, we must consider reflection losses at interfaces inside the cryostat. We determine correction factors to account for these losses. The details of calculating these factors are explained in Appendix B.1.

After consideration of reflection losses, we determine the total estimated powers $P_{\lambda}^{\text{est,probe}}$, where $\lambda = \text{R, T, and IN}$. From these estimated powers, it is possible to calibrate the probe absorption spectra.

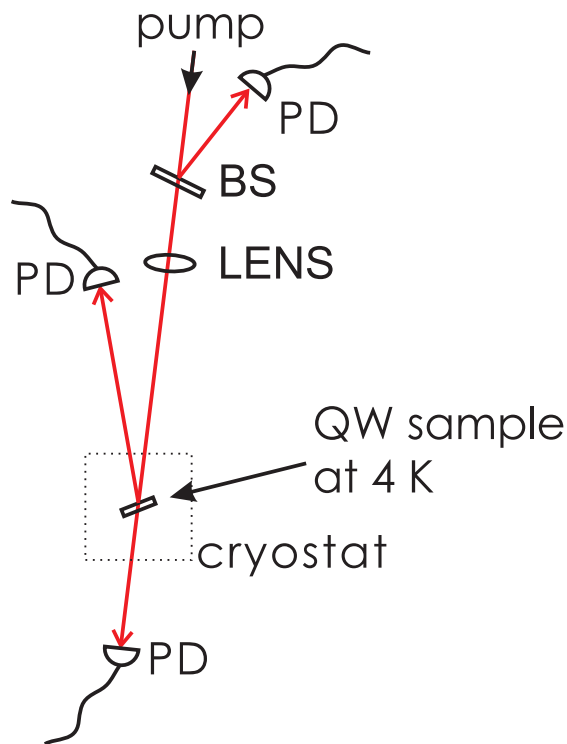


Figure 3.7: Setup for simultaneous measurement of the pump powers on photodetectors (PDs); BS, 1% beam sampler.

We use a novel lock-in detection technique to calibrate the transmitted and reflected probe spectra in both the presence and absence of the pump light. The pump and probe beams are both chopped by an optical chopper at frequencies around 2 kHz so that a lock-in amplifier can be used for phase-sensitive detection. This technique is described in detail in Appendix A. A calibration procedure described in Appendix B.2 allows the probe spectra to be converted into absolute units such that

$$\int P_{\lambda}^{\text{probe}}(\omega) d\omega = P_{\lambda}^{\text{est,probe}}, \quad (3.12)$$

From our careful measurement of the infer that the bulk material produces a background absorption of 28% that is essentially constant since the bulk continuum spectral feature has little variation over the relevant energy range. The fractional absorption by the bulk material is independent of excitation density because the densities necessary for achieving nonlinearities requires even higher photon densities than for the QW. Thus, removing the

bulk absorption from the measured absorption for pump or probe beams determines the QW absorption by $\alpha_{\text{QW}}(\omega) \equiv \alpha(\omega) - 0.28$ for this sample. This means that the pump or probe absorbed by the QW can be calculated by:

$$\begin{aligned} P_{\alpha}^{\text{QW}} &= [\alpha - 0.28] P_{\text{IN}}^{\text{est}} \\ &= \left[1 - \frac{P_T^{\text{est}}}{P_{\text{IN}}^{\text{est}}} - \frac{P_R^{\text{est}}}{P_{\text{IN}}^{\text{est}}} \right] P_{\text{IN}}^{\text{est}} - 0.28 P_{\text{IN}}^{\text{est}}. \end{aligned} \quad (3.13)$$

Measurement of the calibrated pump powers along with Eqn. 3.13 allow an estimate of the power absorbed by the QWs. We can use this estimate to set either the input power ($P_{\text{IN}}^{\text{est}}$) or the power absorbed by the QWs (P_{α}^{QW}).

Because of the careful calibration, the low-intensity probe always yields the same T and R spectra as the white-light source measurement, as shown in Fig. 3.4. In this figure the absorption from the bulk material is subtracted from the total probe absorption.

Combining the measurements of the pump powers with the calibrations discussed in Appendix B.1 allow accurate estimates of the number of photons absorbed by the QWs. The arguments in §3.3.3 then help to infer the excited carrier densities in the QWs. Knowledge of the carrier densities allows comparison of the QW response for different excitation pulse shapes that inject the same number of carriers into the QWs, as we will explore in Chapter 8.

3.4 Extraction of line shape parameters

After probe absorption data is collected, an extraction of relevant parameters provides observables for comparing the response due to different excitation conditions.

For the parameter extraction, we use a model-independent fit. Model functions such as a Lorentzian and Gaussian successfully fit the data for low intensities, but fail close to saturation, where comparison is often the most important. We extract the peak height of the absorption, the center resonance position, and the full-width at half maximum (FWHM) of the line shape.

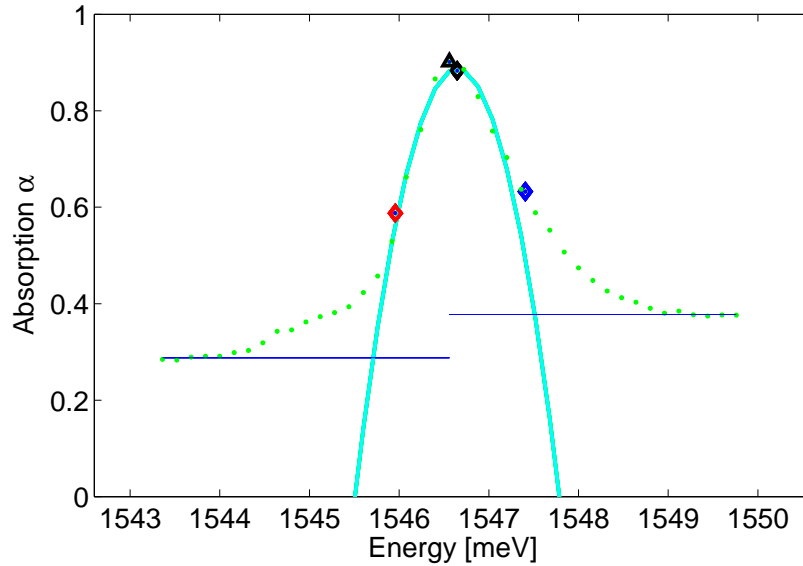


Figure 3.8: Model-independent fit procedure. The black triangle is the first guess of the resonance peak. The parabola fit (cyan line) results in a maximum (black diamond) that yields the peak height and center resonance position. The two baselines (blue lines) at high and low energy are used to estimate the half-widths (blue and red diamonds) on either side of the resonance. Note that the low-energy baseline is used to estimate the bulk absorption ($\alpha_{\text{Bulk}} = 0.28$).

The parameters are extracted from the HH $1s$ -resonance absorption curve by fitting a parabola near the center of the peak of the line shape. The fit procedure is illustrated in Fig. 3.8. The peak position of the absorption is first approximated by simply finding the maximum absorption value measured. Since the resolution of the spectrum recorded limits the accuracy of this peak point, the four nearest points on either side of this position on the absorption curve (nine points total) are fit with a parabola function. The center energy of the parabola approximates of the center of the resonance, and the maximum of the parabola approximates the peak absorption height.

Additionally, we extract the FWHM of the line shape. The FWHM is found by fitting a line to a group of four points on each side of the maximum around a guessed location at the half-way point between the peak height and the baseline on each side. The value at the center of this line approximates the half-width position on each side of the resonance. The FWHM is the sum of the half-widths. The FWHM-extraction is challenging in practice

because the nonlinear line shape has asymmetric baselines on either side, as illustrated in Fig. 3.8. In the extreme case of saturation, the high-energy side baseline is not distinguishable from the peak of the resonance. The extracted FWHM thus does not consistently provide a meaningful measure of the nonlinear width. Thus, we primarily use the peak height and center position from the model-independent fits as indicators of the nonlinear effects.

The model-independent fits are useful for understanding the trends in the data. The microscopic theory extracts parameters through a model that contains the sample structure and detailed physics. However, the theoretical fits are computationally intensive; thus, the model-independent procedure can provide real-time feedback about the nonlinearities.

3.5 Cross-correlation measurement of the pump

We record an intensity cross-correlation between the pump and probe by replacing the sample with a Beta-Barium Borate (b-BaB₂O₄, or BBO) crystal and recording the second-harmonic generation (SHG) signal generated from the interaction between the two beams. The geometry for a cross-correlation measurement is shown in Fig. 2.8 for the $\vec{k}_{\text{SHG}} = \vec{k}_1 + \vec{k}_2$ direction. A spectral filter with a bandwidth around the doubled frequency ($\lambda_{\text{SHG}} = \lambda_0/2 = 400$ nm) is placed between the BBO crystal and a photodetector to filter out any scattered light at λ_0 since the frequency-doubled signal is very weak. The delay τ between the pump and probe pulses is varied over a range greater than the pulse duration. The frequency-doubled signal measured in this background-free direction is detected on a photodetector, and electronically filtered using lock-in detection. The measured cross-correlation trace is proportional to the convolution of the pump and probe intensities:

$$S(\tau) \propto \int_{-\infty}^{\infty} \varepsilon_{\text{probe}}^2(t - \tau) \varepsilon_{\text{pump}}^2(t) dt, \quad (3.14)$$

where $\varepsilon_{\text{probe (pump)}}$ is the envelope of the electric field for the probe (pump) beam. Assuming that the two beams have a Gaussian line shape, the width of the cross-correlation function

$S(\tau)$ is the addition of the pulse durations in quadrature, or

$$\Delta\tau_S = [\Delta\tau_{\text{probe}}^2 + \Delta\tau_{\text{pump}}^2]^{1/2}. \quad (3.15)$$

In the case where the pump and probe have the same electric field, the trace is called an autocorrelation and $\Delta\tau_S = 1.414\Delta\tau_{\text{pulse}}$.

The pump pulse temporal duration is longer than the probe duration since the pump spectrum is narrowed compared to the probe spectrum (Fig. 3.4). A cross-correlation of pump with the probe yields a measured width $\Delta\tau_S = 520$ fs. Using Eqn. 3.15 along with a measured probe width of $\tau_{\text{probe}} = 287$ fs, we find that the pump pulse is 51% longer in time duration than the probe pulse. In the pulse shaping experiments described in Chapter 8, where the pump pulses are stretched out in time, the pump pulse temporal intensity profile is characterized by the cross-correlation trace since $\Delta\tau_{\text{pump}} \gg \Delta\tau_{\text{probe}}$. In these experiments, the probe intensity $\varepsilon_{\text{probe}}^2(t)$ is essentially a δ -function.

3.6 Conclusion

The experimental setup, calibrations, and considerations described in this chapter pave the way for experiments that mark new levels of quantitative measurement. These measurements, when combined with a microscopic theory, unveil the interactions that give rise to the nonlinear effects observed. Additionally, this experimental setup, with the pulse shaper active in the pump arm, opens an area of exploration where we are able to manipulate the spectral phase of our pulses in order to gain deeper insight concerning the many-body dynamics.

Chapter 4

Coulomb-induced nonlinearities in semiconductor quantum wells

4.1 Introduction

In this chapter, we report quantitative spectrally resolved transient probe absorption in a GaAs multiple quantum-well structure for a variety of excitation conditions. Comparison of the novel measurements with a microscopic theory allows for an unprecedented level of analysis and insight concerning the many-body interactions of excitons and carriers in the quantum wells. We draw conclusions about the sources of the nonlinearities, the effects of spin selection, as well as the observed transfer of energy between the pump and probe in the coherent regime. Unexpectedly, we find that true exciton populations do not significantly contribute to spectral broadening because the resonance blue shifts we observe are dominated by excited carrier densities. Characterization of the origins of the blue shifts and other observed nonlinear responses pave the way for the pulse shaping experiments, which we present in later chapters.

4.2 Theory development

To analyze the experimental observations and extract physical meaning from our data, we collaborate with Mack Kira, Hanno Steiner, Martin Schaefer, and Stephan Koch, at the Department of Physics and Material Sciences Center, Philipps-University Marburg, in Marburg, Germany. These researchers use a fully microscopic theory [7] to describe Coulomb-scattering contributions to excitonic nonlinearities. The theory uses the refractive-index

profile fixed from the white-light measurements described in §3.1. The theory includes up to two-particle scattering in a systematic cluster-expansion approach [94]. By fixing all parameters in the microscopic theory except the overall carrier density (n), the fraction of the carriers that are bound exciton pairs (x), and the polarization (P), we are able to map the density and temperature at the location of excitation with 10% accuracy.

While in principle the quantities n , x , and P could be computed by the theory that includes all the dynamics, high computational costs made it necessary to leave these three quantities as free parameters. Exciton formation dynamics are well understood in theory. Thus it is not necessary to include the full physics in the fitting procedure, and a single (n, x, P) combination uniquely fits a given spectrum.

To generate a theoretical optical response from the sample, Kira et al. evaluate the dynamics of the microscopic probe-generated polarization $\delta p_{\mathbf{k}}$ at the crystal momentum \mathbf{k} using the semiconductor Bloch equation [95]:

$$i\hbar \frac{\partial}{\partial t} \delta p_{\mathbf{k}} = \epsilon_{\mathbf{k}} \delta p_{\mathbf{k}} - (1 - f_{\mathbf{k}}^e - f_{\mathbf{k}}^h) \delta \Omega_{\mathbf{k}}(t) + \Gamma_{\mathbf{k}} - P_{\mathbf{k}} \sum_{\lambda, \mathbf{k}'} \delta f_{\mathbf{k}'}^{\lambda} + (\delta f_{\mathbf{k}}^e + \delta f_{\mathbf{k}}^h) \Omega_{\mathbf{k}}, \quad (4.1)$$

which contains the pump-generated electron (hole) distribution $f_{\mathbf{k}}^{e(h)}$, the polarization $P_{\mathbf{k}}$, the Coulomb-renormalized energy $\epsilon_{\mathbf{k}}$, and the renormalized Rabi energies, $\Omega_{\mathbf{k}}(t) \equiv d E_{\text{pump}}(t) + \sum_{\mathbf{k}'} V_{\mathbf{k}'-\mathbf{k}} P_{\mathbf{k}'}$ and $\delta \Omega_{\mathbf{k}}(t) \equiv d E_{\text{pro}}(t) + \sum_{\mathbf{k}'} V_{\mathbf{k}'-\mathbf{k}} \delta p_{\mathbf{k}'}$. The interactions involve the dipole-matrix element d , the electric field $E_{\text{pump}}(t)$ [$E_{\text{pro}}(t)$] for the pump [probe], and the Coulomb-matrix element $V_{\mathbf{k}}$.

The probe $\delta p_{\mathbf{k}}$ couples to two-particle Coulomb correlations $\Gamma_{\mathbf{k}}$ that produce screening of the Coulomb interaction, higher-order energy renormalizations, and Boltzmann-type scattering of $\delta p_{\mathbf{k}}$ from various quasi particles and transition amplitudes [7]. When the pump $P_{\mathbf{k}}$ is still present, the carrier densities are changed linearly by $\delta f_{\mathbf{k}}^{\lambda}$ whose dynamics

$$\hbar \frac{\partial}{\partial t} \delta f_{\mathbf{k}}^{\lambda} = 2\text{Im} [\delta \Omega_{\mathbf{k}}^* P_{\mathbf{k}} + \Omega_{\mathbf{k}}^* \delta p_{\mathbf{k}}] + r_{\mathbf{k}} \quad (4.2)$$

also change the probe response. The term $r_{\mathbf{k}}$ provides relaxation of the carrier distributions toward equilibrium.

Use of Eqns. 4.1 and 4.2 allow construction of the linear optical response of the probe. This response follows directly from the linear QW susceptibility $\chi(\omega) \equiv \frac{1}{\mathcal{S}} \sum_{\mathbf{k}} \frac{\delta p_{\mathbf{k}}(\omega)}{E_{\text{pro}}(\omega)}$ after we Fourier transform E_{pro} and δp with the normalization area \mathcal{S} . The true QW absorption is then evaluated via a transfer-matrix computation that has both $\chi(\omega)$ and the full dielectric structure of the sample as inputs. This procedure includes all the Coulomb-induced nonlinearities (discussed in chapter 2) for a given pump-generated many-body configuration. The mean-field quantities, i.e., $f_{\mathbf{k}}^{e(h)}$ and $P_{\mathbf{k}}$, represent the simplest part of the excitation configuration, while bound excitons and biexciton amplitudes determine pair-wise correlations. The microscopic influence of these quantities on $\chi(\omega)$ is systematically evaluated with the cluster-expansion approach [7]. We find that the QW absorption, α_{QW} , is extremely sensitive to the pump-induced $f_{\mathbf{k}}^{e(h)}$, $P_{\mathbf{k}}$, and exciton populations that compose the many-body configuration.

In Eqn. 4.1, the phase-space filling factor $(1 - f_{\mathbf{k}}^e - f_{\mathbf{k}}^h)$ actually has spin dependence according to the selection rules introduced in Chapter 2. Specifically, the phase-space filling $(1 - f_{\mathbf{k},s}^e - f_{\mathbf{k},s}^h)$ defines the amount of carriers a resonant optical pulse is able to excite. Here $f_{\mathbf{k},s}^{e(h)}$ is the electron (hole) occupation with momentum \mathbf{k} and spin s , where $s = \uparrow$ or \downarrow for electrons, and $s = \{-3/2, -1/2, 1/2, 3/2\}$ for holes. As a reminder of selection rules for these states for the heavy hole (HH) $1s$ -exciton resonance, σ^+ -polarized light excites along $s = -3/2 \rightarrow s = \downarrow$, and σ^- -polarized light excites along $s = +3/2 \rightarrow s = \uparrow$. Linearly-polarized light excites the HH exciton transitions with equal probability.

In the past, the actual pump-generated many-body configuration has only been computed for one-dimensional quantum wires [96, 7] because of the overwhelming numerical complexity involved. For our present studies, we significantly extend our numerical analysis and solve Eqns. (4.1)–(4.2) for the two-dimensional QW system for any combination of $f_{\mathbf{k}}^{e(h)}$, $P_{\mathbf{k}}$, and exciton populations. We use $f_{\mathbf{k}}^{e(h)}$ in the form of a Fermi-Dirac distribution with

a given temperature at a total density of $n = \frac{1}{S} f_{\mathbf{k}}^{e(h)}$. We also allow $P_{\mathbf{k}}$ to be a mixture of $1s$ and 10 higher s -like exciton states. Because of the resonant excitation conditions of the experiment, a fraction x of excited carriers is allowed to form $1s$ exciton populations. We perform the calculations for a large number of physically reasonable parameter combinations.

For any given configuration, we can evaluate a normalized deviation between the computed and measured QW absorptions:

$$\epsilon \equiv \frac{\int d\omega |\alpha_{\text{th}}(\omega) - \alpha_{\text{QW}}(\omega)|}{\int d\omega |\alpha_{\text{QW}}(\omega)|}. \quad (4.3)$$

The computed excitation configurations are then searched via a multidimensional optimization to minimize ϵ , yielding a unique maximum-likelihood excitation configuration. We also determine a confidence interval for the found configurations, yielding $< 5\%$ variation in ϵ .

4.3 Results and discussion

By combining quantitative experimental measurements with the microscopic theory, we acquire a deeper understanding of the many-body physics of QWs. The theory finds very close match to the measured absorption spectra. Figure 4.1 presents α_{QW} , the measured probe absorption (shaded areas), for three different pump powers using (a) co-circular (CC) and (b) co-linear (CL) polarization configurations (described in Chapter 3) for the pump and probe. In both cases, the α_{QW} recorded for the lowest pump excitation power behaves linearly. We see that the linear absorption contains a clear $1s$ resonance yielding $\alpha_{\text{QW}} = 57\%$ with a half width at half maximum (HWHM) of $\gamma_{1s} = 0.75$ meV. Roughly half of this width results from radiative decay in the nontrivial dielectric structure, which is corroborated by the high absorption levels [7]. When the pump excitation power is increased, α_{QW} experiences nonlinear changes. The $1s$ resonance is broadened and becomes strongly asymmetric, similarly to prior observations [3, 14, 15]. We also see that the CC and CL configurations yield very different nonlinearities. Under CC conditions, we obtain an almost 2 meV blue shift of the $1s$ resonance while the CL configuration only exhibits a smaller, less than 1 meV,

blue shift before saturation is reached. The nonlinear CL spectra are about 50% broader than the CC spectra for the same excitation densities.

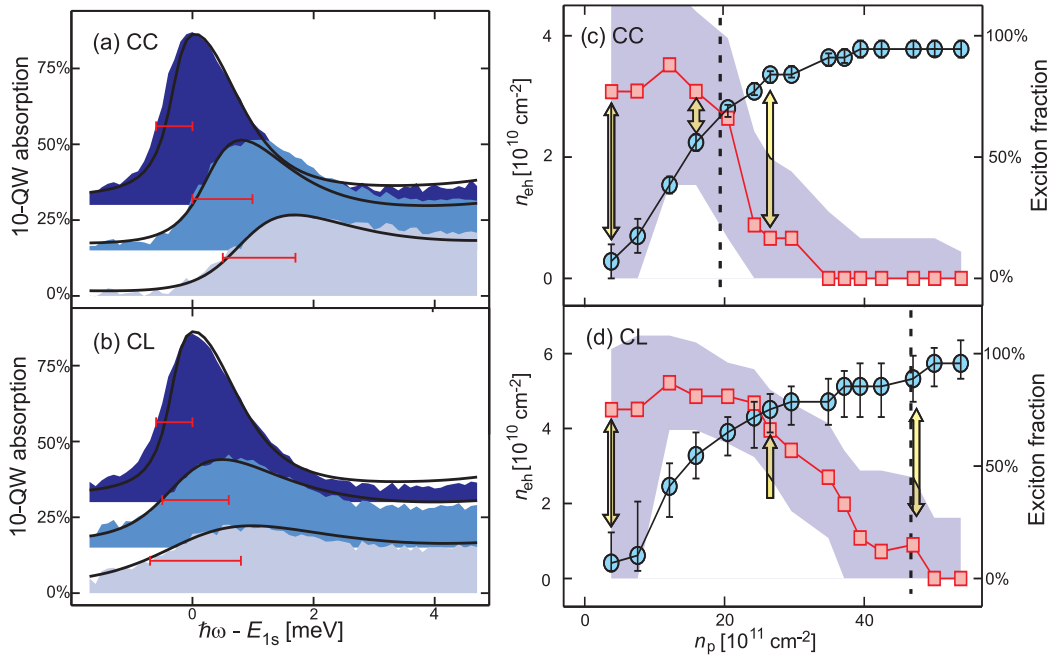


Figure 4.1: Probe QW absorption at large $\tau = 13$ ps delay. (a) The measured CC-configuration α_{QW} (shaded areas) are shown for pump-pulse photon densities $n_p = 3.9, 16,$ and $27 \times 10^{11} \text{ cm}^{-2}$ and compared to microscopically computed spectra (solid lines) for e-h densities $n_{eh} = 0.14, 2.2,$ and $3.4 \times 10^{10} \text{ cm}^{-2}$, from top to bottom. The spectra are vertically offset by 15%. The horizontal lines indicate the HWHM of the respective exciton resonances. (b) The corresponding CL comparison with $3.9, 27,$ and $48 \times 10^{11} \text{ cm}^{-2}$ pump-photon densities (shaded areas) and calculations for the densities $0.21, 4.4,$ and $5.0 \times 10^{10} \text{ cm}^{-2}$ (solid lines). (c) and (d): The deduced ML e-h densities (circles, left scale) and exciton fraction (squares, right scale) as a function of photon density for CC and CL experiments, respectively. The arrows indicate the spectra presented in the left-side panel; the dashed vertical lines mark saturation.

The theory matching the data elucidates the microscopic interactions. Figure 4.1 shows the α_{th} (solid lines) of the extracted ML configuration that reproduces the respective experimental result (shaded areas). The insets give information about the actual ML e-h density n_{eh} (circles) and exciton fraction x (squares) as a function of the photon density, along with error bars (shaded area for x) marking the confidence interval for each different experiment separately. Since the pump-generated polarization has completely decayed for long delay times ($\tau = 13$ ps), we only need to find the $f_{\mathbf{k}}^e, f_{\mathbf{k}}^h,$ and x configurations that match the experimental spectra by minimizing the deviation in Eqn. 4.3. The extremely good

quantitative agreement shown in Fig. 4.1 is found when the electron-hole density n first grows linearly as a function of excitation power and then saturates (circles, insets). This saturation is simply explained by the ionization of the $1s$ -exciton resonance for elevated densities, which strongly reduces the ability of the pump to generate more carriers. Saturation occurs close to that ML configuration where the phase-space filling factor $1 - f_0^e - f_0^h$ becomes zero (dashed vertical line). The exciton fraction is initially high due to the almost 100% efficiency in polarization-to-population conversion. Onset of ionization causes the exciton fraction to rapidly decrease as a function of e-h density. For the cases studied, the best-fit electron and hole temperatures are 38 K and 11 K, respectively, producing $f_{\mathbf{k}}^e \approx f_{\mathbf{k}}^h$ as expected if the electrons and holes are bound in an exciton and in agreement with the theoretical prediction [7]. At low densities, based on a temperature-dependence experimental study, we estimate the thermal contribution as less than 1% of the line width.

The pronounced differences between the CL and CC experiments are related to the fact that the CC case excites carriers only into one spin state, while under CL conditions, one populates both spin states. Since the Coulomb-scattering of $\delta p_{\mathbf{k}}$ with the e-h plasma is spin sensitive, the CL and CC cases lead to different Coulomb-induced shifts of the $1s$ resonance. The fact that the shifts persist to saturation, where no excitons exist, verifies that the e-h plasma and not the exciton population is mostly responsible for the blue shift of the $1s$ resonance. The enhanced broadening of the CL relative to the CC case is explained by the fact that there are twice as many scattering partners for $\delta p_{\mathbf{k}}$ in the CL case due to the e-h occupations in both spin states.

The theory can also separate out two categories of decay processes in the QW system. The internal QW dephasing rate γ_{int} consists of a superposition of broadening via Coulomb and phonon scattering as well as disorder effects. Radiative decay results from a direct coupling of polarization to light; in other words, a created polarization decays with at a rate Γ_{rad} as it emits an electric field. The rates γ_{int} and Γ_{rad} can be deduced from the experimental absorption spectrum measured in absolute units. Figure 4.2 presents the actual γ_{int} (circles)

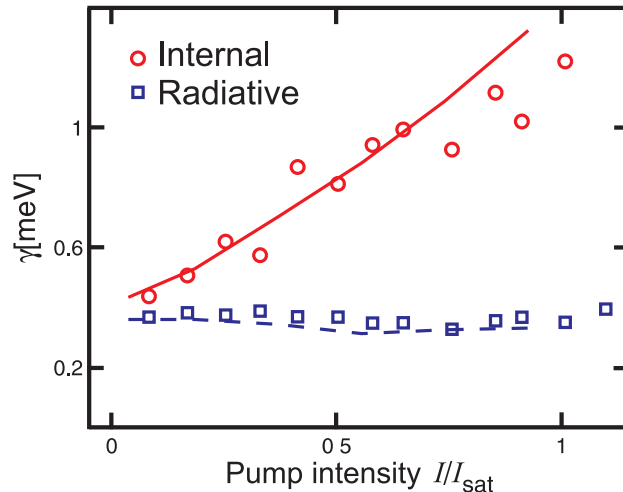


Figure 4.2: Internal decay rates γ_{int} (circles) and radiative-decay rates Γ_{rad} (squares) extracted from the experimental measurements (squares and circles) along with theoretical predictions (lines). The excitation saturates the probe response at intensity I_{sat} .

and Γ_{rad} (squares) retrieved from the experiments compared to the microscopic theory (solid and dashed lines, respectively) using the formulae:

$$\gamma_{\text{int}} = \frac{\gamma_m}{2} \left(1 - \sqrt{1 - 2\frac{\alpha_m}{\beta}} \right), \quad \Gamma_{\text{rad}} = \frac{\gamma_m}{2} \left(1 + \sqrt{1 - 2\frac{\alpha_m}{\beta}} \right), \quad (4.4)$$

where α_m is the measured peak absorption with respect to the bulk-absorption background and γ_m is the measured half-width half-maximum of the $1s$ resonance. The constant $\beta = 1.15$ extracted from the data determines how the radiative coupling is modified due to the radiative environment.

We find that the radiative environment combined with the coupling among 10 QWs enhances the radiative decay to $\Gamma_{\text{rad}} = 0.390$ meV, eight times larger value than for a single QW. We also see that Γ_{rad} is insensitive to the excitation level, which implies that the oscillator strength of the $1s$ resonance remains nearly constant up to its bleaching in agreement with Ref. [97]. At the same time, the low density γ_{int} is 0.4 meV. As a result, the internal dephasing of the studied system is comparable with radiative coupling at low excitation levels. Thus, the QW is capable of absorbing and converting a major portion of light into excited carriers. By increasing the pump intensity by a factor of 7, the carrier

excitation level increases so much that we find $\gamma_{\text{int}} = 1.2$ meV due to excitation induced dephasing.

We find that excitation produces excitation-induced dephasing that is 3 times the low-density γ_{int} . Thus, this system exhibits significant nonlinearities and it is a good candidate to demonstrate how the nonlinear response can be altered through the quantum statistics of the pump pulse [98].

As a further test of our ML extraction procedure, we consider short pump-probe delay conditions where coherent transients [99] and excitonic gain [5] have been observed previously. Fig. 4.3 shows the measured α_{QW} (dark area) and the extracted ML α_{th} (solid line) just after the excitation ($\tau = 3$ ps) for (a) the CC and (b) the CL excitation. The short delay α_{QW} and α_{th} not only agree but they are also distinctly different from the long delay α_{QW} (light shaded area). In particular, the CC case yields a 15% gain feature (negative absorption) just below the $1s$ resonance. As a main difference to the long delay investigations, the short-delay ML configuration contains a significant portion of pump-generated $P_{\mathbf{k}}$. Since the presence of the induced QW polarization is needed to produce gain, the gain is transient and can be attributed to coherent polarization transfer between pump and probe.

The transient gain delicately depends on the excitation conditions. It is not seen for the CL case due to the above mentioned enhanced dephasing of $\delta p_{\mathbf{k}}$. For CC excitation, we obtain the strongest transient gain for elevated e-h densities close to the $1s$ -saturation. To obtain analytic insight on how $\delta f_{\mathbf{k}}^{\lambda}$ influences the coherent transients, we also solve Eqns. (4.1)–(4.2) for the case where scattering is omitted. We find that $\delta f_{\mathbf{k}}^{\lambda}$ is proportional to $(1 - f_{\mathbf{k}}^e - f_{\mathbf{k}}^h)^{-1}$ showing that the coherent transients become increasingly strong near the $1s$ -exciton saturation because the phase-space filling factor approaches zero. To verify this, we plot in the inset to Fig. 4.3a the measured maximum values of α_{QW} gain (open circles) as a function of pump density. We clearly see that the transient gain reaches its maximum value close to the $1s$ -ionization threshold (saturation), indicated by the vertical dashed line. The inset to Fig. 4.3b presents the energetic position of the measured CL

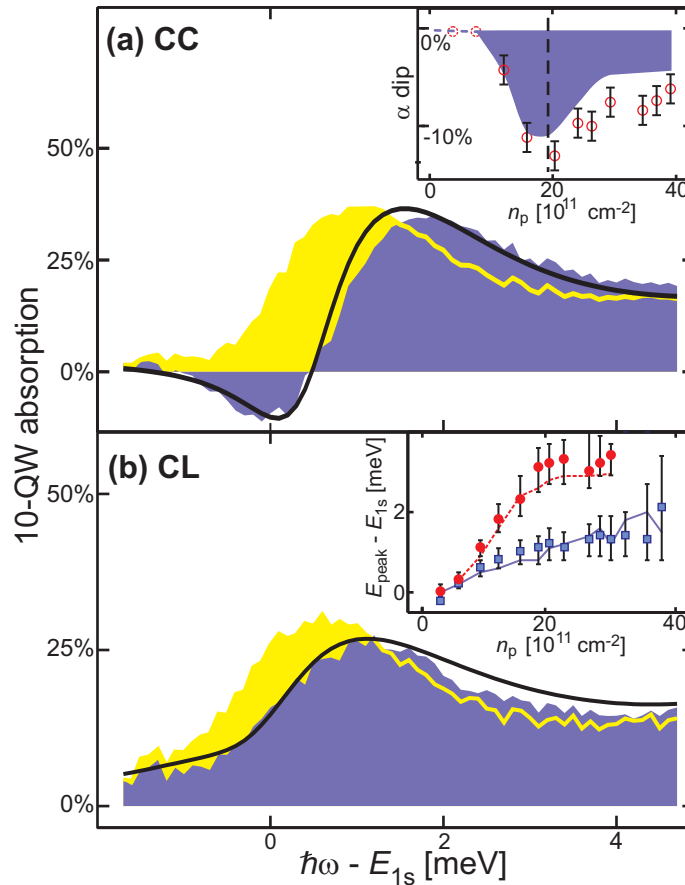


Figure 4.3: Probe QW absorption for the short $\tau = 3$ ps delay. (a) CC conditions with pump photon density $n_p = 16 \times 10^{11} \text{ cm}^{-2}$: the measured α_{QW} (dark shaded), the computed α_{th} (solid line), and the long-time delay α_{QW} (light shaded). Inset: the measured (open circles) and computed (shaded area) absorption dip (gain maximum) as a function of pump-photon density. The dashed vertical line marks saturation. (b) Same as (a), but for the CL configuration with the photon density $27 \times 10^{11} \text{ cm}^{-2}$. Inset: the absorption peak shift for CL (squares) and CC (circles) measurements compared with theory (lines).

(squares) and CC (circles) α_{QW} , while the lines are from the ML calculations. We find that the pump-generated polarization also produces an additional blue shift for both CL and CC excitations. In particular, the short delays produce blue shifts up to 2 meV (CL) and 4 meV (CC), which are roughly a factor of two larger than for those at long delays.

The ML analysis can also be used to quantitatively determine the role of excitons. The inset to Fig. 4.4 shows the 5% ϵ confidence interval (shaded area) in carrier density and exciton fraction when the intermediate-intensity CL experiment of Fig. 4.1b is analyzed. The overall difference between theory and experiment is minimized around a single (n_{eh}, x) con-

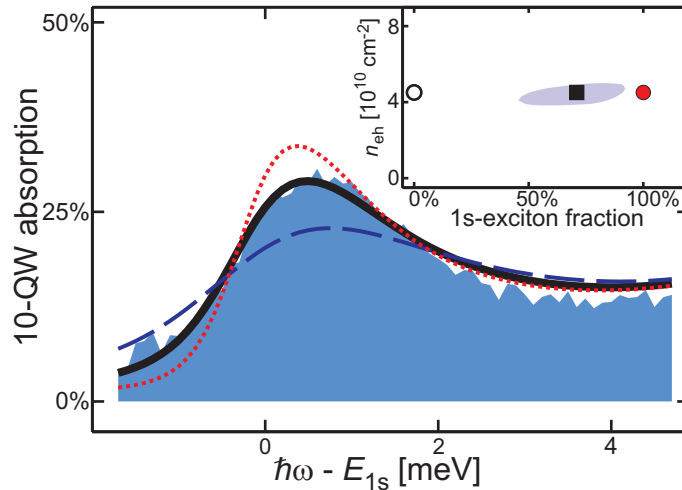


Figure 4.4: Influence of exciton populations on nonlinear α_{QW} . The long-delay measured α_{QW} (shaded area) for $n_p = 16 \times 10^{11} \text{ cm}^{-2}$ pump is compared with the ML result (solid line) as well as computations having 0% (dashed line) and 100% (dotted line) excitons. Inset: The ML configuration (square) and the 5% confidence interval (shaded area) plotted in (n_{eh}, x) space. The 0% (open circle) and 100% (filled circle) represent exciton configurations used for the dashed and dotted lines, respectively.

figuration (square). Fig. 4.4 shows the corresponding experimental α_{QW} spectrum (shaded area) together with the ML result (solid line) as well as cases where the exciton fraction is reduced to $x = 0\%$ (dashed line) or raised to $x = 100\%$ (dotted line). Increasing the exciton fraction leads to a reduction of the excitation-induced broadening and blue shifting of the $1s$ -resonance. These effects follow because the scattering of the probe induced $\delta p_{\mathbf{k}}$ becomes less likely when electrons and holes are bound into charge-neutral excitons ($x = 100\%$) than when they remain as an ionized plasma ($x = 0\%$). It is also interesting to see that formation of excitons ($x = 100\%$) yields only a small energy renormalization that does not produce an additional blue shift, in contrast to polarization studied in Fig. 4.3.

4.4 Conclusion

We have performed unprecedented quantitative measurements of spectrally resolved probe absorption in a GaAs multiple QW sample under a variety of excitation conditions. Detailed comparison between quantitative experiments and theory shows that the absorptive nonlinearities in α_{QW} depend so sensitively on the many-body configuration that we can

extract the maximum likelihood many-body excitation configuration with great confidence. The analysis identifies the role of coherent polarization, exciton and electron-hole plasma contributions. We find that carrier-polarization scattering dominates the nonlinear heavy-hole $1s$ exciton line shape. The exciton populations are found to have little effect on the nonlinear line shape compared with the effects of polarization and free carriers. In addition, the theory matches spin-selective measurements, demonstrating the effects of phase-space filling. For the short-time co-circular pump-probe configuration, pronounced transient gain is observed with a strength controlled by the pump.

4.5 Transition to the study of QW system response to light statistics

The work in this chapter demonstrates that the QW system has a strong nonlinear response, and that the probe absorption is sensitive to the many-body configurations. Our theorist collaborators, Mack Kira and Stephan Koch, predict that this system has strong enough nonlinearities to display quantum statistics-dependent nonlinear effects. Their theory predicts that quantum-optical fluctuations of an excitation source can alter the optical response. We explore their theory and our experimental work to realize their predictions in the remaining chapters.

Chapter 5

Background on light statistics and predicted interaction with matter

This chapter introduces the quantum optics involved in the research discussed in the remainder of this thesis. Our theorist collaborators have predicted that the quantum statistics of a light field should influence the many-body interactions in a GaAs quantum well structure. In this chapter, we review the quantum mechanical properties of the light field, and then use this to explain the predictions of our theorist team.

5.1 Coherence of a classical field

In this section we use classical fields to introduce the concept of coherence. A classical electromagnetic field in vacuum is a solution to the source-free and current-free Maxwell's wave equation [93]:

$$\nabla^2 \mathbf{E} = \frac{1}{c^2} \frac{\partial^2 \mathbf{E}}{\partial t^2}, \quad (5.1)$$

where $\frac{1}{c^2} = \mu_0 \epsilon_0$. A vector quantity solution for a planar monochromatic wave may be written as:

$$\mathbf{E}(\mathbf{r}, \mathbf{k}, t) = E e^{i(\mathbf{k} \cdot \mathbf{r} - \omega t)} \hat{\mathbf{n}} + E^* e^{-i(\mathbf{k} \cdot \mathbf{r} - \omega t)} \hat{\mathbf{n}}, \quad (5.2)$$

where E is the complex field amplitude, \mathbf{k} is the direction of propagation of the field and $\hat{\mathbf{n}}$ is the polarization vector, $\omega = c |\mathbf{k}|$. This representation of the field allows comparison with the quantized field, discussed in §5.2.1. A field may be a sum over many wave vectors.

Coherence is a property of a wave that describes the correlation between its amplitudes. In general terms, a physical process is typically defined as coherent if there exists a well-defined, deterministic phase — in other words, if the phase is not subject to random noise. For a light wave, coherence describes the correlation between the amplitudes of a wave separated in time or space. There are two types of coherence for a light wave: spatial and temporal. We are concerned with temporal coherence, where we are interested in the phase relationship between fields at the same place that are separated in time, as opposed to the phase relationship between fields at different locations across the beam profile.

5.1.1 First-order coherence

The degree to which a light wave is temporally coherent is quite complicated in general. A first measure of the temporal coherence of a light source is the first-order coherence function $g^{(1)}(\tau)$ defined by:

$$g^{(1)}(\tau) \equiv \frac{\langle E^*(t)E(t-\tau) \rangle}{\langle E^*(t)E(t) \rangle}, \quad (5.3)$$

where E is the complex field amplitude in Eqn. 5.2. The denominator is simply the intensity of the field $I = \langle |E(t)|^2 \rangle$. The symbol $\langle \dots \rangle$ means averaging over an ensemble. For a light source whose fluctuations are produced by ergodic random processes, the average over an ensemble is equivalent to averaging over a long time interval T [100]:

$$\langle E^*(t)E(t-\tau) \rangle = \lim_{T \rightarrow \infty} \frac{1}{T} \int_{-T/2}^{T/2} E^*(t)E(t-\tau)dt. \quad (5.4)$$

The quantity $g^{(1)}(\tau)$ is called the first-order coherence function because it is based on the properties of the first power of the electric field. This quantity might be measured by interfering two beams using a Michelson interferometer to control the relative time delay τ between two fields from the same light source, as shown in Fig. 5.1.

For a quasi-monochromatic field with a time-varying phase $\phi(t)$, the electric field is

$$E(t) = E_0 e^{-i\omega_0 t + i\phi(t)}. \quad (5.5)$$

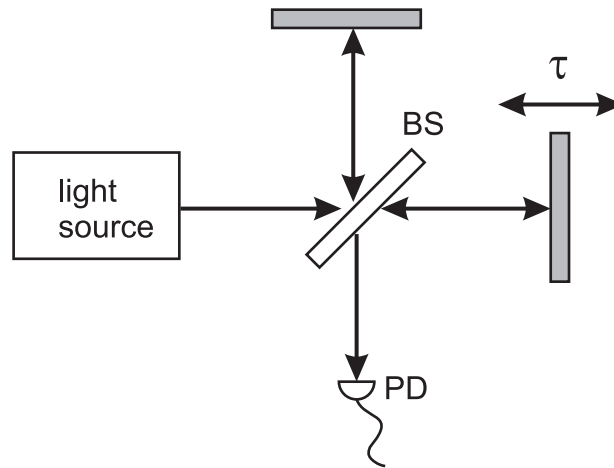


Figure 5.1: A Michelson interferometer with adjustable relative delay τ between the optical path lengths of the two beams, split by a beam splitter (BS). As the delay is scanned, the beams constructively and destructively interfere on a photodetector (PD), producing ‘fringes.’ This measurement yields information about the coherence properties of the light source.

Substitution of $E(t)$ into Eqn. 5.3 yields the first-order coherence:

$$g^{(1)}(\tau) = e^{-i\omega_0\tau} \langle e^{i[\phi(t-\tau)-\phi(t)]} \rangle. \quad (5.6)$$

From this we see that $|g^{(1)}(\tau = 0)| = 1$ for all fields. We observe that the real part of this expression yields an oscillatory function, or ‘fringes,’ with periodicity $2\pi/\omega_0$ and unity amplitude if the field has a constant phase $\phi = \phi_0$ for all times. However, if the phase is a time-varying function, the phase relationship becomes weaker between the field at one time and another, meaning that field amplitudes for two different times separated by τ correlate less. A time-varying phase results in $e^{i[\phi(t-\tau)-\phi(t)]}$ averaging to zero as the delay τ is increased past the coherence time, leading to a decrease in the amplitude of the oscillatory function. The coherence time must be finite for all light sources in practice because all fields have a bandwidth broader than a δ -function.

The signal that is recorded on the photodetector (PD) in Fig. 5.1 for a single frequency using a Michelson interferometer is:

$$I_{PD}(\tau) = I_0(1 - \cos(\omega_0\tau)), \quad (5.7)$$

where I_0 is proportional to the intensity of the light source. For a spectral density, $I(\omega)$, of

a given light source, the signal measured by the photodetector is the linear superposition of the interference patterns in Eqn. 5.7 over all frequencies:

$$I_{PD}(\tau) = \int_0^\infty I(\omega)(1 - \cos(\omega\tau))d\omega. \quad (5.8)$$

While the first term is simply proportional to the total intensity of the light source, the second term may be identified as the cosine Fourier transform of the spectrum, which may be reverse-transformed to reveal the power spectrum of the light source $I(\omega)$. In other words, the measurement of the coherence length of the light simply gives information that is available by recording the power spectrum! In experiments, a measurement of the power spectrum is routine with a spectrometer device.

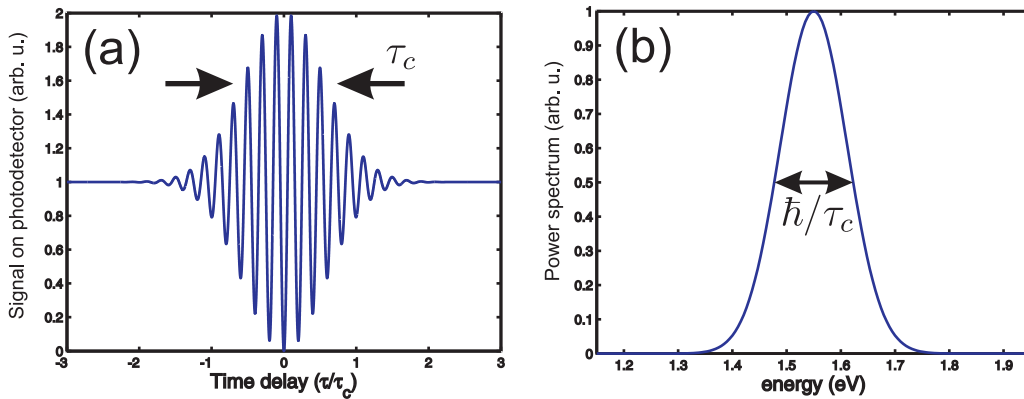


Figure 5.2: (a) The signal $I_{PD}(\tau)$ read on a photodetector in a Michelson interferometer for varying delay τ . The coherence time was chosen to be five times longer than the optical period. (b) The power spectrum of the light source is the Fourier transform of $I_{PD}(\tau)$. The inverse relationship between the widths of in the time and frequency domains are depicted with arrows.

We illustrate the relationship between coherence time and bandwidth with a simple example. The theoretical intensity measured by an interferometer for a quasi-monochromatic beam ($\lambda_0 = 800$ nm, or $\hbar\omega_0 = 1.55$ eV) while scanning the delay τ is illustrated in Fig. 5.2. The measured signal is related to $g^{(1)}(\tau)$ by

$$I_{PD}(\tau) = 1 - \text{Re}[g^{(1)}(\tau)]. \quad (5.9)$$

In this example, the field has a bandwidth of $\hbar\Delta\omega = 0.15$ eV. This bandwidth corresponds to a coherence time $\tau_c = 1/\Delta\omega = 28$ fs, which is five times the optical period of 800 nm light.

For time delays beyond τ_c , the amplitude of the fringes decreases to zero, corresponding to a loss in first-order coherence between fields that are separated by more than the coherence time. Thus, the broader the spectrum, the shorter the coherence time τ_c is measured.

Although the first-order coherence function is illustrative of the concept of coherence measurement, it provides no more information than a measurement of the frequency spectrum of the light field. Since the first-order coherence does not yield new information about the light source, we need a more sophisticated approach in quantifying the phase coherence.

5.1.2 Second-order coherence

The first-order coherence function says nothing about the statistical properties of the light. That is, first-order coherence experiments are unable to distinguish between states of light with identical spectral distributions but with different temporal intensity distributions.

The process for measuring the higher-order coherence of a light source originated with an astronomy experiment, the Hanbury-Brown and Twiss experiment [101]. Hanbury-Brown and Twiss were interested in determining the spatial coherence of light emitted from a star. The researchers realized that a star of finite spatial extent emits an angular pattern of bright and dark fringes that is related to the spatial coherence of the light emission from the star. The visibility of these fringes as a function of angular spread between detectors then allowed inference of the size of the star with high accuracy. They set up two detectors a variable distance from each other, and measured the correlations in intensity fluctuations between the detectors.

Extending this concept to the measurement of temporal coherence, a beam of light may be split into two paths and intensity correlations on two separate photodetectors may be monitored for varying time delay, as shown in Fig. 5.3. The second-order coherence function of a light source is defined by:

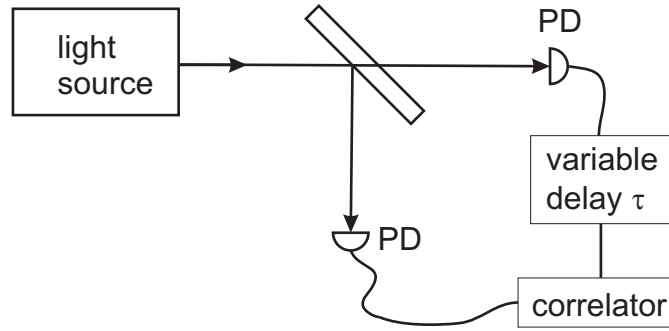


Figure 5.3: A temporal coherence measurement based on the Hanbury-Brown and Twiss experiment. The intensity of the light source is recorded on two separate photodetectors, and a variable delay (typically digital) allows a computer to correlate the intensities at two times in the same light source, yielding the second-order coherence function.

$$g^{(2)}(\tau) \equiv \frac{\langle E^*(t)E^*(t-\tau)E(t-\tau)E(t) \rangle}{\langle E^*(t)E(t) \rangle \langle E^*(t-\tau)E(t-\tau) \rangle} \quad (5.10)$$

$$= \frac{\langle I(t)I(t-\tau) \rangle}{\langle I(t) \rangle \langle I(t-\tau) \rangle} \quad (5.11)$$

Because both terms in the denominator are integrated over a large time similar to Eqn. 5.4, they are equivalent. For a light source with time-varying fluctuations around a constant intensity $I(t) = \langle I(t) \rangle + \Delta I(t)$, $g^{(2)}(\tau)$ can be written as:

$$g^{(2)}(\tau) = 1 + \frac{\langle \Delta I(t)\Delta I(t-\tau) \rangle}{\langle I(t) \rangle^2}, \quad (5.12)$$

where the second term is a measure of the correlation in intensity fluctuations between the light source at two different times.

We gain insight about how $g^{(2)}(\tau)$ can distinguish between light sources with different temporal intensity distributions by calculating its value for two extreme cases of intensity distributions: chaotic and coherent light sources.

An idealized electric field for a chaotic light source can be imagined to be waves emitted from a group of atoms, each at a frequency ω_0 but with a different independent time-varying phase $\phi_k(t)$. The total electric field is [102]:

$$E(t) = E e^{-i\omega_0 t} \sum_k e^{i\phi_k(t)}, \quad (5.13)$$

where again, E is the complex field envelope. The chaotic light field has fluctuations in intensity that are correlated for times within a coherence time τ_c . The correlations in the intensity fluctuations between two short times τ lead to a positive second term in 5.12, limiting to $g^{(2)}(\tau = 0) = 2$. As τ is increased beyond τ_c , the intensity fluctuations become uncorrelated, and $g^{(2)}(\tau \gg \tau_c) = 1$. The second-order coherence function for Doppler-broadened chaotic light is illustrated in Fig. 5.4, according to calculations in Ref. [102].

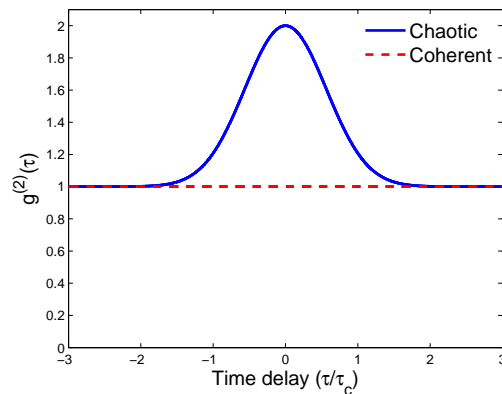


Figure 5.4: Second-order coherence for classical chaotic and coherent light sources.

In contrast, a coherent light source can be written as Eqn. 5.5 with a time-varying deterministic phase. Inserting this definition into Eqn. 5.10, we see that $g^{(2)}(\tau) = 1$. Comparing this result with Eqn. 5.12, we find that $\langle \Delta I(t) \Delta I(t - \tau) \rangle = 0$, or that there are no correlations in the intensity fluctuations for coherent light. We plot $g^{(2)}(\tau)$ for coherent light in Fig. 5.4 for comparison with $g^{(2)}(\tau)$ for chaotic light. We notice that the quantities are indistinguishable for long time delays.

The function $g^{(2)}$ has a different interpretation than $g^{(1)}$. Similar to the first-order coherence, for coherent light $g^{(2)}(\tau) = 1$ for all τ . However, when there exist correlations between fluctuations at two nearby times, $g^{(2)}$ can be greater than 1. The intensity fluctuations separated in time by more than τ_c no longer have correlations, leading to $g^{(2)}(\tau) = 1$. The second-order coherence function $g^{(2)}(\tau)$ can be seen to be a measure of how well intensity fluctuations are correlated between different times.

The correlations in the fluctuations for chaotic light causing $g^{(2)}(\tau) > 1$ are related to an effect called photon bunching, which will be discussed in the next section. The observation of bunching in photodetection events was a surprise to the researchers Hanbury-Brown and Twiss, and their discovery helped in opening the field of quantum optics through their intensity correlation measurements [103, 104]. Their measurements contradicted classical theory and led scientists to consider in more detail the process of photon detection. We gain more insight about the statistics of a light field if we treat the field quantum mechanically.

5.2 Statistics of the quantized electromagnetic field

5.2.1 Quantum-mechanical representation of the field

The quantum theory of light, including optical coherence, was developed originally by Glauber [105]. In the theory, a photodetection event corresponds to the absorption of a photon and the corresponding generation of an electron, which is measured via an electric current. The classical field is transformed into a quantum mechanical representation:

$$\begin{aligned}\hat{E}(\mathbf{r}, t) &= \hat{E}^+(\mathbf{r}, t) + \hat{E}^-(\mathbf{r}, t) = \sum_{\mathbf{k}} [\varepsilon_k \mathbf{U}_{\mathbf{k}}(\mathbf{r}) \hat{a}_{\mathbf{k}} - \varepsilon_k \mathbf{U}_{\mathbf{k}}^*(\mathbf{r}) \hat{a}_{\mathbf{k}}^\dagger], \\ \varepsilon_k &= \sqrt{\frac{\hbar \omega_k}{2V \epsilon_0}}, \\ \mathbf{U}_{\mathbf{k}}(\mathbf{r}) &= e^{i\mathbf{k} \cdot \mathbf{r} - i\omega_k t} \hat{\mathbf{n}},\end{aligned}\tag{5.14}$$

where ε_k is the vacuum-field amplitude, $\omega_k = c|\mathbf{k}|$, V is the quantization volume, $\mathbf{U}_{\mathbf{k}}(\mathbf{r})$ is a plane wave with polarization direction $\hat{\mathbf{n}}$, and $\hat{a}_{\mathbf{k}}$ and $\hat{a}_{\mathbf{k}}^\dagger$ are the Bosonic annihilation and creation operators, respectively, and the sum is over all wave vectors. This formulation determines the quantum-electrodynamical properties of the light field. The positive part and negative part of the field operator are Hermitian conjugates of each other, $\hat{E}^+ = (\hat{E}^-)^\dagger$. The field representation is analogous to Eqn. 5.2, where $E_0 \rightarrow \varepsilon_k \hat{a}_{\mathbf{k}}$ and $E_0^* \rightarrow \varepsilon_k \hat{a}_{\mathbf{k}}^\dagger$.

We consider only cases where the spatial variation of the field over the atomic system

dimensions is negligible, or

$$\frac{\lambda}{2\pi} = \frac{1}{|\mathbf{k}|} \gg |\mathbf{r}_{\text{atom}}|. \quad (5.15)$$

In this case, $e^{\pm i\mathbf{k}\cdot\mathbf{r}} \approx 1 \pm i\mathbf{k}\cdot\mathbf{r}$, and we can approximate the exponential function in Eqn. 5.14 as unity to obtain the dipole approximation representation of the field:

$$\hat{E}(\mathbf{r}, t) \approx \hat{E}(t) = i\varepsilon_k \hat{\mathbf{n}} [\hat{a}e^{-i\omega_k t} - \hat{a}^\dagger e^{i\omega_k t}]. \quad (5.16)$$

The annihilation and creation operation have the commutation property $[\hat{a}, \hat{a}^\dagger] = 1$. We can use this representation of the electric field for calculations of the statistical properties of light fields.

5.2.2 Density matrix

The density matrix is a tool for describing the statistical state of a system. For a statistical mixture of states $|\psi_j\rangle$ each having probability P_j of occurring,

$$\hat{\rho} = \sum_j P_j |\psi_j\rangle \langle\psi_j|. \quad (5.17)$$

In a transformed basis, wavefunctions may be written as superposition states, of the form $\Psi = \frac{1}{\sqrt{2}}(\psi_a + \psi_b)$. This representation leads to a density matrix with off-diagonal elements $|\psi_a\rangle \langle\psi_b|$. The density matrix is written more generally as:

$$\hat{\rho} = \sum_{jk} P_{jk} |\psi_j\rangle \langle\psi_k|. \quad (5.18)$$

Calculation of the expectation value of an operator \hat{A} involves taking the trace over the density matrix:

$$\langle \hat{A} \rangle = \sum_j P_j \langle\psi_j| \hat{A} |\psi_j\rangle = [\hat{\rho}\hat{A}]. \quad (5.19)$$

5.2.3 Coherence properties of light sources

Knowledge of the density matrix for a particular state of light allows calculation of the coherence functions and other quantities. Following the example of Eqns. 5.3 and 5.10 to

compute the coherence functions by replacing the electric fields with the operators of Eqn. 5.16, the first-order coherence function $g^{(1)}$ is given by:

$$\begin{aligned}
g^{(1)}(\tau) &= \frac{\langle E^-(t)E^+(t-\tau) \rangle}{\langle E^-(t)E^+(t) \rangle} \\
&= \frac{\langle \hat{a}^\dagger(t)\hat{a}(t-\tau) \rangle}{\langle \hat{a}^\dagger(t)\hat{a}(t) \rangle} \\
&= \frac{\text{Tr}[\hat{\rho}\hat{a}^\dagger(t)\hat{a}(t-\tau)]}{\text{Tr}[\hat{\rho}\hat{a}^\dagger(t)\hat{a}(t)]},
\end{aligned} \tag{5.20}$$

where the trace is taken in the last line following Eqn. 5.19. The second-order coherence function $g^{(2)}$ is given by:

$$\begin{aligned}
g^{(2)}(\tau) &= \frac{\langle E^-(t)E^-(t-\tau)E^+(t)E^+(t-\tau) \rangle}{\langle E^-(t)E^+(t) \rangle^2} \\
&= \frac{\langle \hat{a}^\dagger(t)\hat{a}^\dagger(t-\tau)\hat{a}(t-\tau)\hat{a}(t) \rangle}{\langle \hat{a}^\dagger(t)\hat{a}(t) \rangle^2} \\
&= \frac{\text{Tr}[\hat{\rho}\hat{a}^\dagger(t)\hat{a}^\dagger(t-\tau)\hat{a}(t-\tau)\hat{a}(t)]}{\text{Tr}[\hat{\rho}\hat{a}^\dagger(t)\hat{a}(t)]^2}.
\end{aligned} \tag{5.21}$$

While we can now calculate the degree of coherence for many different light fields, we are most concerned with the distinction in properties between coherent and thermal light states. Other examples of states of the light field include squeezed, Fock, and Schrödinger cat states. Although the coherence functions may be computed as a function of delay, for simplicity we calculate the functions for $\tau = 0$ for the purpose of comparing the properties of these two light states. For these two extreme cases, it turns out that the result is time-delay independent.

The coherent state is the quantum-mechanical description of the classical field in Eqn. 5.2, as we will discuss in §5.2.6. The coherent state is an eigenstate of the annihilation operator [105]:

$$\hat{a}|\alpha\rangle = \alpha|\alpha\rangle, \tag{5.22}$$

where the eigenvalue α is a complex number. The coherent state can be written as a superposition of Fock states:

$$|\alpha\rangle = e^{-|\alpha|^2/2} \sum_{n=0}^{\infty} \frac{\alpha^n}{\sqrt{n!}} |n\rangle. \tag{5.23}$$

The density matrix for a coherent state can then be written in the number state basis:

$$\begin{aligned}\hat{\rho}_{\text{coherent}} &= |\alpha\rangle\langle\alpha| = \sum_{m,l=0}^{\infty} C_{ml} |m\rangle\langle l| \\ &= \sum_{m,l=0}^{\infty} e^{-|\alpha|^2} \left(\frac{\alpha^m}{\sqrt{m!}}\right) \left(\frac{\alpha^l}{\sqrt{l!}}\right) |m\rangle\langle l|,\end{aligned}\quad (5.24)$$

where $|\alpha|^2$ can be identified with the average photon number \bar{n} . The coherent density matrix $\hat{\rho}_{\text{coherent}}$ satisfies $\text{Tr}[\hat{\rho}_{\text{coherent}}^2] = 1$ and $\hat{\rho}_{\text{coherent}}^2 = \hat{\rho}_{\text{coherent}}$. These are the criteria for a pure ensemble, meaning that there exists a basis for representation of $\hat{\rho}$ for which all $P_j = 0$ in Eqn. 5.17 except one [45]. That basis of representation for the coherent density matrix is simply the basis of the coherent state, $|\alpha\rangle$.

Thermal light is electromagnetic radiation emitted by a hot body. The density matrix for thermal light with some average number of photons \bar{n} is determined via Boltzmann's law to be a mixture of Fock states [49]:

$$\hat{\rho}_{\text{thermal}} = \sum_{n=0}^{\infty} P_n |n\rangle\langle n| = \frac{1}{1 + \bar{n}} \sum_{n=0}^{\infty} \left(\frac{\bar{n}}{1 + \bar{n}}\right)^n |n\rangle\langle n|. \quad (5.25)$$

The density matrices for the coherent and thermal state may be inserted into Eqns. 5.20 and 5.21 to learn how the properties of these states differ. Substitution of these expressions into Eqns. 5.20 and 5.21 yields for a coherent and thermal source:

$$\begin{aligned}g^{(1)}(\tau) &= \begin{cases} 1 & \text{coherent} \\ 1 & \text{thermal} \end{cases} \\ g^{(2)}(\tau) &= \begin{cases} 1 & \text{coherent} \\ 2 & \text{thermal} \end{cases}\end{aligned}\quad (5.26)$$

It is interesting to make a comparison with the classical analysis in §5.1. While the first-order coherence function cannot distinguish different statistical states of light, the second-order coherence shows a distinction between coherent and thermal light. Furthermore, thermal light can be identified as having similar intensity fluctuations as the phase-randomized chaotic light in Eqn. 5.13 since they share the same value for $g^{(2)}(\tau = 0)$.

5.2.4 Photon number distributions

As a further exploration of the properties of thermal and coherent light, we calculate the photon number probability distribution and the variance in photon number for both states. The distribution expresses the probability of measuring n photons in a time window T much shorter than the coherence time τ_c , or $T \ll \tau_c = 1/\Delta\omega$, where $\Delta\omega$ is the bandwidth of the light source. The photon number probability distribution P_n can be calculated by projecting a density matrix into the number state (Fock) basis by calculating the expectation value of the projection operator $|n\rangle\langle n|$:

$$P_n^{\text{thermal}} = \text{Tr}[\hat{\rho}_{\text{thermal}} |n\rangle\langle n|] \quad (5.28)$$

$$= \langle n| P_n |n\rangle = \frac{1}{1 + \bar{n}} \left(\frac{\bar{n}}{1 + \bar{n}} \right)^n \quad (5.29)$$

$$P_n^{\text{coherent}} = \text{Tr}[\hat{\rho}_{\text{coherent}} |n\rangle\langle n|] \quad (5.30)$$

$$= \langle n| C_{nn} |n\rangle = e^{-\bar{n}} \frac{\bar{n}^n}{n!}, \quad (5.31)$$

where $\bar{n} = \langle n \rangle$. The coherent photon probability distribution is also known as the Poisson distribution, which limits to a Gaussian function in the limit of large \bar{n} .

The photon probability distributions are compared in Fig. 5.5 for the same average number of photons \bar{n} in a given time window T . While the coherent photon distribution peaks near \bar{n} , the thermal distribution is highest at $n = 0$. This fact implies that one is likely to measure the average number of photons \bar{n} in a time window for coherent light, but is most likely to measure *zero* photons in the same time window for light with thermal statistics. This property of thermal light is called ‘photon bunching.’ This property refers to the fact that a photons in a thermal light source tend to travel together, with large gaps of time in between where no photons are found.

Thermal and coherent light differ also in their fluctuations in photon number,

$$\langle \Delta n^2 \rangle = \langle (\hat{n} - \langle n \rangle)^2 \rangle = \langle n^2 \rangle - \langle n \rangle^2. \quad (5.32)$$

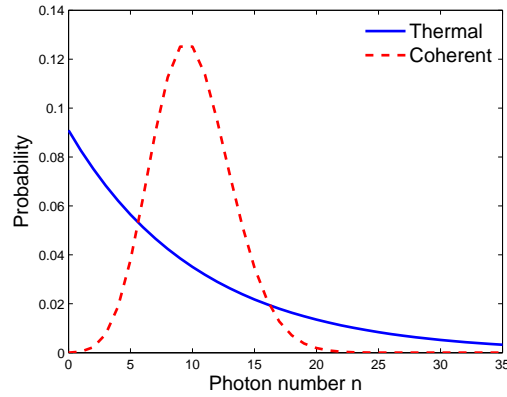


Figure 5.5: Comparison of photon number probability distributions for coherent and thermal light sources, both with $\bar{n} = 10$.

For the coherent state, representation in the Fock basis allows simple calculation of this quantity. We first calculate the expectation value of the number operator:

$$\langle \hat{n} \rangle = \langle \hat{a}^\dagger \hat{a} \rangle = |\alpha|^2, \quad (5.33)$$

validating the previous assertion from Eqn. 5.24 that $\bar{n} = |\alpha|^2$. The other term in Eqn. 5.32 can be calculated in a similar fashion:

$$\langle \hat{n}^2 \rangle = \langle \hat{a}^\dagger \hat{a} \hat{a}^\dagger \hat{a} \rangle = |\alpha|^2 + |\alpha|^4. \quad (5.34)$$

Combining these results we find that the photon number variance $\langle \Delta n^2 \rangle = \bar{n}$. The standard deviation for the fluctuations of the photon number above and below the mean is given by $\sqrt{\bar{n}}$. Dividing this by \bar{n} reveals that the fractional fluctuations decrease as we increase the photon number for coherent light as $1/\sqrt{\bar{n}}$.

For thermal light, it is not possible to write the state as an eigenstate of any operator (and therefore as any superposition of pure states). Instead, we rely on the density matrix (Eqn. 5.25) to compute the variance.

$$\langle \hat{n} \rangle = \text{Tr}[\hat{\rho}_{\text{thermal}} \hat{a}^\dagger \hat{a}] = \bar{n} \quad (5.35)$$

$$\langle \hat{n}^2 \rangle = \text{Tr}[\hat{\rho}_{\text{thermal}} \hat{a}^\dagger \hat{a} \hat{a}^\dagger \hat{a}] = \bar{n} + 2\bar{n}^2 \quad (5.36)$$

$$\therefore \langle \Delta n^2 \rangle = \langle \hat{n}^2 \rangle - \langle \hat{n} \rangle^2 = \bar{n} + \bar{n}^2 \quad (5.37)$$

This result shows that the fractional fluctuations of the photon number about the mean does not decrease since with increasing \bar{n} because $\sqrt{\langle \Delta n^2 \rangle} / \bar{n} \rightarrow 1$ in the limit of large \bar{n} . We should thus expect thermal light to have more fluctuations than coherent light for any average photon number \bar{n} . Though there exist other incoherent sources of light including Fock states, the distinct contrast that thermal light has to coherent light leads us to use the terms ‘thermal statistics’ and ‘incoherent’ interchangeably in this thesis.

5.2.5 Singlet quantities

Another feature that distinguish the thermal to the coherent state is the expectation values of the singlet quantities $\langle a \rangle$ and $\langle a^\dagger \rangle$. For the thermal state, the singlet quantities $\langle a \rangle = 0$ and $\langle a^\dagger \rangle = 0$, which can easily be seen by using the thermal density matrix (Eqn. 5.25) with Eqn. 5.19. In contrast the expectation values of the singlet quantities for the coherent state are $\langle a \rangle = \alpha$ and $\langle a^\dagger \rangle = \alpha^*$. The singlet quantities and the second order coherence function will be the quantities that distinguish our thermal source from a coherent source in chapter 6.

5.2.6 Coherent state is the classical field

The coherent state is the quantum-mechanical state that reproduces the measurements of the classical state described in §5.1. Since the coherent state is an eigenstate of the \hat{a} , the raising and lowering operators can be replaced by complex amplitudes according to

$$a \rightarrow \alpha, a^\dagger \rightarrow \alpha^*. \quad (5.38)$$

The expectation value of the electric field has the form

$$\langle \alpha | \hat{E}(\mathbf{r}, t) | \alpha \rangle = 2|\alpha| \frac{\varepsilon}{\sqrt{V}} \sin(\omega t - \mathbf{k} \cdot \mathbf{r}), \quad (5.39)$$

which can be identified as the classical field Eqn. 5.2 for $E_0 = |\alpha| \frac{\varepsilon}{\sqrt{V}}$. In addition, the fluctuations in the field can be shown to be the same as those for a vacuum state [106]. The

fractional fluctuations in the field decrease as the photon number (\propto field intensity $|E|^2$) increases. The quantum theory of light is more fundamental than the classical theory, and it follows that all states of light must have some quantum features (e.g., noise). Since coherent light has a correspondence to the classical field and has the minimal field fluctuations, the coherent state is the correct description for a classical field.

5.3 Phase-space representations of light fields

Phase-space offers useful visualization of the photon statistics of light fields. The derivation of the quantized field (Eqn. 5.14) makes use of the canonical position-like and momentum-like operators \hat{q} and \hat{p} , where

$$\hat{q} = (\hat{a} + \hat{a}^\dagger)/2 \quad (5.40)$$

$$\hat{p} = (\hat{a} - \hat{a}^\dagger)/2i. \quad (5.41)$$

These operators can be substituted into Eqn. 5.16 yielding the field operator in a new form:

$$\hat{E}(t) = \varepsilon_k \hat{\mathbf{n}} [\hat{q} \cos(\omega t) - \hat{p} \sin(\omega t)]. \quad (5.42)$$

It is evident that \hat{q} and \hat{p} are associated with field amplitudes oscillating out of phase with each other by 90° . These operators satisfy the commutation relation

$$[\hat{q}, \hat{p}] = \frac{i}{2}, \quad (5.43)$$

which implies an uncertainty relation between these variables [45]:

$$\langle \Delta \hat{q}^2 \rangle \langle \Delta \hat{p}^2 \rangle \geq \frac{1}{16}. \quad (5.44)$$

This relation leads to an uncertainty in the measured electric field amplitude and phase. A convenient representation of the distribution of photons in a quantum state of light is in \hat{q} - \hat{p} space, as shown in Fig. 5.6. This representation is similar to but more thorough than the photon number probability distribution since the photon number $n = (q^2 + p^2)^{1/2}$. The

phase of the field for single measurement is given by $\theta = \tan^{-1}(p/q)$. The spread of these phases and amplitudes takes the form of a ‘fuzz-ball’ in phase space, with the center of the ball around \bar{n} for the coherent state, and around zero for the thermal state, consistent with Fig. 5.5. The \hat{q} - \hat{p} allows an intuitive visualization of the statistics of amplitude and phase for a given source of light.

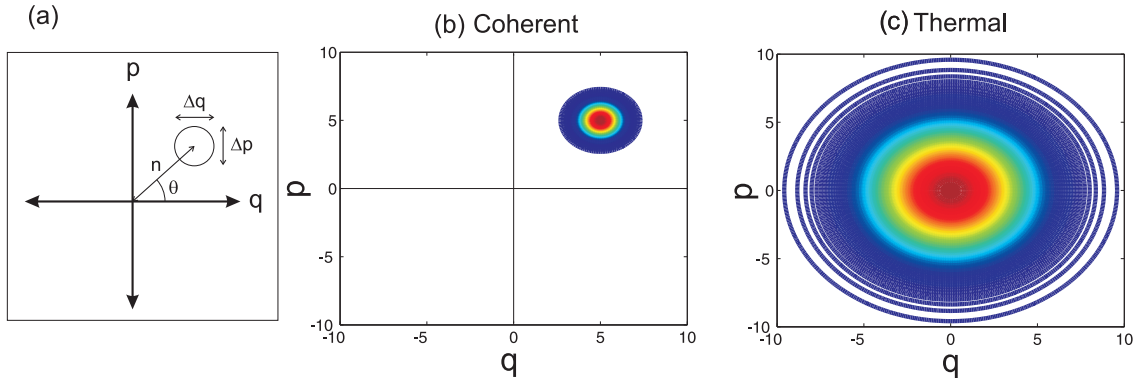


Figure 5.6: Phase-space portraits in \hat{q} - \hat{p} space. (a) The schematic for how amplitude n and phase θ of a single measurement are plotted, resulting in a ‘fuzz-ball’ of uncertainty with widths Δq and Δp . The distribution of measurements is shown for (b) a coherent state and (c) a thermal state.

We note that the thermal state distribution is centered in phase space at $(q, p) = (0, 0)$. The zero expectation values $\langle q \rangle = \langle p \rangle = 0$ are a consequence of the vanishing singlet quantities $\langle a \rangle = \langle a^\dagger \rangle = 0$, as can be seen in Eqn. 5.40. The vanishing singlet operators help us to visualize that the photon number most likely to be measured is 0, even though $\langle n \rangle = n$. This picture is consistent with the discussion of photon number distributions in §5.2.4.

Furthermore, in the figure it can be seen that the thermal state does not have a well-defined phase. In other words, it is equally likely to measure a field with any θ .

In contrast, the center position for the coherent distribution is $\langle n \rangle = \bar{n} = |\alpha|^2$. We identified $|\alpha|^2$ earlier as the average photon number for the coherent state. Thus, these phase space representation provides a helpful means of visualizing the quantum state of light. Also, the phase is well-defined for a coherent state within some spread. Note also that the states in Fig. 5.6 are exaggerated for the purposes of illustration. In reality, a coherent state with

large photon number \bar{n} has a comparatively small fuzzball with large displacement from the origin.

The difference in quantum statistics between coherent and thermal light sources can be described mathematically and measured experimentally. The theory of Kira and Koch predicts that the quantum statistics of exciting light sources may have an effect on the many-body interactions in semiconductor quantum wells.

5.4 Theoretical predictions concerning many-body interactions excited by light having incoherent statistics

The Kira-Koch theory predicts that light statistics can influence the many-body dynamics in GaAs quantum wells at high excitation densities [98, 7, 94, 107]. The exploration of the effects of light statistics on matter is called quantum-optical spectroscopy [94]. We consider the chosen system, GaAs quantum wells, then we summarize the theoretical predictions.

5.4.1 Why excitons in GaAs quantum wells?

We are interested in observing quantum optical effects in a semiconductor system. Quantum optics can be observed in systems that demonstrate a nonlinear response to an electric field. We study excitons in a GaAs quantum-well (QW) system in an effort to realize the predictions of the Kira-Koch theory.

The theory focuses on this system for the study of nonlinear effects because of several properties of the system. First, the system demonstrates clear nonlinear responses to optical excitation, as discovered in §4.3. This is because the wave functions of electrons in a semiconductor are delocalized throughout the crystal since they are eigenfunctions of momentum, as compared with the localized wave functions of atoms. The delocalization means that the wavefunctions for multiple electrons overlap, which leads to strong collective effects and many-body interactions compared with the few-body interactions in atoms. The observable

nonlinear responses, including excitation-induced dephasing and excitation-induced shifting, are discussed in §2.10.1 and in our recent publication [108].

The material GaAs is a direct-gap material, which means that it is possible to induce optical interband transitions of electrons from the maximum of the valence band to the minimum of the conduction band without any change in crystal momentum, as discussed in Chapter 2. A direct-gap material thus allows direct coupling between the light-field and electronic transitions, including excitons.

Excitons, delocalized bosons in the GaAs lattice, are the spectral feature we use to monitor the nonlinearities in the QW system. Excitons in QWs have a large oscillator strength and a lifetime of around 100 ps (which is long compared to optical pulse durations). The Kira-Koch theory predicts that true incoherent optical excitation can create a quantum degenerate state of low-momentum exciton states, analogous to Bose-Einstein condensation. This prediction takes advantage of the fact that excitons have center-of-mass coordinate momentum eigenfunctions. A QW also suppresses polariton effects, which can complicate the interpretation of observed dynamics [50].

Quantum-optical effects have been observed in atomic systems. Successful observation of Rabi oscillations [20], collapse and revival of atomic inversion [21], and single-atom nonlinearities [22] demonstrate quantum-optics for cavity-atom systems. Although these experiments typically involve few photons, the cavity enhances the interaction with a small number of atoms so that nonlinear effects are observed. We search for quantum-optical effects in a more complicated system where there are many ($> 10^{10}$) states. To observe nonlinearities, we must excite the system with an intense light source. We explore Kira and Koch's predictions concerning the dependence on quantum statistics for intense optical excitation of GaAs QWs in the next sections.

5.4.2 Semiconductor Bloch equations

When a QW system is optically excited, the light field creates a macroscopic polarization in the system. Maxwell's equation describes the coupling of the classical electromagnetic field to the material's response [98]:

$$\left[\nabla^2 - \frac{n^2}{c^2} \frac{\partial^2}{\partial t^2} \right] E = \mu_0 \frac{\partial^2}{\partial t^2} P, \quad (5.45)$$

where E is the electromagnetic field, μ_0 is the magnetic susceptibility, n is the nonresonant index of refraction of the material, and P is the macroscopic resonant polarization response of the material.

The polarization P is the sum of all transition amplitudes between the eigenstates of the system. In crystalline materials, this sum may be expressed in the Bloch basis, $P = \sum_{\mathbf{k}} d_{cv} P_{\mathbf{k}} + c.c.$, where $P_{\mathbf{k}}$ is the polarization amplitude (interband coherence), d_{cv} is the optical interband dipole matrix element between the conduction and valence bands, and \mathbf{k} is the crystal momentum of the charge carriers. By including all optically induced interband transitions and the Coulomb interaction between carriers, the semiconductor Bloch equations (SBEs) can be derived. These equations couple the polarization amplitude $P_{\mathbf{k}}$ to the occupation probabilities $f_{\mathbf{k}}^a$ for the electron ($a = e$) and hole ($a = h$) states. The SBEs are [44]:

$$\begin{aligned} \frac{\partial}{\partial t} P_{\mathbf{k}} &= -i(\epsilon_{\mathbf{k}}^e(t) + \epsilon_{\mathbf{k}}^h(t)) P_{\mathbf{k}} - i(f_{\mathbf{k}}^e(t) + f_{\mathbf{k}}^h(t) - 1) \Omega_{\mathbf{k}}^R + \frac{\partial}{\partial t} P_{\mathbf{k}}|_{scatt} \\ \frac{\partial}{\partial t} f_{\mathbf{k}}^e &= -2Im(\Omega_{\mathbf{k}}^R P_{\mathbf{k}}^*) + \frac{\partial}{\partial t} f_{\mathbf{k}}^e|_{scatt} \\ \frac{\partial}{\partial t} f_{\mathbf{k}}^h &= -2Im(\Omega_{\mathbf{k}}^R P_{\mathbf{k}}^*) + \frac{\partial}{\partial t} f_{\mathbf{k}}^h|_{scatt}. \end{aligned} \quad (5.46)$$

Here $\Omega_{\mathbf{k}}^R = d_{cv} E(t) + \sum_{\mathbf{k} \neq \mathbf{k}'} V_{|\mathbf{k}-\mathbf{k}'|} P_{\mathbf{k}'}(t)$ is the renormalized Rabi energy, which includes the fact that the system does not react to the applied field alone but the effective field which is a combination of the applied field with the dipole field of all generated electron-hole excitations. The renormalized energies are $\epsilon_{\mathbf{k}}^a(t) = E_k^a - \sum_{\mathbf{k} \neq \mathbf{k}'} V_{|\mathbf{k}-\mathbf{k}'|} f_{\mathbf{k}'}(t)$, where E_k^a

are the electron and hole energies given by the band structure of the unexcited material. Renormalization of the band structure and fields is done in the Hartree-Fock approximation, in which the nonlinear equations treat each particle as if it is subjected to the mean field created by all other particles.

The equations also consider interactions beyond the Hartree-Fock approximation, in which multiple particles interact with each other. The final term represents all the correlations due to scattering, which include exciton formation, dephasing of the polarization, screening of the interaction potential, relaxation of the carrier distributions, and scattering events between carriers.

These equations provide the basis for most of the community's understanding of the optical properties of semiconductors [44]. The next few sections explore the predictions of the SBEs for coherent and incoherent excitation of semiconductor QWs.

5.4.3 Coherent on-resonance excitation

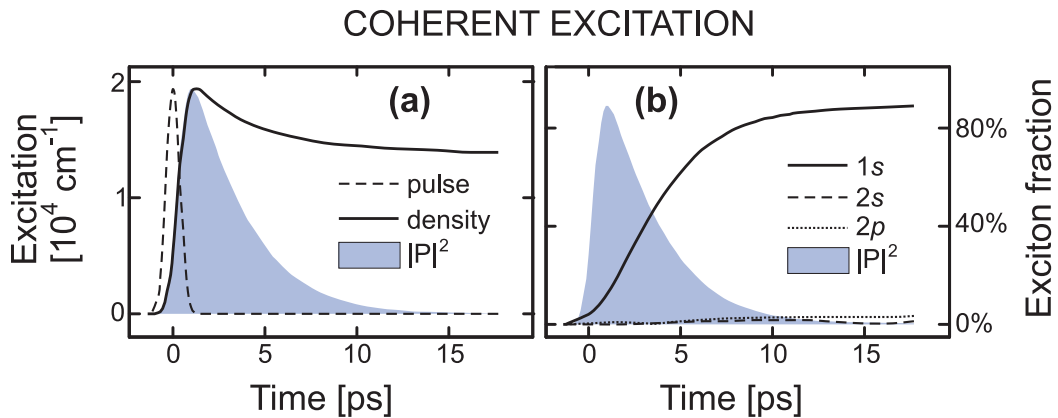


Figure 5.7: Quantum wire (1D) calculation of on-resonance excitation dynamics. (a) A short pulse generates a carrier density and polarization $|P|^2$. (b) The polarization decays, generating an exciton population. Most of the excitons are created in the ground 1s state. Figure from [7].

The absorption, transmission, and reflection of a resonant classical electromagnetic field by a material are completely determined by the complex-valued optical polarization of the material. The polarization, a coherent quantity, cannot be described by a thermodynamic

distribution function, where the temperature and chemical potential determine the occupation probabilities of the allowed states. An optical pulse generates a macroscopic polarization in the material as well as promotes electrons from the valence band to the conduction band, as we saw in §2.6. After the generation of a polarization by an optical pulse, microscopic scattering interactions between the polarization and the generated carriers lead to the decay of the polarization resulting the formation of the $1s$ exciton population, as illustrated in Fig. 5.7a. Pure exciton populations, created indirectly via the decay of polarization, are considered incoherent quantities since they are not subject to phase-destroying processes.

5.4.4 Radiative recombination of carriers and excitons

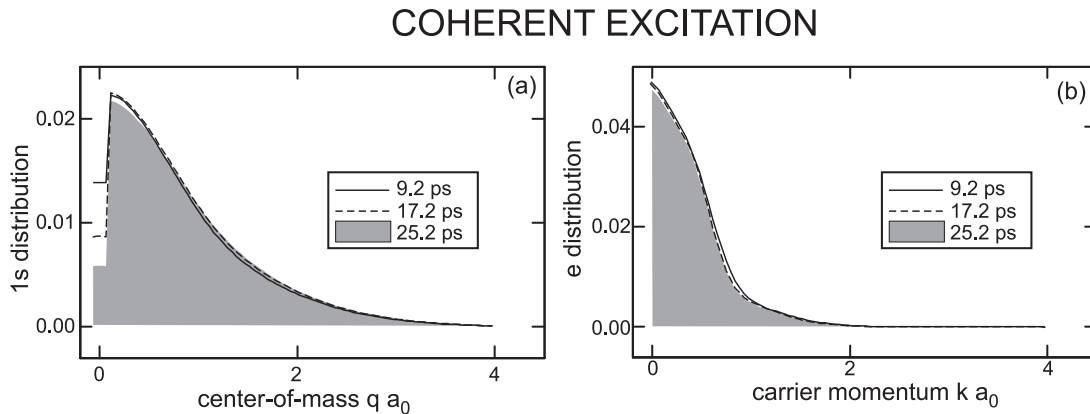


Figure 5.8: (a) Computed $1s$ exciton and (b) free carrier distributions in center-of-mass k -space for three times after coherent resonant excitation. The absence of excitons in the low-momentum states is due to radiative recombination. Figure from [7].

For on-resonance excitation, the polarization scatters via Coulomb interactions and phonons, which results in exciton populations. The excitons that are within the light cone (low momentum states – described in §2.4) may recombine, radiating a photon. These “bright” states depopulate by spontaneous emission of photons, leaving behind higher-momentum “dark” states that are unable to couple with the light field (and thus cannot produce light through radiative recombination – hence the terms “bright” and “dark”). The system dynamics illustrated in Fig. 5.8a show that the bright states deplete rapidly via ra-

diatively recombination while the higher-momentum dark exciton states exhibit a slow decay. These excitons eventually decay to bright states via inelastic collisions, where they are then available to recombine radiatively. At any moment after resonant classical excitation, less than 5% of the excitons are found in the low-momentum states because of the fast radiative recombination rates for excitons. Excitons recombine rapidly because the wave functions for the electron and hole are spatially nearby.

In contrast, free electrons and holes, shown in Fig. 5.8b, are less likely to recombine because their wave functions are spread throughout the crystal. Additionally, an electron with arbitrary momentum can recombine with a hole with similar momentum, leading to a thermal distribution in momentum-space. Radiative recombination leads to slow (nanosecond) changes in their populations. This difference in the radiative recombination between excitons and free carriers highlights that excitons have non-thermal distributions.

5.4.5 Impact of quantum light statistics on matter

The Kira-Koch theory predicts that quantum-statistically incoherent (thermal photon statistics) excitation can result in direct conversion of photons into a low-momentum exciton population without the production of a polarization [94, 107]. To motivate this theory, we discuss the relation between incoherent excitation and spontaneous emission.

For a classical excitation, the resulting polarization converts into an exciton population via scattering. The motivation for the research described in this thesis arose from considering the possibility of bypassing the polarization to directly convert photons into excitons, which is the inverse process of spontaneous emission. Spontaneous emission from recombination of excitons results in the emission of light with incoherent light statistics, i.e. $g^{(2)} > 1$.

While a classical electromagnetic field must generate a polarization that decays into an incoherent population, Kira and Koch hypothesize that the absorption of light with incoherent quantum statistics directly creates incoherent exciton populations without generating a polarization. This can be understood intuitively by realizing that the photons emitted from

spontaneous emission lack temporal phase coherence. It follows that photons lack phase coherence might generate exciton states that oscillate out of phase with one another, i.e., have no macroscopic polarization. The creation of a large number of excitons in the bright states (within the light cone) would be considered a quantum-degenerate distribution. It is predicted that such a highly singular state would modify the many-body interactions for similar densities as a classically-excited system.

5.4.6 Quantum-optical spectroscopy

Quantum-optical spectroscopy is the exploration of the nonlinear response of a system given different quantum statistics of the excitation source [94, 107]. We have explored the many-body dynamics of a system under resonant classical excitation: a coherent polarization is generated which is converted into an exciton population that is broadly-distributed in momentum space with the low-momentum exciton states rapidly decaying due to radiative recombination.

Kira and Koch predict that the quantum-statistical properties of exciton states are governed by that of the exciting light source, leading to nontrivial modifications in the nonlinearities compared with a classical coherent source of the same photon density. Their theory predicts that for an incoherent (thermal) light source creating the same excitation density as a coherent source, the many-body effects are modified.

The essential effects predicted for incoherent excitation are long-range order, anomalous reduction of Coulomb and phonon scattering, and enhanced and directional photoluminescence (PL) emission, all compared with coherent excitation of the same density.

The qualitative differences between the predicted response of the QW excitons generated by coherent versus thermal statistics are illustrated in Fig. 5.9. This calculation was performed for a 1D quantum wire (due to computation costs), which scales to two dimensions without loss in generality. We focus here on the optically active excitons, or bright excitons (within the light cone). In Fig. 5.9a, for a coherent excitation, the bright exciton population

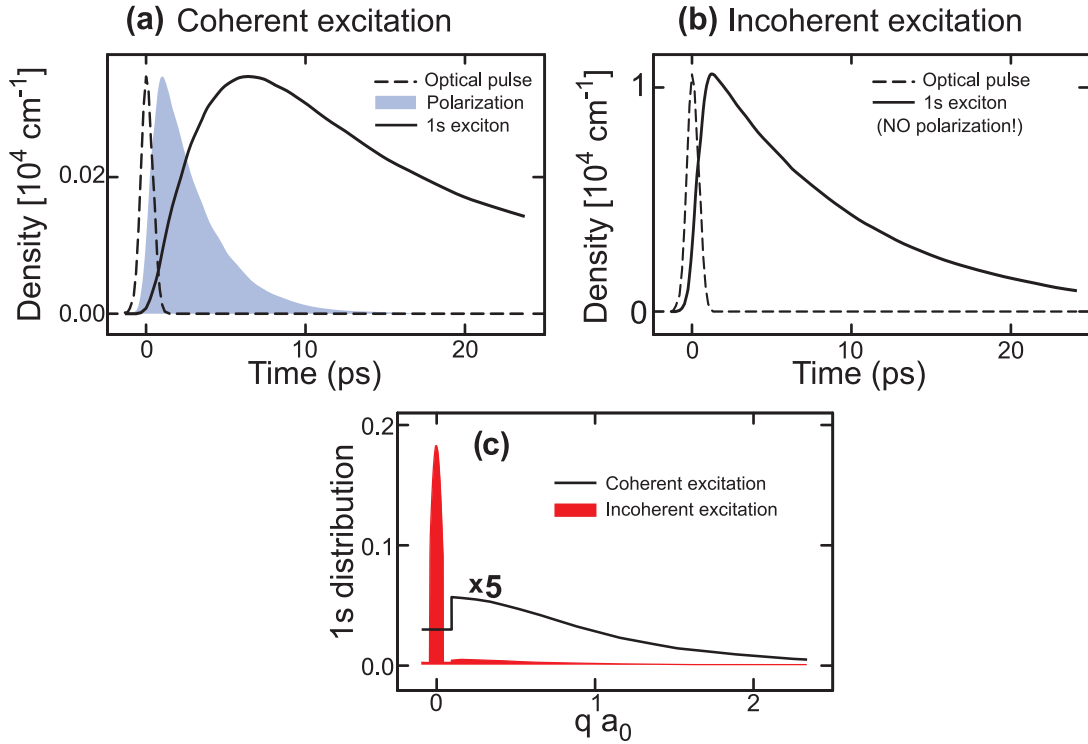


Figure 5.9: Comparison of excitation dynamics resulting from a pulse with coherent vs. incoherent statistics. (a) Coherent excitation; the optical excitation pulse (dashed line, scaled) is shown with the generated polarization (shaded area, scaled) and the bright $1s$ exciton population (solid line). (b) Incoherent excitation; the incoherent optical pulse (dashed line, scaled) is shown with the generated density of bright $1s$ exciton populations (solid line). Note the dramatically different scale for the density compared with the coherent excitation, and that no polarization is generated. (c) The generated exciton population in momentum space for coherent excitation (solid line, multiplied by 5) and incoherent excitation (shaded area) 11 ps after optical pulse maximum. Figure from [7].

risers with the decay of the generated polarization. In contrast, an excitation with thermal light statistics gives rise to a large (almost 50 times the density) bright exciton population without generating any polarization, as seen in Fig. 5.9b. Lastly, the figure compares the $1s$ exciton distributions after excitation with a thermal and coherent source. For the thermal excitation, a degenerate population of bright exciton states is created. This is in contrast to the absence of bright exciton states with a broad momentum distribution generated by a coherent excitation.

While the theoretical details may be found in [7], the QW response to thermal excitation is calculated through the SBEs (Eqns. 5.46) and by taking into account the incoherent

nature of thermal statistics.

The SBEs predict that for an incoherent light source, the polarization is suppressed. We learned in chapter 4 that polarization-carrier scattering is the main cause of shifting and broadening of the nonlinear $1s$ exciton lineshape. It follows from the SBEs that a suppressed polarization results in a decrease in the nonlinear broadening, as illustrated in Fig. 5.10. The half-width at half maximum (HWHM) broadening in this figure is read as a modification to the linear linewidth. The coherent excitation predicted is in agreement with the data presented in chapter 4. The thermal excitation in the nonlinear regime is an experimental goal that we discuss in next chapters.

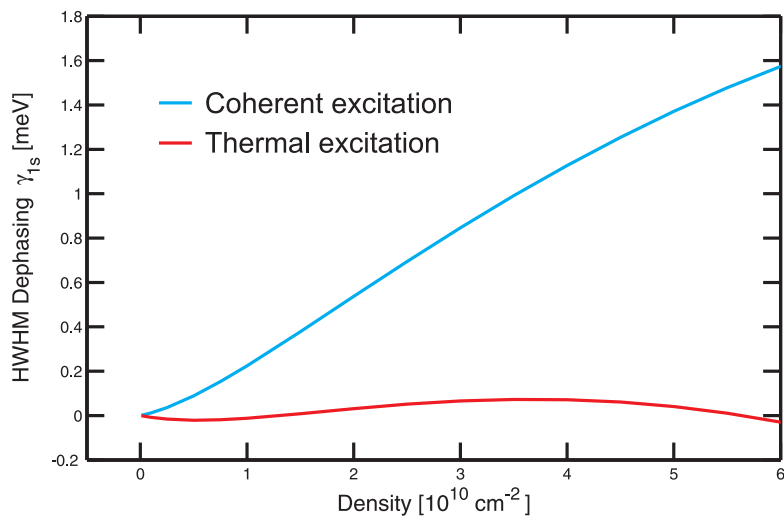


Figure 5.10: Theoretical prediction of the excitation-induced dephasing (EID) half-width at half maximum (HWHM) in addition to the linear $1s$ resonance width (≈ 0.75 meV) for coherent vs. thermal excitation. Thermal excitation is predicted to suppress scattering compared with coherent excitation for similar carrier excitation levels. Suppressed scattering leads to lower dephasing rates.

5.4.7 Jaynes-Cummings model

The theory of quantum-optical spectroscopy describes the coupling of a light field with the material response in a QW. The SBEs involve summing over many wave vectors \mathbf{k} and including correlations between single- and double-particle quantities [7]. To gain insight about the physics of excitation with thermal light statistics, we perform a simplified

calculation using a Jaynes–Cummings model which does not include k -dependence or many-body correlations. However, the key result of the Kira-Koch theory is qualitatively predicted, namely that a thermal excitation source produces a population without polarization. The predicted effects including the suppression of scattering and long-range ordering in the full microscopic calculation can be attributed to the anomalous reduction in the polarization.

In this model, we consider two-level system interacting with a single quantized mode of the radiation field. Analogous to an atom, the ground and excited states of the two-level system describe the exciton quasiparticle and its absence. Ground state means no exciton; excited state means we have an exciton in the $1s$ state.

We begin by defining the Hamiltonian describing a two-level system interacting with a light field:

$$\begin{aligned}\hat{H} &= \hat{H}_A + \hat{H}_F + \hat{H}_I \\ &= \frac{1}{2}\hbar\omega_0\hat{\sigma}_3 + \hbar\omega\hat{a}^\dagger\hat{a} - g(\hat{a}\hat{\sigma}_+ + \hat{a}^\dagger\hat{\sigma}_-).\end{aligned}\tag{5.47}$$

The first term \hat{H}_A is the energy of the atomic state, the second term \hat{H}_F is the energy in the field, and the third term \hat{H}_I represents the interaction between atom and photon for this 2-level system. The operator $\hat{\sigma}_3$ is the energy operator on the atomic state, $\hat{\sigma}_+$ and $\hat{\sigma}_-$ are the transition operators acting on the atomic state, and \hat{a} and \hat{a}^\dagger as annihilation and creation operators of the photon. The transition operators $\hat{\sigma}_+$ and $\hat{\sigma}_-$ have a representation in the basis of the atomic states $\{|g\rangle, |e\rangle\}$:

$$\hat{\sigma}_+ = |e\rangle\langle g| = \begin{pmatrix} 0 & 1 \\ 0 & 0 \end{pmatrix},\tag{5.48}$$

$$\hat{\sigma}_- = |g\rangle\langle e| = \begin{pmatrix} 0 & 0 \\ 1 & 0 \end{pmatrix},\tag{5.49}$$

and have the action $\hat{\sigma}_+|g\rangle = |e\rangle$ and $\hat{\sigma}_-|e\rangle = |g\rangle$. The inversion operator $\hat{\sigma}_3$ can be similarly

written in the atomic state basis as:

$$\hat{\sigma}_3 = |e\rangle\langle e| - |g\rangle\langle g| = \begin{pmatrix} -1 & 0 \\ 0 & 1 \end{pmatrix}. \quad (5.50)$$

This operator assigns an energy to a given atomic state. In this calculation, zero energy is chosen to be halfway between the ground and excited states, such that $H_A |g\rangle = -\frac{1}{2}\hbar\omega_0$ and $H_A |e\rangle = +\frac{1}{2}\hbar\omega_0$.

The atomic state operators can be identified as Pauli matrices obeying the commutation properties:

$$\begin{aligned} [\hat{\sigma}_+, \hat{\sigma}_-] &= \hat{\sigma}_3 \\ [\hat{\sigma}_3, \hat{\sigma}_+] &= 2\hat{\sigma}_+ \\ [\hat{\sigma}_3, \hat{\sigma}_-] &= -2\hat{\sigma}_-. \end{aligned} \quad (5.51)$$

The field operators operate on the Fock state $|n\rangle$:

$$\begin{aligned} \hat{a} |n\rangle &= \sqrt{n} |n-1\rangle, \\ \hat{a}^\dagger |n\rangle &= \sqrt{n+1} |n+1\rangle, \end{aligned} \quad (5.52)$$

and have the commutation properties:

$$\begin{aligned} [\hat{a}, \hat{a}^\dagger] &= 1, \\ [\hat{a}, \hat{a}] &= [\hat{a}^\dagger, \hat{a}^\dagger] = 0. \end{aligned} \quad (5.53)$$

The interaction term \hat{H}_I acts in the atom-field basis $\{|e, n\rangle, |g, n+1\rangle\}$. Here the first basis state is an atom in the excited state, with n photons in the field; the second state is an atom in the ground state, with $n+1$ photons in the field. We choose this basis is because H_I couples the two states together.

We time evolve the Hamiltonian in the Heisenberg picture to find the time evolution of the atomic operators:

$$i\hbar \frac{d}{dt} \hat{A} = [\hat{A}, \hat{H}]. \quad (5.54)$$

Using the evolution equation with Eqn. 5.47 yields

$$\begin{aligned} i\hbar \frac{d}{dt} \hat{\sigma}_- &= -\hbar\omega_0 \hat{\sigma}_- + g\hat{\sigma}_3 \hat{a} \\ i\hbar \frac{d}{dt} \hat{\sigma}_+ &= \hbar\omega_0 \hat{\sigma}_+ - g\hat{\sigma}_3 \hat{a}. \end{aligned} \quad (5.55)$$

The time dynamics of the exciton states can be calculated through the density matrix for the atomic states, which is the same as Eqn. 2.22:

$$\hat{\rho}^{Atom} = \sum_{j,k=e,g} |j\rangle \langle k| = \begin{pmatrix} \rho_{gg} & \rho_{ge} \\ \rho_{eg} & \rho_{ee} \end{pmatrix}. \quad (5.56)$$

In the semiconductor language, ρ_{ee} corresponds to a pure population of excitons, whereas ρ_{gg} is the nonexistence of excitons. The off-diagonal elements ρ_{ge} and ρ_{eg} correspond to the excitonic polarization (through Eqn. 2.33).

We wish to find the time dependence of ρ_{ee} and ρ_{eg} in response to different quantized radiation fields. In other words, we would like to know the time evolution of the density matrix of the atomic states.

The density matrix at time zero ($t = 0$) can be written as a product of the field density matrix $\hat{\rho}^F$ and atomic density matrix $\hat{\rho}^A$ because they are uncoupled:

$$\hat{\rho}(0) = \hat{\rho}^F(0) \otimes \hat{\rho}^A(0) \quad (5.57)$$

The dynamics of this density matrix for $t > 0$ is governed by the interaction part of the Hamiltonian \hat{H}_I in Eqn. (5.47). The terms \hat{H}_A and \hat{H}_F only contribute to an overall global phase, which does not affect the physics.

The evolution of the system is given by [45]:

$$\frac{\partial \hat{\rho}}{\partial t} = -\frac{i}{\hbar} [\hat{H}_I, \hat{\rho}], \quad (5.58)$$

which has the solution

$$\hat{\rho}(t) = \hat{U}_I(t) \hat{\rho}(0) \hat{U}_I^\dagger(t), \quad (5.59)$$

where the time evolution operator (with the interaction Hamiltonian) is

$$\hat{U}_I(t) = e^{-i\hat{H}_I t/\hbar}. \quad (5.60)$$

The matrix representation of the time evolution operator in the $\{|e, n\rangle, |g, n+1\rangle\}$ basis is

$$\hat{U}_I(t) = \begin{pmatrix} C(t) & S'(t) \\ S(t) & C'(t) \end{pmatrix} \quad (5.61)$$

where

$$\begin{aligned} \hat{C}(t) &= \cos(g' \sqrt{\hat{a}\hat{a}^\dagger} t) \\ \hat{S}(t) &= -i\hat{a}^\dagger \frac{\sin(g' \sqrt{\hat{a}\hat{a}^\dagger} t)}{\sqrt{\hat{a}\hat{a}^\dagger}} \\ \hat{C}'(t) &= \cos(g' \sqrt{\hat{a}^\dagger\hat{a}} t) \\ \hat{S}'(t) &= -i\hat{a} \frac{\sin(g' \sqrt{\hat{a}^\dagger\hat{a}} t)}{\sqrt{\hat{a}^\dagger\hat{a}}} \\ g' &= g/\hbar \end{aligned} \quad (5.62)$$

The C and S functions are operators with t as a parameter.

Assuming that we begin in the atomic ground state (i.e. no excitons), $\hat{\rho}^A(0) = |g\rangle\langle g|$, the time evolution of the total density matrix (using Eqns. (5.61), (5.62), and (5.59)) is:

$$\hat{\rho}(t) = \begin{pmatrix} -\hat{S}'(t)\hat{\rho}^F(0)\hat{S}(t) & \hat{S}'(t)\hat{\rho}^F(0)\hat{C}'(t) \\ -\hat{C}'(t)\hat{\rho}^F(0)\hat{S}(t) & \hat{C}'(t)\hat{\rho}^F(0)\hat{C}'(t) \end{pmatrix}. \quad (5.63)$$

We perform a partial trace over the field states to obtain the reduced density operator of the atom:

$$\hat{\rho}_{jk}^A(t) = \sum_{n=0}^{\infty} \langle j, n | \hat{\rho}(t) | k, n \rangle, \quad (5.64)$$

where the summation is over the field states and $j, k = e, g$. Now we are in a good position to see how different photon statistics affects the off-diagonal element ρ_{eg} and the diagonal element ρ_{ee} of the density matrix.

We evaluate the result for thermal photon statistics first, because it is mathematically simpler. The density matrix for thermal light is diagonal in the Fock basis and can be expressed as:

$$\hat{\rho}_{thermal} = \sum_{n=0}^{\infty} P_n |n\rangle \langle n| = \frac{1}{1 + \bar{n}} \sum_{n=0}^{\infty} \left(\frac{\bar{n}}{1 + \bar{n}} \right)^n |n\rangle \langle n|. \quad (5.65)$$

We may find the time evolution of the atomic density matrix components by using Eqns. (5.64) and (5.62)-(5.63). The matrix elements evaluate to

$$\begin{aligned} \rho_{ee} &= \sum_{n,m=0}^{\infty} \frac{\sin(g' mt)}{m} \frac{\sin(g'(n+1)t)}{n+1} \langle e, n | \hat{a} P_m | m \rangle \langle m | \hat{a}^\dagger | e, n \rangle \\ &= \sum_{n=0}^{\infty} \frac{\sin^2(g' nt)}{n^2} (n+1) P_n \end{aligned} \quad (5.66)$$

$$\begin{aligned} \rho_{gg} &= \sum_{n,m=0}^{\infty} \cos(g' mt) \langle e, n | \hat{a} P_m | m \rangle \langle m | \cos(g' mt) | g, n \rangle \\ &= \sum_{n=0}^{\infty} P_n \cos^2(g' nt) \end{aligned} \quad (5.67)$$

$$\begin{aligned} \rho_{ge} &= \sum_{n,m=0}^{\infty} \langle g, n | \cos(g' mt) P_m | m \rangle \langle m | (-i) \frac{\sin(g'(n+1)t)}{n+1} \hat{a}^\dagger | e, n \rangle \\ &= \sum_{n,m=0}^{\infty} \cos(g' mt) P_m \delta_{m,n} (-i) \frac{\sin(g'(n+1)t)}{n+1} \delta_{m,n+1} \\ &= 0 \end{aligned} \quad (5.68)$$

$$\begin{aligned} \rho_{eg} &= \sum_{n,m=0}^{\infty} \langle e, n | (-i) \frac{\sin(g' mt)}{m} \hat{a} P_m | m \rangle \langle m | \cos(g' nt) | g, n \rangle \\ &= \sum_{n,m=0}^{\infty} (-i) \frac{\sin(g' mt)}{m} P_m \delta_{n+1,m} \cos(g' nt) \delta_{n,m} \\ &= 0 \end{aligned} \quad (5.69)$$

This analysis reveals that excitation of a two-level system using quantum statistics generates population the polarization elements $\rho_{eg} = \rho_{ge} = 0$, consistent with the predictions from the SBEs. The population exhibits nontrivial flopping behavior where the population is periodically inverted. For certain thermal photon distributions, the system population may undergo collapse and revivals [109].

In contrast, the density matrix for a coherent state is

$$\hat{\rho}_{\text{coherent}} = \sum_{m,l=0}^{\infty} C_{ml} |m\rangle \langle l| = \sum_{m,l=0}^{\infty} e^{|\alpha|^2} \left(\frac{\alpha^m}{\sqrt{m!}} \right) \left(\frac{\alpha^l}{\sqrt{l!}} \right) |m\rangle \langle l|. \quad (5.70)$$

Evaluation of the time-evolution of the density matrix in a similar fashion yields that the polarization matrix elements ρ_{eg} and ρ_{ge} as well as the population matrix elements ρ_{ee} and ρ_{gg} are non-zero in general (not particularly illuminating, but nonzero). This means that coherent light generates population and polarization for a two-level system. This result matches qualitatively the theoretical predictions of §5.4.6 because the polarization is suppressed for thermal excitation.

5.5 Summary: thermal vs. coherent light statistics

We saw in chapter 4 that polarization-carrier scattering dominates the homogeneous linewidth in excitation-induced dephasing. A true thermal source would generate a population of excitons with a vanishing polarization. This excitation would result in the suppression of the scattering, leading to a narrower excitonic linewidth compared with a coherent excitation of the same density.

Summarizing the requirements for a thermal source, we require that the thermal source have vanishing singlet quantities $\langle \hat{a} \rangle = \langle \hat{a}^\dagger \rangle = 0$ and $g^{(2)} = \langle \hat{n}^2 \rangle / \langle \hat{n} \rangle^2 = 2$. In comparison, a coherent source has nonvanishing singlet quantities $\langle \hat{a} \rangle = \langle \hat{a}^\dagger \rangle = \alpha$, and $g^{(2)} = \langle \hat{n}^2 \rangle / \langle \hat{n} \rangle^2 = 1$. For both coherent and thermal statistics, we have a nonvanishing photon number expectation value $\langle n \rangle = \langle \hat{a}^\dagger \hat{a} \rangle$. These are the criteria we use to distinguish thermal from coherent photon statistics.

As we will see in the next chapter, the source we choose to study the QW response to a thermal excitation is not actually a thermal source but an ensemble of coherent pulses. The ensemble of these pulses, however, mimics thermal statistics when an averaging technique is implemented. Thus, we expect that the analysis of this chapter has qualitative predictive power for the ensemble-averaging techniques described in the next chapter.

Chapter 6

Toward a thermal source

The previous chapter explained the theoretical prediction that, given a sufficiently intense quantum-statistically incoherent light source, the many-body effects in a quantum-well (QW) system should be modified compared with a coherent source of the same photon density. The demonstration of incoherent light statistics affecting the system response is a first step in the experimental realization of quantum-optical spectroscopy [94]. We identified in §2.10.2 that the density necessary for saturating the QW system (Mott density) is around 10^{11} photons/cm². To generate these densities in our GaAs 10-QW sample, the photon energy of the source should have a photon density of at least 10^{12} photons/cm² within the exciton absorption linewidth of approximately 1 meV at a photon energy of 1.55 eV (800 nm), corresponding to the $1s$ exciton energy, E_{1s} . In addition, this photon density must exist within the time window of the exciton lifetime, $T_1 = 100$ ps. In practice, the photon density must be about two orders of magnitude higher – approximately 10^{14} photons/cm² because of reflection losses at dielectric interfaces.

In an effort to achieve a source that satisfies these parameters, we explored different possibilities and ultimately arrived at a pulse-shaping technique as a way to mimic incoherent photon statistics. We discuss some early efforts to achieve a light source with incoherent quantum statistics. Once we rule these options out because of their low optical intensities, we explain the spectral-phase randomization of femtosecond pulses as a means for exploring the quantum-optical response of our system.

6.1 Early efforts for a thermal light source

Since the goal for performing quantum-optical spectroscopy entails generating a source with thermal statistics, we first considered sources of light that are commercially available. Namely, we considered constant-intensity sources: incandescent bulbs, light-emitting diodes (LEDs), and a below-threshold diode laser. We also designed a cavity-dumping experiment to produce pulses of incoherent light. However, all of the attempts described in this section do not produce enough intensity to induce a strong nonlinear response in the QW system.

6.1.1 Incandescent bulbs

An incandescent light bulb is a simple device with thermal quantum statistics. The bulb, like the sun, emits blackbody radiation depending on temperature. Planck's law for the frequency dependence of the radiation intensity of a black body object at temperature T is: [110]

$$I(\nu, T) = \frac{2h\nu^3}{c^2} \frac{1}{e^{h\nu/k_B T} - 1}, \quad (6.1)$$

where k_B is Boltzmann's constant, c is the speed of light, and h is Planck's constant. The intensity is in units of power per unit area of emitting surface, per unit solid angle, per unit frequency. We convert the units from Eqn. 6.1 to find the relationship between photon density per second within a 1 meV bandwidth and photon energy. This relationship is plotted in Fig. 6.1 for three radiating temperatures, assuming that the entire emitting surface can be imaged onto a two-dimensional spot. The intensity at a given wavelength increases with the temperature. Thus it is desirable to have a very hot source to maximize the intensity output at $E_{1s} = 1.55$ eV. The light source could be spectrally narrowed by use of interference filters to achieve the desirable spectrum.

The brightness (or radiance) theorem in geometrical optics states that the intensity of an image formed by any passive optical system cannot exceed that of the light-emitting object [110]. Thus, the photon densities plotted from the Planck equation 6.1 are upper bounds

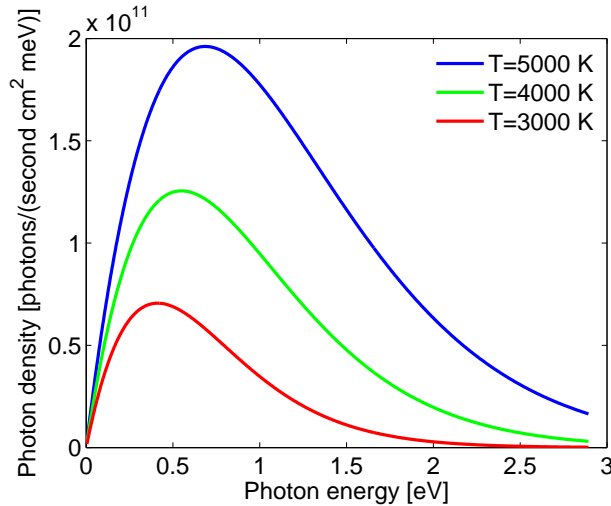


Figure 6.1: Photon densities per second within a 1 meV bandwidth for blackbody radiation at a few temperatures. The intensity at 1.55 eV increases with blackbody temperature.

for the photon density that may be achieved by focusing a thermal blackbody source. Even though there are $\approx 10^{11}$ photons arriving in a second from a blackbody source, the photon density within a time window of the lifetime of excitons ($T_1 = 100$ ps) is much smaller than the density required for creating nonlinearities in the QW system. The maximum photon density in a 1 meV bandwidth emitted from a hot blackbody such as a halogen bulb (100 W, 5000 K) within 100 ps is <10 photons/cm², more than 10 orders of magnitude below the required photon density for generating many-body configurations in GaAs QWs. To achieve photon densities of 10^{12} photons/cm² in a 1 meV bandwidth about $E_{1s} = 1.55$ eV and within a 100 ps time window would require temperatures of over 10^{15} K! Even imaging our sun ($T = 5800$ K) would not produce photon densities higher than an incandescent bulb because of the limits on focusing indicated by the brightness theorem. As a reality check, we calculate the photon density from the sun. With a luminosity of 4×10^{26} W and a diameter of 1×10^9 m, the sun's intensity of 5×10^{12} W/cm² corresponds to less than 1000 photons/cm² within a 100 ps time window.

Light from a thermal source is unfeasible for quantum-optical spectroscopy. Thermal events generated from electron-positron or hadron colliders (100 GeV of thermal energy

corresponds to 10^{15} K) may produce the intense thermal light necessary for generating many-body configurations in GaAs QWs. However, since imaging and filtering light from a collider is experimentally unfeasible, we consider other potential sources of bright incoherent light.

6.1.2 Light-emitting diodes

Since no realistically attainable true thermal blackbody radiation source exists for generating many-body configurations, we considered light-emitting diodes (LEDs). LEDs are p - n diodes that when forward biased cause electron hole recombination that emits light (spontaneous emission) corresponding to the band gap energy of the semiconductor [23]. The radiated light lacks temporal coherence since the recombination events are independent processes. An LED can emit at a narrower bandwidth than a blackbody source, leading to brighter emission within a small frequency window. These advantages make the LED a good candidate for generating many-body configurations in GaAs quantum wells.

We perform a calculation to determine the feasibility of LEDs for quantum-optical spectroscopy. The highest intensity LEDs available on the market are superluminescent LEDs. These devices can emit up to 500 mW from an area of 0.001 cm^2 (typically $1000 \mu\text{m} \times 100 \mu\text{m}$). This corresponds to a near-field intensity of 500 W/cm^2 . Appealing to the brightness theorem again, we find that it is not possible to generate a photon density of more than $2 \times 10^{11} \text{ photons/cm}^2$ within the time window of the exciton lifetime, $T_1 = 100 \text{ ps}$. However, this calculation does not consider that the bandwidth of LEDs is typically 20-100 meV. Since the light needs to be within a 1 meV bandwidth, the relevant photon density is at least an order of magnitude lower. Additionally, superluminescent LEDs may also be partially coherent, which could complicate the experiment. While LEDs remain a potential option for the future, the best-available LEDs now on the market are not powerful enough to generate the required densities to observe nonlinear effects. We also consider a similar device for our studies, a laser diode.

6.1.3 Below-threshold diode laser

A laser diode, like the LED, uses a forward biased $p - n$ junction to inject electrons and holes to generate light [23]. However, the laser structure has a reflective optical cavity that guides emitted photons back into the junction to induce stimulated emission. In the case that there are enough electrons and holes injected at the junction, the optical feedback will induce enough stimulated emission to cause lasing, i.e., condensation of photons into a coherent state [92]. However, for lower electrical currents into the diode, the optical feedback has the effect of amplifying the spontaneous emission without lasing. The light emitted from a laser cavity before the onset of lasing is incoherent, which we desire for our experiments.

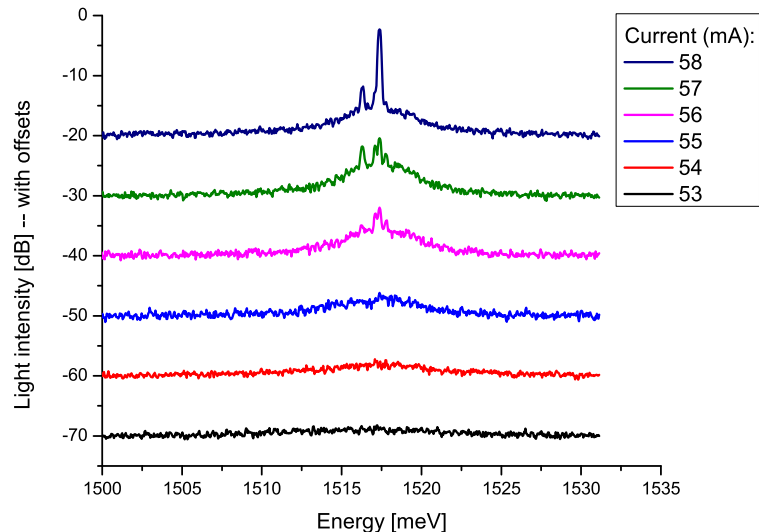


Figure 6.2: Diode laser output spectra for a range of carrier-injection currents. The peaks in the spectra are evidence of lasing above a current threshold of 55 mA.

We use a wavelength-tunable Toptica DL100 Diode Laser System. While designed to lase with a power of up to 220 mW with a bandwidth of $\Delta E = 2$ meV around 1.5 eV, we coat the output coupler with an anti-reflection layer that suppresses lasing. We vary the carrier-injection current up to the threshold of lasing and measure the light emitted from the cavity. The amplified spontaneous emission has a characteristic of a broader bandwidth, and the

onset of lasing is marked by a pronounced peak in the optical spectrum. The results of the measurements are shown in Fig. 6.2 at around 1.515 eV for a proof-of-principle experiment. The feedback grating in the laser makes the center wavelength in principle tunable to the HH $1s$ -resonance at $E_{1s} = 1.55$ eV. The laser diode outputs 3.3 mW power within a 6.6 meV bandwidth for a current of 55 mA that amplifies the spontaneous emission light without lasing. The area of emission from the diode is $75 \mu\text{m} \times 100 \mu\text{m}$. Using the brightness theorem, these facts means that the maximal intensity of 440 kW/cm^2 corresponds to a photon density of 1.8×10^{10} photons/cm² within the time window of the exciton lifetime $T_1 = 100$ ps. Filtering the bandwidth to 1 meV to match E_{1s} also makes the photon density smaller by about a factor of 2. This density, while quite high, proves to be inadequate for generating many-body configurations in GaAs QWs. Again, this technique also may have partial coherence, similar to LEDs. We next consider the related system of another laser cavity below lasing threshold.

6.1.4 Cavity dumping

Realizing that no incoherent light sources are available with sufficient intensity to produce many-body effects in our GaAs QW sample, we attempt to dynamically amplify spontaneous emission in a Ti:sapphire laser cavity.

We follow a technique for generating pulses from a laser cavity called cavity dumping [111, 112]. While cavity dumping was originally designed to output high intensity pulses of laser light, the same geometry can be used to output amplified spontaneous emission (ASE).

A laser operates by amplifying spontaneous emission on successive round trips of light in a cavity until a critical density of photons is achieved that marks the onset of lasing, when the gain in the cavity exceeds or equals the losses [92]. Before lasing, the ASE is incoherent [113, 114], and matches the photon statistics of the thermal source discussed in 5. With the onset of lasing, the source transitions into coherent photon statistics. We attempted to extract the photons from a pumped cavity just before the onset of lasing to achieve a high

intensity source with incoherent photon statistics.

Our experiment involves inserting an acousto-optic modulator (AOM) into a cavity that was aligned for lasing and another AOM in the path of the beam that optically pumps the gain medium, as shown in Fig. 6.3. The AOMs were both Isomet 1205C, each with a switching time of 12 ns. The gain medium is ti:sapphire, which lases near the relevant photon energy for the $1s$ heavy-hole exciton resonance of 1.55 eV. The cavity focuses the spontaneously emitted light from the gain crystal back into the gain crystal from both sides. The cavity length of 1.97 m corresponds to a repetition rate of $f_{\text{rep}} = 76$ MHz, or a roundtrip time of 13 ns. Thus, the switching time of the AOMs is as fast as the roundtrip time in the cavity, meaning that it is possible to manipulate the light on the time scale of an arbitrary number of round trips.

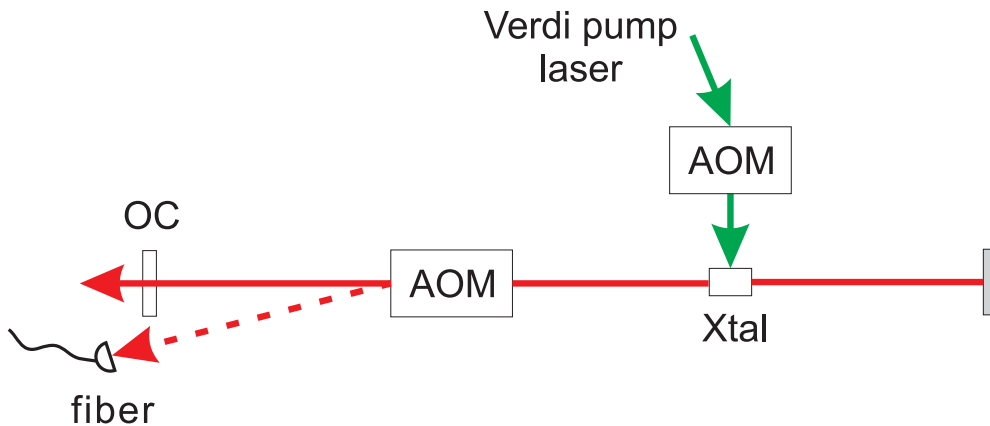


Figure 6.3: Schematic of setup used for cavity-dump experiment. OC, output coupler; AOM, acousto-optic modulators; Xtal, the Ti:sapphire gain crystal. A 5 watt Verdi laser pumps the gain crystal. The dumped light is collected with a fiber.

The AOMs are synchronized by means of a Stanford Research Systems digital delay generator (DG645) [?]. The “pump and dump” schematic is illustrated in Fig. 6.4. In this procedure, the pump AOM is turned on at a time t_1 , allowing the 2.33 eV (532 nm) pump laser to excite the gain medium. The excited gain medium initiates the process building up photons in the cavity as spontaneously emitted photons make round trips in the optical cavity. Before the onset of lasing, the intracavity AOM is turned on. This “dumps” the

incoherent photons out of the cavity. The resulting light is collected with a fiber to be spectrally resolved on an optical spectrum analyzer. The optical power is measured with a power meter.

We find that for a build up time $t_2 - t_1 = 590$ ns, we were able to recover a spectrum with no evidence of lasing. This corresponds to 45 round trips in the cavity, and a total average power per pulse of 120 mW. The broad ASE spectrum in Fig. 6.5 at t_2 indicates that the lasing has not yet started. The spectrum just after t_3 shows the dramatic change in the output spectrum after the onset of lasing.

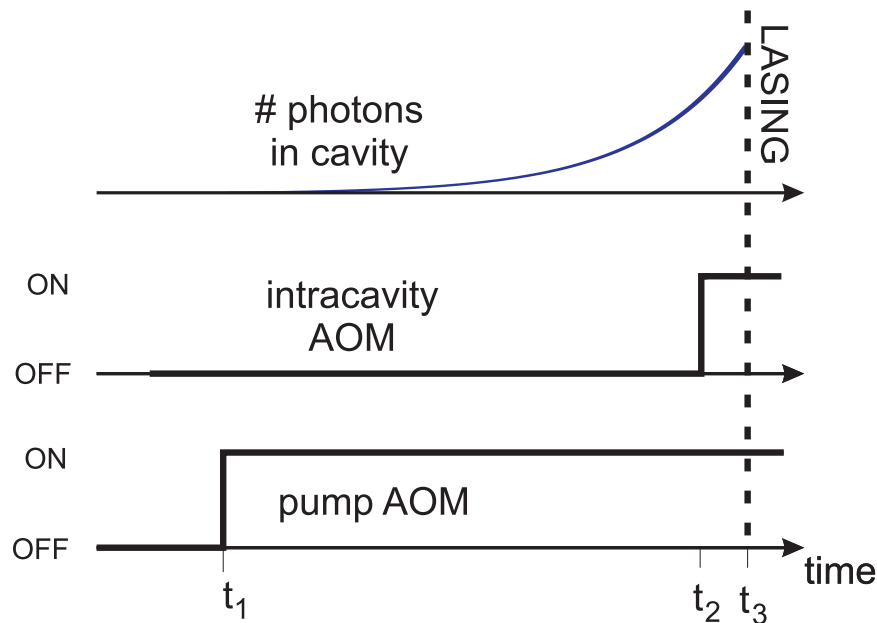


Figure 6.4: “Pump and dump” technique. The pump AOM switches on at t_1 to allow cavity build up. The intracavity AOM switches on at t_2 before the onset of lasing (at t_3) to dump the incoherent photons out of the laser cavity.

The cavity-dumping strategy does not generate a high enough intensity of incoherent photons. We found that the 120 mW of average power in the ASE pulse contained 2.1% of its power in the 1 meV bandwidth of the 1s exciton that we wish to pump, meaning that the exciton is pumped with 2.5 mW average power. Since the pulse width is determined by the round-trip time in the cavity, the incoherent pulse duration is approximately 12 ns. Thus, approximately 1% of the photons arrive within the exciton lifetime $T_1 = 100$ ps. Appealing to

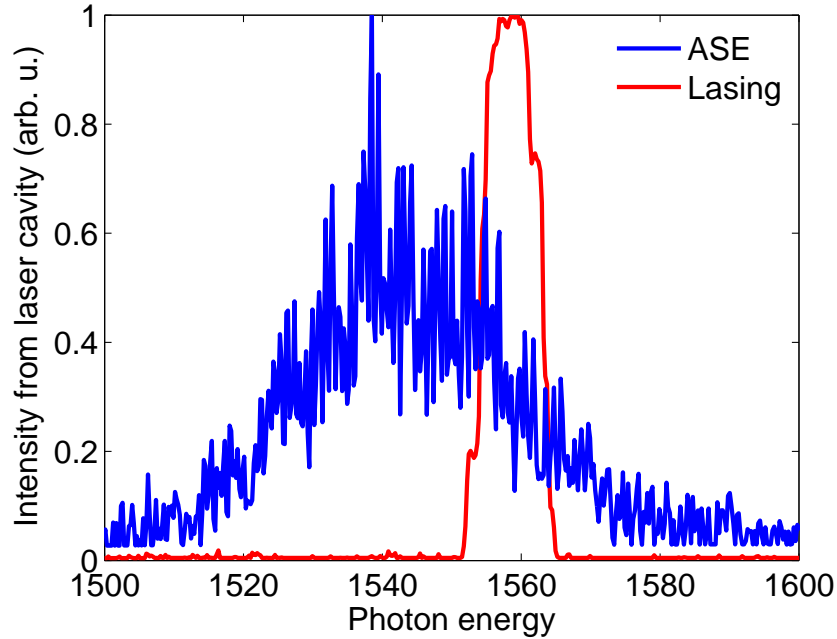


Figure 6.5: The dumped spectra at $t = t_2$ (blue), and for $t > t_3$ (red), corresponding to ASE and lasing, respectively.

the imaging theorem described earlier [110], and assuming a spot size on the gain crystal of $20 \mu\text{m}$, we expect a maximum photon density of 5×10^{10} photons/ cm^2 in a single pulse, which is several orders of magnitude below the density required ($\approx 10^{14}$ photons/ cm^2) for generating many-body configurations in our GaAs QW system. The cavity-dumping technique could be slightly improved (an order of magnitude) by shortening the cavity length to generate shorter incoherent pulses, but still would not be capable of saturating the QW system.

We explored several approaches theoretically and experimentally for generating a source of intense incoherent radiation at the E_{1s} energy. We stress that the numbers calculated in this section are all for the ideal conditions, i.e., optimal efficiencies and focusing of the source. The photon densities calculated are at least four orders of magnitude lower than would be necessary to saturate the QW system. Since the options for true incoherent light sources are not intense enough for performing quantum-optical spectroscopy, we explore a novel technique using coherent femtosecond pulses to explore the response of the QW system to

incoherent excitation.

6.2 Phase modulation of ultrashort pulses for incoherent light generation

After exploring a variety of strategies for producing high-intensity incoherent light in a narrow bandwidth, we developed with our theorist team a strategy that uses pulse-shaping techniques with coherent optical pulses in order to explore the effects of quantum statistics on the many-body state in GaAs QWs. The technique involves randomizing the spectral phase of a mode-locked Ti:sapphire laser spectrum in order to mimic the incoherent statistics of thermal light. Although the theory by which we motivate the use of phase-randomized pulses has philosophical issues concerning the interpretation of quantum mechanics, we have chosen to follow through with the experiments in order to test the theory.

6.2.1 Density-matrix ensemble averaging

In quantum mechanics, a single detection event produces only one outcome following a probability distribution related to a specific quantity [115]. While quantum theory provides a description of the probability distribution of repeated measurements, it cannot predict the outcome of a single measurement with certainty. Nonetheless, one can experimentally construct the probability distribution by repeating a measurement multiple times if the initial conditions are identical between measurements. The possibility to construct this distribution is a consequence of Born's rule [116].

Born's rule allows measurement of the expectation value of an observable q is possible through repeated measurements via

$$\langle q \rangle = \int qP(q)dq = \lim_{N \rightarrow \infty} \frac{1}{N} \sum_{j=1}^N q_j^{\text{meas}}, \quad (6.2)$$

where N is the total number of measurements, q_j^{meas} is the outcome of a single measurement, and $P(q)$ is the probability distribution function. By categorizing many measurements in a

histogram, it is possible to reconstruct the probability distribution function $P(q)$ by

$$P(q) = \lim_{\Delta q \rightarrow 0} \left(\lim_{N \rightarrow \infty} \frac{1}{N} \frac{N_q}{\Delta q} \right), \quad (6.3)$$

where Δq is the histogram bin interval, and N_q is the number of counts for corresponding to an observable q .

The theorists Kira and Koch found that Born's rule can be applied to the interaction of matter using a scheme known as density-matrix ensemble (DME) averaging. The concept of DME averaging explores the possibility of experimentally measuring a probability distribution function by changing the initial conditions in a controlled manner. The intention is to introduce a well-defined ensemble of classical excitation pulses that allow exploration of a system's response to quantum statistics of light other than classical. The initial conditions are varied by changing the spectral phase of each pulse from a mode-locked laser and measuring the many-body state in the QW system. We define the ensemble-averaged quantity

$$\langle\langle q \rangle\rangle = \lim_{N_{\text{ens}} \rightarrow \infty} \frac{1}{N_{\text{ens}}} \sum_{r=1}^{N_{\text{ens}}} \langle q \rangle_r^{\text{ens}}, \quad (6.4)$$

where N_{ens} is the size of the ensemble and $\langle q \rangle_r^{\text{ens}}$ refers to the quantity detected by many measurements of the single r^{th} realization. The ensemble-averaged expectation value is distinguished from the standard definition via $\langle\langle \dots \rangle\rangle$. An ensemble-averaged probability distribution may be determined:

$$\langle\langle P(q) \rangle\rangle = \lim_{N_{\text{ens}} \rightarrow \infty} \frac{1}{N_{\text{ens}}} \sum_{r=1}^{N_{\text{ens}}} P_r^{\text{ens}}(q), \quad (6.5)$$

where the single-realization distributions $P_r^{\text{ens}}(q)$ are defined in Eqn. 6.3. In analogy to the ensemble-averaged probability distribution, an ensemble-averaged density matrix can be constructed that determines the outcomes measurements from a system generated by an excitation with quantum statistics other than coherent light:

$$\rho^{\text{eff}} = \langle\langle \rho \rangle\rangle = \lim_{N_{\text{ens}} \rightarrow \infty} \frac{1}{N_{\text{ens}}} \sum_{r=1}^{N_{\text{ens}}} \rho_r^{\text{ens}}, \quad (6.6)$$

where ρ_r^{ens} is the density matrix of the r^{th} realization. Thus, if a suitable combination of realizations is chosen such that their density matrices average to an effective density matrix ρ^{eff} that describes different quantum statistics, then the measurements acquired from the ensemble of realizations allows reconstruction of the system response to the statistics of ρ^{eff} .

According to the theory, probes of the system dynamics may be averaged as in Eqn. 6.4 to reveal the system response under excitation conditions different from coherent light. If absorption spectra are measured from a sample for each realization, the average absorption spectrum $\langle\langle S_{\text{avg}}(\omega) \rangle\rangle$ can be found by:

$$\langle\langle S_{\text{avg}}(\omega) \rangle\rangle = \lim_{N_{\text{ens}} \rightarrow \infty} \frac{1}{N_{\text{ens}}} \sum_{j=1}^{N_{\text{ens}}} S_j(\omega), \quad (6.7)$$

where $S_j(\omega)$ is the absorption spectrum measured from the j^{th} realization.

To realize the Kira-Koch theory, we are specifically interested in choosing a combination of pulses with coherent photon statistics that average to an effective density matrix that corresponds to thermal photon statistics. We consider phase-randomized pulses to achieve this averaging.

6.2.2 Ensemble averaging for phase-randomized fields

The proposed scheme that we have followed involves randomizing the spectral phase of successive mode-locked pulses from a Ti:sapphire laser. The details of the experimental implementation of this is explained in the next chapter. This section justifies how this strategy produces an ensemble of pulses that average to thermal statistics in the limit of a large number of realizations.

The concept of phase randomization is illustrated in Fig. 6.6. The light from the pulse of a mode-locked laser travels through a device called a pulse shaper that is able to manipulate the spectral phase of the pulse. The phase function $\Delta\phi(\omega)$ is divided into discrete spectral bins of size $\Delta\omega_{\text{bin}}$. The value at each bin varies randomly in the interval $0 < \Delta\phi(\omega) < 2\pi$.

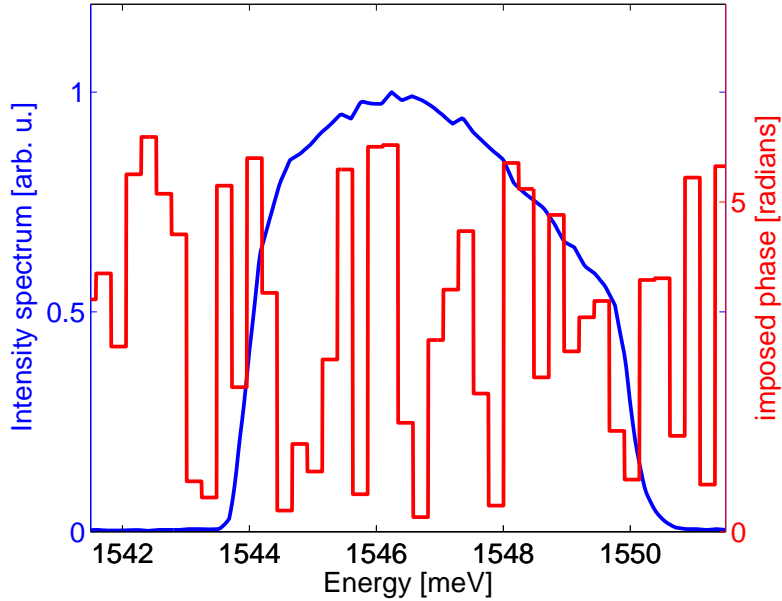


Figure 6.6: A spectrum from a mode-locked ti:sapphire laser with a random spectral phase function with spectral bin sizes of $\Delta\omega_{\text{bin}} = 200 \mu\text{eV}$. There are $N_{\text{bins}} = 30$ spectral bins across this spectrum.

The electric field of a single pulse realization in the frequency domain can then be written in the form [115]:

$$E(\omega) = \sum_{j=1}^{N_{\text{bins}}} E_j^0 e^{i\Delta\phi_j}, \quad (6.8)$$

where E_j^0 is the amplitude of the electric field in the absence of any phase modulation at the j^{th} bin, $e^{i\phi_j}$ is the random phase at the j^{th} bin, and N_{bins} is the total number of bins across the full-width at half maximum of the spectrum.

We can calculate the quantum statistics of the phase-randomized light fields using DME averaging by transforming the field operators in Eqn. 5.16 according to Eqn. 6.8:

$$\begin{aligned} \hat{a} &= \sum_{j=1}^{N_{\text{bins}}} e^{i\Delta\phi_j[r]} \hat{\alpha}_j \\ \hat{a}^\dagger &= \sum_{j=1}^{N_{\text{bins}}} e^{-i\Delta\phi_j[r]} \hat{\alpha}_j^\dagger, \end{aligned} \quad (6.9)$$

where $\hat{\alpha}_j$ and $\hat{\alpha}_j^\dagger$ are the field operators associated with the j^{th} spectral bin, r refers to a particular realization, and N_{bins} is the number of bins across the spectrum. The field

operator $\hat{\alpha}_j$ ($\hat{\alpha}_j^\dagger$) can be replaced by the complex-valued α_j (α_j^*) whenever it appears within an expectation value since the light in each spectral bin corresponds to a coherent state. In other words, the operator $\hat{\alpha}_j$ behaves like Eqn. 5.22 for each spectral bin:

$$\hat{\alpha}_j |\alpha_j\rangle = \alpha_j |\alpha_j\rangle. \quad (6.10)$$

From the definition of these operators, we obtain the following ensemble-averaging rules:

$$\langle\langle e^{i\Delta\phi_j} \rangle\rangle = \lim_{N_{\text{ens}} \rightarrow \infty} \frac{1}{N_{\text{ens}}} \sum_{r=1}^{N_{\text{ens}}} e^{i\Delta\phi_j[r]} = 0, \quad (6.11)$$

$$\langle\langle e^{i[\Delta\phi_j[1] + \Delta\phi_j[2] + \dots + \Delta\phi_j[J]]} \rangle\rangle = 0. \quad (6.12)$$

These both hold because each realization is completely random with respect to all of the others. Both quantities approach zero in the limit of large N_{ens} .

As a test of the quantum statistics of the ensemble average, we first compute the singlet quantity using the ensemble-averaging procedure defined in Eqn. 6.4:

$$\langle\langle \hat{a} \rangle\rangle = \lim_{N_{\text{ens}} \rightarrow \infty} \frac{1}{N_{\text{ens}}} \sum_{r=1}^{N_{\text{ens}}} \langle \hat{a} \rangle = \sum_j \langle\langle e^{i\Delta\phi_j} \rangle\rangle \alpha_j = 0. \quad (6.13)$$

Similarly $\langle\langle \hat{a}^\dagger \rangle\rangle = 0$ for this ensemble average.

A calculation of the photon number (the numerator of the first-order coherence function, Eqn. 5.3) for the randomized ensemble yields

$$\langle\langle \hat{a}^\dagger \hat{a} \rangle\rangle = \sum_{j,k} \langle\langle e^{i[\Delta\phi_k - \Delta\phi_j]} \rangle\rangle \alpha_j^* \alpha_k. \quad (6.14)$$

Since $\Delta\phi_k$ and $\Delta\phi_j$ are random with respect to each other for $j \neq k$, only the $j = k$ term contributes to Eqn. 6.14. Consequently,

$$\langle\langle \hat{a}^\dagger \hat{a} \rangle\rangle = \sum_{j=1}^{N_{\text{bins}}} \alpha_j^* \alpha_j = \sum_j |\alpha_j|^2, \quad (6.15)$$

which is both nonvanishing and a real quantity. Assuming that each spectral bin has the same amplitude $\alpha_j = \alpha$ (but each spectral bin has a different phase), we find that

$$\langle\langle \hat{a}^\dagger \hat{a} \rangle\rangle = N_{\text{bins}} |\alpha|^2, \quad (6.16)$$

To determine the statistics of ρ^{eff} , we calculate the second-order coherence function $g^{(2)}$ according to Eqn. 5.21 but in frequency space (essentially, the t 's and τ 's are dropped). We have already evaluated the denominator of $g^{(2)}$ in Eqn. 6.16. The numerator of $g^{(2)}$ can be evaluated using the ensemble-averaging procedure as:

$$\langle\langle [\hat{a}^\dagger]^2 \hat{a}^2 \rangle\rangle = |\alpha|^4 \sum_{j^{(1)}=1}^{N_{\text{bins}}} \sum_{k^{(1)}=1}^{N_{\text{bins}}} \sum_{j^{(2)}=1}^{N_{\text{bins}}} \sum_{k^{(2)}=1}^{N_{\text{bins}}} \left\langle \left\langle \exp \left(i \sum_{s=1}^2 [\Delta\phi_j^{(s)} - \Delta\phi_k^{(s)}] \right) \right\rangle \right\rangle, \quad (6.17)$$

where the index $s = 1, 2$ refers to the $j^{(s)}$ and $k^{(s)}$ indices of the outer sum. The sums in Eqn. 6.17 produce nonvanishing values only for each $j^{(s)}$ value matching the $k^{(s)}$ value. All nonvanishing terms produce the same result $\frac{2 N_{\text{bins}}!}{(N_{\text{bins}}-2)!}$ times. Using this result, we can evaluate Eqn. 6.17:

$$\begin{aligned} \langle\langle [\hat{a}^\dagger]^2 \hat{a}^2 \rangle\rangle &= 2(N_{\text{bins}} |\alpha|^2)^2 \left[\frac{N_{\text{bins}}!}{N_{\text{bins}}^2 (N_{\text{bins}} - 2)!} \right] \\ &= 2(N_{\text{bins}} |\alpha|^2)^2 \left[1 - \frac{1}{N_{\text{bins}}} \right] \\ &= 2 \langle\langle \hat{a}^\dagger \hat{a} \rangle\rangle^2 [1 + \mathcal{O}(N_{\text{bins}}^{-1})], \end{aligned} \quad (6.18)$$

where the last line uses the result from Eqn. 6.16. The term of order N_{bins}^{-1} is dropped in the limit $N_{\text{bins}} \gg 2$. We find by insertion of this result into Eqn. 5.21 that $g^{(2)} = 2$ for our ensemble-averaged source. This result is worked out in general for $g^{(m)}$ in [115]; however, the second-order coherence $g^{(2)}$ is calculated here since this quantity is of primary interest for distinguishing the statistics of thermal source from a coherent source.

We find that the statistics in Eqn. 6.18 corresponds to thermal light statistics. Since the singlet quantity $\langle\langle \hat{a} \rangle\rangle$ is vanishing, the expectation value of the photon number $\langle\langle n \rangle\rangle = \langle\langle \hat{a}^\dagger \hat{a} \rangle\rangle$ is finite, and $g^{(2)} = 2$, we conclude that the phase-randomized ensemble of pulses satisfy the criteria for thermal statistics. Consequently, we expect that a series of separate measurements performed for an ensemble of phase-randomized pulses, each with the same number of large number of spectral bins $N_{\text{bins}} \gg 2$, will allow construction of the density-matrix for a true thermal source. Construction of the density matrix for a thermal source

has the power to reveal the nonlinear system response to light with true thermal photon statistics.

To test the opposite limit where the number of spectral bins $N_{\text{bins}} = 1$, we expect that we recover the statistics for the coherent state since there would be no phase modulation across the spectrum. For this situation, the sums in the product of sums in Eqn. 6.17 each have just one term. The phase $\Delta\phi$ is identical for the $j^{(1)} = k^{(1)} = j^{(2)} = k^{(2)} = 1$ terms for every realization. Therefore,

$$\begin{aligned} \sum_{j^{(1)}=1}^1 \sum_{k^{(1)}=1}^1 \sum_{j^{(2)}=1}^1 \sum_{k^{(2)}=1}^1 \left\langle \left\langle \exp \left(i \sum_{s=1}^2 [\Delta\phi_j^{(s)} - \Delta\phi_k^{(s)}] \right) \right\rangle \right\rangle \\ = \langle \langle \exp (i2[\Delta\phi_{j=1} - \Delta\phi_{k=1}]) \rangle \rangle = 1 \end{aligned} \quad (6.19)$$

The calculation of this product of sums combined with Eqn. 6.17 shows that

$$\langle \langle [\hat{a}^\dagger]^2 \hat{a}^2 \rangle \rangle = |\alpha|^4. \quad (6.20)$$

Combining this result with Eqns. 6.18 and 5.21 results in $g^{(2)} = 1$, consistent with our expectations for coherent light.

6.3 Philosophical issues

Although the theory described in 6.2.2 is mathematically self-consistent, it is important to inquire about how this theory describes the experiment to be performed. The protocol from the theory suggests that measurements from a large number of phase-randomized excitation pulses be separately recorded. While each measurement records the system response to a coherent pulse of light, the ensemble of measurements make up the information necessary for construction of the system response to thermal photon statistics.

The concept of DME averaging suggests that a source with quantum statistics can be constructed from a coherent pulsed laser. This result is challenging to understand since the realizations need not interfere with each other in the QW system. The data for each realization could be recorded on separate days, and the DME technique would allow construction

of the QW response to a different thermal statistics.

Results from quantum mechanics state that a system with density matrix composed of field and matter parts $\hat{\rho} = \hat{\rho}^F \otimes \hat{\rho}^M$ evolves in time as:

$$i\hbar \frac{\partial \hat{\rho}}{\partial t} = -[\hat{\rho}, H], \quad (6.21)$$

where H is the Hamiltonian of the system [45]. This evolution was worked out for a simple case using true thermal and coherent photon statistics in §5.4.7. It may seem counter-intuitive that the dynamics for a system could be constructed from the traces of many time-evolved density matrices from different realizations, since information is lost when one traces over a density matrix. Additionally, there is no possibility of interference between subsequent realizations in the experimental setup, as we will discuss in chapter 8. The theory claims that construction of a new density matrix based on the trace of an ensemble of density matrices is possible. While this claim is puzzling, we have chosen to proceed with experiments that seek to verify this assertion.

To generate pulses of light that satisfy the criteria for thermal light in DME averaging, we use the experimental technique of pulse shaping, which is introduced in the next chapter.

Chapter 7

Pulse-shaping techniques

7.1 Concept of a pulse shaper

A pulse shaper is an apparatus that allows manipulation of the spectral amplitude and phase of an ultrashort optical pulse. The apparatus has application in stretching and compressing pulses, coherent control, optical imaging, and optical communications [9]. A pulse shaper operates by converting an ultrashort pulse into the frequency domain, where linear filtering can be applied, before converting the pulse back into the time domain.

We are interested in applying pulse-shaping techniques to our mode-locked laser pulses in order to explore quantum-optical spectroscopy with density-matrix ensemble averaging, as discussed in chapter 6. We specifically wish to manipulate the phase of the spectrum of a pulse as shown in Fig. 6.6. In this chapter we discuss the operation of a pulse shaper, consider experimental parameters and limitations to obtaining an arbitrary pulse waveform.

7.2 Experimental setup

The basic experimental design for a $4f$ pulse shaper is illustrated in Fig. 7.1. The design is called $4f$ because the total distance between the center of the first grating to the center of the second grating is four times the focal length f of the lenses used. A pulse from a mode-locked laser enters from one side. The pulse diffracts from a grating, which converts the wavelengths of the pulse into angle in the first-order diffraction direction according to

the grating equation [9]:

$$\theta_{\text{diffracted}}(\lambda) = \sin^{-1} \left(\frac{\lambda}{d} \right), \quad (7.1)$$

where d is the spacing of the grating lines, and λ is the wavelength of light. The spread in wavelengths is then collimated with a cylindrical lens of focal length f . The spread in wavelengths is now mapped to a positional spread. Besides collimating the diffracted beam, the lens focuses each frequency component onto the plane of the mask. The different frequencies may then be manipulated individually at the plane of the mask by linear filtering of the amplitude or phase. This filtering can be accomplished with a variety of devices, such as a spatial light modulator or acousto-optic modulator [9], or any material with varying optical thickness or varying transparency. Undesired frequency components can thus easily be blocked at the plane of the mask.

To reconstruct the pulse after linear filtering, the process that took place before the mask is time-reversed by the remaining optics into a single collimated beam with an output pulse shape given by the Fourier transform of the pattern transferred by the mask onto the spectrum. For an absent phase mask, the output pulse should be identical to the input pulse.

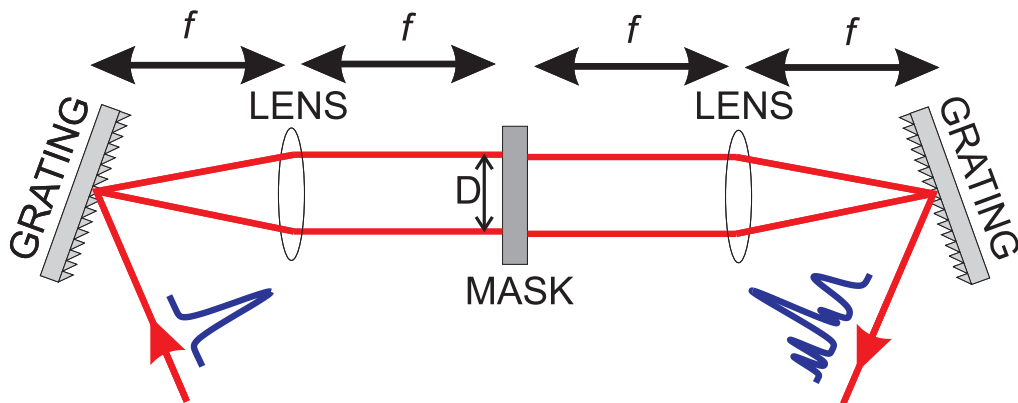


Figure 7.1: Layout for a $4f$ pulse-shaper apparatus. The spatial spread D corresponds to a spread in optical wavelengths $\Delta\lambda$.

Various factors determine the appropriate design parameters for the pulse-shaper apparatus. We discuss the design considerations in the frequency domain in the next section.

7.3 Shaper design considerations in the frequency domain

7.3.1 Spectral resolution constraints

To choose appropriate design parameters for the pulse shaper, we consider the fixed conditions of the experiment and requirements for the experiment in the frequency domain. The Ti:sapphire laser center wavelength is $\lambda_0 = 800$ nm ($\hbar\omega_0 = 1.55$ eV) with a bandwidth of around $\Delta\lambda = 3.5$ nm ($\hbar\Delta\omega = 7$ meV). The theory estimates a constraint of needing to have at least 6 bins across the 1s exciton spectrum in order to perform quantum-optical spectroscopy using density matrix ensemble averaging, discussed in Chapter 6. The full-width half maximum (FWHM) of the linear exciton absorption line shape is $\gamma_{1s}^{FWHM} = 1.5$ meV, determined in Chapter 4. Thus we require the resolution on the pulse-shaper system to have an upper bound of $\delta E_{res} = 250$ μ eV. A smaller energy resolution provides flexibility in the possible manipulations of the pulse.

We estimate the resolution of the pulse shaper by determining the wavelength-to-displacement conversion at the plane of the mask, allowing the spatial spot size of a single color mode to be converted into an estimate of the spectral resolution. We use Eqn. 7.1 to determine the spatial spread D across the phase mask for a small bandwidth $\Delta\lambda$ in order to calibrate wavelength to displacement along the plane of the mask in the paraxial ray approximation [92]:

$$\begin{aligned} D &= [\theta_1(\lambda + \Delta\lambda/2) - \theta_1(\lambda - \Delta\lambda/2)] f \\ &= \left[\sin^{-1} \left(\frac{\lambda + \Delta\lambda/2}{d} \right) - \sin^{-1} \left(\frac{\lambda - \Delta\lambda/2}{d} \right) \right] f, \end{aligned} \quad (7.2)$$

where f is the focal length of each lens in the setup. The ratio $\Delta\lambda/D$ can be used to convert a spatial spread into a spread in wavelength. We then calculate the spot size of a single color focused onto the shaper for a beam of initial waist w_i according to [9]:

$$w_0 = \frac{\cos\theta_i}{\cos\theta_d} \frac{\lambda f}{\pi w_i}, \quad (7.3)$$

where $\theta_i = 40^\circ$ and $\theta_d = 74^\circ$ are the incident and diffracted angles with respect to the plane of the first grating, respectively. The diffracted angle θ_d is determined by Eqn. 7.1.

The resolution of the shaper is then estimated by using $\Delta\lambda/D$ to convert the units of w_0 from spatial spread into spectral spread:

$$\delta\lambda_{\text{res}}[\text{nm}] = \frac{\Delta\lambda = 1[\text{nm}]}{D[\text{mm}]} \times w_0[\text{mm}]. \quad (7.4)$$

While it is strange to see a conversion between two length units, [nm] indicates a wavelength and [mm] indicates a spatial spread.

The spectral resolution expression $\delta\lambda_{\text{res}}$ allows us to see which parameters affect the resolution. Since both D and w_0 are proportional to the focal length f , the resolution of the shaper apparatus is completely independent of choice of focal length. The focal length choice is determined by the pixel size of the mask device, which we will discuss next. The parameters that we can choose to optimize the resolution of the pulse shaper are the initial beam waist w_i and the grating spacing d .

It is desirable to have a large initial beam waist and small grating spacing according to Eqn. 7.4. The beam waist was expanded to a large but manageable size of $w_i = 10$ mm going into the pulse-shaper apparatus. This parameter creates a spot size of $w_0 = 34\mu\text{m}$ at the plane of the phase mask. The grating was chosen to have a spacing of $d = 833$ nm (1200 lines/mm), nearly the smallest spacing before matching the laser wavelength of 800 nm, at which the efficiency of the grating vanishes [110]. We calculate the resolution using these parameters to be $\delta\lambda_{\text{res}} = 0.006$ nm. This resolution corresponds to $\delta E_{\text{res}} = 12\mu\text{eV}$, which is an order of magnitude better than the estimated theoretical constraint of $\delta E_{\text{res}} = 250\mu\text{eV}$, allowing flexibility in the choice of spectral bin size for the experiment.

7.3.2 Phase mask device

Of the many devices available for a mask in the pulse-shaper apparatus, we chose Boulder Nonlinear Linear Series Spatial Light Modulator (SLM) with a $1 \times 12,288$ pixel array.

The device offers programmability, full-range ($0 - 2\pi$) phase modulation, a small pixel size (pixel pitch = $1.6\mu\text{m}$), and a large screen area (19 mm). This device can independently modulate the phase of light rays reflected from each of its 12,288 pixels.

The SLM is reflective, which means that the $4f$ shaper design is folded on itself as shown in Fig. 7.2. To collect the output beam with minimal compromise in alignment, we adjust the vertical pointing of the reflected beam so that it is one beam diameter lower than the input beam, allowing pick-off with a compact mirror.

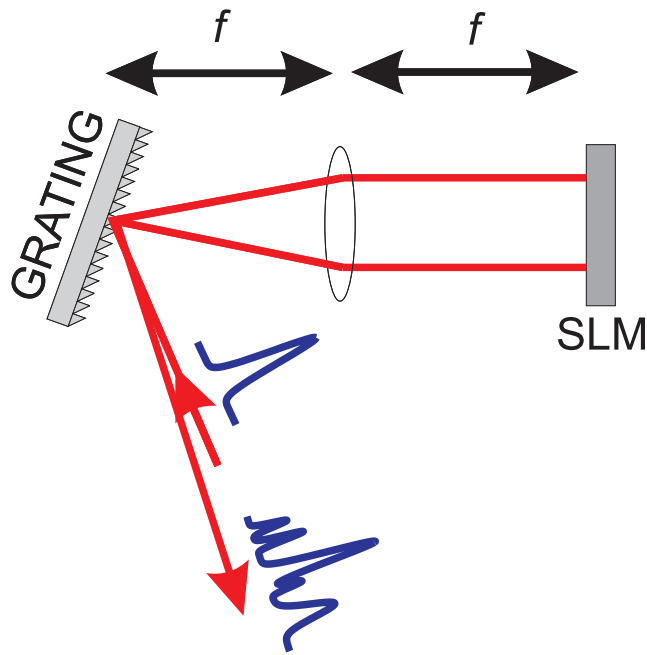


Figure 7.2: Layout for a $4f$ pulse-shaper apparatus in reflective geometry. Reflected beam is vertically offset from the input beam, but shown at a slightly different horizontal angle here only for illustration purposes.

To utilize the many pixels of the shaper, we choose a long focal length of $f = 50$ cm. This focal length produces a spread of 7.5 mm at the plane of the mask, given the other parameters, named earlier. This large spatial spread does not overflow the 19 cm wide liquid crystal screen of the SLM. The choice of focal length allows up to 4700 pixels across a 7 nm (13 meV) bandwidth spectrum. Thus, we have flexibility in choosing arbitrary spectral bin size with experimentally manageable parameters.

A schematic of the device is shown in Fig. 7.3. The $1.6 \mu\text{m}$ pixel pitch provides the flexibility to fit a large number of pixels across the spectrum if necessary. The space in the interpixel gap ($0.6 \mu\text{m}$) does not reflect any light, meaning that $0.6\mu\text{m}/1.6\mu\text{m} = 37.5\%$ of the incident light is lost due to diffraction at the interface. Aside from a change in the total efficiency, the interpixel gap does not modify the resolution or other properties of the shaper apparatus because the spot size at the single-color spot size according to Eqn. 7.3 is $w_0 = 34\mu\text{m}$, which is much larger than the pixel pitch.

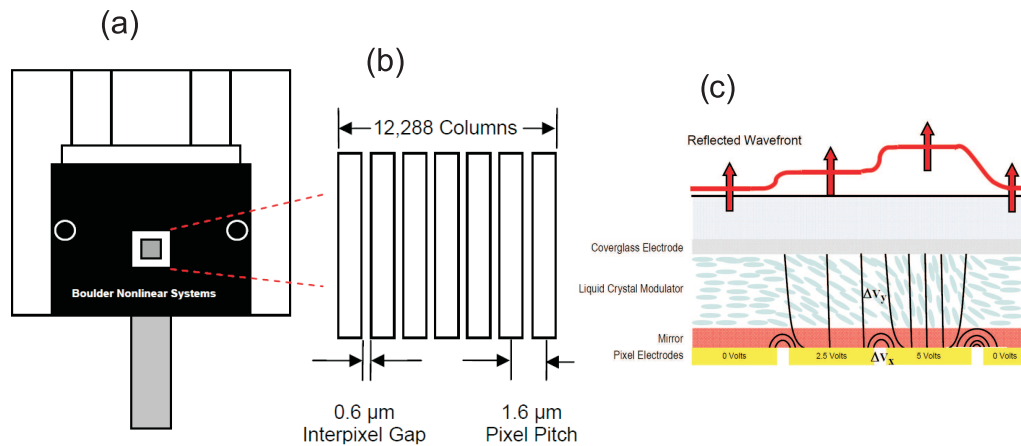


Figure 7.3: Schematic of the Spatial Light Modulator (SLM) [8]. (a) A front-view drawing of the device. (b) Detail of the pixel geometry. (c) Principle of operation using liquid crystals.

The principle of operation of the SLM is illustrated in Fig. 7.3c. The screen of the SLM consists of a one-dimensional array of liquid crystals. The light at the plane of the mask travels through the liquid crystals and is reflected by a mirror. Each pixel of the liquid-crystal array has an electrode with adjustable voltage 0-5 V. For 0 V applied to a pixel, the liquid crystals in that pixel are aligned parallel to the electrode. However, as the voltage increases, the liquid crystals begin to align with the electric field produced between the pixel electrode and the cover-glass electrode. The liquid crystals have the electro-optic property of birefringence, which means that their alignment alters the index of refraction for one polarization component (horizontal in this device) of an incident light field. We polarize our beam horizontally to maximize the modulation of phase. Thus, the application of a

different voltage on each of the liquid crystals can change the effective optical path length by up to one full wavelength (800 nm), providing a phase shift $\Delta\phi$ in the interval $0 < \Delta\phi < 2\pi$. Figure 7.3c demonstrates the phase retardance for 0 V, 2.5 V, and 5 V applied voltage. Since the phase retardance has nonlinear dependence on the applied voltage, the device is calibrated by an interferometer to create a look-up table that relates the two quantities.

We have discussed the design considerations and principles of operation of a pulse-shaper apparatus. We next explore the limitations of a pulse shaper in producing a pulse with arbitrary spectral phase and amplitude.

7.4 Physical limitations in pulse shaping

An ideal pulse shaper takes in a pulse of light and applies a spectral phase and amplitude in the Fourier domain, outputting an electric field with Fourier transform [9]:

$$E_{out}(\omega) = E_{in}(\omega)H(\omega), \quad (7.5)$$

where $H(\omega)$ is an arbitrary complex filter function in frequency space. However, because of the finite spot size of each single color and the fact that the spectrum is continuous¹ means that there exists spatial overlap between single-color modes in the beam at the plane of the phase mask.

Due to the finite spatial extent of each single-color mode, the filter function $H(\omega)$ is a convolution of the spatial mask function $M(x)$ with the intensity profile of the beam [9]:

$$H(\omega) = \left(\frac{2}{\pi w_0^2} \right)^{1/2} \int dx M(x) e^{-2(x-\alpha\omega)^2/w_0^2}, \quad (7.6)$$

where

$$\alpha = \frac{\lambda^2 f}{2 \pi c d \cos(\theta_d)}, \quad (7.7)$$

¹ For long integration times compared to the repetition rate of the laser ($T \gg f_{\text{rep}}^{-1}$), a temporal train of pulses Fourier transforms into a comb of frequencies spaced by $f_{\text{rep}} = 76$ MHz, or $0.3 \mu\text{eV}$. However, since the dynamics of the GaAs QW system completely decay in the time between pulses ($f_{\text{rep}}^{-1} = 12$ ns), this is not relevant. The system ‘sees’ the continuous spectrum of a single pulse.

and w_0 is given by Eqn. 7.3. Here α is the spatial dispersion with units $\text{cm} (\text{rad/s})^{-1}$. The effect of this convolution is to limit the spectral FWHM resolution to

$$\begin{aligned}\delta\omega &= (\ln 2)^{1/2} w_0 / \alpha \\ &= 2(\ln 2)^{1/2} \cos \theta_i \frac{c d}{\lambda w_i},\end{aligned}\tag{7.8}$$

which predicts a spectral resolution (using the above-mentioned numbers) that is in agreement with the analysis from Eqn. 7.4. It is clear to see here that the resolution is independent of the focal length f . Since the wavelength λ is a fixed parameter and the grating spacing d can only be as short as the wavelength, the resolution can be made smaller by choosing a large input beam waist w_i .

The use of the convolution in Eqn. 7.6 allows accurate simulations of the effects of various phase masks on the frequency- and time-domain electric fields by substituting $H(\omega)$ into Eqn. 7.5.

While simulations accurately predict the effects of spectral phase masks on the amplitude of the power spectrum, we develop an intuitive picture of why amplitude modulation is unavoidable for a pulse shaper designed to modulate the phase. The consequence of the overlap of single-color modes is illustrated in Fig. 7.4. Here five nearby single-color modes with spatial widths determined by Eqn. 7.3 overlap spatially at the plane of the phase mask. The location $50 \mu\text{m}$ marks a phase jump between two pixels. For the sake of this illustration, the phase of the left-side pixel is $\phi_L = 0$ radians and the right-right $\phi_R = \pi$ radians such that the difference in phase between the two pixels is $\Delta\phi = \pi$. This phase difference means that most of mode A undergoes a phase shift of $\phi_L = 0$ and most of mode E undergoes a phase shift of $\phi_R = \pi$. However, since the overlap between single-color modes is unavoidable, each mode that lies between A and E will have a fraction of their light that undergoes both phase shifts.

In the case of the single-color mode that lies at the phase discontinuity (mode C), half of the mode will undergo a phase shift of $\phi_L = 0$ and the other half will undergo a phase

shift of $\phi_R = \pi$, resulting in complete cancellation of the field for that spectral mode. For a phase discontinuity of $\Delta\phi = \pi$ between two pixels, the intensity will drop to zero with a width proportional to the resolution of the shaper, Eqn. 7.8.

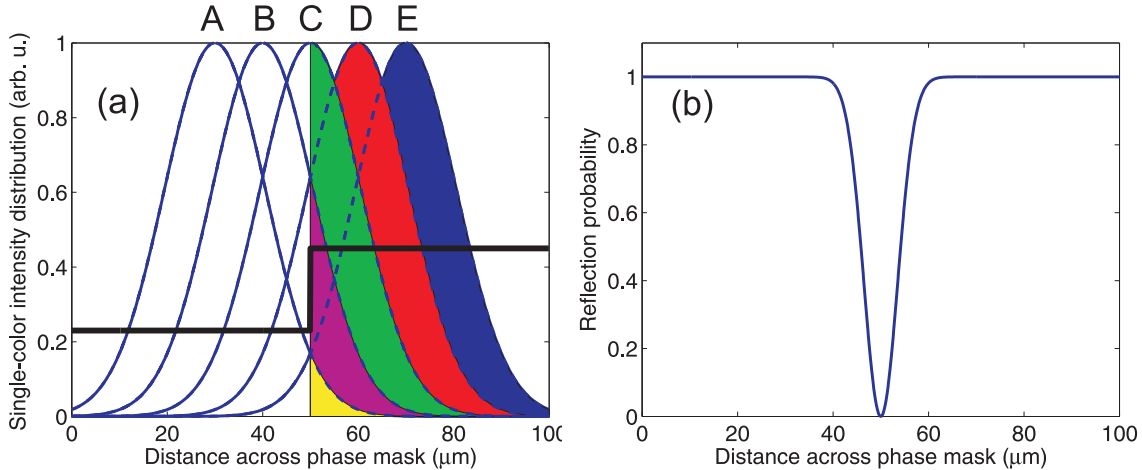


Figure 7.4: (a) Illustration of the intensity distribution of overlapping single-color modes (A–E, blue lines) at the plane of the phase mask in a pulse shaper. The spectral phase function across the mask (thick black line) is shown with arbitrary units. (b) The consequence of finite spot size in a pulse shaper is amplitude modulation at phase discontinuities with width corresponding to Eqn.7.8.

This picture reveals that regardless of the spectral resolution of the pulse shaper, there is necessarily some amplitude modulation of modes that lie near phase discontinuities along the phase mask. The effect of amplitude modulation can be minimized by designing a high-resolution apparatus as we have done.

To understand the effects of shaping pulses, it is helpful to have an intuitive picture of the relationship between the time- and frequency-domain representations of the electric field.

7.5 Relationship between time- and frequency-domains

7.5.1 Time duration and bandwidth

The time- and frequency-domain representations of an optical field are related to each other through the Fourier transform [117]:

$$\begin{aligned}\varepsilon(t) &= \mathcal{F}\{\tilde{\varepsilon}(\omega)\} = \int_{-\infty}^{+\infty} d\omega \tilde{\varepsilon}(\omega) e^{i\omega t} \\ \tilde{\varepsilon}(\omega) &= \mathcal{F}^{-1}\{\varepsilon(t)\} = \frac{1}{2\pi} \int_{-\infty}^{+\infty} dt \varepsilon(t) e^{-i\omega t},\end{aligned}\quad (7.9)$$

where $\varepsilon(t)$ and $\tilde{\varepsilon}(\omega)$ are the envelopes of the electric field in the time- and frequency-domains, respectively. The first line is the forward Fourier transform, and the second line is the inverse Fourier transform. Manipulation of the phase and amplitude of the frequency-domain electric field $\tilde{\varepsilon}(\omega)$ affects the time-domain electric field through these two equations.

We can use Eqn. 7.9 to explore the relationship between the time duration and bandwidth of an ultrashort pulse. For a pulse with Gaussian temporal pulse width τ_p , we may represent the field envelope $\varepsilon(t)$ in the time domain as:

$$\varepsilon(t) = \varepsilon_0 e^{-t^2/(2\tau_p)^2}, \quad (7.10)$$

where the FWHM duration of the temporal intensity of the pulse $I(t) = |\varepsilon(t)|^2$ is $\Delta\tau = 2\sqrt{2\ln 2}\tau_p \approx 2.355\tau_p$. The field in the frequency domain is calculated through Eqn. 7.9 as:

$$\tilde{\varepsilon}(\omega) = \mathcal{F}^{-1}\{\varepsilon(t)\} = \varepsilon_0 \sqrt{4\pi\tau_p^2} e^{-\tau_p^2\omega^2}. \quad (7.11)$$

A Gaussian temporal profile thus transforms into a Gaussian spectral profile. While center frequency $\omega_0 = 0$ here for clarity purposes, this analysis is easily transferrable to any center frequency with the replacement $\omega \rightarrow (\omega - \omega_0)$.

The time duration and bandwidth have an inverse relationship with each other. The bandwidth in Eqn. 7.11 is the FWHM of the power spectrum $|\tilde{\varepsilon}(\omega)|^2$ is $\Delta\omega = 2\sqrt{2\ln 2}/(2\tau_p) \approx 1.177/\tau_p$. Thus, from Eqns. 7.10 and 7.11 we can see that a short temporal width corresponds to a wide bandwidth. For any shape pulse, the FWHM of the power spectrum and

FWHM of the temporal intensity have a time-bandwidth product:

$$\Delta\omega\Delta\tau \geq 2\pi c_B, \quad (7.12)$$

where the equal sign holds for transform-limited pulses, i.e., with no spectral phase modulation. For the Gaussian pulses introduced, $\Delta\tau\Delta\omega/2\pi = c_B = 0.441$, indicating that the pulse is transform-limited. From the time-bandwidth product relationship we see that a larger bandwidth makes shorter temporal features possible.

A helpful visualization of the Fourier relationships is shown in Fig.7.5. For a Gaussian pulse shape, the total bandwidth B in the frequency domain has the relationship $B\delta t \approx 0.44$ with the shortest temporal feature in the time-domain [117]. The largest spread in the time-domain T is related to the smallest spectral feature δf by $T\delta f \approx 0.44$.

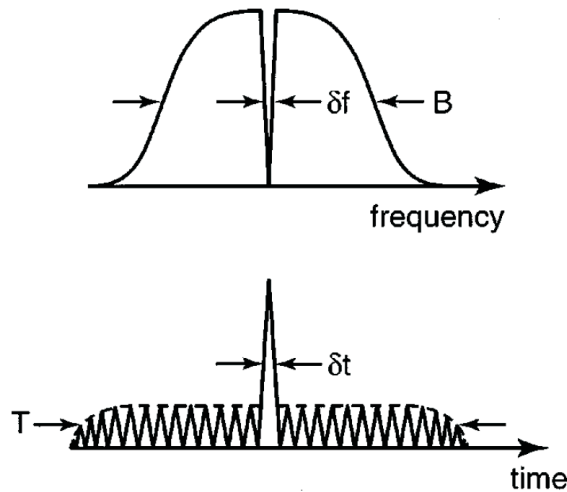


Figure 7.5: Pictorial relationship between the power spectrum (frequency domain) and temporal intensity (time domain) features. Figure from [9].

This picture has consequences for the time-domain output of a pulse shaper. First, the maximal temporal spread is limited by the resolution of the pulse shaper. For the parameters chosen in our apparatus, the estimated limit on the temporal spread is roughly $T \approx 0.44/\delta f = 0.44/12 \mu\text{eV} = 8.8 \text{ ps}$. Second, the shortest temporal feature is determined by the bandwidth B in our experiment according to $\delta t \approx 0.44/B = 0.44/7 \text{ meV} = 260 \text{ fs}$,

which is very close to the estimated pulse duration out of the laser, $\Delta\tau = 287$ fs FWHM. Narrowing the bandwidth in the pulse shaper limits the sharpness of temporal features in addition to spreading the pulse out in time.

The Fourier relationship described between the time- and frequency-domains applies to the modulation of spectral phase as well as amplitude. We discuss how spectral-phase modulation affects the temporal fields of an ultrashort pulse.

7.5.2 Effects of the spectral phase in the time domain

Since it is possible to choose any arbitrary phase mask function $M(x)$ (given the limitations presented in §7.4) to modulate the spectral phase of the electric field, we explore the effects of spectral-phase modulation in the time domain.

To understand the effects of spectral phase in the time domain, it is helpful to separate the spectral phase of a pulse into components via a Taylor expansion of the phase [117]:

$$\phi(\omega) = \phi(\omega_0) + \phi'(\omega_0)(\omega - \omega_0) + \frac{1}{2!}\phi''(\omega_0)(\omega - \omega_0)^2 + \frac{1}{3!}\phi'''(\omega_0)(\omega - \omega_0)^3 + \dots, \quad (7.13)$$

where ω_0 is the center frequency of the pulse. In this section, we consider the effects of the first three terms of Eqn. 7.13 on a pulse in the time domain. A spectral phase function $\phi(\omega)$ can be applied to a field in the frequency domain by the multiplication $\tilde{\varepsilon}(\omega)^{\text{modified}} = e^{i\phi(\omega)} \tilde{\varepsilon}(\omega)$.

7.5.2.1 Zero-order phase

The simplest phase application is a flat phase, or the first term in Eqn. 7.13. To see the effects of a flat phase in the time domain, we multiply the field $\tilde{\varepsilon}(\omega)$ in Eqn. 7.11 by the zero-order phase function $e^{i\phi(\omega_0)} = e^{i\phi_0}$. Taking the Fourier transform of the modified

frequency-domain field,

$$\begin{aligned}
 \varepsilon^{\text{flat}}(t) &= \mathcal{F} \{ \tilde{\varepsilon}(\omega) e^{i\phi_0} \} \\
 &= e^{i\phi_0} \mathcal{F} \{ \tilde{\varepsilon}(\omega) \} \\
 &= e^{i\phi_0} \varepsilon(t).
 \end{aligned} \tag{7.14}$$

Thus, the electric field acquires a global phase ϕ_0 , corresponding to the carrier-envelope phase, which relates the phase of the electric field to its temporal envelope [117]. While the global phase is important in some experiments [118], the experiments performed in this work are not affected because interfering beams have an angle with respect to each other at the sample, averaging out the global phase [11]. A flat phase mask does not affect the temporal intensity of the pulse $I(t) = |\varepsilon(t)|^2$. Since the global phase does not affect the physics for this work, we omit it in the following analysis for clarity.

7.5.2.2 Linear phase

Next, we consider application of a linear spectral phase, or $e^{i\phi'(\omega_0)\omega} = e^{ia\omega}$. In this case, we find that the time domain is affected as

$$\begin{aligned}
 \varepsilon^{\text{linear}}(t) &= \mathcal{F} \{ \tilde{\varepsilon}(\omega) e^{ia\omega} \} \\
 &= \varepsilon_0 e^{-(t+a)^2/(2\tau_p)^2} \\
 &= \varepsilon(t+a).
 \end{aligned} \tag{7.15}$$

We find that a linear spectral phase function shifts the pulse in time, but otherwise does not affect the temporal properties.

7.5.2.3 Quadratic phase

Lastly, we consider a quadratic spectral phase. The multiplication of $\tilde{\varepsilon}(\omega)$ by $e^{i\phi''(\omega_0)\omega^2/2} = e^{ib\omega^2}$ yields the time-domain field:

$$\begin{aligned}\varepsilon^{\text{quadratic}}(t) &= \mathcal{F} \left\{ \tilde{\varepsilon}(\omega) e^{ib\omega^2} \right\} \\ &= \varepsilon_0 \frac{\tau_p}{\sqrt{\tau_p^2 - ib}} \exp \left\{ -i\tilde{b}t^2 - \frac{t^2}{(2\tilde{\tau}_p)^2} \right\},\end{aligned}\quad (7.16)$$

where

$$\begin{aligned}\tilde{b} &= \frac{b}{4(b^2 + \tau_p^4)}, \\ \tilde{\tau}_p &= \frac{b^2 + \tau_p^4}{\tau_p^2}.\end{aligned}\quad (7.17)$$

The last line of Eqn. 7.16 shows that the temporal phase $\Phi(t)$ increases quadratically with time. The instantaneous frequency of the pulse in time can be found by differentiating the phase with respect to time:

$$\omega(t) = \frac{d}{dt}\Phi(t) = \frac{d}{dt}(\omega_0 t + \tilde{b}t^2) = \omega_0 + 2\tilde{b}t. \quad (7.18)$$

The instantaneous frequency increases linearly with time for $b > 0$. In analogy with acoustic frequencies, this is the sound that a bird makes when she chirps, increasing the pitch (frequency) with time. For this reason, $\phi''(\omega_0)$ is often called the ‘chirp’ parameter because of its influence in the time domain. For $b > 0$, the lower frequencies (‘red’) are shifted to earlier times, and the higher frequencies (‘blue’) are found at later times.

It is helpful to visualize the chirp with a spectrogram that captures the time and frequency information about a pulse. Spectrograms from a transform-limited pulse and a chirped pulse are compared in Fig. 7.6. A projection of the spectrogram onto the frequency axis is the power spectrum; a projection onto the τ axis is the temporal intensity profile. While the spectrum is (ideally) not modified for a positively chirped pulse, the red frequency components tend to show up at earlier times than the blue components.

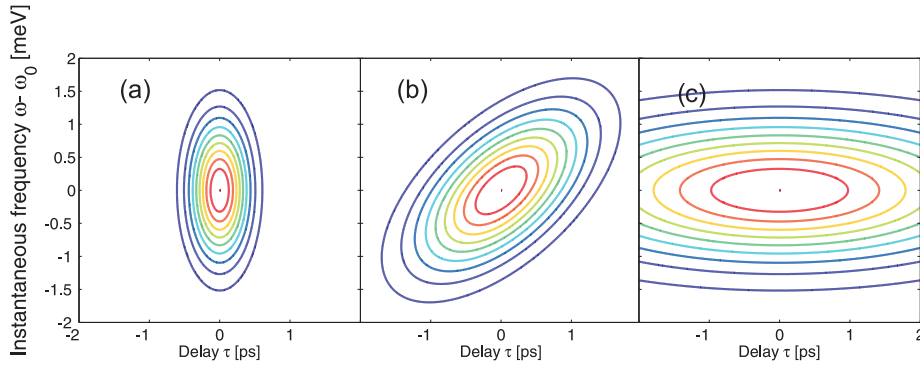


Figure 7.6: Spectrograms for ultrashort pulses with varying chirp: (a) no chirp ($b = 0$, or transform-limited), (b) moderate chirp ($b = 0.5 \text{ ps}^{-2}$), and (c) strong chirp ($b = 5 \text{ ps}^{-2}$). Chirp ‘rotates’ the spectrogram in this phase space.

The slope of the frequency \tilde{b} in Eqn. 7.18 exhibits nontrivial dependence on the chirp parameter b . The dependence is shown in Fig. ???. As seen in the figure, for $|b| \ll \tau_p^2$, $\tilde{b} \propto b$. However, for large spectral chirp parameter b , the instantaneous frequency exhibits very weak dependence on time. The spectrogram for a large amount of chirp is seen in Fig. 7.6c, where the projection in time is broad. For the pump bandwidth used in this thesis ($\Delta E = 5.9 \text{ meV}$), the spectral chirp parameter that maximizes \tilde{b} is $|b| = 2.7 \text{ meV}^{-2}$. A rough way to picture the effect of chirp on the time distribution of frequencies is as a rotation of the spectrogram in frequency-time space. The actual picture is more complicated since the temporal duration also increases for increasing $|b|$.

To see the effect of chirp on the temporal duration, we calculate the temporal intensity:

$$I(t) = \varepsilon^*(t)\varepsilon(t) = \varepsilon_0^2 \left[\frac{\tau_p^2}{\sqrt{b^2 + \tau_p^4}} \right]^2 \exp \left\{ -\frac{t^2}{2(\tau_p^4 + b^2)/\tau_p^2} \right\}. \quad (7.19)$$

The pulse width spreads in time with increasing chirp parameter b , and we recover the original transform-limited field intensity for $b \rightarrow 0$. The modified FWHM time duration of the intensity envelope is $\Delta\tau = 2\sqrt{2\ln 2} \left[\tau_p^2 + \left(\frac{b}{\tau_p}\right)^2 \right]^{1/2}$, where τ_p is the transform-limited pulse duration.

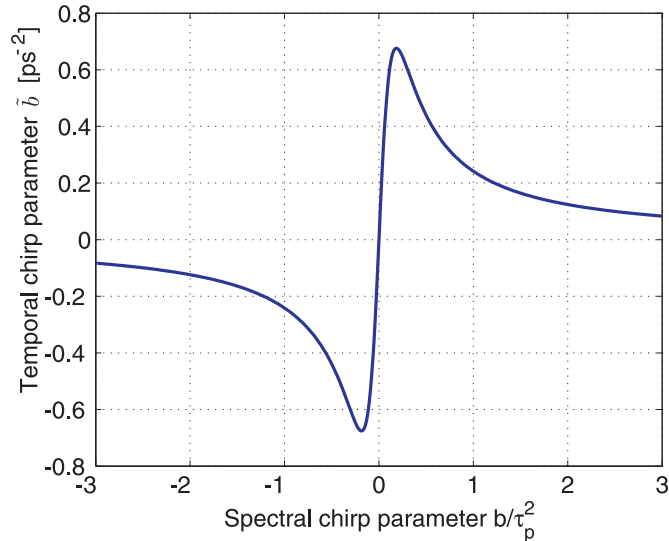


Figure 7.7: Relationship between the temporal chirp parameter \tilde{b} and the spectral chirp parameter b . Increasing the spectral chirp beyond $|b| > 0.18 \tau_p^2$ weakens the instantaneous frequency dependence on time as the pulse spreads in time.

7.5.2.4 Summary of phase effects

Summarizing the effects of the first three terms of Eqn. 7.13 on a pulse in the time domain, the zero-order phase $\phi = \phi_0$ provides an overall phase shift, resulting in a change of the carrier-envelope phase. Linear phase $\phi = a\omega$ causes a pure temporal shift of the pulse. Quadratic phase, or chirp parameter $\phi = b\omega^2$, is the lowest-order spectral phase that affects the temporal intensity shape of a pulse.

In general, higher order spectral phase contributions have more complicated effects on the temporal pulse intensity, but generally lead to a broadening of the pulse in time. The random-phase masks, which we will introduce at the end of this chapter, contain many higher-order phase contributions in the spectral phase, leading to a nontrivial temporal pulse shape.

7.6 Alignment of the pulse shaper apparatus

Using the described SLM in the reflective $4f$ geometry with the chosen grating spacing ($d = 833$ nm), focal length ($f = 50$ cm), and input beam waist ($w_i = 10$ mm), we proceed

to align the shaper apparatus according to a procedure outlined in [9]. The pulse shaper apparatus is aligned to optimize the spectral resolution, to minimize spectral dependence on the spatial beam profile (known as ‘spatial chirp’), and to minimize the spectral chirp ($\phi = b\omega^2$).

The reflective geometry of the pulse shaper (Fig. 7.2) presents a potential tradeoff between optimal alignment and efficiency. The optimal alignment would involve placing a beam splitter in the path of the input beam so that the reflected beam traces exactly the input path. This setup would result in a 75 % loss in power using a 50:50 beam-splitter. The loss in power would make the experiment difficult since we need a high optical power to achieve saturation of the QW system.

We find that the vertical-pointing pick-off geometry as described in §7.3.2 does not hinder the alignment significantly. We calculate from the cross-correlation FWHM of 388 fs that the pulse width out of the pulse shaper is $\Delta\tau = 274$ fs. Combining this measurement with a measured 4 nm bandwidth FWHM ($= 1.18 \times 10^{13}$ rad/s), we use Eqn. 7.12 to calculate the time-bandwidth product as $c_B = 0.51$. This value is close to the transform limit $c_B = 0.441$ for a Gaussian pulse. The temporal pulse duration for a transform limited Gaussian pulse would be $\Delta\tau = 241$ fs. The pulse coming out of the laser has only approximately a Gaussian temporal envelope, so it is not surprising that the time-bandwidth product does not exactly correspond to a Gaussian function.

7.6.1 Spatial mode filtering

The analysis in §7.4 assumes that the output Gaussian spatial mode is selected to match the input mode. Filtering the spatial mode helps to ensure that this is experimentally the case.

The spatial mode out of the mode-locked laser in our experimental setup is a transverse electromagnetic $TEM_{0,0}$ mode with a Gaussian spatial intensity profile. This mode is sent into the pulse shaper apparatus. In the process of applying a spectral phase mask to the

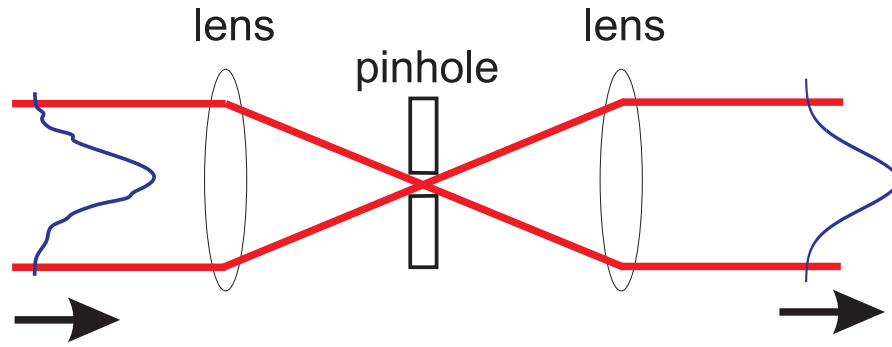


Figure 7.8: Spatial mode filtering using two lenses with a pinhole. The input distorted spatial mode is ‘cleaned up’ into a $\text{TEM}_{0,0}$ spatial mode by focusing the light through the pinhole.

pulse, higher order spatial modes are introduced, necessitating the filtering of modes higher than the $\text{TEM}_{0,0}$ mode.

Mode filtering is accomplished by constructing a spatial mode filter from two lenses and a small pinhole aperture, as shown in Fig. 7.8. The principle of spatial mode filtering is that the $\text{TEM}_{0,0}$ Hermite-Gaussian spatial mode focuses to a smaller spot size than the higher order modes [92]. Consequently, the higher order modes are mostly blocked by the aperture.

To determine the initial beam waist size w_i , focal lengths f , and pinhole diameter D appropriate for filtering out the $\text{TEM}_{0,0}$ mode and maintaining high efficiency, we consider the focusing properties of the Hermite-Gaussian modes. The spatial profile of the electric field of a Gaussian mode is the solution to the wave equation in the paraxial approximation [92]:

$$E(x, y, z) = E_0 H_m \left[\frac{2^{1/2}x}{w(z)} \right] H_p \left[\frac{2^{1/2}y}{w(z)} \right] \frac{w_0}{w(z)} \exp \left[-\frac{x^2 + y^2}{w^2(z)} \right], \quad (7.20)$$

where the beam waist

$$w(z) = \sqrt{w_0^2 \left[1 + \left(\frac{z}{z_0} \right)^2 \right]}, \quad (7.21)$$

w_0 is the minimal spot size for the $\text{TEM}_{0,0}$ mode, E_0 is the electric field amplitude, and H_m is the Hermite polynomial of order m .

We evaluate the electric fields for a variety of $\text{TEM}_{m,0}$ modes and integrate the in-

tensities at their foci over the pinhole diameter D in order to determine the efficiency with which each Hermite-Gaussian mode passes through the pinhole. Results for a sample of pinhole diameters and $\text{TEM}_{0,0}$ spot sizes are plotted in Fig. 7.9. From the pinhole diameters commercially available, we chose the $D = 20 \mu\text{m}$ with a $\text{TEM}_{0,0}$ spot size $w_0 = 10 \mu\text{m}$ because this combination offers high efficiency of the $\text{TEM}_{0,0}$ with reasonable suppression of the higher-order modes. The chosen spot size corresponds to a focal length choice of $f = 5$ cm for the spatial mode filter apparatus.

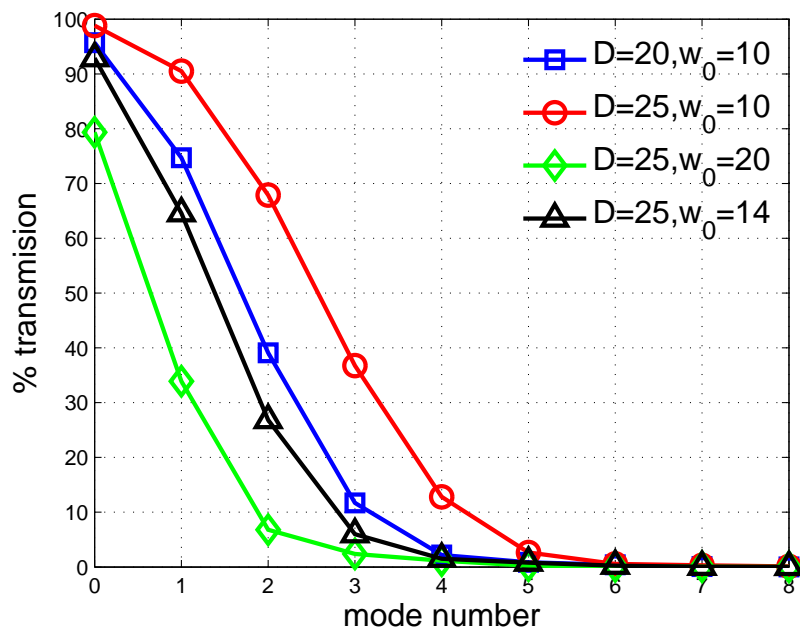


Figure 7.9: Transmission of the Hermite-Gaussian modes $\text{TEM}_{m,0}$ through a spatial mode filter. A series of diameters D and $\text{TEM}_{0,0}$ spot sizes w_0 (both in μm) allow choice of appropriate mode-filtering geometry.

7.7 Calibration and testing of phase masks

7.7.1 Calibration procedure

After alignment of the shaper, we calibrate the phase masks to have the accurate control of the spectral phase. To calibrate the SLM, we take advantage of the fact that phase discontinuities produce a dip in the spectrum, as discussed in §7.4. The procedure for

calibration of the SLM is illustrated in Fig. 7.10. For a variety of phase masks with a single phase discontinuity, we record the spectra on a monochrometer and note the pixel number at which the discontinuity happens. The spectral positions are then plotted with the pixel number, and a linear fit determines the relationship between photon energy and pixel number on the SLM. From the linear fit we find the relationship $Y[\text{meV}] = 0.00463 X[\text{pixel \#}] + 1499.74$.

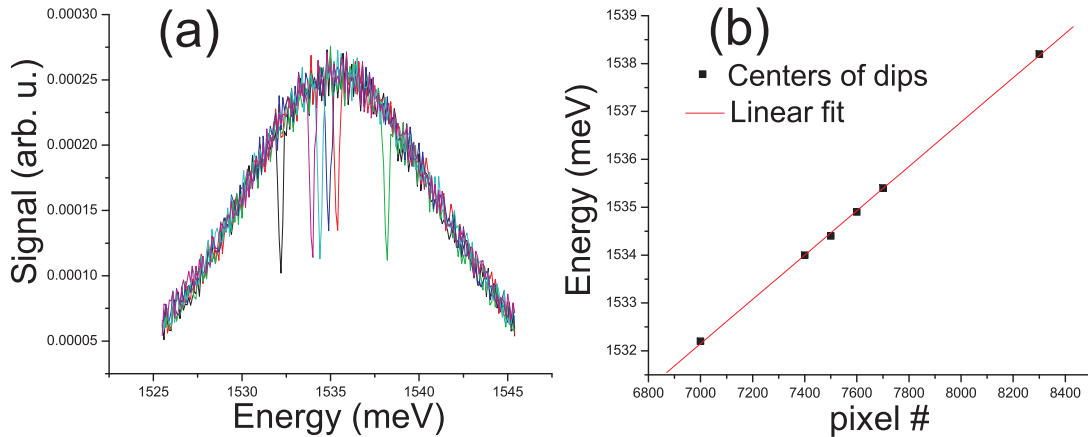


Figure 7.10: (a) A variety of power spectra, each with a single phase discontinuity that results in a dip in the spectrum. (b) The center positions of the dips along with the recorded pixel number on the SLM allow calibration of the SLM via a linear fitting procedure.

7.7.2 Comparison of simulation with experiment

To test the accuracy of the effects of the spectral phase masks in our experimental setup, we perform simulations using Eqns. 7.6 and 7.5 to compare with the measured effects of some simple phase masks. We explore the modulation of the linear and quadratic spectral phase.

To test that the SLM is calibrated, we compare simulations to experimental measurements for a variety of simple phase masks. For the simulations, we choose a transform-limited pulse with the same power spectrum as measured in the experiment. Experimentally, we measure the output pulses after the pulse shaper apparatus by measuring a cross-correlation trace, $S(\tau)$. The measurement technique is explained in chapter 3. We extract parameters

such as temporal center positions and widths from $S(\tau)$ using a nonlinear fitting procedure that fits a Gaussian function to each trace.

As demonstration of our control over the spectral phase, we create phase masks with only linear phase, and only quadratic phase, in order to observe the effects of each phase component in Eqn. 7.13 individually.

A linear phase $\phi = \phi'(\omega_0)(\omega - \omega_0)$ is applied to the SLM for a range of slopes from $\phi'(\omega_0) = 0 \text{ meV}^{-1}$ up to $\phi'(\omega_0) = 18.2 \text{ meV}^{-1}$. We expect the temporal pulse to be shifted in time according to Eqn. 7.15. A simulation of the output pulse yields a pure shifting of the pulse. The predicted shifts in time compare well with the experimentally measured time shifts, as shown in Fig. 7.11.

Similar matching between simulation and experiment is achieved for negative linear slopes in spectral phase, which results in negative temporal shifts of the pulse, or effectively lengthening the optical path length which the pulse travels.

We attribute slight discrepancies between the measured and simulated shifts to the imperfect factory calibration of the SLM for the voltage to phase retardance at a wavelength of 800 nm.

In addition, simulation predicts the broadening of a pulse with the application of quadratic spectral phase. The chirp parameter $\phi''(\omega_0)/2$ in Eqn. 7.13 is varied from 0 meV^{-2} up to 5.8 meV^{-2} . We expect that the quadratic phase leads to a broadening in the temporal pulse duration without shifting the pulse in time, according to Eqn. 7.19. We extract the time duration of the experimentally measured cross-correlation. We find good comparison between the experiment and simulation, as shown in Fig. 7.12. The pulse duration levels off for higher chirp parameters because the maximal time duration is limited by the spectral resolution of the pulse shaper, as discussed in §7.5.1. The observed cross-correlation duration limit of $\Delta\tau_S = 10.8 \text{ ps}$ (corresponding to a pulse duration of 10.8 ps since $\Delta\tau_{\text{probe}} \ll \Delta\tau_S$ in Eqn. 3.15) is roughly consistent with the estimated maximum temporal width of 8.8 ps, calculated in §7.5.1. We attribute the slight discrepancies between

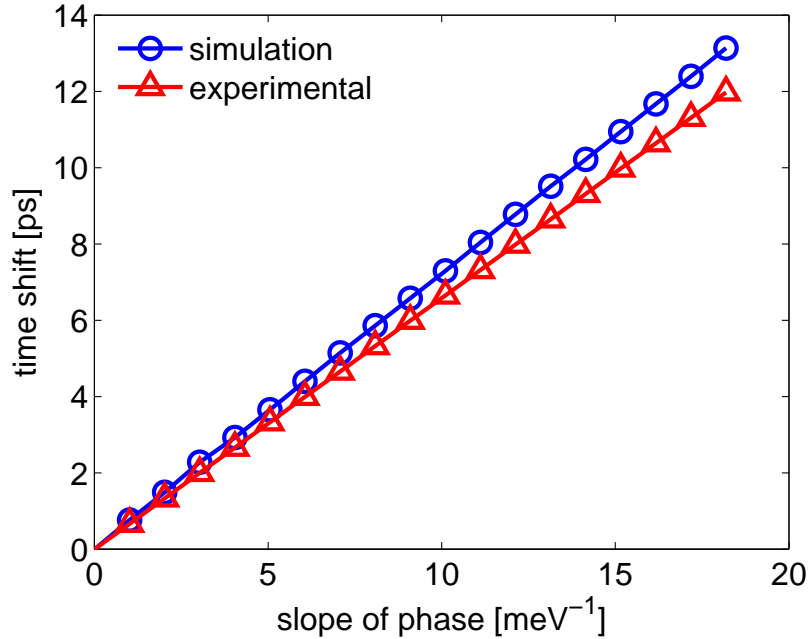


Figure 7.11: Simulated and measured time shifts generated by a linear phase mask.

simulation and experiment to imperfect factory calibration of the SLM. The discrepancies compared with the simulation are not critical because we record the experimental parameters in the analysis of the experiments.

Similar agreement between simulation and experiment is found for negative chirp parameters. The sign of the quadratic phase has no effect on the temporal intensity profile (in both simulation and experiment), as predicted from Eqn. 7.19.

7.8 Comparison of chirp parameter range with material dispersion

One relevant inquiry is how the chirp that we impose on an ultrashort pulse compares to the amount of quadratic phase that is incurred when a pulse travels through dispersive media. The sign of chirp for most dispersive media is positive, which means that the red part of the pulse experiences negative delay relative to the blue part, as can be seen in Eqn. 7.18. Thus, the red part of the spectrum arrives before the blue part of the spectrum for most dispersive materials.

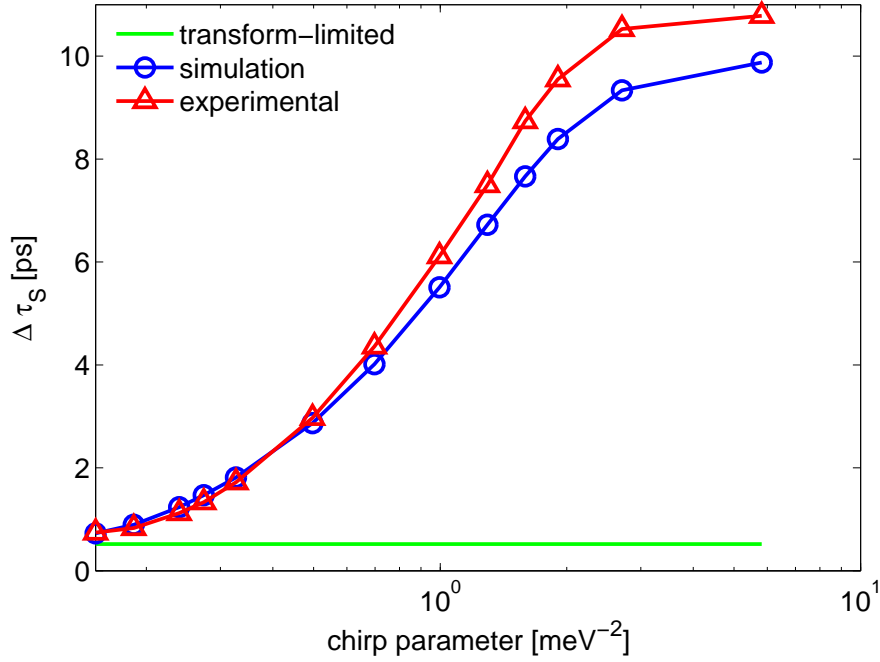


Figure 7.12: Simulated and experimentally measured cross-correlation widths $\Delta\tau_S$ for a range of chirp parameters. Cross-correlation width of $\Delta\tau_S = 520$ fs for a transform-limited pulse is shown as a baseline.

We compare the range of applied chirp using the pulse shaper to the material dispersion for a common optical material, fused silica. We calculate the second-order dispersion of fused silica at 800 nm using the Sellmeier equation to be $\psi''(\omega_0)/2 = 0.262$ meV⁻²/meter. The chirp from dispersion is then given by $\phi''(\omega_0)/2 = \psi''(\omega_0)/2 \times L$, where L is the length traveled through the material [117]. Using this value, we find that a distance of $L = 29$ cm would be necessary to achieve 0.15 meV⁻² of chirp, and a distance of $L = 11$ m would be necessary to achieve 5.8 meV⁻² of chirp. The amount of material that the laser light travels through for the work in this thesis is on the order of a couple cm. Consequently, the amount of material used produces chirp much lower than an amount that would broaden the pulses significantly for pulses of spectral width around $\Delta\omega = 8$ meV FWHM.

7.9 Arbitrary pulse shape generation

We have demonstrated the ability to control the linear and quadratic phase of an ultrashort pulse. However, we desire to use the pulse shaper to study the effects of other pulse shapes, and especially to realize the criteria for density-matrix ensemble averaging, as discussed in §6.2.

As a proof of principle, we apply a randomized phase mask to a pulse spectrum (which in this case is not spectrally narrowed) with large energy bin spacing $\Delta\Omega_{EBS} = 4.4$ meV. The original spectrum is modified at the locations of phase discontinuity, as shown in Fig. 7.13. While the agreement is not perfect (perhaps because of factory calibration error of the SLM), the features of the width, location, and depth of the spectral dips are roughly matched. The largest dip occurs at $E - E_{1s} = 0$ meV, where there is a phase discontinuity of 0.82π , consistent with the arguments presented in §7.4. The phase discontinuity at $E - E_{1s} = 8.8$ meV, while large in appearance, is actually a small phase jump because the phase ‘wraps around’ between 2π and 0. Thus, the phase jump at this location is only 0.23π and corresponds to a smaller fractional dip in the spectrum.

7.10 Prepared for density-matrix ensemble averaging

We conclude that we are able to create a large variety of pulses with almost arbitrary phase modulation. We note the physical limitation of the dips in the spectrum at places of phase discontinuity on the SLM. However, this does not present a problem for the experiments since we monitor the created carrier density in the QW system (discussed in §3.3.4), and can correct for the amplitude modulation. We proceed in the next chapter to explain the experiments that realize the density-matrix ensemble averaging scheme using the pulse shaper apparatus.

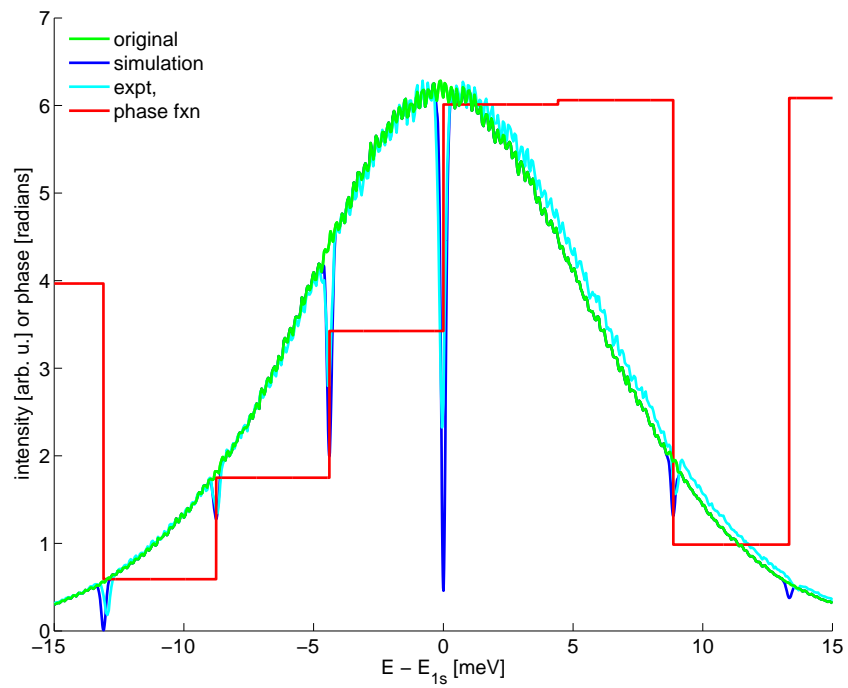


Figure 7.13: Comparison of simulation and experiment for a randomized phase mask function applied to a pulse spectrum.

Chapter 8

Phase-randomized pulse experiments

The last few chapters explained the motivations and techniques for using phase-randomized pulses of light to learn about the response of the GaAs quantum-well (QW) system under incoherent excitation conditions. We refer to the phase-randomized pulses as ‘scrambled’ pulses. The scrambled pulses excite the sample, which is then inquired by a transform-limited weak probe pulse.

We present the procedure for characterizing the statistics of scrambled pulses using density-matrix ensemble averaging. We then describe simulations performed using the optical Bloch equations (OBEs) to qualitatively predict the effects of single realizations. We describe the experimental methods used to measure the nonlinear response of the QW system under scrambled-pulse excitation, and then present the results of the measurements.

8.1 Characterization of average statistics

We seek to produce an ensemble of pulses that have the statistical properties of thermal light, in contrast to the properties of coherent light. We demonstrate in this section the techniques for characterizing the ensemble averages for the scrambled pulses, and discuss the limitations in the measurements.

To perform experiments with the scrambled realizations, we prepare a group of randomized phase masks. A set of N_{real} phase masks is created with random phases for each frequency bin $\Delta\omega_{\text{bin}}$ using a pseudo-random number generator. Before using these pulses

to perform transient absorption measurements, we analyze time-domain statistics to ensure that the statistics of the ensemble corresponds to a thermal source.

We characterize the statistics of the set of pulse realizations through time domain measurements. Typical cross-correlation traces for the scrambled realizations compared with the transform-limited (flat mask) case are shown in Fig. 8.1. We observe that the pulses are stretched out in time, and that the intensity at any given delay τ fluctuates between realizations. We specifically seek the second-order coherence function $g^{(2)}$, which is obtained through measurement of the photon probability distribution. This function can be calculated by constructing the probability distribution function from a collection of cross-correlation traces.

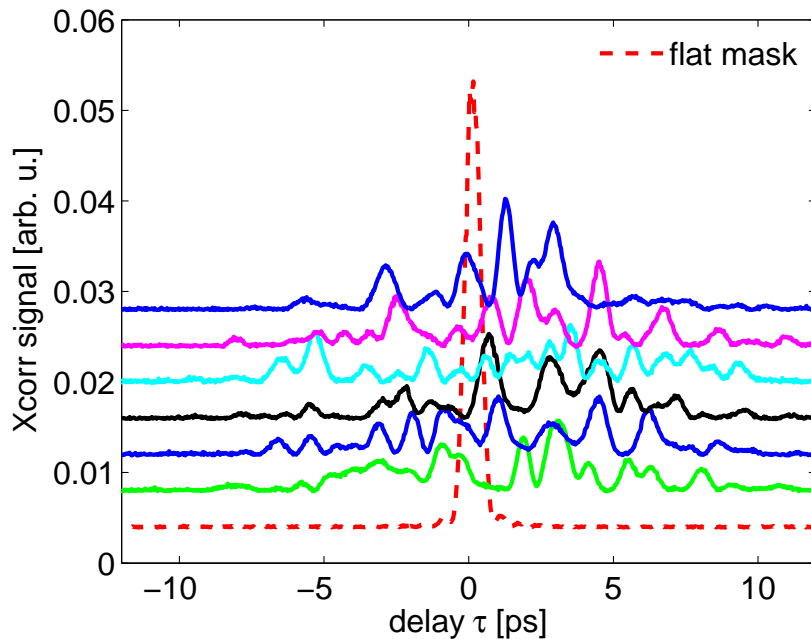


Figure 8.1: Cross-correlation traces for six different scrambled realizations. All traces are normalized so that the area is unity. For comparison, the normalized transform-limited pulse (flat spectral phase mask) is shown as a dashed red line.

The photon number distribution P_m , discussed in §5.2.4, defines the probability of measuring m photons in a time window T shorter than the coherence time of the light source. The probability distribution has a one-to-one correspondence with the k^{th} -order

coherence function value [119, 102]:

$$g^{(k)} = \langle \hat{n}^k \rangle / \langle \hat{n} \rangle^k = \frac{1}{\langle \hat{n} \rangle^k} \sum_{m=k}^{N_{\text{ph}}} \frac{m!}{(m-k)!} P_m, \quad (8.1)$$

where N_{ph} is the maximum number of photons that is measured in a particular time window T and $\langle \hat{n} \rangle = \bar{n}$ is the average number of photons per pulse. We are most interested in the second-order coherence function because this distinguishes coherent statistics from thermal statistics. The second-order coherence function value is found by setting $k = 2$ in Eqn. 8.1:

$$g^{(2)} = \langle \hat{n}^2 \rangle / \langle \hat{n} \rangle^2 = \frac{1}{\langle \hat{n} \rangle^2} \sum_{m=k}^{N_{\text{ph}}} m(m-1) P_m. \quad (8.2)$$

To calculate statistics for our ensemble, we obtain the probability distribution P_m by measuring the intensity profile for a large number of pulse realizations. The temporal intensity profile of a single pulse realization can be approximated by a cross-correlation measurement with the short-duration probe pulse, as explained in §3.5. We measure the cross-correlations for 500 different pulse realizations. We histogram the intensity distribution at a fixed delay for the many realizations. This histogram represents the intensity probability distribution and is proportional to P_m . From the intensity probability distribution, we calculate the coherence functions according to Eqn. 8.1 for the ensemble of $N_{\text{real}} = 500$ realizations of scrambled pulses.

We measure the cross-correlations for $N_{\text{real}} = 500$ different pulse realizations. The cross-correlation traces are averaged according to:

$$S_{\text{avg}}(\tau) = \frac{1}{N_{\text{real}}} \sum_{r=1}^{N_{\text{real}}} S_r(\tau), \quad (8.3)$$

where $S_r(\tau)$ is the normalized cross-correlation trace for the r^{th} realization. Each trace is normalized to have the same number of photons per realization. This simulation does not take into account the more complicated nature of the differences in the fractional absorption by the QWs between realizations. However, the difference in fractional absorption between pulse realizations with the same number of photons is typically on the order of 5%. Thus,

normalization of the cross-correlation traces is a reasonable approximation for our purpose of determining the statistics of the ensemble of pulse realizations.

We select a particular delay τ' and record the value $S_r(\tau')$ for each realization r . The results are then histogrammed, creating a photon number probability distribution function P_m . The distribution function can then be translated into a second-order coherence value $g^{(2)}$ by Eqn. 8.2. We compare the $g^{(2)}$ for different bin spacings to quantify the statistics compared with thermal statistics where $g^{(2)} = 2$.

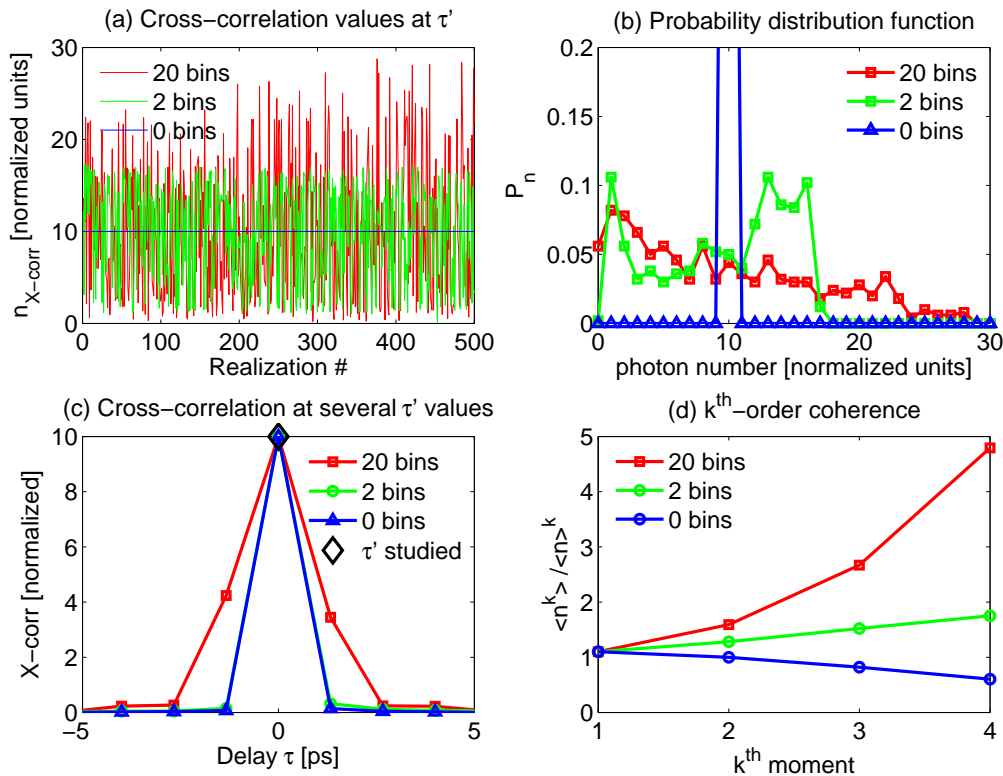


Figure 8.2: (a) Cross-correlation values at time delay $\tau' = 0$. (b) Probability distribution function for the normalized cross-correlation values. (c) Cross-correlation values for several τ values. (d) m^{th} -order coherence values calculated by Eqn. 8.2.

We plot some typical results for varied frequency bin spacing $\Delta\omega_{\text{bin}}$ in Fig. 8.2. We compare frequency bin spacings of $\Delta\omega_{\text{bin}} = 0.3$ meV, $\Delta\omega_{\text{bin}} = 3.0$ meV, and a flat phase mask case. The flat mask case is equivalent to a bin spacing of $\Delta\omega_{\text{bin}} \rightarrow \infty$. The three cases correspond to 20 bins, 2 bins, and 0 bins across the $\Delta\omega = 6$ meV spectrum. We choose the

delay $\tau' = 0$ for comparing these three cases. In Fig. 8.2a we notice that the 20-bins case has the largest intensity fluctuations at $\tau' = 0$ compared to the other two cases, whereas the 0-bin case has uniform intensity at $\tau' = 0$.

To collect statistics on each sequence of realizations, we perform a normalization procedure. The total intensity measured from each cross-correlation is normalized, as it is also in the transient absorption experiment, where we adjust the energy of each realization to be the same. The total set of cross-correlations is divided by a constant so that the average number of photons at $\tau' = 0$ is normalized to $\bar{n}(\tau' = 0) = 10$. This second normalization is performed for simplicity in the analysis and does not change the comparative result between data sets.

The limitation in the accuracy of these measurements is from the number of realizations for which we record traces. Ideally, the number of measurements should approach ‘infinity’ to have the most accurate measurements. However, we record only 500 traces because this measurement already requires many hours. Having a finite number of realizations means that the histogram bins must be chosen to be large enough to count multiple values in each bin, but small enough so that the photon number distribution can be observed with some resolution. A bin size spacing of 10% of the total intensity combined with the normalization procedure described earlier satisfies these two criteria. To determine the trend in accuracy as we increase the number of measurements, we calculate $g^{(2)}$ for a variable number of traces and use a nonlinear fitting procedure to fit the exponentially asymptotic function

$$\tilde{g}(N_{\text{real}}) = a_1 + a_2 (1 - e^{-a_3 N_{\text{real}}}), \quad (8.4)$$

where a_i are constants determined by the fitting procedure. The measured $g^{(2)}$ values are shown in Fig. 8.3 along with the fit and the asymptote of the fit. The fitting procedure neglects measurements for $N_{\text{real}} < 50$ because it is clear from Fig. 8.3 that these points are noisy because of the small sample size. We consider the asymptote value $\lim_{N \rightarrow \infty} \tilde{g}(N)$ to be the measured value of $g^{(2)}$ for an infinite number of measured realizations. This procedure

shows that for $N_{\text{real}} > 300$ we match $\lim_{N \rightarrow \infty} \tilde{g}(N)$ to within 7.3%.

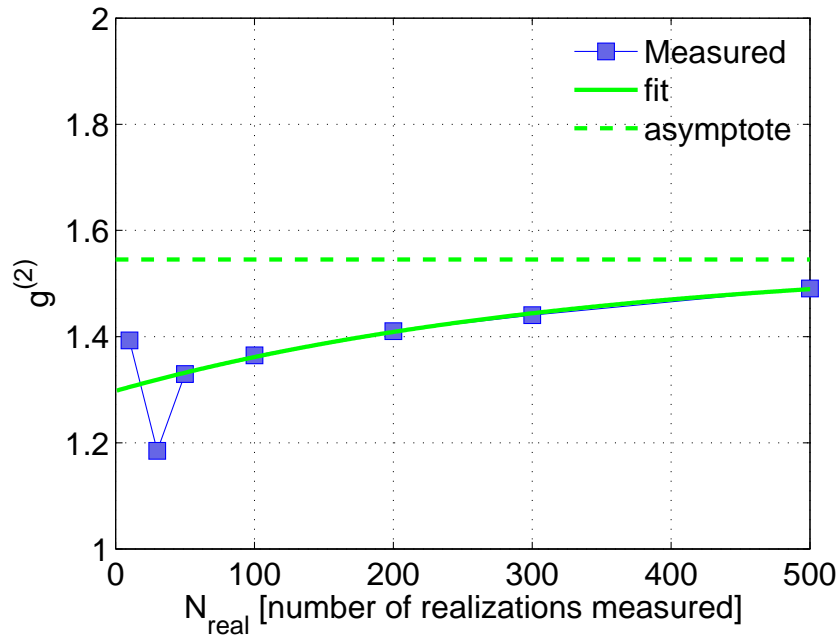


Figure 8.3: Convergence of the measured second-order coherence function values $g^{(2)}$ as the number of realizations is increased. The measured $g^{(2)}$ function (blue squares) is fit with an asymptotic function \tilde{g} (green line) to determine the error in $g^{(2)}$ measuring a finite number of realizations. Asymptote of \tilde{g} is shown for $\lim_{N \rightarrow \infty} \tilde{g}$. This example uses the data from $\Delta\omega_{\text{bin}} = 0.3$ meV, or the 20-bins case.

To interpret the results of the statistical study, it is necessary to consider the finite number of traces measured. A consequence of the finite number of measured traces is seen in the histogram in Fig. 8.2b. The probability distribution function for the 0-bin case (coherent light) peaks to a probability of 1 at $n = 10$ photons. However, a glance back at Fig. 5.5 reminds us that coherent photon number statistics should follow a Poisson distribution with some finite width. Because of the limited number of measurements, it is necessary to choose the histogram width to be large enough that multiple values in each bin can be counted. The 2-bin case exhibits coherent behavior, with a peak around $n = 14$ (the peak at $n = 2$ is a consequence of chosen bin size). However, for the 20-bin case, the probability distribution function roughly decays exponentially, very similar to the thermal probability distribution curve in Fig. 5.5.

The cross-correlations that we measure are averaged in Fig. 8.2c. We notice that the width of the intensity profile increases as the number of bins increases. This fact is consistent with the analysis accompanying Fig. 7.5. The smaller the frequency feature δf in the frequency domain, the longer the pulse shape is in the time domain. Because the cross-correlation is shown here for only a few delays, it is difficult to see that the 2-bins case is longer in time duration than the 0-bin case. The cross-correlation width for the 0-bin case is $\Delta\tau_S = 520$ fs, as reported in §3.5. The cross-correlation width for the 2-bin case is closer to $\Delta\tau_S = 3$ ps. In fact, since the spectral feature $\delta f \propto 1/N_{\text{bins}}$, the time duration of the pulses is estimated to scale roughly as [115]:

$$\Delta\tau(N_{\text{bins}}) \approx N_{\text{bins}} \Delta\tau_0, \quad (8.5)$$

where the width of the cross-correlation $\Delta\tau_0 = 520$ fs for $N_{\text{bins}} = 0$. As a reality check of this estimate, the averaged temporal width $\Delta\tau_{S_{\text{avg}}}(20) = 4.5$ ps $= 8.7 \Delta\tau_0$ for the average cross-correlation for the 20-bin case. The estimate in Eqn. 8.5 is reasonable considering that the width of $S_{\text{avg}}(\tau)$ is an approximation of the temporal extent of the average sequence of pulses. The extended time duration of the pulses is relevant to interpretation of measurements in the QWs. However, the feature that we are as interested in for this statistical analysis is the ensemble-averaged coherence value.

It is possible to see a clear difference in the measured k^{th} -order coherence value $g^{(k)}$ for the different bin spacings. We show in Fig. 8.2d that the first-order correlation function is independent of bin spacing. The higher-order correlation functions diverge as k increases. We primarily care about second-order coherence function values. The $g^{(2)}$ values in Fig. 8.2d are plotted in Fig. 8.4 with measured values from several other bin sizes. In all cases $N_{\text{real}} = 500$ realizations were measured to calculate $g^{(2)}$. We find that the second-order coherence function value increases as we increase the number of bins across the spectrum, consistent with Eqn. 6.17. Note that inconsistencies with the theory here are both because of the finite number of measurements and the fact that the theory is valid only for $N_{\text{bins}} \gg 2$.

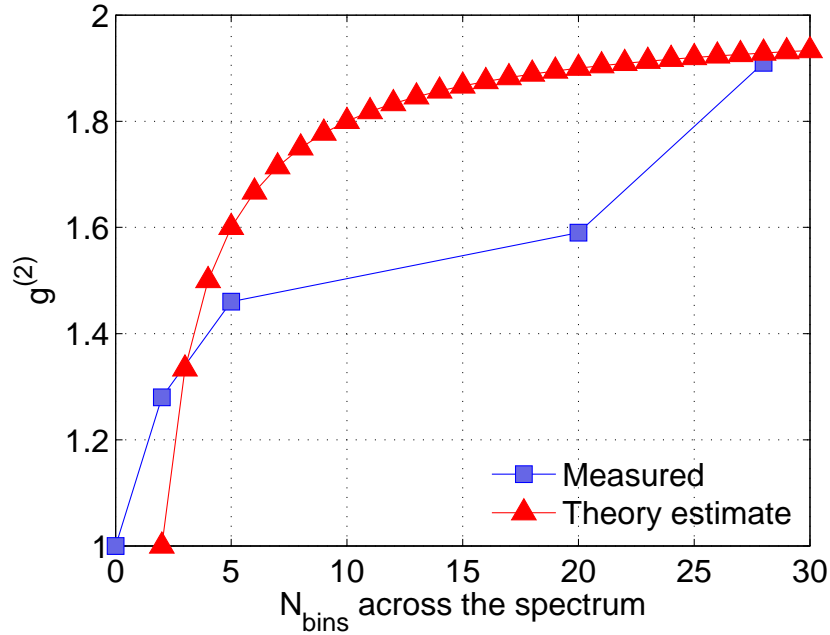


Figure 8.4: Measured second-order coherence function values for several different bin spacings. Measured values correspond to the trend predicted in Eqn. 6.17.

We have characterized the statistical properties for an ensemble of pulses for different bin spacings and have found that indeed the photon statistics are closer to thermal light than coherent in the limit of a large number of bins across the laser spectrum, as predicted by the Kira-Koch theory [115].

Another prediction from the DME averaging scheme is that the average of the scrambled pump spectra $S_{\text{avg}}^{\text{scram}}(\omega) = \frac{1}{N_{\text{ens}}} \sum_r^{N_{\text{ens}}} S_r^{\text{scram}}(\omega)$ should limit to the transform-limited spectrum $S^{\text{flat}}(\omega)$ (with a flat spectral phase mask). As a test of this, we successively average the spectra of an increasing number of realizations to confirm that the spectra of the scrambled realizations converge to the transform-limited spectrum. We illustrate the convergence of the pump spectra in Fig 8.5. The standard error of the normalized spectra $\sigma^2 = \sum_i [S_{\text{avg}}^{\text{scram}}(\omega_i) - S^{\text{flat}}(\omega_i)]^2 < 10^{-6}$ for $N_{\text{ens}} > 50$ realizations.

Considering that a single realization is a collection of multiple temporal modes, as illustrated in Fig. 8.1, we investigate the possibility that a single scrambled realization may

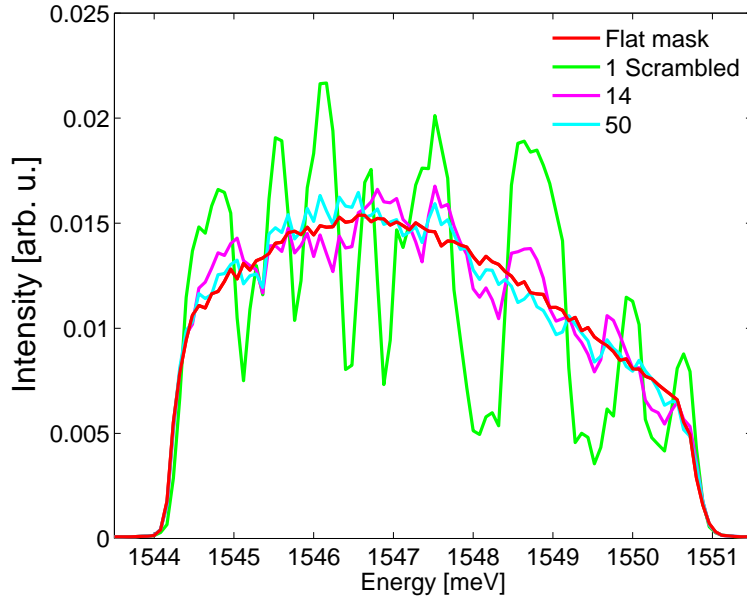


Figure 8.5: The average scrambled pump spectrum (shown for $N_{\text{ens}} = 1, 14, 50$) converges to the flat mask spectrum as the number of realizations N_{ens} is increased.

produce some of the predicted effects. We simulate single scrambled realizations in a simple model to gain insight about the effects of phase randomization.

8.2 Qualitative predictions using the optical Bloch equations

Each scrambled realization contains a small ensemble of pulses with varied peak intensity, temporal phase, and relative time delay to the other pulses in the realization. These three variables are selected from a distribution determined by the spectral phase bin size. It is thus reasonable to inquire whether a single scrambled realization might have an effect on the many-body interactions in the QW system when compared with a coherent light pulse that creates the same electron-hole carrier density.

To estimate qualitative effects of using scrambled realizations, we perform a simulation using the optical Bloch equations (OBEs), discussed in §2.6. We also compare the results with other pulse shapes to predict how temporal pulse duration affects system dynamics. The pulse-shaper simulation discussed in Chapter 7 allows generation of the electric field in the

time domain. The temporal intensity waveforms from these electric fields agree with cross-correlation measurements. Based on the matching between measurement and simulation, we use the generated electric fields as an input to the optical Bloch equations simulation. Even though this simulation does not include many-body interactions, we expect that conditions giving rise to a lower polarization for the same generated carrier population should give rise to anomalous reduction in scattering and other effects, as discussed in §5.4.

We assume in our simulation that the electric field gives rise to excited carrier populations and off-diagonal density matrix elements according to the OBEs (Eqn. 2.30). We attempt to see the qualitative effects of different temporal waveforms on the dynamics. This simulation has nothing to do with the photon statistics. It is a semi-classical approach to understanding two-level system dynamics.

For the model, a population decay time of $T_1 = 1/\gamma_{ee} = 10$ ps and a dephasing time of $T_2 = 1/\gamma_{eg} = 1$ ps are chosen. The dynamics of $\rho_{ee} - \rho_{gg}$ and ρ_{eg} are simulated, corresponding to the population and polarization, respectively. As an indicator of how much polarization is generated for a given population, we record the maximal ratio of the population to the polarization. We take the ratios of each absolute-value quantity squared so that we have a magnitude (instead of a complex value) for comparison between different pulse realizations.

An example of the dynamics for a transform-limited pulse excitation as simulated by the OBEs is shown in 8.6. The excitation pulse drives the population inversion and polarization terms in Eqn. 2.30. The population inversion $\rho_{ee} - \rho_{gg} = 2\rho_{ee} - 1$ ranges between -1 and 1, corresponding to full population in the ground state and the excited state, respectively. The term ρ_{eg} is proportional to the macroscopic polarization, as discussed in §2.6. Both terms are presented in absolute value squared to simplify the complex quantities. This simulation can also reveal qualitative understanding of the dynamics for more complicated waveforms.

To apply the OBEs to different temporal intensity waveforms, we start with the spectrum in Fig 3.4, and use our pulse-shaping simulation (described in §7.7.2) to generate three sets of complex electric field envelopes $\varepsilon(t)$. The generated fields drive the OBEs, and the

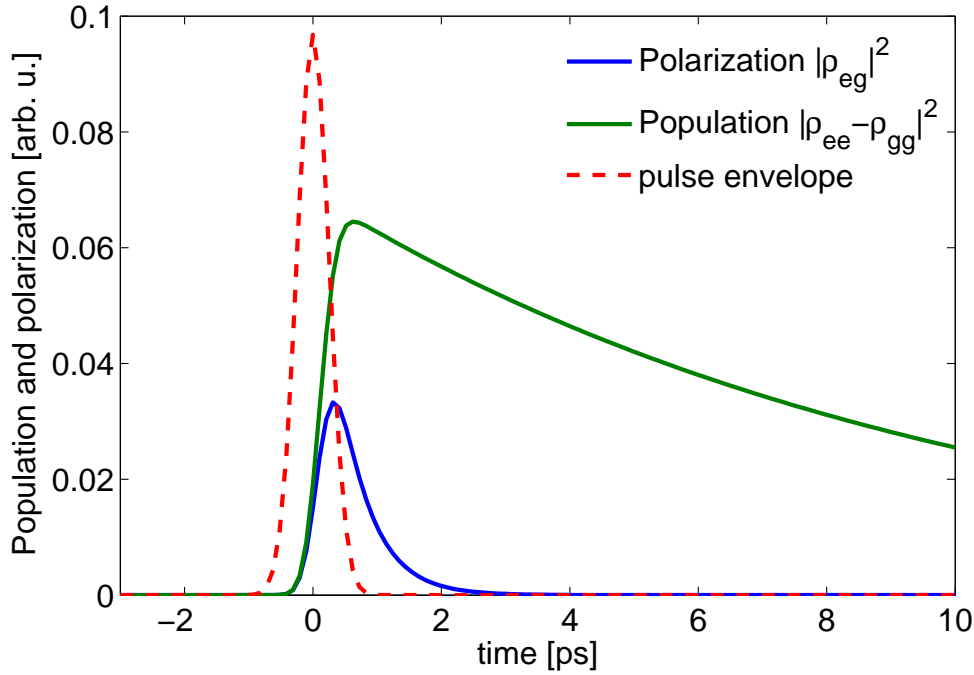


Figure 8.6: Simulation using the optical Bloch equations (Eqn. 2.30) of the optical excitation of a two-level system including phenomenological decay terms. The population term is offset such that 0 means population is completely in the ground state.

results from the realizations are compared.

In one case, the spectrum of the pulse is narrowed, yielding a longer pulse duration in the time domain. In another case, two pulses are chosen to be a variable time delay apart from each other. We compare both of these cases to the scrambled pulses, where we apply a random phase mask with varying energy bin spacing $\Delta\omega_{\text{bin}}$. The smaller the bin spacing, the longer the duration of the pulse sequence (illustrated in Fig. 7.5). In all three cases, the temporal duration is varied over a range from 0.5 ps up to 100 ps. The maximal population-to-polarization ratio $|\rho_{ee} - \rho_{gg}|^2 / |\rho_{gg}|^2$ is recorded for each realization. We choose this observable because we are interested finding trends concerning which waveforms give rise to a low polarization for a fixed population.

To compare the results for the three separate cases, we quantify the temporal extent

of each realization by the second moment:

$$\langle t^2 \rangle = \frac{\int_{-\infty}^{\infty} t^2 \varepsilon^*(t) \varepsilon(t) dt}{\int_{-\infty}^{\infty} \varepsilon^*(t) \varepsilon(t) dt}. \quad (8.6)$$

The second moment quantifies the temporal duration, allowing a rough comparison between the results for the different realizations.

The maximal population-to-polarization ratio is plotted in Fig. 8.7 as a function of the temporal duration of each realization. At short durations the three cases exhibit similar behavior. However, for longer temporal durations, we see that the ratio is maximized for the spectrum-narrowing case. This result is closely matched by the two-pulse configuration. The randomized-phase realizations follow a trend similar to the other two cases, but the ratio appears to flatten out for long temporal durations. The error bars at each point show the standard deviation from five simulations of different scrambled realizations with the same energy bin spacing $\Delta\omega_{\text{bin}}$.

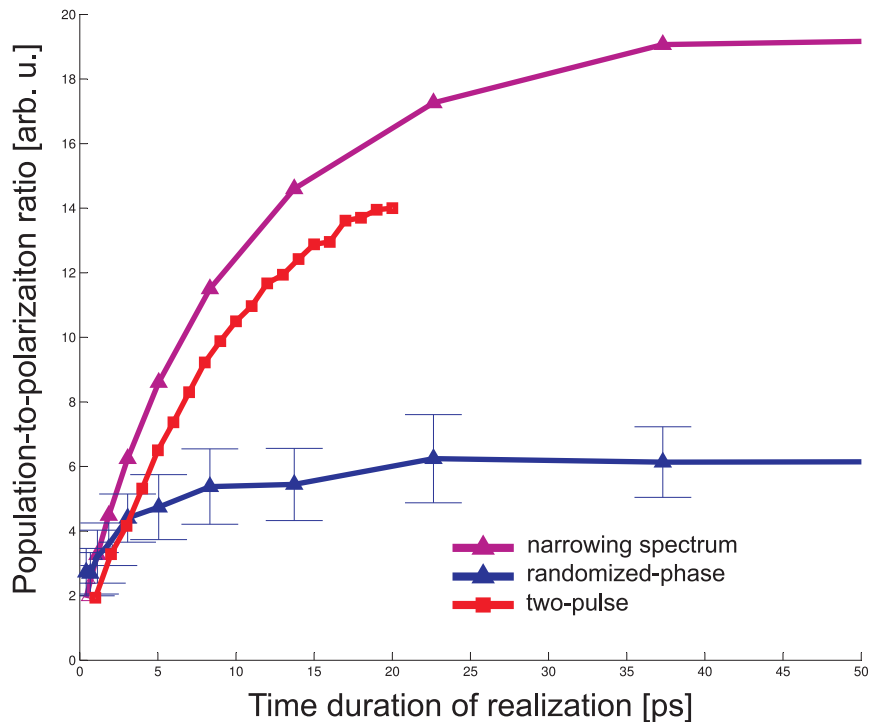


Figure 8.7: Population-to-polarization ratios for three cases where the temporal duration is systematically varied.

The simulations show that the population-to-polarization ratio increases with the temporal duration of a waveform, regardless of the type of realization. Since polarization scattering dominates the excitation-induced effects, as shown in Chapter 4, this simulation predicts that the excitation-induced effects should be weaker for longer duration pulses compared to the effects for a transform-limited pulse that create the same population. The weaker excitation-induced effects manifest in a less saturated HH 1s resonance absorption spectrum: a higher peak height, less blue shift, and a narrower linewidth. We now proceed to test the effects of the scrambled realizations in the QW system, and in the next chapter we explore the measured affects of different pulse shapes.

8.3 Experimental methods

We have verified that the ensemble of scrambled realizations corresponds to a thermal source, and simulation indicates that single scrambled realizations may show a difference to transform-limited excitation. A group of measurements is performed to quantify the QW response to scrambled realizations.

We perform spectrally resolved transient absorption measurements of the QW system after excitation by each scrambled realization. The procedure for transient absorption measurements is very similar to the methods described in Chapter 3. The modifications are as follows. Between each measurement, we change the phase mask on the spatial light modulator in the pulse shaper to modulate the spectral phase of the pump light source. The technique for spectral phase modulation is discussed in Chapter 7. Since the masks have discontinuities in the phase leading to unavoidable amplitude modulation of the pulse, the average power is slightly different for each scrambled realization.

We monitor the pump input power $P_{\text{IN}}^{\text{pump}}$ continuously as discussed in §3.3.4. We adjust the power of each phase mask realization so that $P_{\text{IN}}^{\text{pump}}$ is the same for all realizations. Additionally, the reflected and transmitted pump powers are measured continuously. These three calibrated measurements allow calculation of the pump power absorbed by the QW

system $P_{\text{QW}}^{\text{pump}}$ by Eqn. 3.13. We spectrally resolve the absorption $\alpha(\omega)$ of a probe pulse that arrives at the sample a delay τ after the pump pulse creates a many-body configuration. This delay must be chosen carefully since spectral phase modulation broadens out the pump pulse in time, as discussed in §7.5 and shown in Fig. 8.1. To simplify the interpretation of the results, we want to compare the effects of the scrambled realizations to that of transform-limited pulses in the incoherent regime, where the polarization has decayed. Consequently, the choice of a long probe delay $\tau = 27$ ps ensures that the polarization has decayed by the time the probe arrives at the sample.

We repeat the measurement for a matrix of phase masks and $P_{\text{IN}}^{\text{pump}}$ powers, including multiple measurements using the flat phase mask to ensure repeatability. From the spectrally resolved probe absorption response, parameters are extracted via our model-independent fitting procedure (§3.4) to allow comparison between different realizations.

8.4 Results of phase-randomized experiments

We present results from the measurements of the QW system response when excited with scrambled light. From each probe spectrum measured at one of the matrix of powers and phase mask realizations, we extract the peak height and the center resonance position. These observables relate information about how strongly the many-body configuration is saturating the exciton resonance. The peak heights and the center resonance positions are shown in Fig. 8.8. As a reminder of the results from Chapter 4, stronger nonlinearity means a lower peak height and a stronger blue shift of the center resonance position.

The peak height and center position both indicate that the scrambled realizations give rise to less saturation than the transform-limited pulse for similar powers absorbed by the QW ($P_{\text{QW}}^{\text{pump}}$). Fitting a line through the data for both the transform-limited pulse data and the scrambled data, we see that the differences in nonlinear effect become more noticeable as $P_{\text{QW}}^{\text{pump}}$ increases. The probe spectra converge at the lowest excitation densities, as expected for the probe spectra in the absence of any pump excitation. The same trends are observed

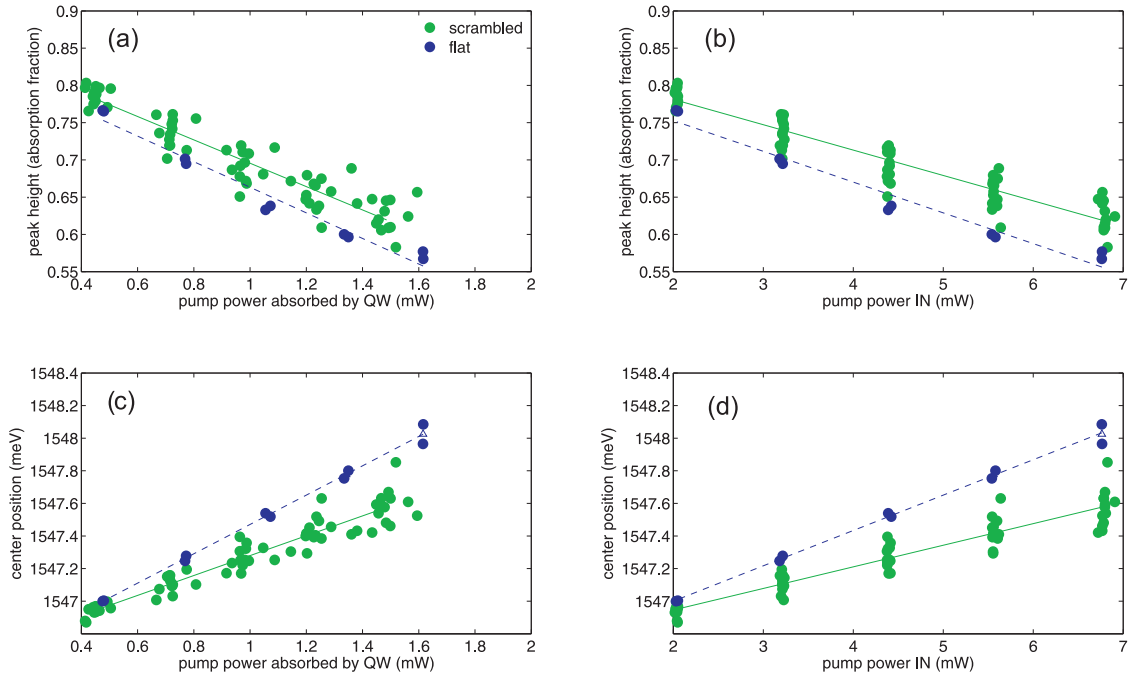


Figure 8.8: Nonlinear observables as a function of power. Peak heights of α_{QW} are shown for varying (a) $P_{\text{QW}}^{\text{pump}}$ and (b) $P_{\text{QW}}^{\text{pump}}$. Center resonance positions are shown for varying (c) $P_{\text{QW}}^{\text{pump}}$ and (d) $P_{\text{QW}}^{\text{pump}}$. Fits (solid lines) through each set of points clarify the trends for the observables.

as a function of the input excitation power $P_{\text{IN}}^{\text{pump}}$.

The results are consistent with the theoretical prediction (§5.4) that the scrambled realizations should produce weaker nonlinear effects compared with the transform-limited pulses for the same excitation densities in the QW. The probe absorption spectra are less saturated for the scrambled realizations compared with the transform-limited (coherent) case. The average absorption spectra, computed according to Eqn. 6.7, are shown in Fig. 8.9, along with the linear absorption spectrum. It is clear in this plot that not only do single scrambled realizations saturate the HH 1s-resonance less than transform-limited excitation for the same $P_{\text{IN}}^{\text{pump}}$, the average absorption spectrum is less saturated for scrambled light excitation than for transform-limited pulse excitation.

These data need confirmation from the theory to determine whether or not they are a true demonstration of quantum-optical spectroscopy. The confirmation will be accomplished through a theory technique known as cluster-expansion transformation, discussed in the

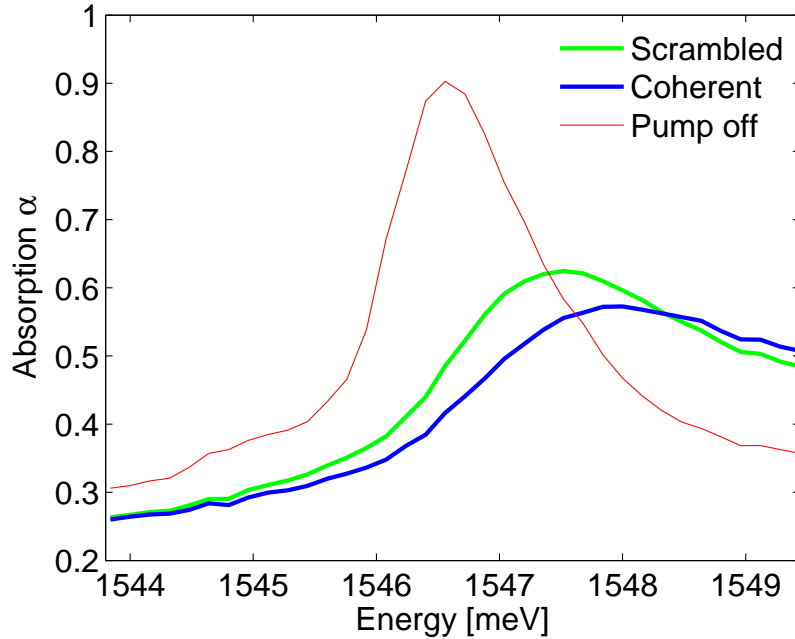


Figure 8.9: The average spectrum from the scrambled realizations saturates the HH $1s$ -resonance less than from coherent excitation with the same $P_{\text{IN}}^{\text{pump}}$. The spectra are shown with the linear absorption (pump off) for comparison.

literature [120].

While we do not yet have confirmation that we have demonstrated quantum-optical spectroscopy, our observations of weaker saturation for the scrambled realizations compared with transform-limited excitation are consistent with the Kira-Koch prediction. However, the OBE simulations performed in this chapter suggest that the suppression of polarization (and thus also suppression of the nonlinear scattering) can be explained by a simpler reason than suggested by the theory. It is possible that the longer temporal pulse duration (or lower peak intensity) is mainly responsible for the observed decrease in excitation-induced effects. To explore this hypothesis, we compare the effects of scrambled realizations to those of different pulse shapes.

Chapter 9

Quantum-well response to other pulse shapes

We found in the previous chapter that each scrambled realization produces decreased nonlinear effects on average in comparison to a transform-limited pulse excitation. The data may possibly validate the theoretical prediction that the coherence properties of the scrambled pulses influence the many-body configurations. However, since the phase-randomization technique also increases the time duration of the pulses (and consequently lowers the peak intensity), we consider the possibility that the longer duration may explain the observed decreased nonlinearities independent of the consequences of the statistics of the exciting light source.

To test this possibility, we create realizations with similar time duration as the scrambled realizations but with no statistical properties beyond that of a coherent state. In the simulations discussed in Chapter 8, pulse shapes other than scrambled light were shown to have effects similar to the phase-randomized realizations in a two-level system. While the case of narrowing the excitation spectrum produces a high population-to-polarization ratio in the simulations, it is difficult to compare this case to the scrambled realizations because the resonance condition is modified for a changed bandwidth [117]. Consequently, we examine the effects of a pulse sequence in comparison to the effects for the scrambled realizations.

9.1 Three-pulse (zero- Φ) excitation

To achieve a set of realizations to compare with the scrambled cases, we create a series of “zero- Φ ” masks with the same energy bin spacing as for the scrambled masks, $\Delta\omega_{\text{bin}} = 0.21$ meV. The mask type is illustrated in the frequency and time domains in Fig. 9.1. Our name for this set of masks describes the spectral phase square wave pattern with modulation amplitude Φ across the spectrum. In contrast to the random temporal nature of the scrambled realizations, the zero- Φ masks produce a simple series of three pulses in the time domain with even spacing. For this reason, we refer to the zero- Φ realizations in the time domain as “three-pulse” realizations. While the two-pulse sequence described above is a slightly simpler candidate for comparison, we experimentally determine that this realization results in a low efficiency, making tests in the nonlinear regime difficult. The three-pulse sequence has a higher efficiency, and powers comparable to the randomized-phase masks are achievable. We test the quantum-well (QW) response for a range of amplitude modulations Φ and shifts in the spectral location θ for the square-wave pattern, shown in Fig. 9.1.

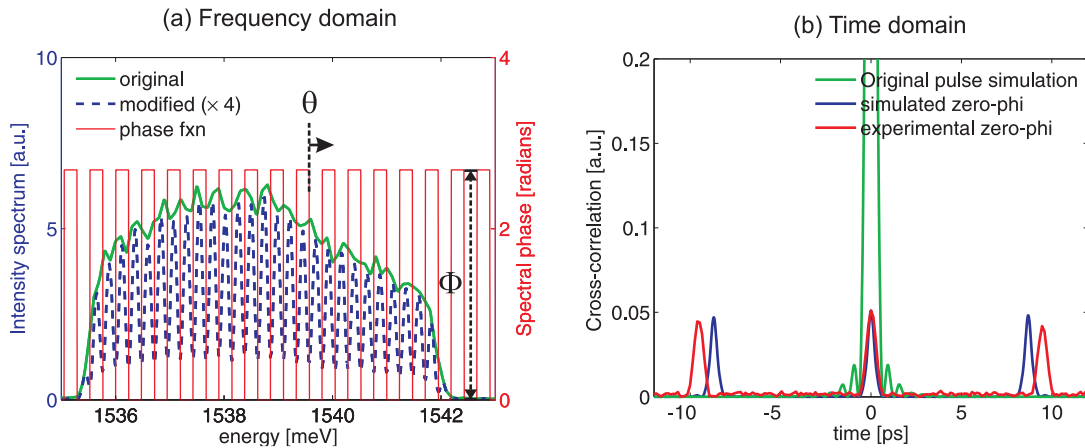


Figure 9.1: (a) Frequency and (b) time domain representations of a zero- Φ (or three-pulse) realization. The simulation is shown to roughly match the experimental cross-correlation data. In (a), the parameters θ and Φ are labeled as described in the text.

We measure cross-correlations of the three-pulse realizations to determine the time-domain intensity profiles, similar to Fig. 9.1. The realizations are ordered in three groups

of three realizations. All of the realizations exhibit a three-pulse sequence with the same relative delay between pulses. In the first group, with modulation between $\Delta\Phi = \pi/1.1$, the outer two pulses are stronger than the central pulse. In the central group, the amplitude of the spectral phase modulation was chosen ($\Delta\Phi = \pi/1.14$) such that the three pulses are approximately equal in intensity. This is the realization shown in Fig. 9.1. In the last group, with lower amplitude of modulation ($\Delta\Phi = \pi/1.3$), the central pulse is stronger than the outer two pulses. For each group, we shift the pattern by $\theta = 0, \frac{\pi}{2}$, and π . We find that the shifting θ has no effect on the cross-correlation. However, simulations (discussed around Fig. 7) show that the shift θ in the frequency domain leads to different relative temporal phases between the pulses in each sequence. For this reason, we try several θ shifts to see if this has any effect on the quantum-well (QW) system response.

We collect spectrally resolved transient-absorption data using these three-pulse realizations along with 13 scrambled phase masks for comparison. The procedure for data collection is the same as for the scrambled masks, discussed in Chapter 8. We apply each phase mask to the spectrally narrowed pump pulse, setting the pump power $P_{\text{IN}}^{\text{pump}}$ to a fixed input value selected from a matrix of five values. The input, reflected and transmitted powers are recorded to construct the power absorbed by the QW according to Eqn. 3.13. The power absorbed by the QW is proportional to the electron-hole density created by the pump realization. The nonlinear response of the probe transmitted through the sample is recorded at a delay of $\tau = 26.7$ ps. Zero delay ($\tau = 0$) corresponds to when the transform-limited pulse arrives. Since the probe reflection is quite small compared with the transmission, and the nonlinear effects we are searching for can be extracted from the transmitted pulse, we approximate the probe absorption to be $\alpha(\omega) \approx 1 - T(\omega)$; this allows measurements to be made in half the time.

We find that each of the three-pulse realizations produce similar QW probe responses that do not show a dependence on the amplitude Φ or shifting θ in the square-wave spectral phase pattern. The lack of dependence on the shifting θ means that the excitation

effects for this bin spacing are insensitive to the exact spectral position of the dips in amplitude as long as the total power is set to a constant. However, it is possible that for wider bin spacings (narrower time between the pulses), differences in relative temporal phases between pulses may give rise to measurable effects.

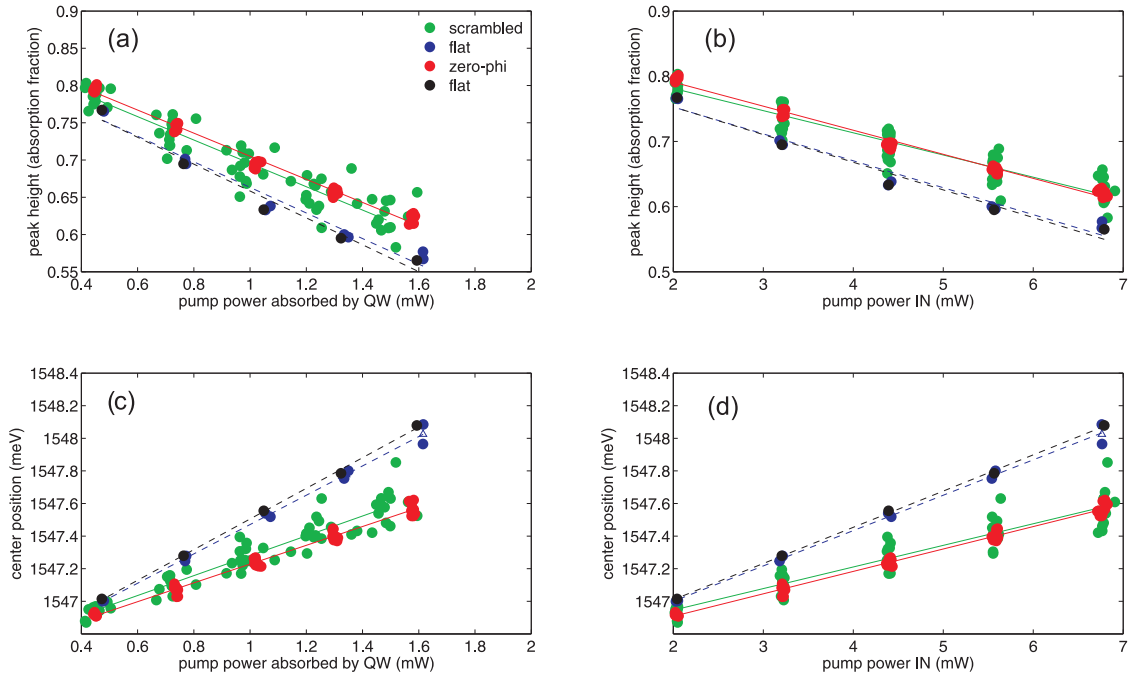


Figure 9.2: Nonlinear observables as a function of power. Peak heights are shown for varying (a) $P_{\text{QW}}^{\text{pump}}$ and (b) $P_{\text{QW}}^{\text{pump}}$. Center resonance positions are shown for varying (c) $P_{\text{QW}}^{\text{pump}}$ and (d) $P_{\text{QW}}^{\text{pump}}$.

The zero- Φ realizations produce very similar nonlinear probe responses compared to the scrambled phase masks for similar powers absorbed by the QW system. For the matrix of input powers used, we extract two observables of the nonlinear effects from the recorded probe absorption response: center position and peak height of the heavy-hole (HH) $1s$ exciton feature, as discussed in §3.4. We plot the observables extracted from the probe absorption as a function of the power absorbed by the QW system. Figure 9.2 shows the center positions and the peak heights of the HH $1s$ exciton as a function of power. The two sets of ‘flat mask’ shown in the figure (black and blue) are multiple measurements from transform-limited excitation to ensure repeatability. We find that there is less spread for the set of zero- Φ

realizations compared with the scrambled realization measurements. We perform a linear fit to each type of realization to see the trends more clearly. The fits show a statistically significant difference for both of these cases from the transform-limited case. Furthermore, the zero- Φ and scrambled realization measurements yield observables that are extremely close to each other. The absorption observables extracted from the probe absorption from the many-body state created by the zero- Φ realizations lie on the same line as the scrambled pulses for both observables, whether we view the observables as a function of the input pump power or of the pump power absorbed by the QW.

Although the zero- Φ and scrambled realizations produce similar results in terms of the nonlinearity, we noticed a difference between the results for the two sets. The fraction of the pump power which is absorbed by the QW for the scrambled pulses is lower on average than for the zero- Φ pulses. This difference in fractional absorption is shown in Fig. 9.3 by comparing the fraction of power absorbed by the QW ($P_{\text{QW}}^{\text{pump}}/P_{\text{IN}}^{\text{pump}}$) as a function of input power. The data reveals that a single scrambled phase mask realization from our set actually yields a higher absorbed fraction by the QW. However, the scrambled realizations have a lower fractional power absorbed by the QW on average compared with the both the zero- Φ and transform-limited (flat mask) realizations.

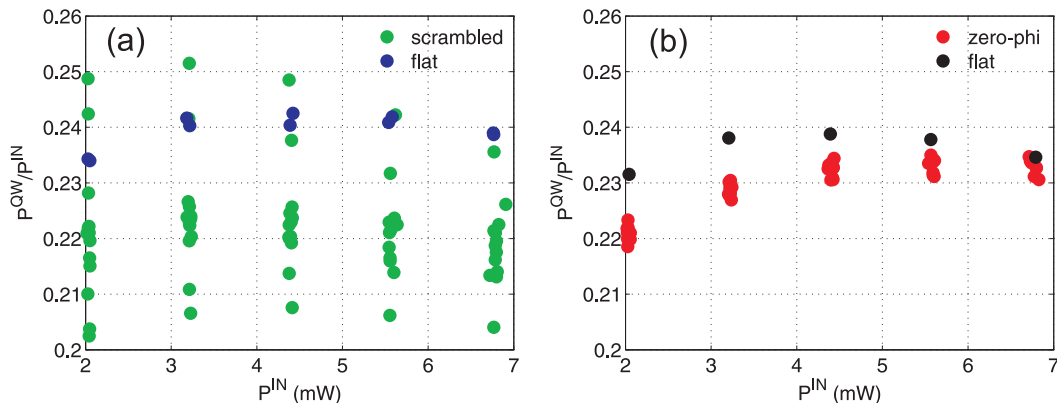


Figure 9.3: Fractional absorption by the QW system as a function of input power, shown for (a) scrambled realizations and (b) zero- Φ realizations.

We attempt to explain in the time domain the results for the zero- Φ realizations concerning the reduced nonlinearity compared with the transform-limited pulses and the close matching with the scrambled excitation. Since we now discuss the dynamics in the time domain, we refer to a zero- Φ realization as a three-pulse sequence.

Since the three-pulse sequence has similar time duration as the scrambled realizations and produces the same nonlinear effects, we hypothesize that the decreased nonlinear effect can be explained by the longer temporal duration of the realization. If the dynamics can be understood from a simple model, then it may be possible to predict the nonlinear effects for different pulse shapes (including the scrambled realizations) given a temporal intensity profile. To test this possible explanation for the measured decrease in nonlinearity, we compare the QW system time dynamics for a three-pulse sequence to the dynamics generated by a single transform-limited pulse.

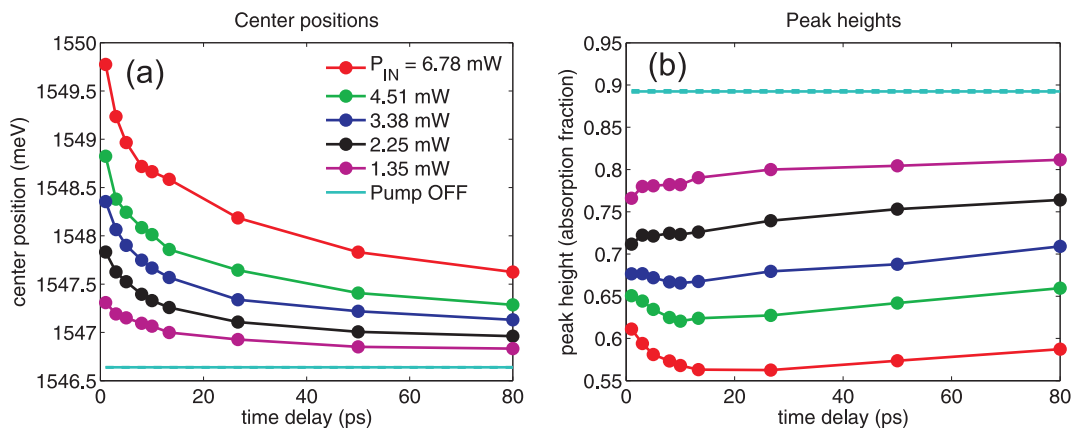


Figure 9.4: Temporal dynamics for observables of the probe absorption line shape: (a) center resonance position and (b) peak height of the HH $1s$ -resonance. The observables in the absence of any pump excitation are also shown (cyan lines).

We measure the probe absorption for the single-pulse transform-limited pump excitation using the previously described procedure but for a series of nine time delays τ as well as five pump powers. The results from this measurement are shown in Fig. 9.4. While the center positions exhibits similar decay patterns for each excitation density, the peak heights exhibit nontrivial behavior. We find that the peak heights decrease as a function of time for

the highest excitation densities before beginning to rise at longer delays. The lower excitation densities produce monotonically increasing peak heights as a function of time, as would be expected for a decay. The relaxation times are much slower for the peak height than for the center position.

To compare the single-pulse data to the three-pulse data, we extract parameters from the single-pulse dynamics and attempt to match the dynamics for a three-pulse sequence by a simulation based on the extracted decay parameters from the single-pulse case. Noticing a linear relationship between $P_{\text{QW}}^{\text{pump}}$ and the center position at time-zero for each pump power, we apply a linear transformation on the data in Fig. 9.4a to yield a measure of the nonlinearity in arbitrary units that sets the unexcited value near zero. The linear transformation is $\omega_{\text{center}} = A \times n + B$, where ω_{center} is the center resonance position, n is the measure of nonlinearity, $A = 1.9$ and $B = 1546.8$.

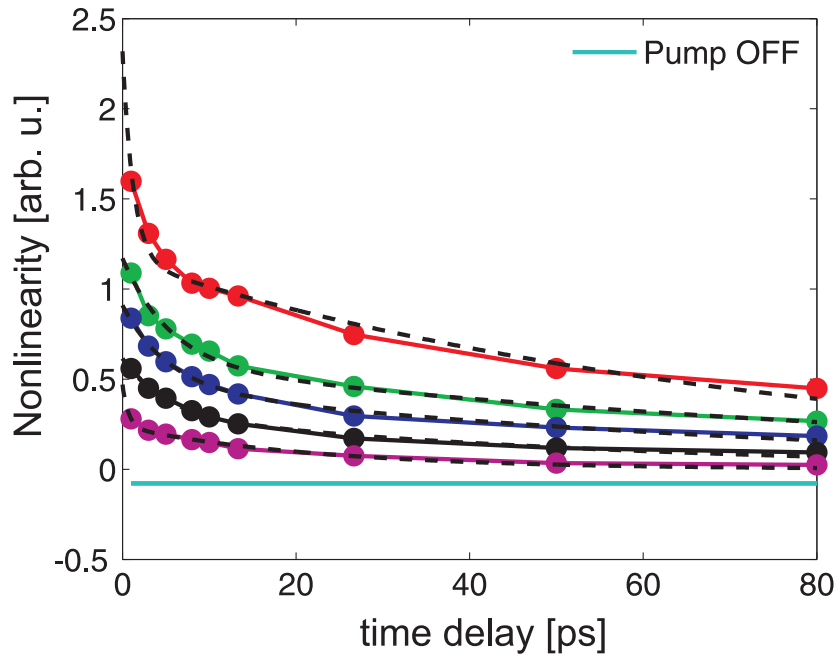


Figure 9.5: Dynamics of the nonlinearity for single-pulse excitation, shown with fits (black dashed lines) for the same powers as shown in Fig. 9.4. The nonlinearity in the absence of pump excitation is also shown (cyan line) near zero.

The fitting procedure for the single-pulse data involves finding decaying exponential

functions that best match each of the dynamics. We find that a single decaying exponential function is unable to fit the data accurately. As discussed in §2.7, we are aware that two time scales of decay processes are responsible for the relaxation: dephasing and interband recombination. Consequently, we fit the single-pulse nonlinearity dynamics with the sum of two decaying exponentials:

$$n(\tau) = n_0 (e^{-\gamma_{\text{pop}}\tau} + e^{-\gamma_{\text{pol}}\tau}), \quad (9.1)$$

with the parameters: n_0 , the initial nonlinearity generated at the moment the pump pulse arrives; γ_{pol} , the polarization decay (dephasing) time; and γ_{pop} , the recombination time (incoherent decay). The linear transformation of the center position dynamics to the nonlinear dynamics along with the fits are shown in Fig. 9.5. From the fits we extract the parameters in Eqn. 9.1.

We find from the single-pulse data that both the recombination time and coherent decay time exhibit a weak dependence on the pump intensity. The results of the fits from the single-pulse data are shown in Fig. 9.6. The average values of the decay parameters are $\gamma_{\text{pol}} = 0.211 \pm 0.076 \text{ ps}^{-1}$, and $\gamma_{\text{coh}} = 0.015 \pm 0.0067 \text{ ps}^{-1}$, corresponding to decay times of $T_{\text{pol}} = 4.7 \text{ ps}$ and $T_{\text{pop}} = 68.4 \text{ ps}$, respectively. We use these decay parameters from the single-pulse data to simulate the three-pulse data. The simulation includes the extracted decay parameters and models each of the three pulses as an impulse function that generates a nonlinearity proportional to its intensity.

To test how well the model predicts a sequence of pulses, we measure the parameter dynamics from a sequence of three pulses that are equal in intensity. For this realization, we set the power to $P_{\text{IN}}^{\text{pump}} = 6.73 \text{ mW}$, allowing comparison with the transformed limited pulse at $P_{\text{IN}}^{\text{pump}} = 2.25 \text{ mW}$. The comparison is reasonable since each of the three pulses each have approximately the same photon density as the transform-limited pulse ($6.73 \text{ mW}/3 \text{ pulses} = 2.24 \text{ mW/pulse}$). As a reminder, the photon density in a pulse is simply proportional to the average power (Eqn. 3.6). We record the probe absorption $\alpha_{\text{QW}}(\omega)$ for a matrix of delays

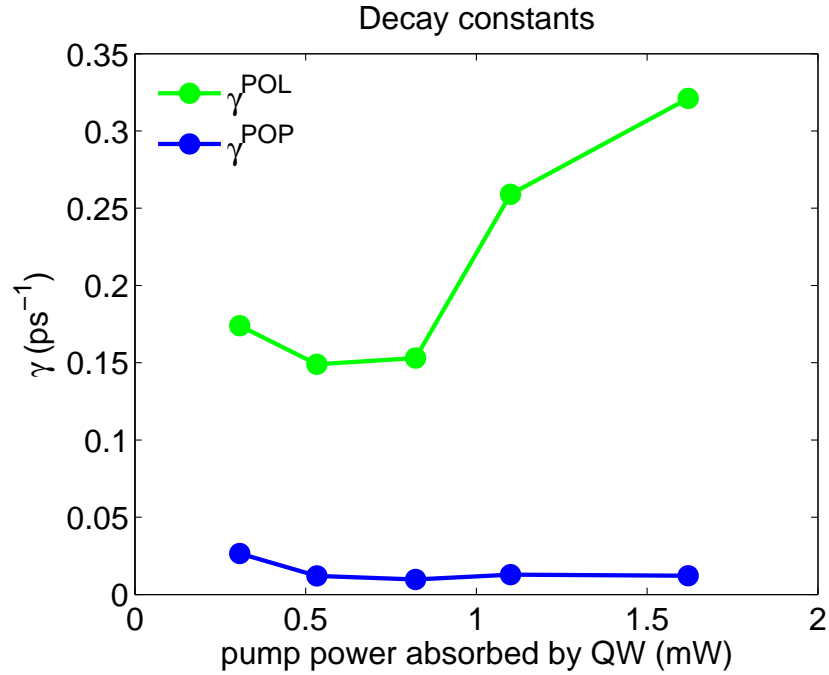


Figure 9.6: Decay parameters extracted from the single-pulse temporal data using Eqn. 9.1.

to capture the dynamics after each of the three pulses.

We observe similar decay behavior for the three-pulse data compared with the single-pulse data, shown in Fig. 9.7. The vertical green lines of the simulation indicate the arrival times of each pulse. After each pulse, the nonlinearity relaxes toward its “pump off” value.

We encounter challenges in matching the simulation with the three-pulse data. First, we notice that there is not the same fractional absorption for the second and third pulses. This fact implies that the fractional absorption depends on the excitation history. We account for the saturated behavior by fitting the function in Eqn. 9.1 to each of the three pulses and extrapolating on each curve to the moment each pulse arrives. With this procedure, we estimate the total absorption from all three pulses to be 1.36 mW. This estimate is close to the direct measurement of 1.55 mW ($= 0.23 \times 6.73$ mW), as shown in Fig. 9.3. However, even after correcting for saturation effects, we see that the rates of decay after the second and third pulse do not match those of the simulation. Namely, the decay times are also affected by the excitation history.

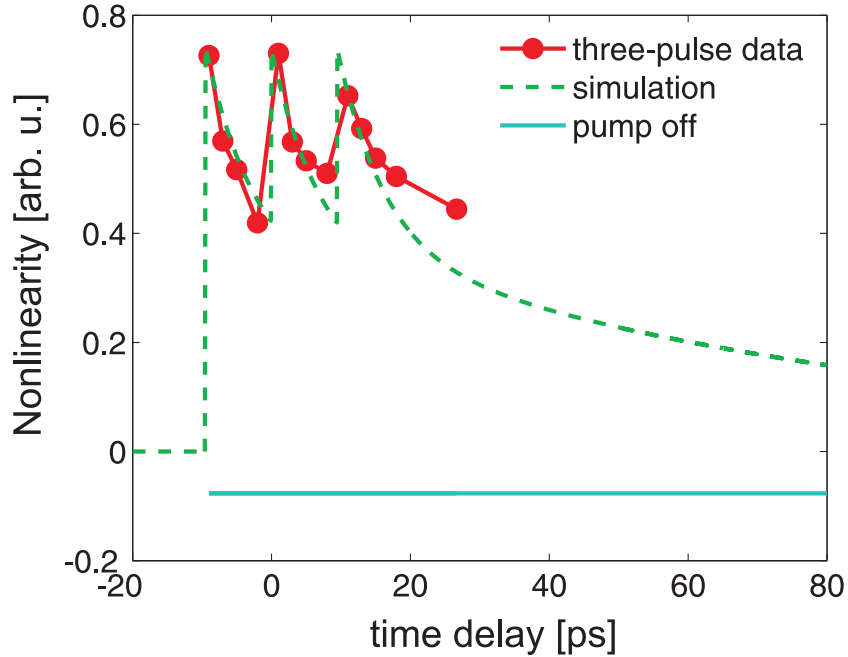


Figure 9.7: Nonlinearity dynamics for the three-pulse realization with a simulation that uses parameters from the single-pulse data and accounts for saturation behavior based on the three-pulse data. The poor fit suggests that the temporal dynamics are nontrivial.

These data with the simulations suggest that the temporal dynamics are both important and non-trivial. Since the theoretical computation that might explain the temporal dynamics for individual scrambled realizations or the three pulse sequence is too expensive, we are motivated to perform another experiment to reveal the nature of the temporal dynamics by using chirped pulses.

9.2 Chirped pulses

Seeing that the QW system response to excitation sources with wide temporal duration exhibits nontrivial behavior, we further characterize the system response by studying the effects of chirped pulses on the QW system dynamics. We have demonstrated in §7.7.2 that chirp (quadratic spectral phase) broadens pulses in time. We apply a range of positive and negative chirp parameters ranging from $\phi''(\omega_0)/2 = 0 \text{ meV}^{-2}$ up to $\phi''(\omega_0)/2 = \pm 5.8 \text{ meV}^{-2}$, corresponding to pulse durations ranging from $\Delta\tau_{\text{pump}} = 430 \text{ fs}$ to $\Delta\tau_{\text{pump}} = 10.8 \text{ ps}$. These

pulse durations are shown as a function of chirp parameter in Fig. 7.12. For each of these chirp parameters, we apply a quadratic phase mask to the pump spectrum, and then repeat the transient absorption measurement as described in §8.3 for a probe delay of $\tau = 13$ ps. For each realization, the input pump power $P_{\text{IN}}^{\text{pump}}$ is set to 7 mW. From the probe absorption spectra $\alpha(\omega)$, we extract the peak height and center position of the HH 1s-resonance using the procedure described in §3.4.

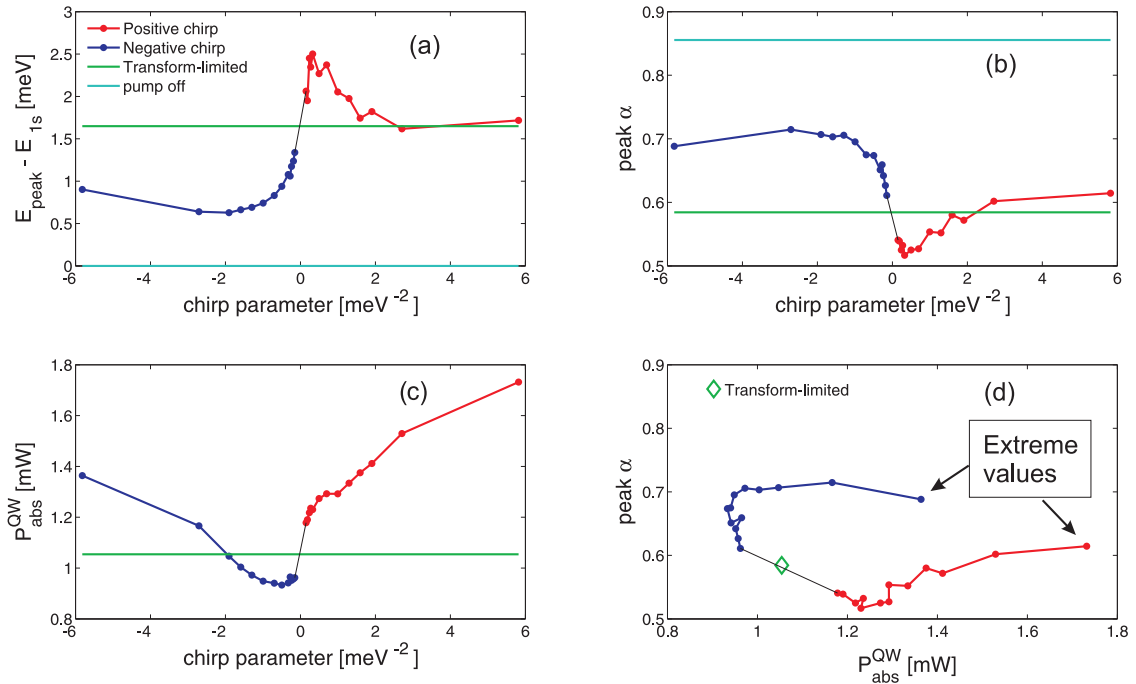


Figure 9.8: Measurements of the QW system response to chirped pulses. From the probe absorption, we extract (a) the peak resonance position and (b) the peak height. The observables in the absence of the pump light are shown for comparison (cyan lines). (c) The power absorbed by the QW exhibits nontrivial dependence on chirp parameter. (d) The nonlinear observables do not follow a simple trend with the absorbed powers. The extreme chirp parameter values at $\pm 5.8 \text{ meV}^{-2}$ are marked. All four frames show the measurement from the transform-limited case for comparison and the black lines guide the eye through the chirp values near $\phi''(\omega_0)/2 = 0 \text{ meV}^{-2}$.

The nonlinear probe measurements from the different chirped-pulse realizations, summarized in Fig. 9.8, demonstrate nontrivial dynamics. The nonlinear observables (higher nonlinearity = blue shifting and lower peak height) and the pump power absorption exhibit asymmetries with respect to the sign of chirp. The peak height and the center resonance position of the probe absorption for all measured values are strongly correlated, with a linear

relationship having coefficient of determination $R^2 = 0.974$. For negative chirp parameters (blue arrives first at the QW), the nonlinearities mostly decrease as with increasing chirp magnitude $|\phi''(\omega_0)/2|$ (with the exception of the most extreme value at $\phi''(\omega_0)/2 = -5.8$ meV $^{-2}$). The positive chirp case (red arrives first) shows stronger nonlinear behavior with increasing chirp up until $\phi''(\omega_0)/2 = 0.3$ meV $^{-2}$, followed by decreasing nonlinearity that levels off to roughly the transform-limited values. The pump power absorbed by the QW system (Fig. 9.8c) for negative chirp is lower than the transform-limited case (excepting the two extreme values). For positive chirp, the pump absorption is consistently higher than the transform-limited case and grows roughly linearly with chirp parameter. A plot of the peak height as a function of the power absorbed by the QW in Fig. 9.8d shows that the change in nonlinearity cannot be simply attributed to a change in the power absorbed by the QW since the different nonlinear effects happens for the same powers absorbed.

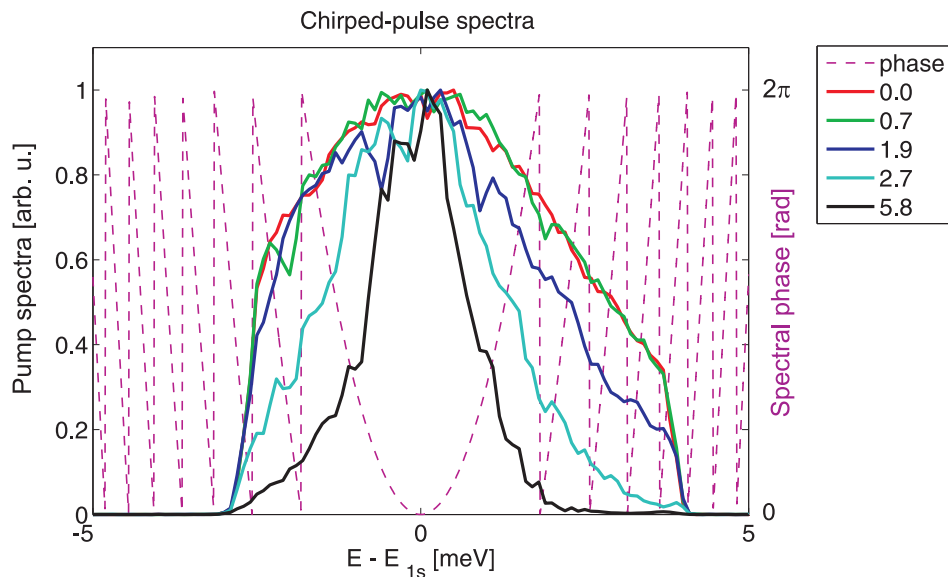


Figure 9.9: Spectra for a variety of spectral chirp parameters $\phi''(\omega_0)/2$ with units meV $^{-2}$ in the legend. Negative chirp parameters produce similar spectra. A quadratic spectral phase $\phi''(\omega_0)/2 = 1.9$ meV $^{-2}$ is also shown (dashed line).

To interpret these data, we also consider that for large chirp parameters the pump spectra are strongly modified. The modification for large chirp parameters results from rapid

changes in phase at the edges of the spectrum. The phase “wraps around” between 0 and 2π , resulting in sharp discontinuities in phase between adjacent pixels. These discontinuities diffract out the light at the spectrum edges according to the theory presented in §7.4. The spectral amplitude modulation becomes noticeable for chirp parameters beyond $|\phi''(\omega_0)/2| > 1 \text{ meV}^{-2}$.

Considering the probe data along with the pump spectra, we attribute the observed behavior to the pump-induced shifting of the center position of the resonance. For small chirp parameters ($|\phi''(\omega_0)/2| < 1 \text{ meV}^{-2}$), the pump spectra are not modified. Since the tendency of the resonance is to blue shift, the positive chirp enhances the nonlinearity for low chirp parameters. This is because the red part of the pump spectrum, arriving first, contributes to some blue shifting of the resonance, then the subsequent blue part of the spectrum is on resonance. Conversely, the negative chirp accomplishes the opposite. The blue part of the spectrum blue-shifts the resonance, causing the subsequent red part of the spectrum to be off resonance. This explains the observed nonlinearities for small chirp parameters.

For larger chirp parameters, the pump spectra become narrower, which changes the resonance condition. For positive chirp, the pump becomes less resonant with the HH 1s-resonance, thus weakening the nonlinearities. However, large values of negative chirp actually begin to *enhance* the nonlinearities even though the pump spectra are narrowed. Because of this, our interpretation is not complete.

The most surprising feature from this study of chirped pulses is that the positively chirped pulses, which are longer in time duration than the transform-limited pulse, can actually produce stronger nonlinearities than the transform-limited case. This fact indicates that the dynamics are complicated and that there is not a straight-forward relationship between the time duration of an excitation pulse and observed nonlinearities.

It is challenging to make a connection between the chirped pulses and the scrambled realizations because the bandwidth of the spectra are strongly modified for large chirp parameters, whereas the bandwidth for the scrambled realizations is not changed. However,

The results suggest that the system response is nontrivial and that analysis using microscopic theory may provide insight concerning the system dynamics in response to different pulse shapes.

Chapter 10

Conclusion

We have explored the nonlinear dynamics of excitons in a GaAs quantum-well (QW) system. The research is broken into two parts: (i) quantitative measurements of the Coulomb-induced nonlinearities, and (ii) a study of the system response to light statistics using pulse-shaping techniques.

Our quantitative measurements combined with a microscopic theory elucidate the many-body interactions that give rise to observed changes in the probe response. The many-body configurations matched by the theory for a variety of excitation conditions quantitatively demonstrate the effects of polarization selection and reveal system dynamics. Specifically, we find that Coulomb scattering of polarization with free-carrier densities dominates the excitation-induced shifting (EIS) and excitation-induced dephasing (EID) of the exciton resonance in our sample. Surprisingly, exciton populations do not significantly contribute to the nonlinear line shape. Strong transient gain is observed only under co-circular pump-probe conditions and is attributed to a transfer coherent transfer of energy between the pump and probe. The combination of experiment with theory provide the most complete description to date of the many-body effects that contribute to observed nonlinear responses.

The work described in Chapters 3–4 established that the nonlinearities are large enough to display light-statistic dependent excitation-induced (nonlinear) effects. To realize the first experimental demonstration of quantum-optical spectroscopy, where the nonlinear material response depends on the light statistics of the excitation source, we introduced a novel

experimental technique combined with a theoretical paradigm known as density-matrix ensemble averaging. We used pulse-shaping techniques to generate spectral-phase-randomized pulse realizations to create a many-body configuration in the QW system and measured the response with spectrally resolved transient absorption techniques described in Chapter 3. We found that single phase-randomized realizations saturated the exciton resonance less than for a transform-limited pulse, on average. An ensemble of probe measurements after phase-randomized realization excitation was averaged to construct the system response to an incoherent excitation source.

Experimental measurements are consistent with the prediction that incoherent excitation at the same excitation densities as transform-limited excitation leads to suppression of polarization (and thus a suppression of saturation effects). However, comparison of the system response to other pulse shapes suggests a simpler explanation for decreased nonlinearities than quantum-statistical fluctuations. We find that a sequence of pulses with similar time duration and excitation density, but with no statistical properties beyond that of a coherent state, yields a similar nonlinear response to phase-randomized realizations. This observation suggests that the observed decrease in saturation is primarily due to the increased time duration of the phase-randomized realizations. While a simpler explanation for the decreased nonlinearities observed in the system has been offered, the averaged experimental phase-randomized data may in fact represent a construction the system response to light excitation with incoherent statistics. This claim will be verified by further theoretical investigation.

10.1 Outlook

We are continuing work with our theorist collaborators to determine the meaning of the constructed system response involving density-matrix ensemble averaging techniques. However, it is also possible that the many-body interactions in our system are influenced by the light statistics of the optical excitation source in ways that we have not been measuring.

We propose a future experiment to further explore quantum-optical spectroscopy of GaAs QWs.

The experimental measurements reported in this thesis consist only of the transient probe response. However, the theory predicts more observable effects than just the suppression of scattering for incoherent excitation. Specifically, incoherent excitation is predicted to generate a macroscopic population of low-momentum states, shown in Fig. 5.9c. The photoluminescence from such a population is predicted to be directional and with incoherent quantum statistics.

Measurement of the photoluminescence properties could directly verify the Kira-Koch predictions for quantum-optical spectroscopy. This could be accomplished via time-resolved measurements of the quantum statistics and directionality of the photoluminescence. The photoluminescence must be time-resolved to separate it from the excitation light. Measurements of the photoluminescence with a balanced homodyne detection setup [121] allows for characterization of the quantum statistics. These additional measurements may give further evidence that phase-randomized pulses corroborate theoretical predictions for quantum-optical spectroscopy.

Bibliography

- [1] M. Fox, *Optical Properties of Solids* (Oxford University Press, Oxford, 2002).
- [2] G. W. Fehrenbach, W. Schfer, and R. G. Ulbrich, Excitonic versus plasma screening in highly excited gallium arsenide, *Journal of Luminescence* **30**, 154 (1985).
- [3] H. Wang, K. Ferrio, D. G. Steel, Y. Z. Hu, R. Binder, and S. W. Koch, Transient nonlinear optical response from excitation induced dephasing in GaAs, *Phys. Rev. Lett.* **71**, 1261 (1993).
- [4] N. Peyghambarian, H. M. Gibbs, J. L. Jewell, A. Antonetti, A. Migus, D. Hulin, and A. Mysyrowicz, Blue Shift of the Exciton Resonance due to Exciton-Exciton Interactions in a Multiple-Quantum-Well Structure, *Phys. Rev. Lett.* **53**, 2433 (1984).
- [5] , .
- [6] J. C. Kim, D. R. Wake, and J. P. Wolfe, Thermodynamics of biexcitons in a GaAs quantum well, *Phys. Rev. B* **50**, 15099 (1994).
- [7] M. Kira and S. Koch, Many-body correlations and excitonic effects in semiconductor spectroscopy, *Progress in Quantum Electronics* **30**, 155 (2006).
- [8] A. Linenberger, Data sheet for Linear Series Spatial Light Modulator, 2006, <http://www.bnonlinear.com/>.
- [9] A. M. Weiner, Femtosecond pulse shaping using spatial light modulators, *Review of Scientific Instruments* **71**, 1929 (2000).
- [10] D.-S. Kim, J. Shah, J. E. Cunningham, T. C. Damen, W. Schäfer, M. Hartmann, and S. Schmitt-Rink, Giant excitonic resonance in time-resolved four-wave mixing in quantum wells, *Phys. Rev. Lett.* **68**, 1006 (1992).
- [11] S. T. Cundiff, Coherent spectroscopy of semiconductors, *Opt. Express* **16**, 4639 (2008).
- [12] N. Peyghambarian, H. M. Gibbs, J. L. Jewell, A. Antonetti, A. Migus, D. Hulin, and A. Mysyrowicz, Blue Shift of the Exciton Resonance due to Exciton-Exciton Interactions in a Multiple-Quantum-Well Structure, *Phys. Rev. Lett.* **53**, 2433 (1984).

- [13] Y. Z. Hu, R. Binder, S. W. Koch, S. T. Cundiff, H. Wang, and D. G. Steel, Excitation and polarization effects in semiconductor four-wave-mixing spectroscopy, *Phys. Rev. B* **49**, 14382 (1994).
- [14] F. Jahnke *et al.*, Excitonic Nonlinearities of Semiconductor Microcavities in the Non-perturbative Regime, *Phys. Rev. Lett.* **77**, 5257 (1996).
- [15] J. M. Shacklette and S. T. Cundiff, Role of excitation-induced shift in the coherent optical response of semiconductors, *Phys. Rev. B* **66**, 045309 (2002).
- [16] S. Mukamel, *Principles of Nonlinear Optical Spectroscopy* (Oxford University Press, Oxford, 1999).
- [17] J. G. Gay, Screening of Excitons in Semiconductors, *Phys. Rev. B* **4**, 2567 (1971).
- [18] C. V. Shank, R. L. Fork, R. F. Leheny, and J. Shah, Dynamics of Photoexcited GaAs Band-Edge Absorption with Subpicosecond Resolution, *Phys. Rev. Lett.* **42**, 112 (1979).
- [19] J. Shah, Hot electrons and phonons under high intensity photoexcitation of semiconductors, *Solid-State Electronics* **21**, 43 (1978).
- [20] M. Brune, F. Schmidt-Kaler, A. Maali, J. Dreyer, E. Hagley, J. M. Raimond, and S. Haroche, Quantum Rabi Oscillation: A Direct Test of Field Quantization in a Cavity, *Phys. Rev. Lett.* **76**, 1800 (1996).
- [21] G. Rempe, H. Walther, and N. Klein, Observation of quantum collapse and revival in a one-atom maser, *Phys. Rev. Lett.* **58**, 353 (1987).
- [22] I. Schuster, A. Kubanek, A. Fuhrmanek, T. Puppe, P. W. H. Pinkse, K. Murr, and G. Rempe, Nonlinear spectroscopy of photons bound to one atom, *Nature Physics* **4**, 382 (2008).
- [23] F. Meier and B. P. Zakharchenya, *Optical Orientation* (North-Holland, Amsterdam, 1984).
- [24] J. Shah, *Ultrafast Spectroscopy of Semiconductors and Semiconductor Nanostructures* (Springer-Verlag, Berlin, 1996).
- [25] N. Sarukura, Y. Ishida, T. Yanagawa, and H. Nakano, All solid-state cw passively mode-locked Ti:sapphire laser using a colored glass filter, *Applied Physics Letters* **57**, 229 (1990).
- [26] A. L. S. J. Moss, *The Chemistry of the Semiconductor Industry* (Springer, New York, 1987).
- [27] R. F. Pierret, *Semiconductor Device Fundamentals* (Addison-Wesley, New York, 1996).

- [28] R. N. Hall, G. E. Fenner, J. D. Kingsley, T. J. Soltys, and R. O. Carlson, Coherent Light Emission From GaAs Junctions, *Phys. Rev. Lett.* **9**, 366 (1962).
- [29] Y. Suematsu, Advances in Semiconductor Lasers, *Physics Today* **38**, 32 (1985).
- [30] S. Schmitt-Rink, D. S. Chemla, and D. A. B. Miller, Linear and nonlinear optical properties of semiconductor quantum wells, *Advances in Physics* **38**, 89 (1989).
- [31] J. Davies, *The Physics of Low-Dimensional Semiconductors* (Cambridge University Press, Cambridge, 1998).
- [32] N. Peyghambarian, S. W. Koch, and A. Mysyrowicz, *Introduction to Semiconductor Optics* (Prentice Hall, New York, 1993).
- [33] O. Madelung, *Semiconductor Data Handbook* (Springer-Verlag, Berlin, 2006).
- [34] J. Singh, *Electronic and Optoelectronic Properties of Semiconductor Structures* (Cambridge University Press, Cambridge, 2003).
- [35] D. A. B. Miller, D. S. Chemla, D. J. Eilenberger, P. W. Smith, A. C. Gossard, and W. Wiegmann, Degenerate four-wave mixing in room-temperature GaAs/GaAlAs multiple quantum well structures, *Applied Physics Letters* **42**, 925 (1983).
- [36] S. W. Kirchoefer, J. N. Holonyak, K. Hess, D. A. Gulino, H. G. Drickamer, J. J. Coleman, and P. D. Dapkus, Absorption measurements at high pressure on AlAs-Al_xGa_{1-x}As-GaAs superlattices, *Applied Physics Letters* **40**, 821 (1982).
- [37] R. Dingle, W. Wiegmann, and C. H. Henry, Quantum States of Confined Carriers in Very Thin Al_xGa_{1-x}As-GaAs-Al_xGa_{1-x}As Heterostructures, *Phys. Rev. Lett.* **33**, 827 (1974).
- [38] D. Chemla, D. Miller, P. Smith, A. Gossard, and W. Wiegmann, Room temperature excitonic nonlinear absorption and refraction in GaAs/AlGaAs multiple quantum well structures, *Quantum Electronics, IEEE Journal of* **20**, 265 (1984).
- [39] R. L. Greene, K. K. Bajaj, and D. E. Phelps, Energy levels of Wannier excitons in GaAs-Al_xGa_{1-x}As quantum-well structures, *Phys. Rev. B* **29**, 1807 (1984).
- [40] G. Bastard, E. E. Mendez, L. L. Chang, and L. Esaki, Exciton binding energy in quantum wells, *Phys. Rev. B* **26**, 1974 (1982).
- [41] G. Bastard, *Wave Mechanics Applied to Semiconductor Heterostructures* (Halsted Press, New York, 1988).
- [42] D. J. Griffiths, *Introduction to Quantum Mechanics* (Prentice Hall, New York, 1994).
- [43] L. Yang, I. V. Schweigert, S. T. Cundiff, and S. Mukamel, Two-dimensional optical spectroscopy of excitons in semiconductor quantum wells: Liouville-space pathway analysis, *Phys. Rev. B* **75**, 125302 (2007).

- [44] H. Haug and S. W. Koch, *Quantum Theory of the Optical and Electronic Properties of Semiconductors, 5th Ed.* (World Scientific Publ., Singapore, 2009).
- [45] J. J. Sakurai, *Modern Quantum Mechanics* (Addison-Wesley, New York, 1994).
- [46] M. Scully and M. S. Zubairy, *Quantum Optics* (Oxford University Press, Oxford, 1997).
- [47] R. Boyd, *Nonlinear Optics, 3rd Ed.* (Academic Press, New York, 2008).
- [48] D. J. Griffiths, *Introduction to Electrodynamics* (Prentice Hall, New York, 1999).
- [49] M. Fox, *Quantum Optics* (Oxford University Press, Oxford, 2006).
- [50] C. F. Klingshirn, *Semiconductor Optics, 3rd Ed.* (Springer, New York, 2006).
- [51] D. Oberhauser, K.-H. Pantke, J. M. Hvam, G. Weimann, and C. Klingshirn, Exciton scattering in quantum wells at low temperatures, *Phys. Rev. B* **47**, 6827 (1993).
- [52] T. Müller, W. Parz, F. F. Schrey, G. Strasser, and K. Unterrainer, Intraband relaxation of photoexcited electrons in GaAs/AlGaAs quantum wells and InAs/GaAs self-assembled quantum dots, *Semiconductor Science and Technology* **19**, S287 (2004).
- [53] A. G. V. Spivey and S. T. Cundiff, Inhomogeneous dephasing of heavy-hole and light-hole exciton coherences in GaAs quantum wells, *J. Opt. Soc. Am. B* **24**, 664 (2007).
- [54] A. Tokmakoff, Introductory Quantum Mechanics II lecture notes, 2009, <http://ocw.mit.edu/OcwWeb/Chemistry/5-74Spring-2009/LectureNotes/>.
- [55] J. D. J. Ingle and S. R. Crouch, *Spectrochemical Analysis* (Prentice Hall, New York, 1988).
- [56] M. D. Sturge, Optical Absorption of Gallium Arsenide between 0.6 and 2.75 eV, *Phys. Rev.* **127**, 768 (1962).
- [57] D. A. B. Miller, D. S. Chemla, T. C. Damen, A. C. Gossard, W. Wiegmann, T. H. Wood, and C. A. Burrus, Electric field dependence of optical absorption near the band gap of quantum-well structures, *Phys. Rev. B* **32**, 1043 (1985).
- [58] G. D. Gilliland, D. J. Wolford, T. F. Kuech, and J. A. Bradley, Luminescence kinetics of intrinsic excitonic states quantum-mechanically bound near high-quality (*n*-type GaAs)/(*p*-type Al_xGa_{1-x}As) heterointerfaces, *Phys. Rev. B* **49**, 8113 (1994).
- [59] S. M. Landi, C. V.-B. Tribuzy, P. L. Souza, R. Butendeich, A. C. Bittencourt, and G. E. Marques, Photoluminescence of GaAs/Al_xGa_{1-x}As multiple quantum well structures containing δ -doping superlattices, *Phys. Rev. B* **67**, 085304 (2003).
- [60] T. Zhang, C. Borca, X. Li, and S. Cundiff, Optical two-dimensional Fourier transform spectroscopy with active interferometric stabilization, *Opt. Express* **13**, 7432 (2005).

- [61] X. Li, T. Zhang, C. N. Borca, and S. T. Cundiff, Many-Body Interactions in Semiconductors Probed by Optical Two-Dimensional Fourier Transform Spectroscopy, *Phys. Rev. Lett.* **96**, 057406 (2006).
- [62] D. Karaiskaj, A. D. Bristow, L. Yang, X. Dai, R. P. Mirin, S. Mukamel, and S. T. Cundiff, Two-Quantum Many-Body Coherences in Two-Dimensional Fourier-Transform Spectra of Exciton Resonances in Semiconductor Quantum Wells, *Phys. Rev. Lett.* **104**, 117401 (2010).
- [63] A. D. Bristow, D. Karaiskaj, X. Dai, T. Zhang, C. Carlsson, K. R. Hagen, R. Jimenez, and S. T. Cundiff, A versatile ultrastable platform for optical multidimensional Fourier-transform spectroscopy, *Review of Scientific Instruments* **80**, 073108 (2009).
- [64] B. Deveaud, F. Clérot, N. Roy, K. Satzke, B. Sermage, and D. S. Katzer, Enhanced radiative recombination of free excitons in GaAs quantum wells, *Phys. Rev. Lett.* **67**, 2355 (1991).
- [65] D.-S. Kim, J. Shah, D. A. B. Miller, T. C. Damen, W. Schäfer, and L. Pfeiffer, Femtosecond-pulse distortion in quantum wells, *Phys. Rev. B* **48**, 17902 (1993).
- [66] F. T. S. Scandolo, Optical Bistability Induced by Charge Separation in Asymmetric Quantum Wells, *physica status solidi (b)* **173**, 453 (1992).
- [67] Grosso, G., Graves, J., Hammack, A., High, A., Butov, L., Hanson M., and Gossard, A., Excitonic switches operating at around 100 K, *Nature Photonics* **3**, 577 (2009).
- [68] A. A. High, E. E. Novitskaya, L. V. Butov, M. Hanson, and A. C. Gossard, Control of Exciton Fluxes in an Excitonic Integrated Circuit, *Science* **321**, 229 (2008).
- [69] K. M. M. Nakayama, Interactions between coherent optical phonons and excitonic quantum beats in GaAs/AlAs multiple quantum wells: strategy for enhancement of terahertz radiation from coherent optical phonons, *physica status solidi (c)* **5**, 2911 (2008).
- [70] R. J. Walters *et al.*, Photovoltaically powered modulating retroreflectors, *Optical Engineering* **45**, 034003 (2006).
- [71] M. Mazzer *et al.*, Progress in quantum well solar cells, *Thin Solid Films* **511-512**, 76 (2006), eMSR 2005 - Proceedings of Symposium F on Thin Film and Nanostructured Materials for Photovoltaics - EMRS 2005- Symposium F.
- [72] H. Azuma, Quantum computation with Kerr-nonlinear photonic crystals, *Journal of Physics D: Applied Physics* **41**, 025102 (2008).
- [73] A. I. Shkrebtii, J. L. P. Hughes, J. E. Sipe, and O. Pulci, Linear and non-linear spectroscopy of GaAs and GaP: theory versus experiment, *Thin Solid Films* **313-314**, 574 (1998).

- [74] S. Wachter, M. Maute, H. Kalt, I. Galbraith, C. Sieh, T. Meier, and S. W. Koch, Excitation induced shift and broadening of the exciton resonance, *Physica B: Condensed Matter* **314**, 309 (2002).
- [75] S. Hunsche, K. Leo, H. Kurz, and K. Köhler, Femtosecond intersubband relaxation in GaAs quantum wells, *Phys. Rev. B* **50**, 5791 (1994).
- [76] D. Morris, D. Houde, B. Deveaud, and A. Regreny, Ultrafast dynamics of intersubband relaxation in GaAs quantum wells: hot carrier and phonon populations effects, *Superlattices and Microstructures* **15**, 309 (1994).
- [77] S. Schmitt-Rink, D. S. Chemla, and D. A. B. Miller, Theory of transient excitonic optical nonlinearities in semiconductor quantum-well structures, *Phys. Rev. B* **32**, 6601 (1985).
- [78] F. Jahnke *et al.*, Excitonic Nonlinearities of Semiconductor Microcavities in the Non-perturbative Regime, *Phys. Rev. Lett.* **77**, 5257 (1996).
- [79] C. Kittel, *Introduction to Solid State Physics, 7th Ed.* (Wiley, New York, 1995).
- [80] G. Tränkle, E. Lach, M. Walther, A. Forchel, and G. Weimann, Optical investigation of 2D Mott transitions in GaAs/GaAlAs quantum well structures, *Surface Science* **196**, 584 (1988).
- [81] G. R. H. Reinholz, Mott effect and screening in quantum well structures, *Contributions to Plasma Physics* **43**, 346 (2003).
- [82] G. W. Fehrenbach, W. Schfer, and R. G. Ulbrich, Excitonic versus plasma screening in highly excited gallium arsenide, *Journal of Luminescence* **30**, 154 (1985).
- [83] D. R. Wake, H. W. Yoon, J. P. Wolfe, and H. Morkoç, Response of excitonic absorption spectra to photoexcited carriers in GaAs quantum wells, *Phys. Rev. B* **46**, 13452 (1992).
- [84] H. Haug and S. Schmitt-Rink, Electron theory of the optical properties of laser-excited semiconductors, *Progress in Quantum Electronics* **9**, 3 (1984).
- [85] L. Banyai and S. W. Koch, Absorption Blue Shift in Laser-Excited Semiconductor Microspheres, *Phys. Rev. Lett.* **57**, 2722 (1986).
- [86] W. W. Chow, A. F. Wright, A. Girndt, F. Jahnke, and S. W. Koch, Microscopic theory of gain for an InGaN/AlGaIn quantum well laser, *Applied Physics Letters* **71**, 2608 (1997).
- [87] J. C. Kim and J. P. Wolfe, Bose-Einstein statistics of an excitonic gas in two dimensions: Excitons and biexcitons in a GaAs quantum well, *Phys. Rev. B* **57**, 9861 (1998).
- [88] R. C. Miller, D. A. Kleinman, A. C. Gossard, and O. Munteanu, Biexcitons in GaAs quantum wells, *Phys. Rev. B* **25**, 6545 (1982).

- [89] D. A. Kleinman, Binding energy of biexcitons and bound excitons in quantum wells, *Phys. Rev. B* **28**, 871 (1983).
- [90] C. Ell, J. Prineas, T. R. Nelson, S. Park, H. M. Gibbs, G. Khitrova, S. W. Koch, and R. Houdré, Influence of Structural Disorder and Light Coupling on the Excitonic Response of Semiconductor Microcavities, *Phys. Rev. Lett.* **80**, 4795 (1998).
- [91] S. Adachi, GaAs, AlAs, and $\text{Al}_x\text{Ga}_{1-x}\text{As}$: Material parameters for use in research and device applications, *Journal of Applied Physics* **58**, R1 (1985).
- [92] J. Verdeyen, *Laser Electronics* (Prentice Hall, New York, 1995).
- [93] J. D. Jackson, *Classical Electrodynamics* (Wiley, New York, 1999).
- [94] M. Kira and S. W. Koch, Quantum-optical spectroscopy of semiconductors, *Phys. Rev. A* **73**, 013813 (2006).
- [95] M. Lindberg and S. W. Koch, Effective Bloch equations for semiconductors, *Phys. Rev. B* **38**, 3342 (1988).
- [96] M. Kira and S. W. Koch, Exciton-Population Inversion and Terahertz Gain in Semiconductors Excited to Resonance, *Phys. Rev. Lett.* **93**, 076402 (2004).
- [97] G. Khitrova, H. M. Gibbs, F. Jahnke, M. Kira, and S. W. Koch, Nonlinear optics of normal-mode-coupling semiconductor microcavities, *Rev. Mod. Phys.* **71**, 1591 (1999).
- [98] S. W. Koch, M. Kira, G. Khitrova, and H. M. Gibbs, Semiconductor excitons in new light, *Nature Materials* **5**, 523 (2006).
- [99] C. Sieh *et al.*, Coulomb Memory Signatures in the Excitonic Optical Stark Effect, *Phys. Rev. Lett.* **82**, 3112 (1999).
- [100] J. Goodman, *Statistical Optics* (Wiley-Interscience, New York, 1985).
- [101] R. H. Brown and R. Q. Twiss, A Test of a New Type of Stellar Interferometer on Sirius, *Nature* **178**, 1046 (1956).
- [102] R. Loudon, *The Quantum Theory of Light* (Oxford University Press, Oxford, 2003).
- [103] E. M. Purcell, The Question of Correlation between Photons in Coherent Light Rays, *Nature* **178**, 1449 (1956).
- [104] B. L. Morgan and L. Mandel, Measurement of Photon Bunching in a Thermal Light Beam, *Phys. Rev. Lett.* **16**, 1012 (1966).
- [105] R. J. Glauber, The Quantum Theory of Optical Coherence, *Phys. Rev.* **130**, 2529 (1963).
- [106] C. Gerry and P. Knight, *Introductory Quantum Optics* (Cambridge University Press, Cambridge, 2005).

- [107] M. Kira, S.W.Koch, G. Khitrova, and H. Gibbs, Direct Optical Excitation of Quantum-Degenerate Exciton States in Semiconductors, submitted 2004, arXiv:cond-mat/0408453/.
- [108] R. Smith, J. Wahlstrand, A. Funk, R. Mirin, S. Cundiff, J. Steiner, M. Schafer, M. Kira, and S. Koch, Extraction of many-body configurations from nonlinear absorption in semiconductor quantum wells, *Phys. Rev. Lett.* .
- [109] G. Rempe, H. Walther, and N. Klein, Observation of quantum collapse and revival in a one-atom maser, *Phys. Rev. Lett.* **58**, 353 (1987).
- [110] M. Born, E. Wolf, A. B. Bhatia, and P. C. Clemmow, *Principles of Optics: Electromagnetic Theory of Propagation, Interference and Diffraction of Light* (Cambridge University Press, Cambridge, 2000).
- [111] Y. S. Liu, Nanosecond pulse generation from a self-injected laser-pumped dye laser using a novel cavity-flipping technique, *Opt. Lett.* **3**, 167 (1978).
- [112] C. Cruz, E. Palange, and F. D. Martini, High power subnanosecond pulse generation in Nd YAG lasers, *Optics Communications* **39**, 331 (1981).
- [113] N. N. Puscas, D. Scarano, R. Girardi, and I. Montrosset, Analysis of output statistics of single and double pass Er-doped LiNbO₃ waveguide amplifiers, *Optical and Quantum Electronics* **29**, 799 (1997).
- [114] W. S. Wong, H. A. Haus, L. A. Jiang, P. B. Hansen, and M. Margalit, Photon statistics of amplified spontaneous emission noise in a 10-Gbit/s optically preamplified direct-detection receiver, *Opt. Lett.* **23**, 1832 (1998).
- [115] S. M. Kira, Quantum-optical spectroscopy with phase-randomized femtosecond pulses, private correspondence, 2006.
- [116] J. Wheeler and W. Zurek, *Quantum Theory and Measurement* (Princeton University Press, Princeton, NJ, 1984).
- [117] J. Diels and W. Rudolph, *Ultrashort Laser Pulse Phenomena* (Elsevier, Burlington, 2006).
- [118] P. A. Roos, X. Li, R. P. Smith, J. A. Pipis, T. M. Fortier, and S. T. Cundiff, Solid-state carrier-envelope phase stabilization via quantum interference control of injected photocurrents, *Opt. Lett.* **30**, 735 (2005).
- [119] M. Orszag, *Quantum Optics* (Springer, Berlin, 2008).
- [120] M. Kira and S. W. Koch, Cluster-expansion representation in quantum optics, *Phys. Rev. A* **78**, 022102 (2008).
- [121] D. F. McAlister and M. G. Raymer, Ultrafast photon-number correlations from dual-pulse, phase-averaged homodyne detection, *Phys. Rev. A* **55**, R1609 (1997).

Appendix A

Double chop method for probe measurements

To optimally record the probe spectrum in the presence and absence of the pump, we develop a novel technique involving an optical chopper. We send the pump and probe beams through the chopper wheel, as shown in Fig. A.1, so that they are modulated at slightly different frequencies that have a fixed phase relationship. There are 30 slots for the outer radius, and 25 slots for the inner radius. The pump beam, traveling through the outer path, is modulated at $f_{\text{pump}} = 2.12$ kHz, whereas the probe beam, traveling the inner path, is modulated at $f_{\text{probe}} = 1.76$ kHz.

The pump and probe beams travel along different paths before converging onto the sample. We then spectrally resolve the probe reflection and transmission and collect the signal using a photodetector. The signal present on the photodetector is a combination of the probe response, scattered pump light, and a signal resulting from the interaction between the two beams. We want to extract the probe spectra in both the presence of and absence of the pump, which involves considering the Fourier components involved. We filter out these components by means of a lock-in detector (Stanford Research Systems, commercial product SR-830). The lock-in detection technique involves narrow-band active filtering to extract the Fourier component of interest from a signal that may contain a large amount of noise or other undesirable signals. The collected signal modulated at frequency f_{probe} contains a mix of the probe response in the presence of, or absence of, the pump since the pump and probe are chopped at slightly different frequencies.

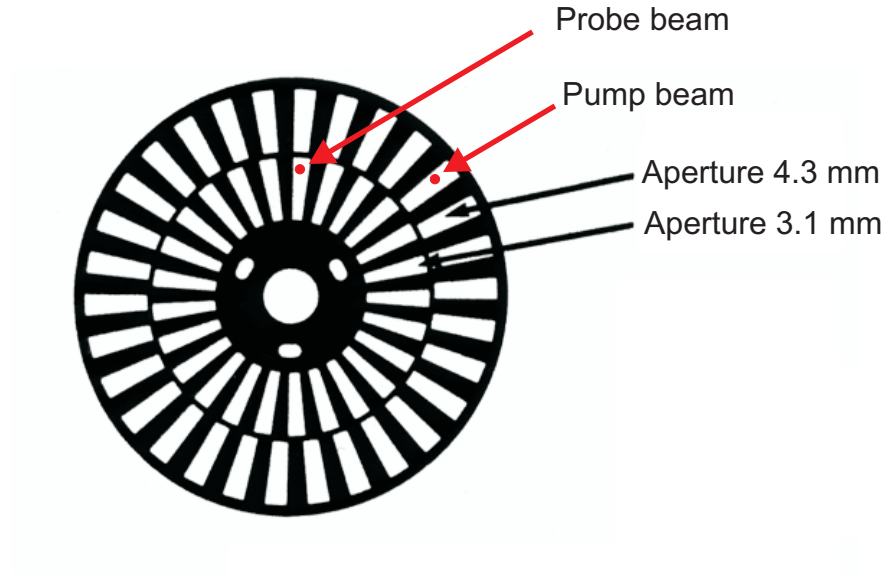


Figure A.1: Schematic shown for pump and probe beams traveling perpendicular to the plane of the optical chopper wheel. As the wheel spins, the pump and probe beams are modulated at slightly different frequencies, a critical aspect to resolving the probe spectra in the presence and absence of the pump.

A nontrivial amount of pump light, $I_{\text{scattered}}^{\text{pump}}$, scatters in the direction of the probe reflection and transmission. Since we modulate the pump light at a different frequency than the probe, we use the chopping frequency modulation in addition to lock-in detection to ignore the scattered-pump-light contribution to the probe signal. Since the time scale of interaction inside the sample is on the order of picoseconds, the interaction signal, $\Delta I_{\text{interaction}}^{\text{probe}}$, depends only on moments when the pump and probe are both present on the sample.

As we will demonstrate, analyzing the frequency contents of these contributions allows the extraction of the probe signal in the presence of the pump, $I_{\text{pumpON}}^{\text{probe}}$, and the probe signal in the absence of the pump, $I_{\text{pumpOFF}}^{\text{probe}}$. The chopping creates square waves that can be represented as Fourier expansions. The signal measured on a photodetector will produce a current with many frequency components ω_i :

$$I_i(t) = \frac{1}{2} + \frac{2}{\pi} \left[\sin(\omega_i t) + \frac{1}{3} \sin(3\omega_i t) + \frac{1}{5} \sin(5\omega_i t) + \frac{1}{7} \sin(7\omega_i t) + \dots \right], \quad (\text{A.1})$$

where $\omega_i/2\pi$ is the chopper modulation frequency f_{pump} or f_{probe} . Since we detect the signal using lock-in detection, we can filter specific frequency components to construct our final

result.

We find the total signal that appears on an oscilloscope (keeping only the first two terms of the Fourier expansion since we filter out the higher harmonics contributing to the square wave) to be

$$I_{\text{total}}^{\text{probe}} = I_{\text{pump OFF}}^{\text{probe}} \left[\frac{1}{2} + \frac{2}{\pi} \sin(\omega_{\text{probe}} t) \right] + I_{\text{scattered}}^{\text{pump}} \left[\frac{1}{2} + \frac{2}{\pi} \sin(\omega_{\text{pump}} t) \right] + \Delta I_{\text{interaction}}^{\text{probe}} \left[\frac{1}{2} + \frac{2}{\pi} \sin(\omega_{\text{probe}} t) \right] \left[\frac{1}{2} + \frac{2}{\pi} \sin(\omega_{\text{pump}} t) \right]. \quad (\text{A.2})$$

Expanding the coefficient of $\Delta I_{\text{interaction}}^{\text{probe}}$ through multiplication, we find two terms at additional frequencies: the sum, $\omega_{\text{probe}} + \omega_{\text{pump}}$, and the difference, $\omega_{\text{probe}} - \omega_{\text{pump}}$. Because of the symmetry of the multiplication (in the pump and probe), these two frequencies contain identical information. We choose to use the sum frequency (3.88 kHz) because there is less noise at higher frequencies. We isolate the sum frequency as a reference signal by sending the ω_{probe} and ω_{pump} transistor-transistor logic (TTL) reference signals from the optical chopper through an XNOR logical gate in combination with active and passive filtering. We enumerate the contributions to the intensity measured in the probe direction at each frequency of interest:

$$I_{\text{DC}} = \frac{1}{2} I_{\text{pump OFF}}^{\text{probe}} + \frac{1}{2} I_{\text{scattered}}^{\text{pump}} + \frac{1}{4} \Delta I_{\text{interaction}}^{\text{probe}}, \quad (\text{A.3})$$

$$I_{\omega_{\text{probe}}} = \frac{2}{\pi} I_{\text{pump OFF}}^{\text{probe}} + \frac{1}{\pi} \Delta I_{\text{interaction}}^{\text{probe}}, \quad (\text{A.4})$$

$$I_{\omega_{\text{pump}}} = \frac{2}{\pi} I_{\text{scattered}}^{\text{pump}} + \frac{1}{\pi} \Delta I_{\text{interaction}}^{\text{probe}}, \quad (\text{A.5})$$

$$I_{\omega_{\text{sum}}} = -\frac{2}{\pi^2} \Delta I_{\text{interaction}}^{\text{probe}}, \quad (\text{A.6})$$

$$I_{\omega_{\text{diff}}} = \frac{2}{\pi^2} \Delta I_{\text{interaction}}^{\text{probe}} \quad (\text{A.7})$$

$$(\text{A.8})$$

where DC means is the time-independent piece at $\omega = 0$, $\omega_{\text{sum}} = \omega_{\text{probe}} + \omega_{\text{pump}}$, and $\omega_{\text{diff}} = \omega_{\text{probe}} - \omega_{\text{pump}}$. We neglect signals at the DC component and at ω_{diff} . From the

remaining quantities, we combine the intensities to construct $I_{\text{pump ON}}^{\text{probe}}$ and $I_{\text{pump OFF}}^{\text{probe}}$:

$$I_{\text{pump OFF}}^{\text{probe}} = \frac{\pi}{2} \left(I_{\omega_{\text{probe}}} + \frac{\pi}{2} I_{\omega_{\text{sum}}} \right), \quad (\text{A.9})$$

$$I_{\text{pump ON}}^{\text{probe}} = I_{\text{pump OFF}}^{\text{probe}} + \Delta I_{\text{interaction}}^{\text{probe}}, \quad (\text{A.10})$$

where

$$\Delta I_{\text{interaction}}^{\text{probe}} = \frac{-\pi^2}{2} I_{\omega_{\text{sum}}}. \quad (\text{A.11})$$

The ability to simultaneously measure the probe signal in the presence and absence of the pump is important for a high-accuracy calibration of the probe transmission and reflection probabilities, as explained in Appendix B.

Appendix B

Calibration of the pump and probe powers

To construct the true absorption $\alpha(\omega) = 1 - T(\omega) - R(\omega)$ for the pump and probe beams, it is necessary to record the transmission $T(\omega)$ and reflection $R(\omega)$ probabilities as accurately as possible. For both the pump and probe powers, we correct for interface reflection losses. Additionally, the simultaneous measurement of the probe signal in the presence and absence of the pump allows calibration of the probe signal in the presence of the pump.

B.1 Correction for reflection losses

In order to correct for the reflection losses at interfaces in our experiment, we consider the geometry of the experimental setup. We record the optical probe power going in ($P_{\text{IN}}^{\text{meas}}$) to the cryostat and the reflected (P_R^{meas}) and transmitted (P_T^{meas}) powers from the sample with a Coherent GS Fieldmaster power meter. However, because of reflection losses inside the cryostat, it is necessary to introduce correction factors to accurately construct the true reflection and transmission probabilities from the sample. We do not introduce a correction factor for the measured input power, but the P_R and P_T powers are corrected by considering all losses starting from before the cryostat until after the cryostat. This procedure allows accurate construction of the reflection and transmission probabilities, $T = P_R^{\text{meas}}/P_{\text{IN}}^{\text{meas}}$ and $T = P_T^{\text{meas}}/P_{\text{IN}}^{\text{meas}}$.

The schematic for the light path is shown in Fig. B.1. The figure shows the multiple

interfaces at which the beam experiences losses due to reflection at an interface between two materials with different indices of refraction. The sample is mounted onto a wedged sapphire disc, which has an antireflection (AR) coating on surface 1 (surf1). An AR coating is applied to the sample after being mounted to surface 2 (surf2) of the sapphire disc to suppress multiple reflections within the material, as discussed in §3.1. Since surface 2 of the sapphire disc is unavoidably also coated with an AR coat designed for the interface between GaAs and vacuum, we expect surface 2 to have a higher reflection probability at our optical wavelength of 800 nm.

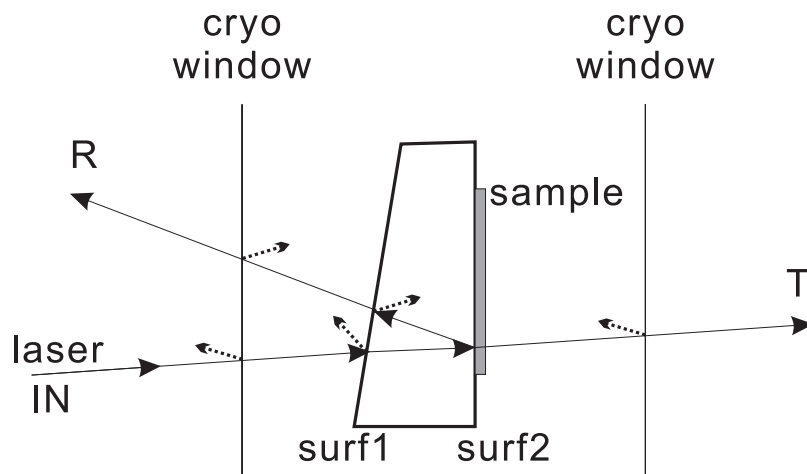


Figure B.1: Schematic for light path going into and out of the cryostat. We account for reflection losses at interfaces (dotted lines) to construct the true transmission and reflection probabilities.

We perform a procedure to determine the reflection probabilities from the sapphire windows and the cryostat windows. We first remove the sample and mount to measure the powers $P_{\text{IN,cryo}}^{\text{meas}}$ and $P_{\text{T,cryo}}^{\text{meas}}$ for the cryostat windows only. Since the beam passes through two cryostat windows, this measurement allows for the induction of the reflection probability (the fractional loss) of a single cryostat window as $R_{\text{Cryo Window}} = 0.0049$.

We then replace the sample mount to measure the powers P_R^{meas} and P_T^{meas} from surface 2 of the sapphire window. The measured reflection and probabilities are given by

$$R_{\text{sapph}}^{\text{meas}} = P_R/P_{\text{IN}} = 0.1033 \quad (\text{B.1})$$

$$T_{\text{sapph}}^{\text{meas}} = P_T/P_{\text{IN}} = 0.8455. \quad (\text{B.2})$$

Combining the measured values with a consideration of the reflection losses from each interface, we relate the measured powers through two coupled equations containing the reflection probabilities of both surfaces of the sapphire disc:

$$R_{\text{sapph}}^{\text{meas}} = (1 - R_{\text{Cryo Window}}^{\text{meas}})(1 - R_{\text{surf1}}^{\text{meas}})^2(R_{\text{surf2}}^{\text{meas}}) = 0.1033, \quad (\text{B.3})$$

$$T_{\text{sapph}}^{\text{meas}} = (1 - R_{\text{Cryo Window}}^{\text{meas}})(1 - R_{\text{surf1}}^{\text{meas}})(1 - R_{\text{surf2}}^{\text{meas}}) = 0.8455. \quad (\text{B.4})$$

Since $R_{\text{Cryo Window}}$ is determined from an independent measurement, these two equations can be then solved for R_{surf1} and R_{surf2} . Solving these equations we find two pairs of solutions, one of which is unphysical. We thus find the values $R_{\text{surf1}} = 0.0378$ and $R_{\text{surf2}} = 0.1127$, consistent with our earlier assertion that surface 2 should have a higher reflectance.

So far, we have only considered measurements through the sapphire (no measurements through the sample up to this point). We use the extracted reflection probabilities $R_{\text{Cryo Window}}$ and R_{surf1} to account for the reflection losses for measurements involving the sample. The AR-coated sapphire surface R_{surf2} is irrelevant here because the sapphire interface under the sample is not coated. Accounting for the reflection losses incurred in the transmission and reflection paths for measurements involving the sample, we derive the conversion equations that estimate the reflected and transmitted powers:

$$P_{\text{IN}}^{\text{est}} = P_{\text{IN}}^{\text{meas}}, \quad (\text{B.5})$$

$$\begin{aligned} P_R^{\text{est}} &= facR \times P_R^{\text{meas}} \\ &= \frac{P_R^{\text{meas}}}{(1 - R_{\text{surf1}})^2 (1 - R_{\text{Cryo Window}})^2} = 1.091P_R^{\text{meas}}, \end{aligned} \quad (\text{B.6})$$

$$\begin{aligned} P_T^{\text{est}} &= facT \times P_T^{\text{meas}} \\ &= \frac{P_T^{\text{meas}}}{(1 - R_{\text{Cryo Window}})^2 (1 - R_{\text{surf1}})} = 1.050P_T^{\text{meas}}. \end{aligned} \quad (\text{B.7})$$

The correction factors $facR$ and $facT$ correct for the losses that happen throughout the cryostat, including the path of the input beam. If the laser is spectrally resolved, $P_{R,T}^{est}(E)$ may be divided by $P_{IN}^{est}(E)$ to obtain the estimated transmission and reflection probabilities:

$$R_{\text{sample}}^{\text{est}} = \frac{P_{R(\text{sample})}^{\text{est}}(E)}{P_{IN}^{\text{est}}(E)}, \quad (\text{B.8})$$

$$T_{\text{sample}}^{\text{est}} = \frac{P_{T(\text{sample})}^{\text{est}}(E)}{P_{IN}^{\text{est}}(E)}. \quad (\text{B.9})$$

$$(\text{B.10})$$

While the correction factors $facR$ and $facT$ are determined by using measurements involving the sapphire interfaces only, they are valid for determining transmission and reflection probabilities for the sample as well.

We test for energy conservation using the measured and corrected values for the sapphire disc. The measured fraction of energy lost (written as absorption α) due to reflections from the sapphire interface is

$$\alpha_{\text{sapphire}}^{\text{meas}} = \frac{P_{IN}^{\text{meas}} - P_R^{\text{meas}} - P_T^{\text{meas}}}{P_{IN}^{\text{meas}}} = 0.0513. \quad (\text{B.11})$$

We find that the application of the correction factors yields a fractional energy loss of

$$|\alpha_{\text{sapphire}}^{\text{est}}| = \frac{P_{IN}^{\text{est}} - P_R^{\text{est}} - P_T^{\text{est}}}{P_{IN}^{\text{est}}} < 10^{-6}, \quad (\text{B.12})$$

consistent with our expectations for a material with vanishing imaginary part of the index of refraction. The balance of energy for the estimated absorption for the sapphire disc implies that the conversion strategy accounts for the powers properly.

The correction factors $facR$ and $facT$ are valid for application to both the pump and probe beams. Applying the correction factors to the measurements of the reflected and transmitted low-intensity probe powers from the sample at 4 K in the absence of the pump,

we find:

$$P_{\text{IN}}^{\text{est}} = 25\mu\text{W}, \quad (\text{B.13})$$

$$P_{R(\text{sapph})}^{\text{est}} = \text{fac}R \times P_{R(\text{sapph})}^{\text{meas}} = 1.091(0.1025P_{\text{IN}}^{\text{est}}) = 0.1118P_{\text{IN}}^{\text{meas}}, \quad (\text{B.14})$$

$$P_{T(\text{sapph})}^{\text{est}} = \text{fac}T \times P_{T(\text{sapph})}^{\text{meas}} = 1.050(0.845482P_{\text{IN}}^{\text{est}}) = 0.8878P_{\text{IN}}^{\text{meas}}. \quad (\text{B.15})$$

$$P_{R(\text{sample})}^{\text{est}} = \text{fac}R \times P_{R(\text{sample})}^{\text{meas}} = 1.091(0.035P_{\text{IN}}^{\text{est}}) = 0.0382P_{\text{IN}}^{\text{meas}}, \quad (\text{B.16})$$

$$P_{T(\text{sample})}^{\text{est}} = \text{fac}T \times P_{T(\text{sample})}^{\text{meas}} = 1.050(0.53P_{\text{IN}}^{\text{est}}) = 0.5567P_{\text{IN}}^{\text{meas}}. \quad (\text{B.17})$$

$$(\text{B.18})$$

The pump powers may be corrected for reflection losses in an identical fashion, allowing estimations of the densities created in the sample by pump excitation.

The above probe values are helpful in calibration of the probe powers in the presence of the pump, as we show in the next section.

B.2 Calibration of probe powers in the presence of the pump

The probe power is spectrally resolved using a scanning monochromator, as described in Chapter 3. We wish to record the effects of different pump excitation configurations (such as intensity and time delay) in the probe absorption. The probe absorption can be constructed as $\alpha(\omega) = 1 - T(\omega) - R(\omega)$, provided that we find $T(\omega)$ and $R(\omega)$ accurately. We describe in this section a procedure for ensuring the accuracy of these measurements.

In the last section, we arrived at estimates for the reflected and transmitted probe powers from the sample at 4 K in the absence of the pump. These powers are constant throughout a measurement containing many pump excitation configurations because the probe is at low-intensity. Since the double-chopping technique described in Appendix A allows simultaneous measurement of the probe power in the presence and absence of the pump light, we can exploit Eqns. B.16 and B.17 to calibrate the probe power in the presence of the pump light.

The probe light is measured by a photodetector placed after the scanning monochromer. A spectrally resolved signal $I(\omega)$ is measured on a photodetector (a current proportional to optical power) with high resolution for the full frequency range of the probe spectrum. The signal can be split according Appendix A into two parts, $I_{\text{pump OFF}}^{\text{probe}}(\omega)$ and $I_{\text{pump ON}}^{\text{probe}}(\omega)$, representing the probe signal in the absence and presence of the pump light, respectively. Since we have estimated the transmitted and reflected powers from the sample for the probe, we can construct conversion factors by normalizing the measured transmitted and reflected probe signals:

$$C^\lambda = \frac{I_{\text{pump OFF}}^{\text{probe},\lambda}(\omega)}{\int I_{\text{pump OFF}}^{\text{probe},\lambda}(\omega)d\omega} P_{\lambda(\text{sample})}^{\text{est}}, \quad (\text{B.19})$$

where $\lambda = R, T$ corresponds to the reflected and transmitted probe. The factors C^λ converts the measured signal into units of power:

$$P_{\text{pump OFF}}^{\text{probe},\lambda}(\omega) = C^\lambda I_{\text{pump OFF}}^{\text{probe},\lambda}(\omega). \quad (\text{B.20})$$

The same factor can also be used to convert the measured probe signal in the presence of the pump light into units of power because both signals are captured simultaneously. Consequently, the part of the spectrally resolved signal from the photodetector after the monochromer that corresponds to the probe power in the presence of the pump can be calibrated by

$$P_{\text{pump ON}}^{\text{probe},\lambda}(\omega) = C^\lambda I_{\text{pump ON}}^{\text{probe},\lambda}(\omega). \quad (\text{B.21})$$

In addition to providing a convenient calibration of the probe powers, this technique makes the experimental measurements insensitive to small pointing fluctuations in the probe beam at the monochromer. Small pointing fluctuations were found to affect the measurements on a long-term (hours) scale for the measurements. The use of this calibration technique corrects for any long-term drifts in power, thus removing the effects from pointing instabilities in the probe beam.